

**UNIVERSITY OF NOTTINGHAM**

**Advanced ROCOF Protection of Distribution  
Systems**

by

**Bohan Liu**

A thesis submitted in partial fulfillment for the  
degree of Doctor of Philosophy

in the

Faculty of engineering

Department of Electrical and Electronic Engineering

March 2012

# Abstract

When islanding occurs, power supply from the main grid is interrupted which causes a problem when distributed generators continue to provide power into distributed networks. An islanding situation should be detected accurately soon after the island is formed. Because failure to trip the islanded distributed resource can lead to a number of problems for the resource and the connected load. Although ROCOF islanding detection method is the most commonly employed anti-islanding protection technique, it provides fast detection and easily implementation. It is sensitive to the system disturbance. Therefore, the application of the ROCOF relay to detect system islanding has been limited.

This thesis proposes a solution to enhance the performance of the ROCOF relay by cooperation with rate of change of power or  $v^2/p$  interlock function. During system load variation, the false operation of ROCOF relay can be blocked effectively. It is validated by applied in grid-connected synchronous generator, Doubly-fed Induction generator (both simulation and experiment) and microgrid. The principle of rate of change of power or  $v^2/p$  interlock function are presented in this thesis. The new interlock function  $v^2/p$  with ROCOF relays works well for different types of DGs within a short detection time without introducing perturbation into the system, which are the advantages over other active and hybrid islanding detection methods. The performances characteristics of ROCOF relays for DGs islanding detection (i.e. frequency measuring methods, measuring windows, generator inertia constant, relay settings and load power factor) are investigated. In addition, two other islanding detection methods (impedance measurement (active method) and the Total Harmonic Distortion Method) are applied to the grid-connected DFIG distributed system, the comparison and effectiveness of these two methods utilized in islanding and load changing conditions are also discussed.

## **Publications by the author**

This work resulted in the publication of a number of academic papers:

B.Liu, D.Thomas, K.Jia, and M.Woolfson, “Advanced ROCOF Protection of Synchronous Generator”, 2011 IEEE PES Innovative Smart Grid Technologies (ISGT), 17-19 Jan 2011, Anaheim, US.

B.Liu, D.Thomas, “ROCOF Protection in distributed system with noise and non-linear load”, 2011 10th Environment and Electrical Engineering (EEEIC), 8-11 May 2011, Rome, Italy.

B.Liu, D.Thomas, “New Islanding Detection Method for DFIG Wind Turbines”, 2011 4th Electric Utility Deregulation and Restructuring and Power Technologies (DRPT), 6-9 July 2011, YanTai, China.

B.Liu, D.Thomas, and K.Jia, “Impedance Estimation and the Total Harmonic Distortion Methods for Islanding Detection” Submitted and has been accepted to the IEEE COMPEL 2012 13th Workshop on Control and Modelling for Power Electronics, February, 2012.

B.Liu, D.Thomas, K.Jia, A.Goodman, and C.Gereda, “Advanced ROCOF Protection of DFIG generator” Submitted to the IEEE Journal of on Power Delivery, March, 2012.

# Acknowledgement

It is an honour for me to express my heartily thankful to Dr. Dave Thomas, my supervisor, whose patience, kindness, as well as his constant encouragement, professional guidance and unwavering support have been invaluable to me. His inspiration and assistance during my whole research stage has sustained me through frustration and depression. Without his illuminating instruction, expert suggestion and insightful criticism, the completion of this thesis would not have been possible.

Besides, I would like to give special thanks to Dr. Ke Jia, Dr. Andrew Goodman, Dr. Chris Gerada, Professor. Mark Sumner who have provided me with project directions and technical supports in the experiment. In addition, I am indebted to many staffs in the School of Electrical and Electronic Engineering who have given me directly and indirectly help throughout this research.

Last but not least, I owe my deepest gratitude to my beloved parents, grandparents and my aunt for their loving considerations and strong confidence in me. My parents have been a constant source of support-emotional, moral and of course financial. Without them I could not have moved forward, dealt with the difficulties and achieved what I have today. I am also grateful to all my friends in Nottingham, for enriching my life experience during the many years I stayed there.

# Content

<b>Chapter 1</b> .....	<b>1</b>
<b>Introduction</b> .....	<b>1</b>
1.1 Distributed Generation.....	1
1.1.1 Wind Power System.....	2
1.1.2 Photovoltaic System.....	2
1.2 Electric Island Formed by Distributed Generators .....	3
1.3 Detection of Islanded Power System .....	6
1.4 Non-Detection Zone and Associated Risks .....	8
1.5 Objective of the Research Project.....	12
1.6 Thesis Structure and Contents .....	12
<b>Chapter 2</b> .....	<b>15</b>
<b>Islanding Detection Methods</b> .....	<b>15</b>
2.1 Introduction.....	15
2.2 Remote Islanding Detection Methods.....	16
2.2.1 Transfer Trip Scheme.....	16
2.2.2 Power Line Signaling Scheme .....	17
2.3 Local Detection Techniques .....	18
2.3.1 Passive Methods.....	19
2.3.1.1 Rate of Change of Output Power.....	20
2.3.1.2 Under/over Voltage and Under/over Frequency Relay .....	22
2.3.1.3 Voltage Surge Relays .....	24
2.3.1.4 Rate of Change of Frequency over Rate of Change of Power ..	26
2.3.1.5 Detection of Voltage Unbalance .....	26
2.3.1.6 Directional Reactive Power Detection .....	28
2.3.1.7 Comparison of Rate of Change of Frequency (COROCOF).....	29
2.3.1.8 Discussion on Passive Methods.....	30
2.3.2 Active methods.....	31
2.3.2.1 Detection of Impedance at a Specific Frequency .....	32
2.3.2.2 Slip Mode Frequency Shift method.....	32
2.3.2.3 Robust Islanding Detection Algorithm.....	33
2.3.2.4 Sandia Voltage Shift (SVS) Method .....	35

2.3.2.5 Automatic Phase Shift Method.....	35
2.3.2.6 PF Technique.....	37
2.3.2.7 Other Active Methods .....	38
2.3.3 Hybrid .....	39
2.3.3.1 Technique Based on Positive Feedback (PF) and Voltage Unbalance (UV).....	39
2.3.3.2 A Hybrid of Method Based on ROCOF, ROCOV and CF .....	40
2.3.3.3 A Hybrid of Method Based on Using Average Rate of Change of Voltage and Real Power Shift .....	41
2.4 Summary .....	41
<b>Chapter 3.....</b>	<b>43</b>
<b>ROCOF Protection of Synchronous Generator.....</b>	<b>43</b>
3.1 Introduction.....	43
3.2 The Principle of ROCOF Relays .....	44
3.2.1 Basic Theory .....	44
3.2.2 Analytical Formulas for Determining the Performance of ROCOF Relays.....	47
3.3 Frequency Estimation Methods .....	49
3.3.1 Fast Fourier Transform .....	49
3.3.2 The Prony’s Method.....	51
3.4 Simulation Results .....	55
3.4.1 Islanding.....	55
3.4.2 Non-islanding.....	64
3.4.2.1 Basic Principle of the Rate of Change of Power .....	66
3.4.2.2 System with Induction Motor Load.....	66
3.4.2.3 Simulation Results of ROCOF Relay with Rate of Change of power Interlock Function .....	68
3.5 Summary.....	70
<b>Chapter 4.....</b>	<b>72</b>
<b>Advanced ROCOF Protection of DFIG Wind Generator .....</b>	<b>72</b>
4.1 Introduction.....	72
4.2 Doubly-fed Induction Generator for Wind Turbines .....	73
4.2.1 The Comparison of Doubly-fed Induction Generator with Other Wind Turbine Systems .....	75

4.3 The Dynamic Operation for Double-fed Induction Generator .....	76
4.3.1 Steady State Equivalent Circuit of DFIG.....	76
4.3.2 The Dynamic Equation for Double-fed Induction Generator .....	77
4.4 Vector Control of PWM Voltage Source Converter.....	81
4.4.1 Vector Control Scheme for Grid-side PWM Voltage Source Converter.....	82
4.4.1.1 Inner Current Control Loop Design .....	86
4.4.1.2 Design of the PI-controller in the DC-link Voltage Control Loop .....	88
4.5 Performances of the Control Schemes.....	94
4.5.1 Performances of Current Control Loops .....	94
4.5.2 Performance of the DC-link Voltage Control Loop.....	96
4.6 Simulation Results .....	96
4.6.1 Islanding.....	96
4.6.2 False Operation .....	100
4.7 Summary.....	106
<b>Chapter 5.....</b>	<b>108</b>
<b>DFIG Islanding Experiment.....</b>	<b>108</b>
5.1 Introduction.....	108
5.2 Basic Theory .....	109
5.3 Experiment Setup.....	110
5.3.1 Experimental Prototype.....	110
5.3.1.1 Main Power PCB .....	111
5.3.1.2 Active Front End .....	114
5.3.1.3 The Switch Box .....	115
5.3.1.4 DFIG.....	116
5.3.1.5 Prime Mover.....	117
5.3.1.6 DC Voltage Supply and Speed Measurement Equipment.....	118
5.3.1.7 Software Development .....	118
5.4 Implementing the Test .....	120
5.5 Test Results.....	122
5.5.1 Islanding Test Results .....	122
5.5.1.1 Results of 3kW Load Islanding Test .....	122
5.5.1.2 Results of 2kW Load Islanding Test .....	127

5.5.2 Load Variation Test Results.....	129
5.5.2.1 Results of 3kW Load Variation Test.....	129
5.5.2.2 Results of 1kW Load variation test.....	131
5.6 Summary.....	133
<b>Chapter 6.....</b>	<b>135</b>
<b>Islanding Detection Method for Microgrid.....</b>	<b>135</b>
6.1 Introduction.....	135
6.2 Islanding Detection for Grid-connected PV System.....	137
6.2.1 Effects of Islanding for Grid-connected PV system.....	137
6.2.1 Grid-Connected Inverter Modelling.....	138
6.3 Simulation results.....	140
6.3.1 Case One.....	140
6.3.2 Case Two.....	145
6.4 Summary.....	145
<b>Chapter 7.....</b>	<b>147</b>
<b>Impedance Estimation and Total Harmonic Distortion Methods for Islanding Detection.....</b>	<b>147</b>
7.1 Introduction.....	147
7.2 Impedance Estimation Method for Islanding Detection.....	148
7.2.1 Transient Injection Principle.....	148
7.2.2 Single Phase System Studied.....	151
7.2.3 Impedance Estimation Method Used in DFIG Wind Generation Grid-connected Distributed System.....	155
7.3 The Proposed Method of THD.....	158
7.4 Comparison of the Impedance Estimation and the Total Harmonic Distortion Method.....	163
7.5 Summary.....	165
<b>Chapter 8.....</b>	<b>167</b>
<b>Conclusions and Future Work.....</b>	<b>167</b>
8.1 Research objectives.....	167
8.2 Conclusions.....	168
8.2.1 Objective 1.....	168
8.2.2 Objective 2.....	169
8.2.3 Objective 3.....	170

8.2.4 Objective 4 .....	171
8.3 Future Work.....	171
<b>Reference .....</b>	<b>176</b>
<b>Appendix A.....</b>	<b>186</b>
<b>Synchronous Generator Model .....</b>	<b>186</b>
<b>Appendix B.....</b>	<b>188</b>
<b>Controller Parameters for Grid-connected Inverter .....</b>	<b>188</b>
<b>Appendix C.....</b>	<b>189</b>
<b>Islanding Detection for Microgrid .....</b>	<b>189</b>

# List of Figures

Fig.1.1 Global wind power cumulative capacity-with forecast.....	2
Fig.1.2 Typical distribution system with distributed generators .....	3
Fig.1.3 Eltra service area. 47 local CHP units, larger than 2MW each, with a production of 347 MW were tripped as a result of a true phase fault. It is unknown how many units smaller than 2MW that were tripped.....	5
Fig.1.4 The impact of non-detection zone for islanding detection .....	9
Fig.2.1 Islanding Detection Techniques .....	16
Fig.2.2 A power line signaling scheme .....	17
Fig.2.3 Power circuit structural of DG coupled to utility grid with RLC load. 19	
Fig.2.4 The algorithm to detect an islanding state.....	21
Fig.2.5 PV array as DG source connected to utility .....	22
Fig.2.6 Frequency relay computational model .....	24
Fig.2.7 Equivalent circuit of a synchronous generator in parallel with utility. 25	
Fig.2.8 Internal and terminal voltage phasors: (a) before the opening of CB; (b) after the opening of CB .....	25
Fig.2.9 Generator operating and trip characteristic.....	29
Fig.2.10 Algorithm for robust islanding detection method .....	34
Fig.2.11 Algorithm for APS method .....	37
Fig.3.1 Equivalent circuit of an embedded generator operating in parallel with utility.....	45
Fig.3.2 Simplified schematic diagram of ROCOF .....	45
Fig.3.3 Model implemented for system frequency estimation .....	46
Fig.3.4 The frequency (top) and the rate of change of frequency estimation (bottom) by using FFT method.....	54
Fig.3.5 The frequency (top) and the rate of change of frequency estimation (bottom) by using Prony's method. ....	54
Fig.3.6 Single line diagram of test system .....	55
Fig.3.7 a) The rate of change of frequency estimation by Fast Fourier Transform Method and the Prony's method with different length of data processing window. ( $\Delta p=33\%$ , $H=1.5s$ , $\beta=-1$ ) b) The rate of change of frequency estimation by Fast Fourier Transform Method and the Prony's method with same length of data processing window.....	56

Fig.3.8 Power imbalance versus detection time by using Fast Fourier Transform and the Prony's method with different length of data processing window .....	57
Fig.3.9 Power imbalance versus detection time by using Fast Fourier Transform and the Prony's method with same length of data processing window .....	58
Fig.3.10 The detection time versus power imbalance by using the Fast Fourier Transform method with different relay setting.....	59
Fig.3.11 Comparison of the rate of change of frequency using different measuring windows .....	60
Fig.3.12 The detection time versus power imbalance by using Fast Fourier Transform method with different generator inertia .....	61
Fig.3.13 The detection time versus power imbalance for different load power factor.....	62
Fig.3.14 ROCOF tripping signal and $df/dt$ (system with 5% band-limited white noise) .....	62
Fig.3.15 ROCOF tripping signal and $df/dt$ (system with 10MW non-linear load).....	63
Fig.3.16 Single-line test system (adding or shedding load) .....	65
Fig.3.17. a) b) c) d) the rate change of power of islanding (negative power imbalance ( $\Delta p = -0.5$ ), positive power imbalance ( $\Delta p = 0.5$ ) non-islanding (add load ( $\Delta p = -0.5$ ), load shedding ( $\Delta p = 0.5$ )) .....	65
Fig.3.18 The waveform of rate of change of power in the system with induction motor load.....	67
Fig.3.19 The rate of change of power interlock function structure .....	68
Fig.3.20 Simulation results of islanding situation the ROCOF relays with $dP/dt$ interlock function.....	69
Fig.3.21 Simulation results of non-islanding situation the ROCOF relays with $dP/dt$ interlock function.....	69
Fig.4.1 Block diagram of a grid-connected wind turbine with a DFIG .....	74
Fig 4.2 Overall structure of the grid-connected wind turbine model .....	74
Fig.4.3 Steady state equivalent circuit of the DFIG .....	76
Fig.4.4 Reference frame and space vector representation.....	78
Fig.4.5 Grid-side PWM voltage source converter.....	82
Fig.4.6 Vector diagram of the dq-reference frame alignment for the grid-side converter .....	84
Fig.4.7 Vector control structure for grid-side PWM voltage source converter	85

Fig.4.8 The schematic diagram of the current control loop .....	87
Fig.4.9 Schematic diagram of the current control loop of the generator.....	88
Fig.4.10 Internal model control system structure .....	89
Fig.4.11 Classic control system structure.....	90
Fig.4.12 Block diagram of the DC-link voltage control system.....	92
Fig.4.13 Grid-side current control loops implementation .....	95
Fig.4.14 Step response of the grid-side current control loops.....	95
Fig.4.15 Step response of the grid-side DC-link voltage control loops .....	96
Fig.4.16 Single line diagram of test system .....	96
Fig.4.17 The estimation of rate of change of frequency by using FFT and Prony's method.....	97
Fig.4.18 Comparison of rate of change of frequency using different measuring window .....	98
Fig.4.19 The detection time versus power imbalance by using Fast Fourier transform with different relay setting .....	99
Fig.4.20 Single-line test system (adding load) .....	101
Fig.4.21 System simplified structure.....	101
Fig.4.22 The values of estimated load impedance, power and voltage of generator side during islanding situation.....	102
Fig.4.23 The values of estimated load impedance, power and voltage of generator side during non-islanding situation .....	103
Fig.4.24 The waveform of $v^2/p$ during non-islanding and islanding situation ( $\Delta p=0.778p.u.$ ) .....	104
Fig.4.25 $v^2/p$ interlock function structure .....	104
Fig.4.26 Simulation results of non-islanding situation the ROCOF relays with $v^2/p$ interlock function.....	105
Fig.4.27 Simulation results of islanding situation the ROCOF relays with $v^2/p$ interlock function.....	106
Fig.5.1 Equivalent circuit of a DFIG operating in parallel with the grid .....	109
Fig.5.2 a) Complete drive assembly b) drive internals c) DFIG and driving motor.....	110
Fig.5.3 Main power PCB .....	111
Fig.5.4 Main power PCB basic schematic.....	112
Fig.5.5 Rotor side controller structure.....	113
Fig.5.6 Active Front End and its relay circuit .....	114

Fig.5.7 The switch box for creating islanding and load changing situation...	115
Fig.5.8 Simplified structure of the switch box .....	116
Fig.5.9DFIG .....	116
Fig.5.10 Prime Mover.....	117
Fig.5.11 DC voltage supply and speed measurement equipment.....	118
Fig.5.12 DFIG dq current frame controller structure .....	119
Fig.5.13 Picture of test set up .....	121
Fig.5.14 Circuit diagram of test set up .....	121
Fig.5.15 The measured three phase voltage and current .....	122
Fig.5.16 Filtered current and voltage calculated amplitude value.....	123
Fig.5.17 The estimated frequency and the voltage waveform.....	124
Fig.5.18 Speed and the rotor side $i_q$ read from the DSP board .....	125
Fig.5.19 The estimated frequency information for islanding with a 3kW load .....	126
Fig.5.20 System impedance estimation.....	126
Fig.5.21 The estimated frequency information for system islanded with a 2kW load .....	128
Fig.5.22 Impedance estimation results of system islanded with 2kW load test .....	128
Fig.5.23 Measured voltage and frequency after a 3kW load added to system .....	129
Fig.5.24 The ROCOF results of a 3kW load added to the system .....	130
Fig.5.25 The output power and voltage of a 3kW load added to the system .	131
Fig.5.26 The voltage and frequency results for a 1kW load shedding .....	132
Fig.5.27 The ROCOF and trip signal results for a 1kW load shedding .....	132
Fig.5.28 The output power and voltage of a 1kW load adding situation .....	133
Fig.6.1 The structure of microgrid .....	136
Fig.6.2 Basic control scheme of a grid-forming inverter .....	139
Fig.6.3 The grid-connected microgrid islanding test system .....	141
Fig.6.4 The islanding situation performance for DFIG ROCOF relay.....	141
Fig.6.5 The islanding situation performance for photovoltaic system ROCOF relay .....	142
Fig.6.6 The islanding situation performance for synchronous generator ROCOF relay.....	142

Fig.6.7 The non-islanding situation performance for DFIG ROCOF relay ...	143
Fig.6.8 The non-islanding situation performance for photovoltaic system ROCOF relay.....	143
Fig.6.9 The non-islanding situation performance for synchronous generator ROCOF relay.....	144
Fig.7.1 Thevenin Equivalent Circuit .....	149
Fig.7.2 Transient injection scheme.....	150
Fig.7.3 Source impedance measurement circuit.....	151
Fig.7.4 The IGBT as a switch in AC system.....	152
Fig.7.5 Current flow during switch on situation.....	153
Fig.7.6 The voltage and current measurement at the injection point .....	153
Fig.7.7 Frequency ranges of the current and the corresponding voltage transient .....	154
Fig.7.8 The waveform of estimated resistance value on time at 1kHz.....	154
Fig.7.9 The waveform of estimated reactance value on time at 1kHz .....	155
Fig.7.10 The real and imaginary value of system impedance with zero power imbalance during islanding and non-islanding load variation (5MW to 13MW) .....	156
Fig.7.11 The real and imaginary value with 3MW power imbalance during islanding and non-islanding load variation (2MW to 10MW) .....	157
Fig.7.12 The real and imaginary value with -3MW power imbalance during islanding and non-islanding load variation (8MW to 16MW) .....	157
Fig.7.13 Proposed algorithm for islanding detection .....	159
Fig.7.14 THD value as used for islanding condition.....	160
Fig.7.15 Simulation results of the islanding situation with the ROCOF relays with the THD interlock function .....	162
Fig. 7.16 Simulation results of non-islanding situation the ROCOF relays with the THD interlock function .....	163
Fig.A.1 Simulation model of grid-connected synchronous generator.....	187
Fig.C.1 The islanding situation performance for DFIG ROCOF relay.....	189
Fig.C.2 The islanding situation performance for photovoltaic system ROCOF relay .....	190
Fig.C.3 The islanding situation performance for synchronous generator ROCOF relay.....	190
Fig.C.4 The non-islanding situation performance for DFIG ROCOF relay..	191

Fig.C.5 The non-islanding situation performance for photovoltaic system ROCOF relay.....	191
Fig.C.6 The non-islanding situation performance for synchronous generator ROCOF relay.....	192

---

# List of Tables

Table 3.1 ROCOF trip operation during system breaker closed condition in different cases with different relay settings.....	64
Table 4.1 Generator parameters .....	93
Table 4.2 PI-controller parameters for grid-side converter .....	94
Table 4.3 ROCOF trip operation during system breaker closed condition in different cases with different relay settings.....	100
Table 5.1 DFIG parameters .....	117
Table 6.1 Evaluation of the non-detection zone .....	144
Table 7.1 Source impedance of supplies .....	152
Table 7.2 Summarises the disadvantages and advantages of the islanding detection techniques. ....	165
Table B.1 PI-controller parameters for grid-connected inverter .....	188
Table C.1 Evaluation of the non-detection zone .....	192

# List of Acronyms

AFD—Active Frequency Drift

APS—Active Phase Shift

AFE—Active Front End

CHP—Combine Heat and Power

COROCOF—Comparison of Rate of Change of Frequency

CB—Circuit Breaker

DFIG —Doubly-fed Induction Generator

DR—Distributed Resource

DSP—Digital Signal Processor

DSG—Distributed Synchronous Generator

DG—Distributed Generation

DFPG—Distributed Fuel Cell Powered Generation

ESL— Equivalent Series Inductance

FFT—Fast Fourier Transform

FPGA—Field Programmable Data Array

IGBT— Insulated Gate Bipolar Transistor

LOM—Loss of Main

MG— Microgrid

NDZ—Non-detection Zone

OFR—Over Frequency Relay

OVR—Over Voltage Relay

- POM—Point of Measurement
- PWM—Pulse Width Modulation
- PCB— Printed Circuit Board
- PLL—Phase Locked Loop
- PF—Positive Feedback
- PV—Photovoltaic System
- PCC—Point of Common Coupling
- ROCOF—Rate of Change of Frequency
- ROCOV—Rate of Change of Voltage
- RPS—Real Power Shift
- SG—Synchronous Generator
- SVS—Sandia Voltage Shift
- SCADA—Supervisory Control and Data Acquisition
- THD—Total Harmonic Distortion
- UVR—Under Voltage Relay
- UFR—Under Frequency Relay
- UV—Voltage Unbalance
- VSR—Voltage Surge Relay

# Chapter 1

## Introduction

### 1.1 Distributed Generation

Distributed generation (DG) also called embedded generation or dispersed generation, is defined as generating electricity from many small energy sources. Most plants are built this way due to number of economic, health and safety, logistical, environmental factors. It reduces the amount of energy lost in transmitting electricity due to the generating near to where is used. It also reduces the size and the power lines that must be constructed. Typical distributed generation power sources scheme have low maintenance, low pollution and high efficiencies. Modern embedded generation system can provide these traits with automated operation and use of renewables such as wind, solar, and geothermal. DG range from 5kW up to 100MW [1], maintenance cost for DG such as fuel cells and photovoltaics is quite low [1-2]. The most common energy sources used for distributed generation are wind and solar power as discussed in following sections.

### 1.1.1 Wind Power System

The number of wind power units installed in power systems around the world has grown significantly in the last two decades. At the end of 2010, worldwide nameplate capacity of wind-powered generators was 197GW [3]. Wind power now has the capacity to generate 430 TWh annually, which is about 2.5% of worldwide electricity usage [3-4]. Over the past five years the average annual growth in new installations has been 27.6 percent. Wind power market penetration is expected to reach 3.35 % by 2013 and 8% by 2018 [5]. Several countries have already achieved relatively high levels of wind power penetration, such as 21% of stationary electricity production in Denmark, 18% in Portugal, 16% in Spain, 14% in Ireland and 9% in Germany in 2010 [3]. As of 2011, 83 countries around the world are using wind power on a commercial basis [6]. Fig.1.1 provides the global wind power cumulative capacity forecast[7].

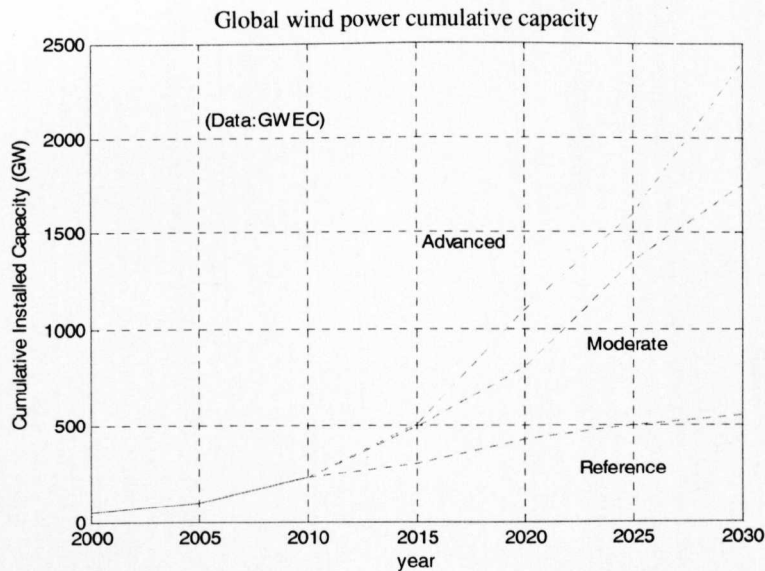


Fig.1.1 Global wind power cumulative capacity-with forecast [7]

### 1.1.2 Photovoltaic System

Photovoltaic system consists of multiple components, including photovoltaic modules, mechanical, and electrical connections and mountings and means of

regulating electrical output. It can be classified as grid-connected system and a stand-alone system. In 2010, solar panels available for consumers can have a yield of up to 19% [8], while commercially available panels went as far as 27% [9]. And a photovoltaic installation in the southern latitudes of Europe or the United states produced  $11\text{kWh}/\text{m}^2/\text{day}$ . The international Energy Agency, IEA, has a database of installed grid connected photovoltaic systems from around the world. The database lists examples of installations rated from a few hundred watts to more than 2MW [10].

## 1.2 Electric Island Formed by Distributed Generators

A typical power distribution system is shown in Fig.1.2 [11]. The substation steps down transmission voltage into distribution voltage and is the sending end of several distribution feeds. One of the feeders is shown in detail. There are many customer connection points in the feeder. Large distributed generators are typically connected to the primary feeders (DG1 and DG2). These are typical synchronous and induction generators present. Small distributed generators such as inverter based PV systems are connected to the low voltage secondary feeders (DG3).

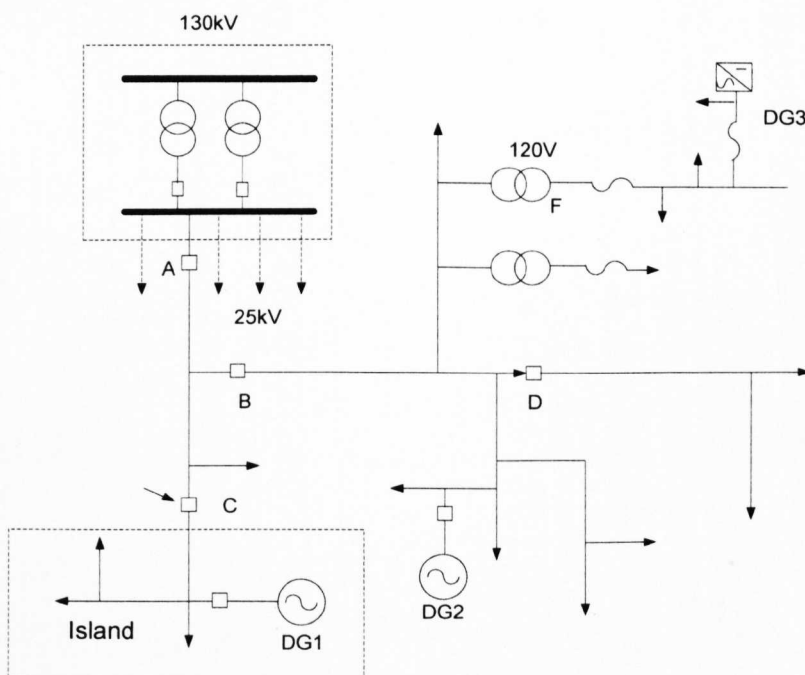


Fig.1.2 Typical distribution system with distributed generators [11]

An islanding situation occurs, for example, when relay C opens. DG1 will feed into the resultant island in this case. The most common cause for a relay to open is a fault in the downstream zone of the relay. A relay with reclosing function is designed to open and re-close two to three times within a few seconds. The intention is to re-connect the downstream system automatically if the fault clears by itself. In this way, temporary faults will not result in the loss of downstream customers. An islanding situation could also happen when there is a permanent fault at point F. In this case, the inverter based DG will feed the local loads, forming a small islanded power system.

The island is an unregulated power system. Its behaviour is unpredictable due to the power mismatch between the load and generation and the lack of voltage and frequency control. The main concerns associated with such islanded system are [12-13]:

- The voltage and frequency provided to the customers in the islanded system can vary significantly if the distributed generators do not provide regulation of voltage and frequency and do not have protective relaying to limit voltage and frequency excursions, since the supply utility is no longer controlling the voltage and frequency, creating the possibility of damage to customer equipment in a situation over which the utility has no control. Utility and DG owners could be found liable for the consequences.
- Islanding may create a hazard for utility line-workers or the public causing a line to remain energized that may be assumed to be disconnected from all energy sources.
- The over current relays of the distribution generators may trip when islanding occurs and the relay in the system would be auto-reclosing. There may be a possibility that the generators are not in synchronism with the system at the instant of reconnection. Such out of phase reclosing can cause a large current into the generators. It will trip the generator relay.
- Islanding may interfere with the manual or automatic restoration of normal service for the neighbouring customers.

The current industry practice is to disconnected all DGs immediately so that the entire feeder becomes de-energized [14-15]. It prevents equipment damage and eliminates safety hazards. To achieve this goal, each DG must have the capability to detect islanding conditions and to automatically disconnect itself from the system. The actual case which was occurred in eastern Denmark was described below to indicate the importance of islanding detection correctly.

In Jutland on 18<sup>th</sup> February 1996 a two-phase short-circuit occurred on a 150kV line with a following voltage dip as a consequence [10]. Distributed production units, with a production of more than 300MM, in a very large area were tripped from the system since the situation incorrectly was treated as an island state by the protection system. If it had not been possible to import power from surrounding countries a deficit of power possibly followed by a voltage collapse could have occurred. Therefore, it is very important to apply a more reliable islanding detection method.

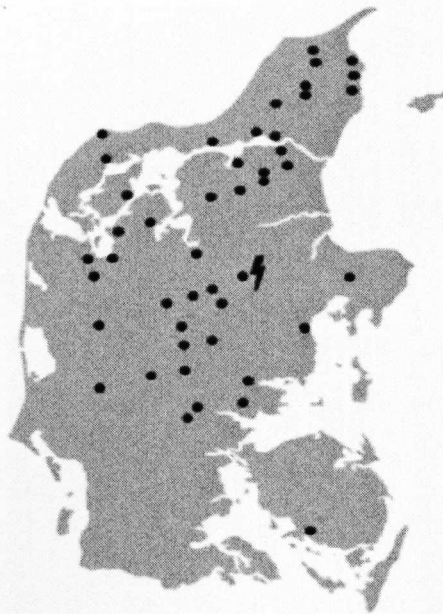


Fig.1.3 Eltra service area. 47 local CHP units, larger than 2MW each, with a production of 347 MW were tripped as a result of a true phase fault. It is unknown how many units smaller than 2MW that were tripped

### 1.3 Detection of Islanded Power System

An islanding situation should be detected soon after the island is formed. The basic requirements for a successful detection are [11]:

- The scheme should work for any possible formations of islands. Note that there could be multiple switchers, reclosers and fuses between a distributed generator and the supply substation. Opening of any one of the devices will form an island. Since each islanding formation can have a different mixture of loads and distributed generators, the behaviour of each island can be quite different. A reliable anti-islanding scheme must work for all possible islanding scenarios.
- The scheme should detect the islanding situation within a required time frame. According to IEEE 1547 standard islanding state should be identified and disconnected within 2 seconds [14, 16-17]. The main constraint is to prevent out-of-phase reclosing of the distributed generators. A recloser is typically programmed to reenergized its downstream system after about 0.5 to 1 second delay. Ideally, the anti-islanding scheme must trip its DG before the reclosing takes place. Typically the islanding situation should be detected within 300ms [18-19].

Many anti-islanding techniques have been proposed and a number have been implemented in actual DG projects [20] or incorporated into the controls of inverters used in utility-interactive DG applications. When selecting an anti-islanding scheme, it is important to consider the characteristics of the distributed generators can be grouped into the following three types:

- Synchronous generator: this type of DG is typically connected to the primary feeder. Its size can go as high as 30MW. Synchronous generators are highly capable of sustaining an island. Due to its large power rating, options are limited to control the generators for the purpose of facilitating islanding detection. As a result, anti-islanding protection for synchronous generators has emerged as the most challenging task faced by the DG industry.

- Induction generator: this type of DGs is typically connected to the primary feeders as well. Its size can also be quite large, for example 10 to 20 MW. Induction generation generators are not capable of sustaining an island due to their need for reactive power support from the electricity network. As a result, anti-islanding protection is not considered as an issue for such induction generators. But in some cases, a capacitor bank is located in the end of induction generator, in order to correct power factor, therefore, the islanding situation could be a safety problem [21].
- Inverter-based generator: this type of DG is commonly connected to the secondary feeder due to its relatively small size (typically in the range of a few hundred watts to 1MW). The inverter is actually an interface between the system and the generator. The generator can be photovoltaic panels, fuel cells, micro-turbines etc. Since it is the inverter that interacts with the supply system, all inverter-based DGs have operating characteristics with respect to grid interaction primarily determined by the inverter topology and controls. The inverter-based DGs are capable of sustaining an island; however, the utility-interactive inverters can be designed to detect and control islanding conditions. As a result, many inverter specific anti-islanding techniques have been proposed.

In this thesis all major islanding detection techniques published or developed will be reviewed. These techniques can be broadly classified into two types according to their working principles. The communication-based schemes are applicable to both the synchronous generator type and the inverter-based distributed generators. The location detection techniques with application to the synchronous generators will be discussed. The local detection techniques associated with the doubly fed induction generator and microgrid will be introduced.

## 1.4 Non-Detection Zone and Associated Risks

All anti-islanding schemes have some limitations which may include [11]:

- High implementation cost.
- Need for coordination between the DG operator and the utility.
- Susceptibility to false detection of islanding (nuisance tripping).
- Possible non-detection of islanding under some conditions.
- Possible reduction of utility power quality and voltage and frequency stability.

Since anti-islanding schemes are not perfect and may impose financial or performance costs, it is necessary to understand the actual probability that an island will occur (such as intentional islanding for system maintenance requirement or unintentional islanding due to a fault occurring in the system) and what risks this unintentional island will present to human safety and the electrical network. This allows the benefits of further risk reduction from better anti-islanding schemes to be balanced against the costs imposed by these schemes. If a simple and low cost anti-islanding scheme reduces risk to a level below other electrical safety risks that are currently considered acceptable, it is debatable whether a scheme with better detection performance, but higher costs (in financial or performance terms), is necessary. This is particularly true when the DG reduces other hazards such as air pollution.

One of the main limitations with local detection schemes is that each scheme has an operation region where islanding conditions cannot be detected in a timely manner. This region is called the non-detection zone (NDZ). The impact of the non-detection zone can be negligible in some cases and can be significant in other cases. Report [11] provides an example of the frequency-based anti-islanding methods, which are the most commonly employed schemes for synchronous generators, used to illustrate the risks associated with the non-detection zone.

The frequency based anti-islanding scheme uses locally measured frequency as a criterion to decide if an island is formed. It is known that when a feeder is connected to the utility supply, the feeder frequency is almost constant. On the

other hand, the frequency of an islanded feeder can have various values depending on the power mismatch between the load and generation in the system. Excess generation will drive up the frequency and deficit generation will result in the decline of frequency. Accordingly, if there is a large power mismatch in an island, the frequency based anti-islanding scheme will be able to detect islanding condition quickly. If the power mismatch is small, however, it will take longer time to detect islanding condition. In the extreme case where the load and generation in the islanded system are very close, the devices could fail to detect an islanding situation within the allowed time period. Thus, the non-detection zone can be specified using mismatch level in an island.

Two factors can significantly affect the power mismatch levels in an island. The first factor is the daily variation of feeder loads. Depending on their operating characteristics, feeder loads could have  $\pm 20\%$  variation around its daily average. The second factor is that different islands could be formed with a DG. Each island will have different load levels. Both factors will work together create more situations where small power mismatch levels could be encountered, leading to an increased risk of non-detection. The impact of a non-detection zone of islanding detection is shown in Fig.1.4.

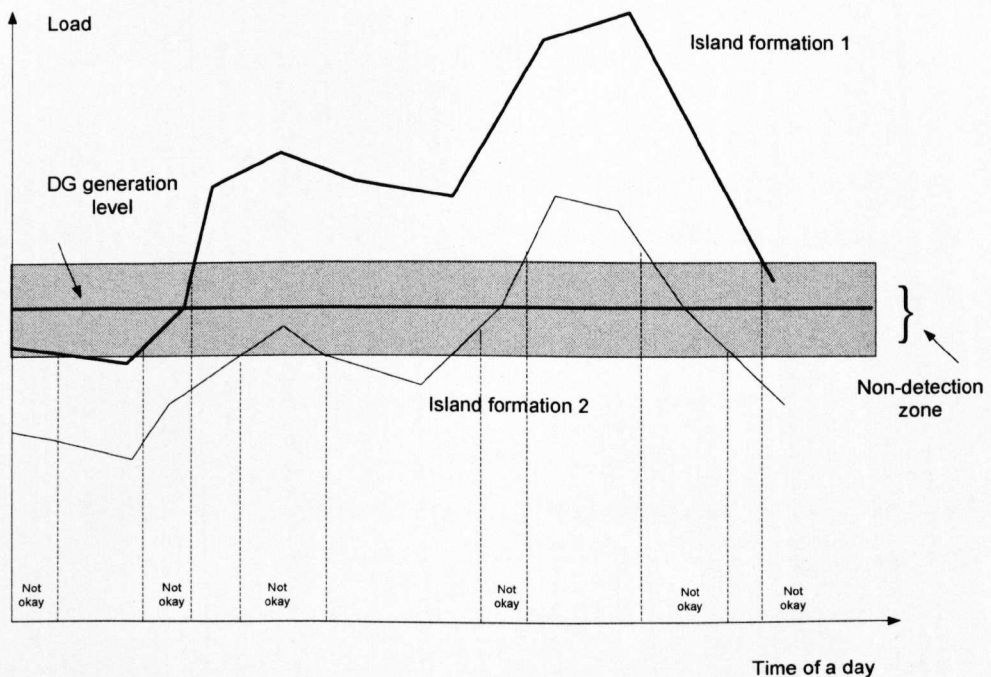


Fig.1.4 The impact of non-detection zone for islanding detection [11]

Fig.1.4 shows the variation of load level during 24 hours period. Two load variation curves are depicted. Each curve corresponds to a different island formation scenario. The power output of the DG is assumed as constant during the 24 hours period. Therefore, it is a horizontal line. The intersections of the DG curve and the load variation curves represent the cases where there is a zero mismatch between load and generation. The non-detection zone is shown as a shaded band. Any load values that fall into the band will result in poor detection of islanding conditions (marked as not okay in Fig.1.4). It can be seen that there are a number of operating periods during which poor or no detection of islanding conditions can occur. If more islanding scenarios are added (i.e. if there are more load variation curves), such periods will increase further. This analysis shows that the risk associated with non-detection zone is real and can be significant. A frequency-based relay can be used reliably only if the distributed generator is less than about half of the smallest load in any possible island formations. In this case, the frequency shift will be sufficient to exceed the frequency limits to allow the UFR/OFR protection to trip [22].

Both the probability of islanding and the risks associated with the formation of an island are typically less for inverter based DGs than for synchronous generator based DGs. Considering risks first, the commonly cited risks or hazards of unintentional island are discussed in Section 1.3[11, 13]:

The actual level of risk associated with automatic reclosure into an island created by an inverter based DG is controversial and appears to depend on national or local practices with regard to use of automatic reclosure. Some European countries (e.g. the Netherlands) use automatic reclosure primarily on medium and high voltage overhead transmission lines and do not believe the inverter based DGs, which are normally connected to the low voltage distributed network, are likely to create islands extending up to the transmission level. Therefore they do not consider automatic reclosure into an island to be a substantial hazard. The current North American position, which is reflected in anti-islanding testing standards for DG inverters, is that automatic reclosure is a potential risk. At the very least, damage to the DG inverter itself, is a possibility [11].

The risk that islanding may interfere with automatic or manual restoration of service depends in part on the probability that an island will be sustained long enough to be present when the utility is reconnected [23]. An island is sustained only while there is a relatively close match between the power output of the DG and the power consumption of the load within the island. Long duration islands are much less likely than short duration islands since both DG power output and load power consumption change with time. Most studies on the risks associated with islanding of inverter based DGs have found that islanding situation lasting more than a few minutes are very unlikely. Therefore this risk is more of an issue with automatic service restoration techniques, such as automatic reclosing, than with manual reconnection.

The hazard to utility line workers or other personnel is commonly reviewed as the most serious risk of islanding operation since it involves human safety rather than potential equipment damage or malfunction. Therefore, this risk has had the most extensive analysis. The risk to utility line workers can be mitigated by following established rules for line maintenance and repairs. An islanding situation will not increase the probability for line workers hazards if line workers operate under established hot-line rules or dead-line rules. However, other personnel, especially emergency responders, such as firefighters, may not have the time or the capability to follow such procedures. Therefore, there is a potential personnel hazard if an islanding situation persists beyond a few seconds.

The personnel safety risk associated with islanding can be analyzed using the fault tree shown in Fig.1.5. The risk of islanding is a combination of the probability of load/generation match combined with the simultaneous loss of mains supply and the failure of the protection to detect the island on demand [23].

$$\text{Risk(islanding)}=P(\text{match})\times P(\text{LOM})\times P(\text{protection failure}) \quad (1.1)$$

## 1.5 Objective of the Research Project

This research described in this thesis, concerns islanding detection for distributed system based on combining ROCOF relays and rate of change of power or  $v^2/p$  interlock functions. The objectives of this research include:

- Reviewing the major islanding detection techniques.
- Investigating the new islanding detection method based on combining ROCOF relays and  $dp/dt$  interlock function applied in synchronous generator distributed system. This algorithm should be able to detect islanding situation quickly and avoid false tripping effectively.
- Investigating ROCOF relays cooperation with  $v^2/p$  interlock function used in DFIG wind turbine distributed system. Due to the system load variation  $v^2/p$  interlock function should block the ROCOF nuisance tripping signal quickly and accurately. This method can also be validated by the experiment for DFIG islanding detection.
- Evaluating the proposed method of ROCOF relays with  $v^2/p$  interlock function utilized in microgrid distributed system.
- Discussing the advantages and drawbacks of impedance measurement (active method) and the Total Harmonic Distortion method (passive method) applied in grid-connected DFIG wind generation system.

## 1.6 Thesis Structure and Contents

Chapter 2 reviews all major islanding detection techniques published or developed. These techniques can be broadly classified into communication-based schemes and local detection schemes according to their working principles. The communication-based schemes used telecommunication means to alert and trip DGs when islands are formed. Local detection schemes rely on the measurement of system parameters at the DG site. Islanding can be detected if indices derived from the signals exceed certain thresholds. The

advantages and drawbacks of these islanding techniques are proposed. The comparison of the methods is also discussed.

Chapter 3 proposes the principle of rate of change of frequency method (ROCOF) which is one of the most commonly employed loss-of mains detection method applied for the synchronous generator distributed generation islanding detection. The frequency estimation method of Fast Fourier Transform (FFT) and the Prony's method are introduced to calculate the deviation frequency. The performances characteristics of ROCOF relays for DGs islanding detection (i.e. frequency measuring methods, measuring windows, generator inertia and relay settings) are investigated. The curve of active power versus detection time is proposed to evaluate the performance of the characteristics. In addition, false operation (system load adding and shedding) is investigated. The interlock function of rate of change of power is applied to cooperate with ROCOF relays to avoid nuisance tripping during system non-islanding situation.

In Chapter 4 grid-connected doubly fed induction generator (DFIG) similar to be GE1.5MW [24] wind turbine generators model is established. Based on the analysis of the equivalent circuits of DFIG and its PWM voltage source converter, a vector control scheme is introduced for grid-side converter controller design, and the controller design for rotor-side converter is used the model of GE1.5MW wind turbine generator. Then, the ROCOF relays applied in DFIG wind turbine distributed system is proposed. The performance characteristics of ROCOF relays which affect the operation responses for DFIG wind turbine islanding detection are investigated. Meanwhile, the non-islanding situation of ROCOF relays false operation is also considered. In this case the new interlock function  $v^2/p$  is utilised, and the performance of ROCOF relays combined with the new interlock function is investigated.

In Chapter 5 the experiment of DFIG (standard 7.5kw machine) islanding detection is implemented. The prototype DFIG islanding detection test rig consisted of the rotor converter, with grid interface active front end, along with the Doubly Fed Induction Generator (DFIG) and the switch box is described. The idea of the ROCOF relays combined with  $v^2/p$  interlock function for

islanding and non-islanding detection is proved by the experimental results with different power imbalance between the generation and the demand of the load.

Chapter 6 provides the islanding detection for a microgrid which includes a photovoltaic system, synchronous generator and DFIG wind turbine. The principle of grid-forming inverter modelling is introduced. The performance of  $v^2/p$  interlock function cooperate with ROCOF relays separately for microgrid islanding and non-islanding detection with different generation portion of photovoltaic system, synchronous generator and DFIG wind turbine are investigated. The non-detection zone analysis for different power imbalance between generation and load demand is discussed.

Chapter 7 investigates two islanding detection methods (impedance estimation method and the Total Harmonic Distortion Method) applied to the DFIG wind turbine system (which was introduced in Chapter 4). According to the simulation results the comparison of these two methods are discussed.

Chapter 8 concludes the thesis by summarising the research work investigated and developed, knowledge gained and the contributions made to this research field. Considering the employment of detailed and complicated microgrid system modelling which can operate in grid-connected mode or in islanded mode, and also considering the application of control scheme used for the microgrid, future work are discussed.

## Chapter 2

# Islanding Detection Methods

### 2.1 Introduction

Islanding in power system can be intentional or unintentional. In the past most of the methods were developed for the phenomenon of unintentional islanding. Recently as the distributed generator (DG) sources are able to control voltage and frequency in the islanded part, the phenomenon of unintentional islanded is not common [12]. If the autonomous operation of sources or intentional islanding is desired, then a fast islanding detection technique is necessary [25]. The main philosophy of detecting an islanding situation is to monitor the DG output parameters and system parameters to decide whether or not an islanding situation has occurred from change in the parameters [26]. As Fig.2.1 shown, islanding detection techniques can be classified as remote techniques and local techniques, and local techniques can be divided into passive methods, active methods and hybrid methods.

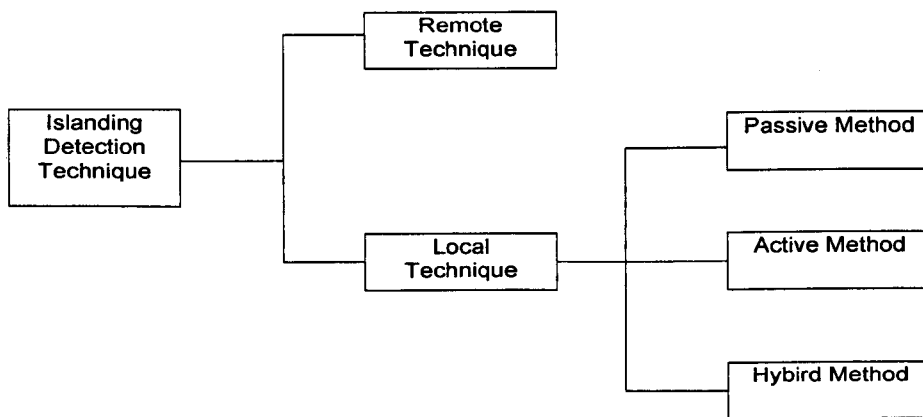


Fig.2.1 Islanding Detection Techniques

In this chapter, several remote and local techniques (passive, active, and hybrid methods) for islanding detection are briefly described. The advantage and limitation of each technique are also introduced. Meanwhile, the comparison of these methods is also discussed.

## 2.2 Remote Islanding Detection Methods

Remote islanding detection methods are based on communication between utilities and DGs. Although these techniques may have better reliability than local techniques, they are expensive to implement and hence uneconomical. Some of the remote islanding detection techniques are as follows:

### 2.2.1 Transfer Trip Scheme

The transfer trip scheme is the most direct method for loss of grid protection and is achieved by monitoring of auxiliary contacts on all circuit breakers on the utility system between its main sources of generation and the dispersed storage and generation units [13, 27]. The basic idea of this method is to monitor the status of all the circuit breakers and reclosers that could island a distribution system. When a switching operation produces a loss of grid, a transfer trip scheme can then be used to open the inter-tie connecting the two systems. Following successful restoration of the utility supply, the dispersed storage and generation units can be resynchronised to the utility and then

reconnected. Unfortunately, several circuit breakers are candidates for creating the loss of grid and a comprehensive monitoring system involving all circuit breakers which could be involved would be unmanageable for most utilities. The installation of an extensive Supervisory Control and Data Acquisition (SCADA) system and network automation can facilitate such a scheme [27]. This method requires a better interaction between the utility and DGs and this often increases the costs for both the utility and DG owners. In addition to high cost, the transfer trip scheme could be very complicated as well, for example, each openable device between DG and supply system needs a transmitter. Some of the devices need to be reconfigured and equipped with the capability of interfacing with the signal transmitter. If the telecommunication coverage is weak or non-existent, the cost of the transfer trip scheme alone could kill a DG project [28]. But Transfer trip scheme can be an effective and simple method for islanding prevention for distribution feeders with fixed topology [11].

## 2.2.2 Power Line Signaling Scheme

Power line signaling scheme is similar to the telecomm-based transfer trip scheme. However, the signal is sent through the power line, which makes the scheme applicable to any distribution systems regardless the availability of telecomm means [28-30]. Fig.2.2 shows a power line signaling scheme. This scheme can be effectively used in multi DG systems.

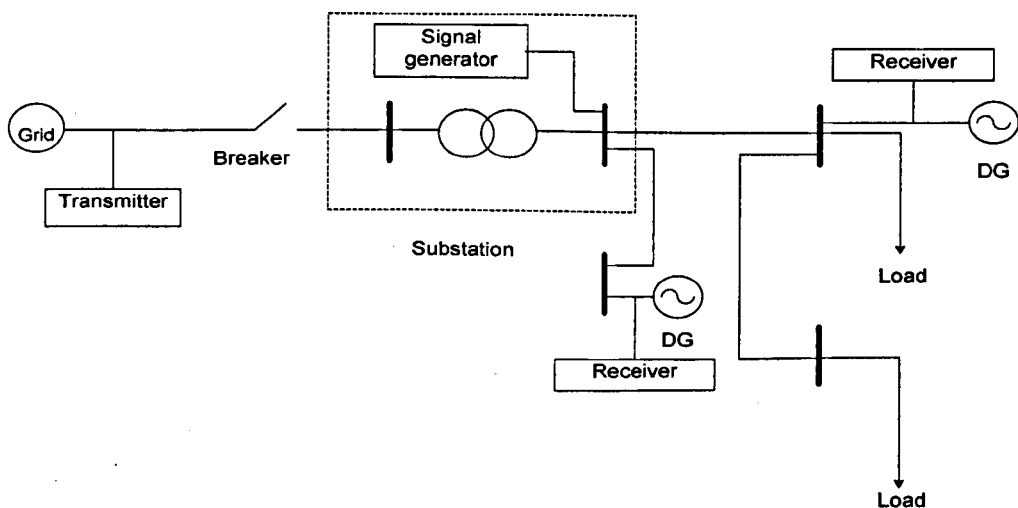


Fig.2.2 A power line signaling scheme

This scheme includes two devices: a signal generator which is connected to the substation bus and single receiver at the terminal of a given DG. The signal generator broadcasts a signal to all distribution feeders with a preset protocol continuously. If the detector of the DG does not sense the signal (caused by the opening of any devices between the substation and the DG) for certain duration, it is considered as an island condition and the DG can be tripped immediately. If the substation bus loses power, which is another islanding condition, the signal generator also loses power and stops broadcasting. So that downstream DGs will also trip. Furthermore, the signal generator has several auxiliary inputs. Any one of the inputs can stop the broadcast, resulting in tripping all DGs in the system. This feature is particularly useful when transmission system operators need to trip the DGs. It is also useful if a transmission system island is formed [28-29].

This scheme works like transfer trip scheme, but it works independent of network topology changes, the opening of any devices can be detected automatically since power line is used as signal carrier. It is economical comparing with transfer trip scheme due to the installation of one signal generator at the substation side which can satisfy the need of all downstream DGs. Besides without actually breaking up all the distribution feeders the scheme can be tested. However, this scheme has two main disadvantages. The first one is the cost of the signal generator. This is a medium voltage device. A step down transformer is required to connect it and it has to be installed in a substation. This cost may be hard to justify if there are only one or two DGs using the service. The second concern is the possible interference of the signal with other power line communication applications such as automatic meter reading. This is a promising technology but there is no field application experience of this technology yet [11].

## **2.3 Local Detection Techniques**

Local detection techniques are based on the measurement of system parameters at the DG site. It is further divided into passive methods and active methods.

### 2.3.1 Passive Methods

Passive methods are based on the information available on the DG site at the point of common coupling (PCC) with the utility grid. Passive anti-islanding techniques rely on the detection of abnormalities at the DG output when islanding occurs. Differentiation between an islanding and grid-connected condition is based upon the thresholds set for the parameters. However, it is usually difficult with passive techniques to set thresholds to detect islanding and prevent nuisance trips at the same time. Conversely, the effectiveness of passive methods is not guaranteed for all loading conditions, in particular when there is a balanced DGs source [22]. Comparing with active method, there is a larger non-detection zone. But passive methods do not disturb the system.

Fig.2.3 shows the power circuit structure of DG connected to the utility grid with passive RLC loads. During the normal operation, because the values are controlled by the stiff grid with constant voltage and frequency, when the island occurs there is a mismatch between the DG power and local load power. The over/under voltage and frequency methods will not work properly to detect the island when the local loads closely match the DG output power. In this case the voltage and frequency shift are insufficient to exceed the voltage and frequency limits to allow the over/under voltage or frequency protection to trip. Since the distributed generation monitors the terminal voltage for its own control purpose; adding passive islanding detection usually requires little additional hardware and can be implemented at low cost [22].

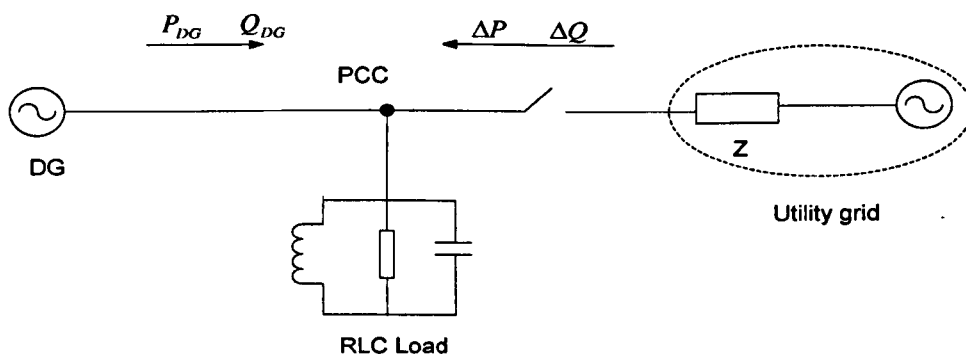


Fig.2.3 Power circuit structural of DG coupled to utility grid with RLC load

### 2.3.1.1 Rate of Change of Output Power

Through monitoring the rate of change of output power  $dP/dt$ , at the DG side, once it is islanded, the value of output power is much greater than that of the rate of change of output power before islanded for the same rate of load change [13]. In this algorithm the active output power of the DG unit will be measured at any time and rate of change of power will be calculated. The output power of the DG unit is calculated with (2.1).

$$P_{DG} = |v_a||i_a|\cos(\theta_a) + |v_b||i_b|\cos(\theta_b) + |v_c||i_c|\cos(\theta_c) \quad (2.1)$$

where  $v_a, v_b, v_c$  are sampled values of instantaneous three phase output voltage of the DG and  $i_a, i_b, i_c$  are sampled value of instantaneous three phase output current of the DG unit. The rate of change of output power is calculated with a time derivative of this power over a period. The problem with this method is that in some cases, such as motor starting, capacitor bank switching, the real time measured data is distorted and this method could cause false tripping. In [21] a method which is based on combination of rate of change of output power with an active method is present. The DG system applied in [21] is induction generator with a capacitor bank as power factor correction unit. Fig.2.4 shows the flowchart of the proposed algorithm.

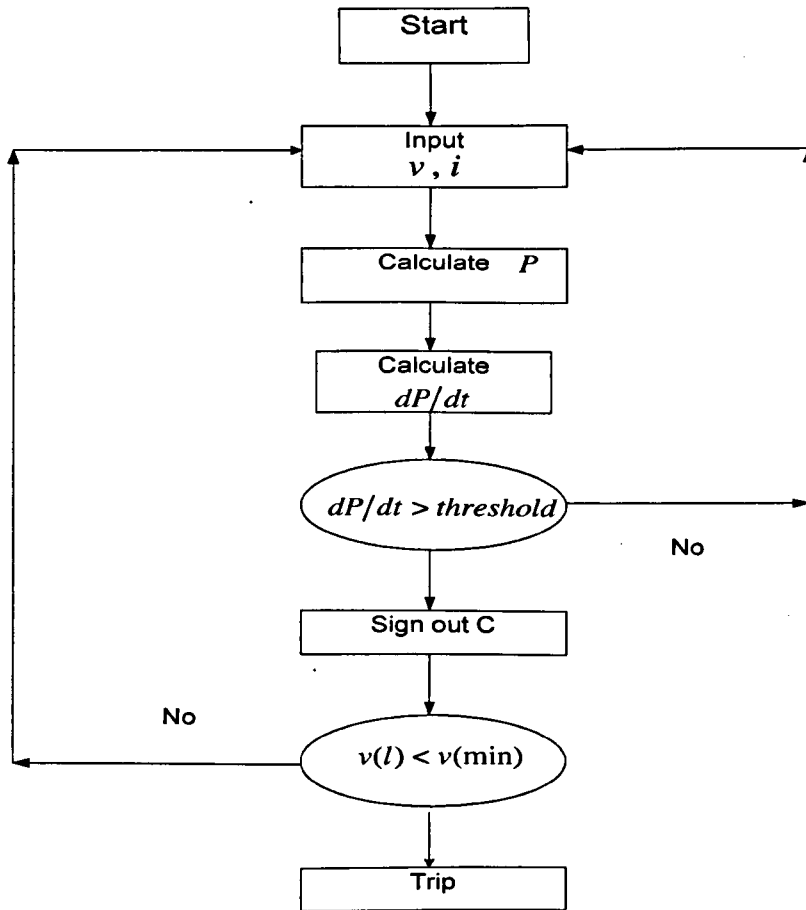


Fig.2.4 The algorithm to detect an islanding state

At first, the rate of change of output power value at any time is calculated, if this value is less than the determined threshold value the system performance is considered normal, but if its value exceeds the threshold value, in this case the capacitor bank of the DG unit become switched out (in order to make sure for the islanding phenomenon). If the RMS value of load voltages drop becomes less than an allowable value. Then this condition is considered to be islanding and the DG unit must be interrupted. Otherwise, the capacitor bank is switch onto the system and DG continuous working [21]. The advantage of this combination method is that even if the rate of change of output power of passive methods operates incorrectly during system disturbance, the active method cooperates with  $dP/dt$  and can easily detect conditions and make appropriate decision to disconnect. But due to introducing perturbations into the system, this scheme could affect power quality of the system. In [27, 31], an algorithm which is based on detecting the fluctuations in the generator's output power was proposed. The algorithm calculates the instantaneous power

from the generator terminal quantities and integrates these changes over a defined sample period. Tripping occurs when the integrated signal exceeds the trip setting. The integrating feature provides immunity to mal-operation during conditions of extreme load unbalance or loss of phase operation. An unbalance in the input waveforms would introduce sinusoidal terms of twice the power system frequency and these can be filtered out by the integrating process. The length of the sampling window was chosen to give a maximum operating time of six cycles. This method remains stable during the system large load changing while the utility grid remains connected and also during local power system fault conditions.

### 2.3.1.2 Under/over Voltage and Under/over Frequency Relay

This is one of the oldest methods adopted for distribution system protection. The under/over voltage (UVR/OVR) and under/over frequency (UFR/OFR) protective relays are placed on the distribution feeders for various types of abnormal conditions [32-37]. Paper [38] introduced the grid-connected PV inverters which are required to have UVR/OVR and OFR/UFR protection methods that cause the PV inverter to stop supplying power to the utility grid if the frequency or amplitude of the voltage at the point of common coupling (PCC) between the customer and the utility strays outside of prescribed limits. Consider the configuration shown in Fig.2.5, in which power flows at node 'a' (PCC) are shown.

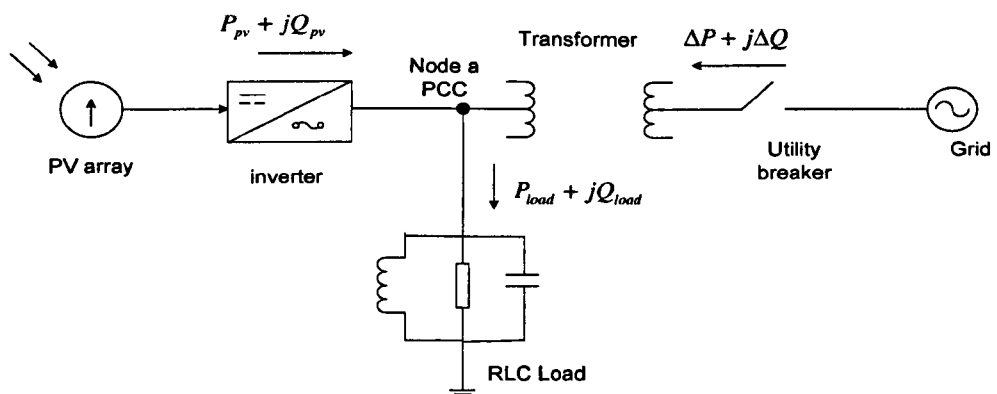


Fig.2.5 PV array as DG source connected to utility

The behaviour of the system at the time of utility disconnection depends on  $\Delta P$  and  $\Delta Q$  at the instant before the island is formed. If  $\Delta P \neq 0$ , then the amplitude of voltage at PCC will change, and UVR/OVR will detect this change and trip the DG source. If  $\Delta Q \neq 0$ , the load voltage will show a sudden change in phase, and thus the frequency of inverter output current will change. This change in frequency is detected by OFR/UFR [38-39].

In [33], the application regions for a frequency relay based OFR/UFR is provided. The frequency relay model implemented in this paper is presented in Fig.2.6, the system frequency  $f$  is determined from the generator electrical speed  $\omega_e$ , if this frequency is larger (or smaller) than the over frequency (under frequency) setting of the relay and the magnitude of the terminal voltage is larger than the minimum voltage setting of  $V_{\min}$ , then the frequency relay sends a trip signal to the generator circuit breaker. Typically, frequency relays can be adjusted using multi-stages, therefore, instantaneous and time-delay settings are employed simultaneously. Usually, frequency can be blocked when the magnitude of the terminal voltage drops below an adjustable level  $V_{\min}$ . This is to avoid actuation the relay during generator start-up. The settings of the application regions of the frequency relays is based on the frequency ranges of the interconnection system response to abnormal frequencies and the performance curves of detection time versus active power imbalance obtained through dynamical simulation. The region of frequency based relays can satisfy both anti-islanding and frequency tripping requirements. Moreover, it is also shown that a frequency relay can reach such objective if its instantaneous and time-delay settings are properly chosen. But it is very difficult to do a setting for these relays. The non-detection zone is large for this method.

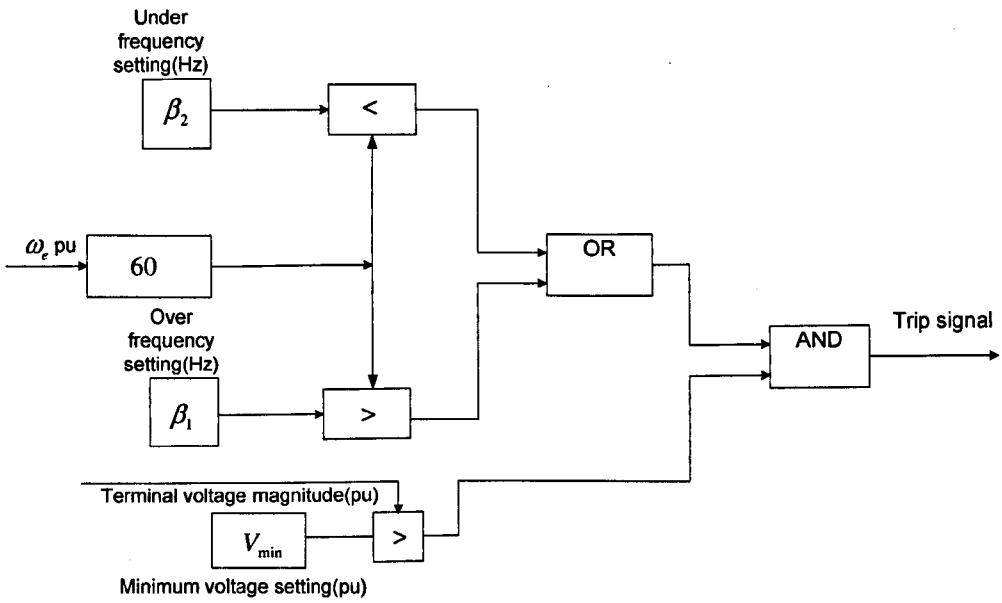


Fig.2.6 Frequency relay computational model

### 2.3.1.3 Vector Surge Relays

Vector surge relay (VSR) is also known as a vector shift or voltage jump relay [38, 40-41]. A vector surge relay is one of the most sensitive frequency-based anti-islanding devices. Paper [41] proposed a systematic and practical method for directly assessing the effectiveness of vector surge relays, by using simple formulas, therefore time may be saved during the planning and implementation stages.

The synchronous generator equipped with a vector surge relay VSR operating in parallel with a distribution network is depicted in Fig.2.7. There is a voltage drop  $\Delta V$  between the terminal voltage  $V_T$  and the generator internal voltage  $E_f$  due to the generator current  $I_{SG}$  passing through the generator reactance  $X_d$  consequently, there is a displacement angle  $\delta$  between the terminal voltage and the generator internal voltage, whose phase diagram is presented in Fig.2.8. In Fig.2.7, if the circuit breaker (CB) opens due to a fault, for example, the system composed by the generator and the load  $L$  becomes islanded. In this situation, the synchronous machine begins to feed a larger load (or smaller) because the current  $I_{SYS}$  provided by (or injected into) the power grid is

abruptly interrupted. Thus the generator begins to decelerate (or accelerate). Consequently, the angular difference between  $V_T$  and  $E_i$  is suddenly increased (or decreased) and terminal voltage phasor changes its direction, as shown in Fig.2.8.

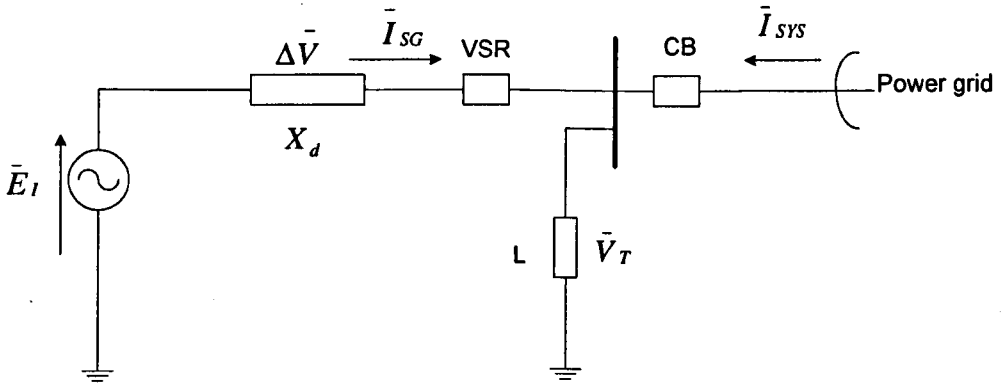


Fig.2.7 Equivalent circuit of a synchronous generator in parallel with utility

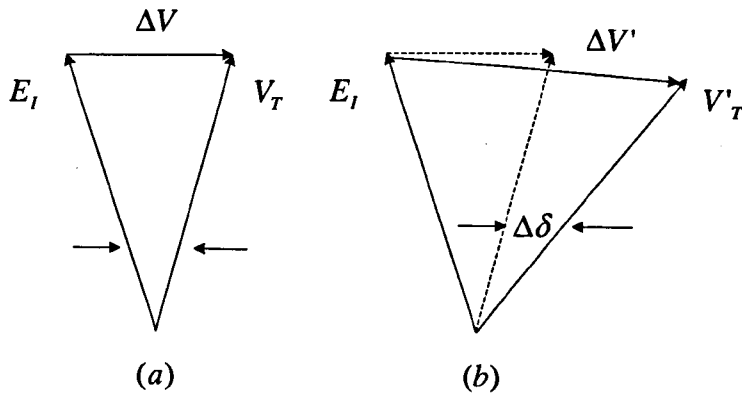


Fig.2.8 Internal and terminal voltage phasors: (a) before the opening of CB; (b) after the opening of CB

Voltage surge relays measure the duration time of an electrical cycle and start a new measurement at each zero rising crossing of the terminal voltage. In an islanding situation, the cycle duration is either shorter or longer, depending if there is an excess or deficit of active power in the islanded system. This variation in the cycle duration results in a proportional variation of the terminal voltage angle  $\Delta\theta$ , which is the input parameter of vector surge relays. If the variation of the terminal voltage angle exceeds a predetermined threshold, a trip signal is directly sent to the circuit breaker. In [40] comparison between

vector surge relays and ROCOF relays was discussed, results showed that ROCOF relays require a smaller active power imbalance level than vector surge relays for successful islanding detection.

### 2.3.1.4 Rate of Change of Frequency over Rate of Change of Power

Paper [42] proposed an islanding detection algorithm for the identification of islanding based on the monitoring of the change of  $df/dP_L$ . This method develops a detection index systematically that serves as a useful islanding indicator for the application. This approach has been tested under different scenarios, including the loss of grid, sudden load change, and parallel operation.

This method could enhance the sensitivity and reliability of protective relays. Test results have shown that for a small power mismatch between the DG and local loads, rate of change of frequency over power is much more sensitive than rate of change of frequency over time. However, the index for different distributed systems is different and needs to be recalibrated.

### 2.3.1.5 Detection of Voltage Unbalance

This method for islanding detection monitors the voltage unbalance after loss of main source [43]. Generally, even though the loading for DG has changed little after islanding, due to the topology changes of the networks and the load, the voltage unbalance varies. Therefore, by monitoring the unbalance of three-phase output voltage of the DG, it is possible to detect an islanding operation of DG. The voltage unbalance (VU) at the monitoring time of the DG terminals can be defined as [12]:

$$VU = \frac{V_{NS,t}}{V_{PS,t}} \times 100 \quad (2.2)$$

where  $V_{NS,t}$  and  $V_{PS,t}$  are negative and positive sequence voltages of the DG output voltage at  $t$ . Normally, the voltage unbalance is averaged over one

fundamental period, while the voltage unbalance variation describes how much it deviates from the steady-state and normal loading conditions. One of the drawbacks of this method is that a voltage unbalance can only be measured in multi-phase systems, this method is not applicable to signal phase systems [44-45].

Due to the large non-detection zone, a combination of methods for islanding detection techniques are proposed by measuring the unbalanced voltage and total harmonic distortion of the current in combination with the conventional voltage magnitude [43]. The method was verified by using the radial distribution network of IEEE 34 bus with a voltage level of 120V. When islanding occurs, the load condition of the DG is suddenly changed in respect to normal operating conditions. This method calculates the first three-phase voltage magnitude of line-to-line voltage at every sampling time. If this measurement does not indicate to a shutdown of the DGs due to the pre-set threshold levels, other monitoring parameters such as the voltage unbalance of three phase voltage and the current THD variation of the inverter are evaluated [22]. Conventional islanding detection methods such as monitoring several parameters: voltage magnitude, phase displacement and frequency change may not be able to detect islanding conditions due to small variations in DGs loadings because these parameters do not change enough. Meanwhile, different loading conditions result in different harmonic currents in the network [46].

Combining two or more methods is more effective, and it works well for a small mismatch between loads and generation power. As a result, it provides good selectivity. The voltage unbalance detection approach has a small non-detection zone (NDZ) compared to conventional methods but is still suitable only for three-phase inverter-based system. Paper [44] concluded that a combination of unbalance voltage magnitude variation as a three-phase average root mean square value of line-to-line based on (2.3):

$$V_{avg,t} = \frac{1}{N} \left[ \frac{\pi}{3\sqrt{2}} \sum_{t=0}^{N-1} (Max(v_a^{t-ti}, v_b^{t-ti}, v_c^{t-ti}) - Min((v_a^{t-ti}, v_b^{t-ti}, v_c^{t-ti}))) \right] \quad (2.3)$$

where  $N$  is a sampling number of one cycle,  $V_a$ ,  $V_b$ , and  $V_c$  are instantaneous voltages of phase  $A$ ,  $B$ , and  $C$  respectively, and  $t$  is the time monitoring. For the situation of induction motor start and unbalanced load variation, this method can avoid false operation.

### **2.3.1.6 Directional Reactive Power Detection**

Typically, if the generation on the feeder is significantly below the feeder load, voltages limits, frequency limits and directional active power are used for unplanned islanding protection of distributed generation. But when the generation on the feeder is more closely matched to the feeder load, the loss of active power import can be relatively small, in this case the frequency shift are insufficient to exceed the frequency thresholds to allow the UFR or OFR to trip, limiting the effectiveness of directional active power and under frequency protection. Paper [47] provides a directional reactive power islanding detection method which is based on monitoring the significant change of reactive power after loss of mains.

If a DG is set-up so that it is always a sink for reactive power when the grid is present, the loss of the grid will force the synchronous generator to begin supplying reactive power, which can then be used to detect an islanding condition. Setting the generator AVR to regulate about a VAR import setting can be used to achieve the pre-fault reactive power absorption condition. Setting the directional reactive power relay to trip a particular reactive power export level can therefore be the islanding detection trip criterion. In order to ensure that the reactive power load on the utility feeder is not unduly high in the pre-fault situation, a VAR import setting corresponding to 0.97 leading power factor at half-rated power is proposed as shown in Fig.2.9.

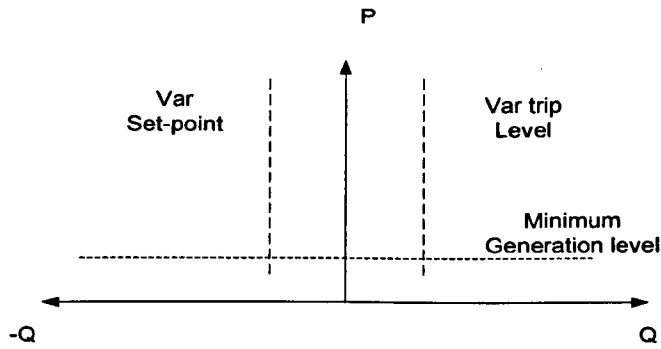


Fig.2.9 Generator operating and trip characteristic

The simulation studies of this method and complimentary fields tests proved that this alternative passive islanding detection method can be used to provide fast and reliable solutions at extremely low cost compared to a transfer trip scheme. But the application is mainly recommended for anti-islanding protection of small synchronous generator DG units on rural feeders with inductive loads, where few or no capacitor banks are installed.

### 2.3.1.7 Comparison of Rate of Change of Frequency (COROCOF)

Like Rate of Change of Frequency (ROCOF), COROCOF assumes that loss of main will cause a sudden change in frequency [48]. However COROCOF discriminates between changes in frequency due to loss of mains, and changes due to widespread system disturbances by using a blocking signal. This is transmitted by COROCOF sending relays to all COROCOF generator protection relays during a change in frequency affecting the whole system. By contrast, a loss of mains would cause a change in frequency at the generator but would not normally affect the frequency of the system as a whole. This assumes that the power island formed is very small compared to that of the rest of the system. No blocking signal would be generated and the COROCOF protection would therefore trip.

However, there is a risk of part of the system suffering a loss of mains at the same time as the rest of the system suffers a frequency transient, generating a blocking signal. Loss of mains protection in the power island so formed would therefore fail to operate until the frequency transient in the rest of the system

ceased. The risk would be avoided by encoding or modulating the blocking signal according to the mains frequency measured by the COROCOF sending relay. A COROCOF generator protection relay would measure the generator frequency and operate if there was a difference between that and the frequency of the rest of the system indicated by the blocking signal.

The advantage of this technique is that it avoids false operation during system disturbances, and it does not disturb the system to which it is connected. However, this loss of mains protection method would not operate if there is a good match between generation and load when system islanded. This also requires a system wide communication system.

### **2.3.1.8 Discussion on Passive Methods**

Some other passive methods for islanding detection have also been proposed in the literature. These methods include: rate of change of frequency [18-19, 33, 40, 49-50], which is also introduced in Chapter3, and another method monitors voltage and changes in the power factor [51]. The total harmonic distortion method [52-53], which is investigated in Chapter 7.

Passive methods for detecting islanding are based on the selection and monitoring of local parameters at the PCC when there is sufficient transition from normal specific conditions [54]. Based on detecting the initiation, transition or the sustained operation, in each of these phases, the potential for discrimination should be considered using the passive measurement of local voltage and frequency. The following general conclusions have been reached [22]:

- Local parameters can achieve fast detection, but they suffer very poor discrimination of islanding initiation.
- Detection methods using measurement voltage parameters in time domain are sensitive to local events, but they have a poor ability to distinguish between islanding and non-islanding events.
- The fundamental frequency is less sensitive to local events but a good discriminator of transition to and sustained operation of the island.

- Unsuitable frequency protection settings are potentially catastrophic for system stability, because of the risk of system-wide loss of generation.
- The islanding detection methods should be appropriate to work properly even in situations where the load and generation are closely matched and should not have a NDZ under realistic conditions.
- Power quality issues should be duly considered in power island operation. Appropriate measures for power quality issues are to be ensured for voltage and frequency control, stability, harmonics, unbalanced loads and voltages, and fault clearance.
- The DG unit should not impose any power quality problems when tied or disconnected from the main grid by following the IEEE standard 1547 for DG interconnection and emphasis on power quality.
- Special care has to be taken while setting the thresholds because if the setting is too aggressive then it could result in nuisance tripping.
- The commercial viability of an islanding operation must be assessed in relation to the enhancement of power quality and system reliability.
- For a general purpose, it is desirable to design a device that can detect all islanding events.
- An islanding detection device must not respond to events or disturbances in the grid other than an islanding event.

### **2.3.2 Active methods**

With active methods, islanding can be detected even under conditions of perfect match between generation and load, which is not possible in case of the passive detection schemes. In active methods perturbations are directly introduced into the power system operation [55]. The principle of active method is that small perturbations will result in a significant change in system parameters when the DG is islanded [56]. Active methods involve some kind of feedback technique or control mechanism that detects changes in the frequency or voltage at the PCC [26]. These methods are briefly discussed below:

### 2.3.2.1 Detection of Impedance at a Specific Frequency

This method is a special case or an extension of the harmonic detection method [38]. The method injects harmonic currents of a specific frequency intentionally into PCC. Typically the impedance is measured at the frequency range between 500Hz to 1KHz for good estimation accuracy, because for a small frequency the estimated impedance will be affected by the system present harmonics, and the estimated resistance will not accurate at a higher frequency due to the large value of estimated reactance. In the presence of the grid, if the grid impedance is greater than the load impedance at harmonic frequency then harmonic current flows into the grid and no abnormal voltage is seen.

Upon disconnection of the utility, harmonic current flows through the load. If the load is linear then the load produces harmonic voltage proportional to the impedance, which can be detected. The method has been given such a name because the amplitude of the harmonic voltage is proportional to the load impedance at the frequency of harmonic currents. This method can give a nuisance trip problem in multiple inverter case. The method has similar NDZ as that of the harmonic detection method [12]. However, if an active load is connected, this may lead to a false trip.

### 2.3.2.2 Slip Mode Frequency Shift method

Slip mode frequency shift (SMS) is one of the few methods that uses positive feedback to detect islanding condition [12, 38, 57]. As seen from (2.4), there are three parameters to which positive feedback can be applied. SMS applies positive feedback to the phase  $\phi_{PV}$  of the voltage at the PCC. This method shifts the phase and hence the short term frequency. However, the frequency of the grid is not affected by this method.

$$i_{PV-inv} = I_{PV-inv} \sin(\omega_{PV} t + \phi_{PV}) \quad (2.4)$$

Normally, PV inverters operate at unity power factor, so that the phase angle between inverter output current and PCC voltage is zero or close to zero. In

SMS method, this angle is made to be a function of frequency of PCC voltage. The phase response curve of the inverter is designed such that the phase of the inverter increases faster than the phase of load (RLC) with a unity power factor in the region near the utility frequency  $\omega_0$ . This makes the line frequency an unstable operating point for the inverter [38]. When the grid is present, the method stabilizes the operating point at the line frequency by providing a solid phase and frequency reference. In the islanded condition, there are perturbations in frequency of PCC voltage. The phase response curve of the inverter causes the phase error to increase, which is function of the positive feedback mechanism and causes instability.

The method is easy to implement and has relatively small NDZ as compared with other active methods. It also proved to be a better islanding detection method in the multiple inverter case [12]. SMS requires a decrease in output power quality of PV inverters. It also causes system level poor quality and transient response problems. This method is shown to be effective both theoretically and experimentally [58]. Some RLC loads have a phase response such that phase of the load increases faster than phase of PV inverter [59]. These are loads having high Q-factor.

### 2.3.2.3 Robust Islanding Detection Algorithm

The Robust Islanding Detection algorithm is developed for Distributed Fuel Cell Powered Generation (DFPG) connected to the utility [12, 60]. The proposed algorithm continuously perturbs the reactive power supplied by DFPG while monitoring utility voltage and frequency. It has been shown that an observable ( $\pm 1\%$ ) frequency deviation is observed if reactive power is perturbed by  $\pm 5\%$ . To confirm islanding DFPG real power is reduced to 80%. If the terminal voltage drops below 0.9 p.u. then DFPG is disconnected. Fig.2.10 shows a flowchart of the algorithm of this method.

This method has been shown to be robust and fast acting. It also has a reduced NDZ as compared to other methods. The algorithm is analyzed on a single unit of DFPG. If multiple DFPG's are connected this method may fail or

malfunction. A cross correlation index of rate of change of frequency with respect to reactive power is suggested to overcome this problem.

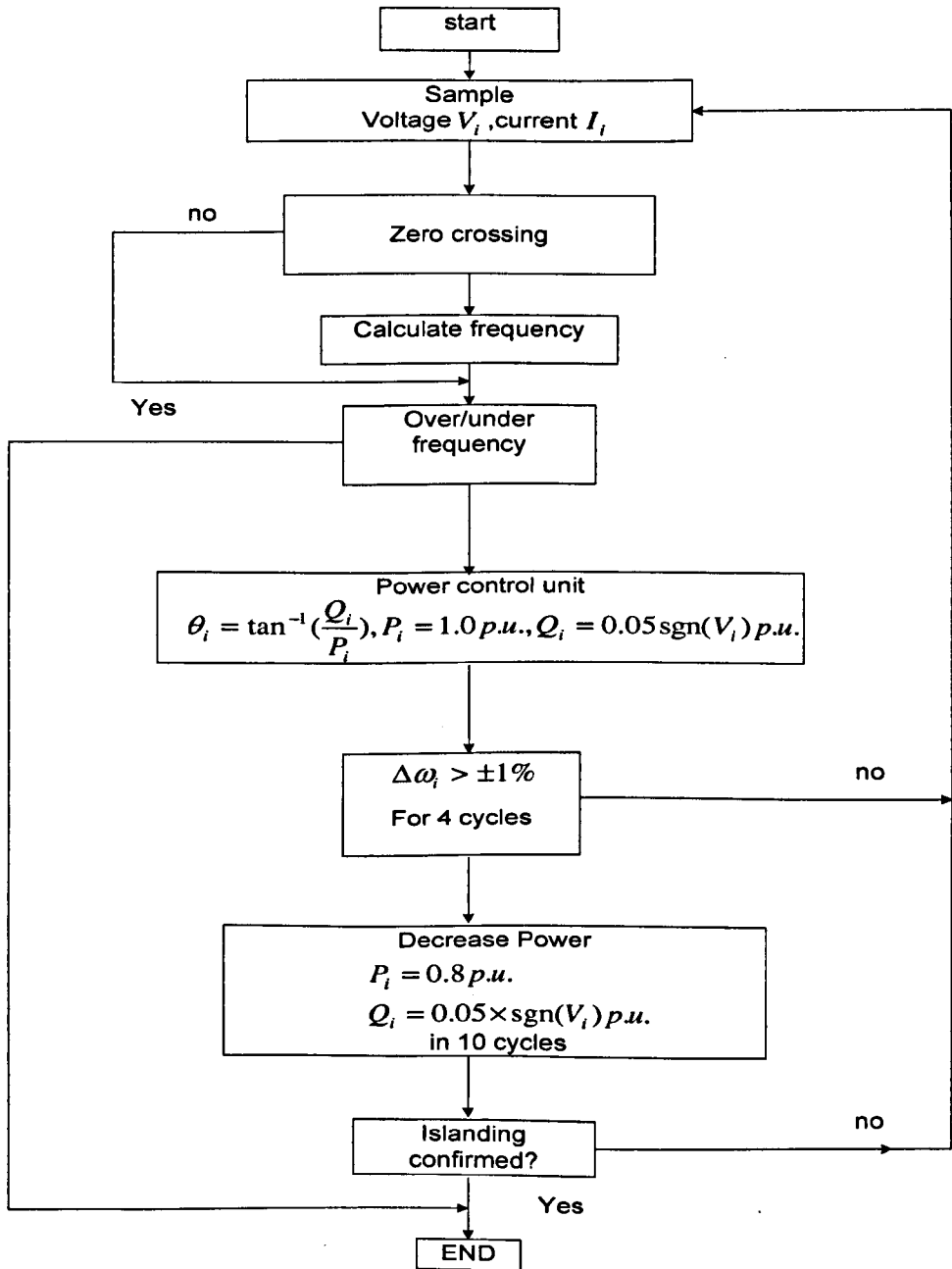


Fig.2.10 Algorithm for robust islanding detection method

#### 2.3.2.4 Sandia Voltage Shift (SVS) Method

When islanding occurs, if  $\Delta P$  and  $\Delta Q$  are small enough, islanding can not be detected because system frequency or voltage will not sufficient to trip the UFR/OFR or UVR/OVR protection. The unintentional islanding will continue until  $\Delta P$  and  $\Delta Q$  become large enough to shift the voltage or frequency beyond the thresholds. The voltage value at PCC is proportional with active power of the inverter, if the active power increases, the voltage will rise [61]. Therefore, during islanding condition by providing a positive feedback technique on the amplitude of voltage at PCC can lead the increasing or reduction in voltage until corresponding over or under voltage protection (OVP/UVP) to trip. It can be achieved by increase or decrease the power output of the inverter.

The voltage shift positive feedback mechanism is based on dq-control. When the measured voltage increases, SVS increases the q-axis current to produce more active power. If the inverter is islanded, the voltage shift will continue increasing until it goes beyond the protection thresholds. If the inverter is grid connected, the voltage will remain stable because the grid holds the voltage firmly. In the case of the measured voltage decreasing, the positive feedback works in such a way that reduced active power can keep the voltage decreasing.

The SVS method has two weaknesses. The positive feedback operation causes a slight reduction in power quality. Also the PV inverter's operating efficiency gets slightly reduced [12, 38].

#### 2.3.2.5 Frequency Shift Method

Active frequency drift method (AFD) is one of the frequency shift methods [62-63]. If the grid is connected in the case of system with unity power factor, the phase angle between the terminal voltage and the output current is zero. When loss of main occurs, phase difference between the terminal voltage and the output current of the inverter depends on the load. It can be detected by the internal phase-locked-loop (PLL). To eliminate the phase difference, the

frequency of the inverter output current is forced to drift up or down. The intention is to make the frequency of the terminal voltage deviate from its nominal value until OFR/UFR is triggered. However, this method becomes ineffective under certain load conditions, especially with paralleled RLC resonant loads [64].

Compared with AFD method, the automatic phase shift method (APS) can reduce the non-detection zone in the case of system with paralleled RLC resonant loads. The flow diagram of the APS algorithm is as shown in Fig.2.11. At the  $k$ th zero-crossing of the terminal voltage, frequency of the previous voltage cycle is first measured. The starting angle  $\theta_{APS}[k]$  of the inverter output current is changed according to the frequency of the previous cycle  $f[k-1]$  using (2.5), but the frequency remains at nominal line frequency.

$$\theta_{APS}[k] = \frac{1}{\alpha} \left( \frac{f[k-1] - 60}{60} \right) \times 360^\circ + \theta_0[k] \quad (2.5)$$

If the steady state frequency of the terminal voltage reached before the under or over frequency (UFR) or (OFR) triggers, the additional phase shift  $\theta_0$  is also changed from:

$$\theta_0[k] = +\theta_0[k-1] + \Delta\theta \times \text{sgn}(\Delta f_{ss}) \quad (2.6)$$

where  $\Delta\theta$  is constant,  $\Delta f_{ss}$  is the change in steady state frequency.

$$\text{sgn}(\Delta f_{ss}) \begin{cases} 1, \Delta f_{ss} > 0 \\ 0, \Delta f_{ss} = 0 \\ -1, \Delta f_{ss} < 0 \end{cases} \quad (2.7)$$

According to the frequency of the inverter output current the starting angle of the inverter output current is changed. An additional phase shift is introduced each time the frequency of terminal voltage stabilizes to new operating point. This algorithm assures that if the grid is disconnected the frequency of the terminal voltage keeps deviating until OFR or UFR triggers.

The APS method reduces the non-detection zone during the system with purely resistive loads and parallel RLC loads with resonant frequency equal to line

frequency. It also works for multiple inverters. The shortcoming of this method is that when the line frequency deviates from its nominal value, the inverter output current would not be in phase with the grid voltage. And for non linear loads such as induction motor having large inertia, this method can give errors [12, 38].

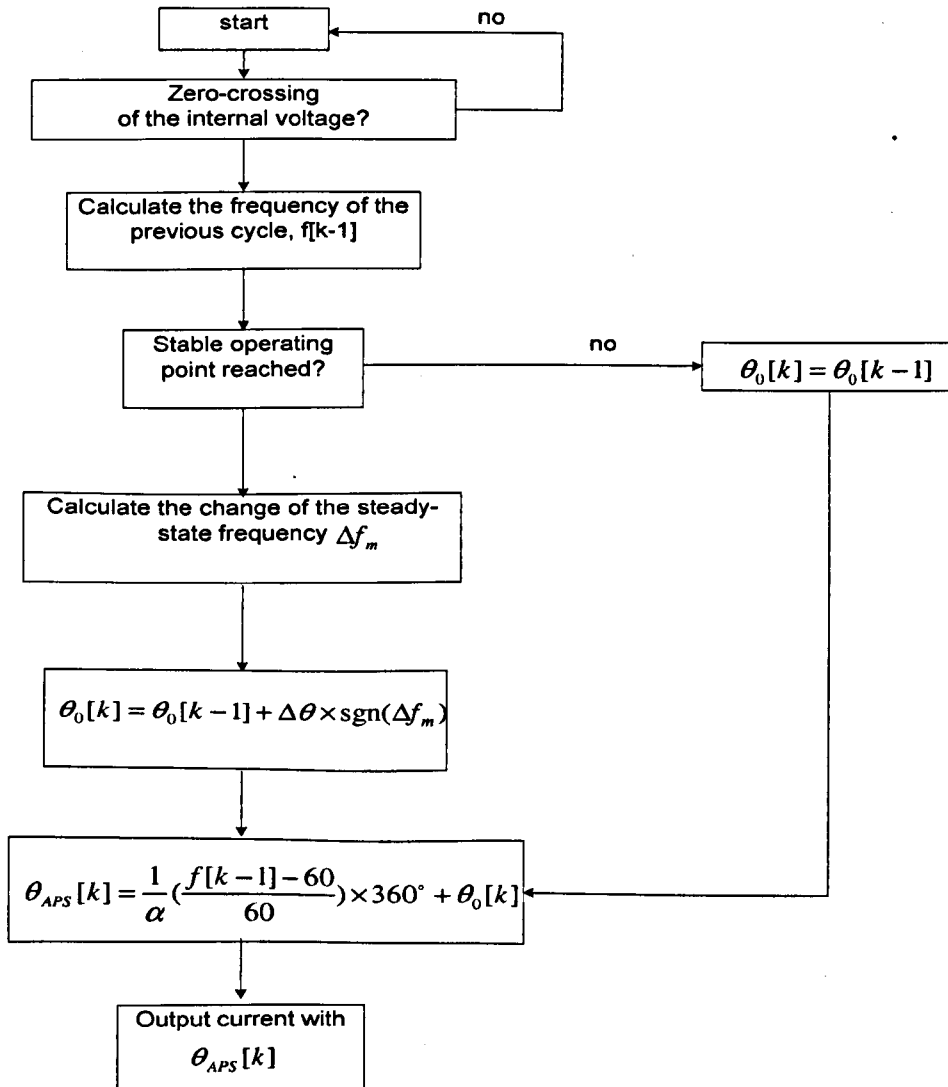


Fig.2.11 Algorithm for APS method

### 2.3.2.6 Positive Feedback (PF) Technique

The PF technique is one of the most dominant existing islanding detection methods [61, 65]. It works by giving the DG a positive feedback of voltage and frequency. As long as the DG-connected to part of the grid or the micro-grid

(MG) is connected to the utility grid, the frequency and voltage of the MG stays at the nominal level. However, as soon as the utility supply is disconnected, due to switching or an electrical fault, the positive feedback of the DGs push the MG frequency and voltage beyond the permissible window of operation of the interfacing inverters, and as a result, they will shut down. Consider an inverter-based DG is connected to the utility grid, under the normal operation conditions, the utility maintains the frequency (i.e.  $f_{fine} = 50$  or 60 Hz), the utility grid is disconnected, the error between the two frequencies ( $\Delta f = |f_i - f_{fine}|$ ) will increase, and as a result,  $f_i$  is pushed higher due to positive feedback. The increase in the value of  $f_i$  will continue until it crosses the permissible window of operation, and the inverter will shut down.

In the PF method, it is assumed that a DG is interfaced through an inverter. This technique works, but it has some serious drawbacks. For example, if several DGs are connected to the utility grid, they together may push the voltage and the frequency error higher, and as a result, the PF technique could destabilize the utility grid.

### 2.3.2.7 Other Active Methods

Several other active islanding methods have been also proposed. QC mode frequency shift method [26] is also developed for synchronous generators. It also applies a fluctuation signal to an automatic voltage regulator. The signal is dependant on power system frequency fluctuation [12]. Reactive power compensation method detects islanding by making a reactive power fluctuation by a reactive power compensator. This method is applicable to induction machine type DRs. Inter-harmonics method injects non integer harmonics to power system. The response of a power system to inter-harmonics changes when islanding occurs. A classification of active methods developed in Japan is provided in [26].

### 2.3.3 Hybrid

Passive and active methods are two major categories of anti-islanding approaches which are being widely used in grid-connected distributed generation (DG) systems. Passive anti-islanding techniques have no negative impact on the inverter's performance however a large non-detection zone is the shortcoming of these techniques. On the other hand, active approaches have a smaller non-detection zone, but these inevitably have negative impact on system power quality. Hybrid methods based on combining the active and passive method are applied to solve these problems [65-67]. The active method is implemented only when the islanding is suspected by the passive technique.

#### 2.3.3.1 Technique Based on Positive Feedback (PF) and Voltage Unbalance (VU)

In paper [65] the hybrid islanding detection technique which is based on the principles of PF and VU/THD techniques was proposed. The three-phase voltages are continuously monitored at the DG terminals, and VU is calculated for each DG. Any disturbance applied to DGs, e.g., as result of random load changes (switching) or islanding could result in a spike in VU. To discriminate between the causes of VU spikes, the frequency set point of DG is gradually lowered from 60 to 59 Hz in one second. The one-second duration was empirically chosen after running many simulations. If the duration is too short, the average values of the spikes closely follow their instantaneous values; hence, the spikes could go undetected. The spikes are detected only if their instantaneous values are considerably larger than their average values. If the duration is too large, for example, an electronically controlled load is added, then there would be an immediate increase in VU. However, it would take some time for the average value to reach a higher level. Therefore, even a small spike could cause false tripping.

Once the frequency set point is changed from 60Hz to 59Hz, the relay starts to continuously monitor the frequency of the DG output voltage. If the estimated frequency falls below 59.2Hz within the next 1.5s, the islanding situation is

confirmed and the trip signal would be sent to the circuit breaker due to the loss of main situation. The frequency set point is restored to 60Hz. Therefore, autonomous operation of the microgrid is achieved.

This technique is suitable for synchronous rotating DGs, it can discriminate large load switching and islanding, and only the DGs in the vicinity of load switching change their frequency set point which is an advantage over PF technique. However, the islanding detection time is too slow.

### **2.3.3.2 A Hybrid of Method Based on ROCOF, ROCOV and CF**

Paper [66] proposed hybrid islanding detecting scheme is based on two stages detecting procedures to achieve higher effectiveness. During the detecting procedure a passive detection method is used as primary protection and active detection method is the backup. The voltage detecting interface and current detecting interface measure the magnitude of terminal voltage and current at the grid-interconnected point; and a zero crossing detecting circuit detects the zero crossing signal of the terminal voltage. A periodical switching signal generator generates the periodic switching command for high impedance load. A digital signal processor DSP calculates the rate of change of frequency (ROCOF), rate of change of voltage (ROCOV), and correction factor (CF) of distributed synchronous generator (DSG) and decides whether the trip conditions are met. In this hybrid method, 5 thresholds values need to be set, the index of ROCOF and ROCOV for larger and smaller real and reactive power imbalance is set separately.

This method is effective and economical. And the detection performance is verified to be less dependent on the load quality factor and power level. However, it is more suitable for small distributed generation systems.

### 2.3.3.3 A Hybrid of Method Based on Using Average Rate of Change of Voltage and Real Power Shift

In [68] the algorithm of combining average rate of voltage change and real power shift, as a hybrid islanding detection method is proposed to overcome the drawbacks of both active and passive techniques. In this method, voltages are measured every period at the DG buses. After  $dV/dt \neq 0$  is detected, the magnitude of average rate of voltage change for 5 periods  $Av5$  is used to determine whether the system has been islanded or not. If  $Av5$  is larger than a minimum set point  $V_{s\min}$ , islanding is suspected. If it is larger than a maximum set point  $V_{s\max}$  due to the large mismatch of the generation and demand, it is clear that the distribution system is islanded. But if  $Av5$  is between  $V_{s\min}$  and  $V_{s\max}$ , then the change in voltage could be caused by other events like switching, load change, etc. Then real power shift (RPS) is applied. The magnitude of average rate of voltage change for 20 periods ( $Av20$ ) is calculated, after initiation of RPS, is used to differentiate islanding from any other event in the system. If  $Av20$  is larger than  $V_{s\max}$  (set point to detect islanding with RPS), then it is from an islanding condition.

This method eliminates the necessity of injecting disturbance from time to time to detect islanding. RPS only changes the real power of DG, which satisfies the condition DG operating at the utility power factor. And islanding condition can be detected even when generation and load closely match. However, the method may fail to detect islanding for a perfect match of demand and generation in the islanded system.

## 2.4 Summary

This chapter provides many islanding detection methods, which can be broadly classified into remote and local techniques, local techniques are further divided into passive active and hybrid techniques. Each technique has its advantage and limitation. Comparison of these methods can provide useful information for determining a method to use, there is no single islanding detection

technique which works satisfactorily for all systems under all situations. It is necessary to know the limitations these islanding methods possess before the comparison. The main considerations are:

- High implementation costs
- Susceptibility to false operation in multiple DG case
- Presence of NDZ's
- Reduction in power quality and system stability due to positive feedback

Choice of the islanding detection technique will largely depend on the type of the DG and system characteristics. Recently hybrid detection techniques have been proposed, compared with passive method, there is a small non-detection zone but longer detection time; the perturbation is introduced in the hybrid method only when an islanding situation is suspected unlike the active method. In chapter 3 and 4 the combination of ROCOF relays with rate of change of power and  $v^2/p$  interlock functions are introduced to detect islanding and avoid false tripping during non-islanding situation (such as load changing), compared with hybrid algorithm the detection time combination of two passive methods is much smaller and there is no perturbation injected into the system, which are the advantages over active and hybrid methods.

## **Chapter 3**

# **Advanced ROCOF Protection of Synchronous Generator**

### **3.1 Introduction**

As described in Chapter 2, many methods have been applied to detect an islanding situation. The core concept is to monitor the system parameters such as voltage, frequency, harmonic distortion, which will vary greatly during an islanding situation. Rate of change of frequency (ROCOF) is the most commonly employed anti-islanding protection technique [33, 40, 69]. However, there are some concerns about nuisance tripping due to the sensitivity to network disturbance, also false operation may happen during a non-islanding situation. Therefore, it is important to detect an islanding situation correctly and block the nuisance tripping signal due to system load variations as quickly as possible.

This chapter introduces the principle of ROCOF relays, the methods of Fast Fourier Transform and the Prony's method that are used for frequency

estimation, and their characteristics (i.e. frequency measuring methods, measuring windows, different relay settings, generator inertia and different load power factor) of ROCOF relays which affect the operation responses are investigated and the analysis of ROCOF performance for an embedded synchronous generator islanding detection is performed. A new interlock function of rate of change of power is proposed, by cooperating with ROCOF relays, it is shown that it can avoid false operation during the system load variation situation quickly and accurately.

## 3.2 The Principle of ROCOF Relays

### 3.2.1 Basic Theory

An equivalent circuit of a synchronous generator equipped with a ROCOF relay operating in parallel with a distribution bus for a load of the power supply is shown in Fig.3.1. In this example the synchronous generator (SG) feeds the load L. The difference between the electrical power  $P_{SG}$  supplied by the generator and the power  $P_{Load}$  consumed by the load is provided (or consumed) by the main grid. Therefore, the power system frequency is kept constant. If the circuit breaker CB opens during a fault, the generator and the load that composes the system become islanded. In this case transients are caused by an electrical power imbalance in the islanded system and the system frequency starts to vary dynamically. Such system behaviour can be used to detect the islanding condition. But if the power imbalance in the system is small, the frequency will change slowly. Thus the rate of change of frequency  $df/dt$  can be used to accelerate the islanding detection in this situation [18, 70].

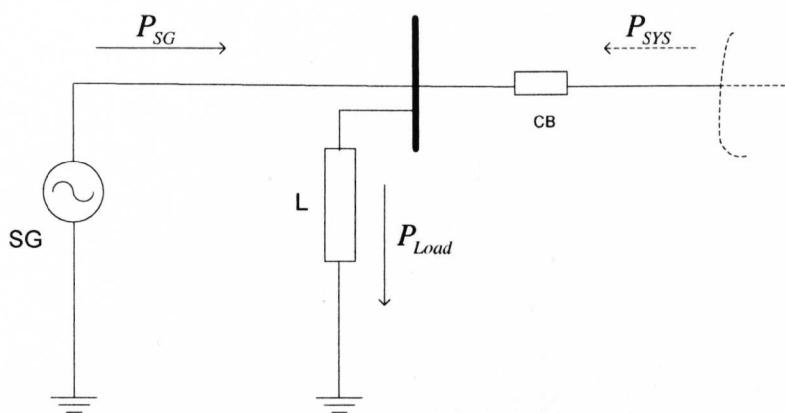


Fig.3.1 Equivalent circuit of an embedded generator operating in parallel with utility

The rate of change of frequency is calculated by using a measuring window of a few cycles (usually between 2 to 40 cycles) from the bus terminal voltage waveform. This signal is processed by filters and then a resulting signal  $K$  is used to detect an islanding situation [18]. If the value of the rate of change of frequency is higher than the threshold value  $\beta$  (relay setting), a trip signal is sent to the circuit breaker of the generator immediately. Fig.3.2. provides a schematic diagram of the operating principle of ROCOF relays. Where the first order transfer function  $1/(T_a s + 1)$  which represents a low-pass filter is used to eliminate high-frequency transients and  $K$  is the rate of change of frequency after a filtrating processing.

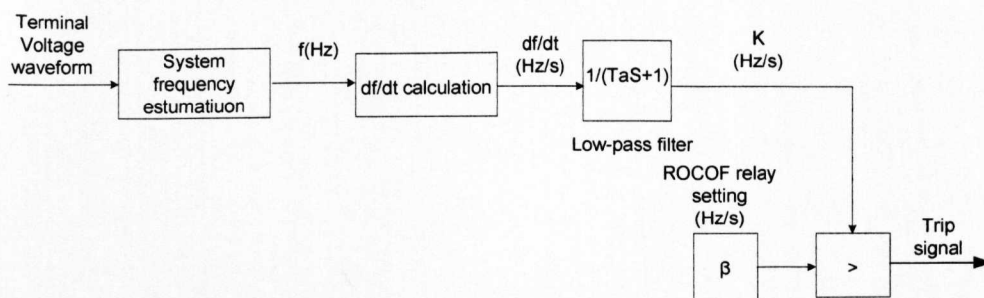


Fig.3.2 Simplified schematic diagram of ROCOF

The system frequency  $f$  is estimated from the terminal voltage waveform, by using a differential function as depicted in Fig.3.3. At each cycle the variation of the voltage angle  $(\theta - \theta_0)$  is calculated, where  $\theta$  is the current phase angle of the voltage waveform;  $\theta_0$  is voltage phase angle of the previous cycle [71]. Once the phase angle is known then the frequency can be estimated as it can be

shown that the frequency error is given by  $\Delta f = (1/2\pi)(d\theta/dt)$ . In order to obtain the frequency, the system frequency  $f_0$  is added to this deviation and the resulting signal is processed by the low-pass filter  $1/(1+sT_{LP})$ , and multiplied by the system frequency  $f_0$  (50Hz).  $T_{LP}$  is the time constant of the low-pass filter and  $f_0$  is the system rated frequency in p.u.

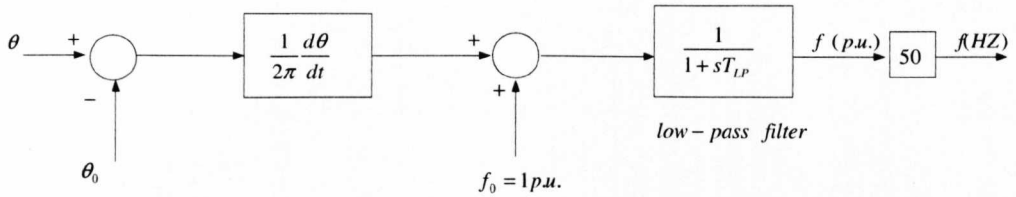


Fig.3.3 Model implemented for system frequency estimation

The system frequency estimated is the input parameter for the rate of change of frequency calculation block (see Fig.3.2). According to (3.1) the effective rate of change of frequency used by the relay is calculated considering the average value of two cycles. Such that:

$$\frac{df}{dt} = \frac{1}{2} \sum_{i=1}^2 \frac{\Delta f_i}{\Delta t_i} \quad (3.1)$$

where  $\Delta f_i$  is the frequency variation within one cycle;  $\Delta t_i$  is the cycle duration and  $i = 1, 2$  is the corresponding cycle. Thus the value of  $df/dt$  is updated every two cycles. This signal is then processed by a first-order transfer function with a time constant  $T_a$ , as presented in Fig.3.2. This filter eliminates high-frequency transients and smoothes the  $df/dt$  signal, yielding the signal  $K$ . If the resulting signal  $K$  is greater than the relay setting  $\beta$ , then the ROCOF relay will send a trip signal to the generator circuit breaker.

### 3.2.2 Analytical Formulas for Determining the Performance of ROCOF Relays

According to the embedded generation system presented in Fig.3.1, the mechanical power  $P_M$  of the synchronous generator is balanced with the electrical power  $P_L$  consumed by the load and the electrical power  $P_{SYS}$  provided by (or injected into) the power grid. Therefore the synchronous generator rotor speed  $\omega$  and angle  $\delta$  are constant. After opening of the circuit breaker CB, the synchronous generator starts running in an islanded mode and a power imbalance increases due to the losses of grid power  $P_{SYS}$ . The magnitude of the power imbalance  $\Delta P$  is equal to  $P_{SYS}$ , and it causes disturbance in the synchronous generator. The dynamic behaviour of the synchronous generator can be determined by means of the machine swing equation [18, 72-73]. The swing equation of the synchronous generator is given by (3.2):

$$\begin{cases} \frac{2H}{\omega_0} \frac{d\omega}{dt} = P_M - P_L = -P_{SYS} = \Delta P \\ \frac{d\delta}{dt} = \omega - \omega_0 \end{cases} \quad (3.2)$$

where  $H$  is the generator inertia constant,  $\omega_0 = 2\pi f_0$  is the synchronous speed,  $f_0$  is the system nominal frequency and the other variables have been defined previously. By solving the equation (3.2) the rate of change of frequency can be calculated as:

$$\frac{df}{dt} = \frac{1}{2\pi} \frac{d\omega}{dt} = \frac{f_0}{2H} \Delta P \quad (3.3)$$

It can be observed from equation (3.3) that the rate of change of frequency is proportional to the power imbalance. As presented in Fig.3.2, the relay trigger signal is processed by a low-pass filter, which can be represented by a first-order transfer function. Therefore, the signal  $K$  used by the ROCOF relay can be described as:

$$K = \frac{f_0 \Delta P}{2H(T_a s + 1)} \quad (3.4)$$

where  $s$  represents the time derivative operator. At  $t = 0$ ,  $K(0) = 0$  (initial state), because the system is operating in steady state, Therefore the solution of (3.4) is given by:

$$K = \frac{f_0 \Delta P}{2H} (1 - e^{-\frac{t}{T_a}}) \quad (3.5)$$

It can be seen from equation (3.5) that the system frequency estimation and the rate of change of frequency calculation processed by the relay suffers a time delay. The measure window usually takes a few cycles of the nodal voltage to calculate the rate of change of frequency. In order to obtain an accurate results for the analytical formula the delay time must be considered in (3.5). The relationship between the time  $t$  and  $t_d$  is given by equation (3.6).

$$t = t_d - \Delta t \quad (3.6)$$

$\Delta t$  is considered as the time duration of the cycles employed to perform the  $df / dt$  calculation and  $t_d$  is the total time delay suffered by the measured signal. The signal  $K$  can now be corrected as:

$$K = \frac{f_0 \Delta P}{2H} (1 - e^{-\frac{-(t_d - \Delta t)}{T_a}}) \quad (3.7)$$

If the value of the signal  $K$  is larger than the value of the relay setting  $\beta$ , the ROCOF relay operates. Both are equal when the relay operates and thus it is possible to replace  $K$  by  $\beta$  in (3.7), resulting in:

$$\beta = \frac{f_0 \Delta P}{2H} (1 - e^{-\frac{-(t_d - \Delta t)}{T_a}}) \quad (3.8)$$

Based on the detection time requirement and the minimum power imbalance during islanding condition, (3.8) can be used to adjust the relay setting. Two

other important expressions can be derived from (3.8). Solving (3.8) for  $t_d$  gives:

$$t_d = -T_a \ln\left(1 - \frac{2H}{f_0 \Delta P} \beta\right) + \Delta t \quad (3.9)$$

Solving (3.8) for  $\Delta P$  gives as follows:

$$\Delta P = \frac{2H}{f_0} \beta \left(1 - e^{-\frac{-(t_d - \Delta t)}{T_a}}\right)^{-1} \quad (3.10)$$

The previous mathematical development can be applied to the following situations:

- 1) If the power imbalance  $\Delta P$  and the detection time requirement  $t_d$  are provided, one can determine the required relay setting  $\beta$  by using (3.8).
- 2) If the power imbalance  $\Delta P$  and the relay setting  $\beta$  are provided, one can determine the necessary detection time  $t_d$  by using (3.9).
- 3) If the detection time requirement  $t_d$  and the relay setting  $\beta$  are provided, one can determine the minimum power imbalance  $\Delta P$  that can be detected by ROCOF relay by using (3.10).

## 3.3 Frequency Estimation Methods

### 3.3.1 Fast Fourier Transform

The Fourier Transform is one of the most frequently adopted signal processing tools for system frequency calculation. For a series of digital recorded sampling signals, the phasor of the fundamental waveform of the voltage can be calculated from  $N$  samples, the DFT can be realized by equation (3.11) [74].

If the sampling window equals one cycle of the basic waveform, the phasor at the time  $t_k = kT$  is given by:

$$G_k = \frac{2}{N} \sum_{n=0}^{N-1} v_{k+n-N+1} e^{-j\omega T n} \quad (3.11)$$

where:

$T$  : sampling interval

$\omega$  : fundamental frequency

$v_{k+n-N+1}$  : sampled values of a voltage

If the  $N$  sample series DFT is performed, it requires  $N^2$  complex multiplications and additions [75]. Due to the symmetrical characteristic of  $e^{-j\omega T n}$ , using the 'butterfly representation' of the numerical process [76], the DFT procedure can be simplified and the number of multiplications can be reduce to  $N \log_2 N$ . This modified calculation is called the Fast Fourier Transform (FFT) which produces the same results as a DFT but is able to greatly speed up the calculations and this is especially true for a data series with a large amount samples.

When implementing the DFT,  $G_k$  is updated at every sampled value. After each sampling cycle, the newest sample is taken into the calculation, while the oldest one is neglected. For each position of the phasor, its argument can be calculated. The instantaneous frequency can be determined from the two consecutive phasors.

$$\omega = \frac{\arg[G_{k+1}] - \arg[G_k]}{T} \quad (3.12)$$

where

$$\arg[G_k] = \tan^{-1} \left\{ \frac{\text{Im}[G_k]}{\text{Re}[G_k]} \right\} \quad (3.13)$$

### 3.3.2 The Prony's Method

Prony's method is an algorithm for modelling the uniformly sampled data as a linear combination of damped exponentials. It has applications in filter designs, exponential signal modelling and system identification (parametric modelling). This method extracts valuable information from an equally sampled signal and constructs a series of frequencies, amplitudes, phases and damping components of a signal [77].

A sampled signal  $x(n)$  having  $N$  data samples  $x[1], x[2], \dots, x[N]$ , can be approximated with a  $p$ -term complex exponential model:

$$\hat{x}[n] = \sum_{k=1}^p A_k \exp[(\alpha_k + j2\pi f_k)(n-1)T + j\theta_k] \quad (3.14)$$

For  $1 \leq n \leq N$ , where,  $T$  is the sample period in seconds,  $A_k$  is the amplitude of the complex exponential,  $\alpha_k$  is the damping factor in 1/seconds,  $f_k$  is the sinusoidal frequency in Hz, and  $\theta_k$  is the sinusoidal initial phase in radians.

In the proposed algorithm, a voltage signal, which is used to track the fundamental frequency, is described by a complex phasor  $G$  [9]. The parameters  $X_a, X_b$  can be calculated from  $N$  sampled values of the signal by the least-square-errors method [78-80].

$$G = X_a - jX_b \quad (3.15)$$

If the sample window is chosen as one cycle of the fundamental period, the complex phasor can be simply described by the sum of the DFT-filtered sampled values in one fundamental period as equation (3.16). For further processing, we need only the time function of the fundamental component of voltage which is equal to the real part of the phasor [78-80].

$$g_k = \frac{2}{N} \sum_{n=0}^{N-1} v_{k+n-N+1} \cos(n\omega T) \quad (3.16)$$

where  $T$  is sampling time,  $\omega$  is fundamental frequency, and  $v_{k+n-N+1}$  is sampled values of voltage.  $g_k$  is updated at every sampled value. To improve the filter properties, applying of a smoothing window is proposed. Rectangular windowing has disadvantages when there is a frequency change. Therefore the signal is windowed in a smooth way by a Hamming window.

The fundamental frequency of the signal is to be identified. Therefore, an undamped complex exponential model is applied to estimate the signal as equation (3.17).

$$\bar{g}_m = A \cos(m\omega T_s + \varphi) \quad \text{for } m = 1, 2, \dots, M \quad (3.17)$$

where  $M$  is the number of samples taken into the approximation. It cannot exceed a half of the number of the sampled points [77] and can be chosen as a third of the number. If the estimation is described in the complex exponential form as equation (3.18), the estimation problem becomes the determination of the optimum values of  $b$  and  $z_1$  so that the error in equation (3.19) is minimized.

$$\bar{g}_m = bz_1^m + b^* z_1^{*m} \quad (3.18)$$

where

$$\begin{cases} z_1 = e^{i\omega T_s} \\ b = \frac{A}{2} e^{j\varphi} \end{cases} \quad (3.19)$$

$$\delta_m = g_m - \bar{g}_m \quad (3.20)$$

Here,  $g_m$  ( $m = 1, 2, \dots, M$ ) is a series of the sample values of the part of the filtered signal.

Prony's method converts this nonlinear problem into a linear fitting problem by minimizing the error  $E$  defined as:

$$E = \sum_{m=p}^{M-1} \varepsilon_m^2 \quad (3.21)$$

where  $p$  is the number of exponents and  $\varepsilon_m$  is defined by:

$$\varepsilon_m = \sum_{k=0}^p a_k \delta_{k+m-1} \quad (3.22)$$

The parameters  $a_k$  are initially unknown and related to the frequency of the sinusoid. The detailed procedure to determine the parameters is referred to [74]. Here, the fundamental frequency to be tracked is calculated by:

$$f = \frac{1}{2\pi T_s} \cos^{-1} \left\{ \frac{\sum_{m=2}^{M-1} (g_{m-1} + g_{m+1})^2}{2 \sum_{m=2}^{M-1} g_m (g_{m-1} + g_{m+1})} \right\} \quad (3.23)$$

The accuracy of this method is mainly determined by the sampling frequency  $f_s$  and the number of the order of the approximation  $M$ . Generally, the Prony's method uses exponential mode to approximate the original signal. Comparing with FFT, it does not require one or more cycles of data to estimate the fundamental frequency.

In order to detect if the ROCOF relay method working properly, a three phase programmable voltage source is first used. The rate of change of frequency is set to 1Hz/s and variation time is 1s. The initial frequency of the three-phase programmable voltage source is 50Hz, the target frequency is 51Hz and the simulation time is 3.25s. Therefore, the rate of change of frequency is 1Hz/s (which mean the slope is 1). Fig.3.4 and Fig.3.5 show the frequency estimation by using FFT and the Prony's method.

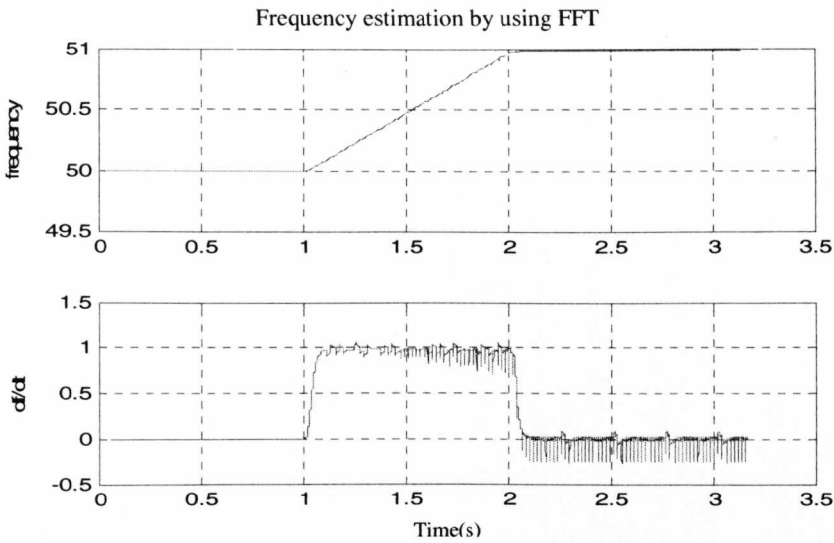


Fig.3.4 The frequency (top) and the rate of change of frequency estimation (bottom) by using FFT method

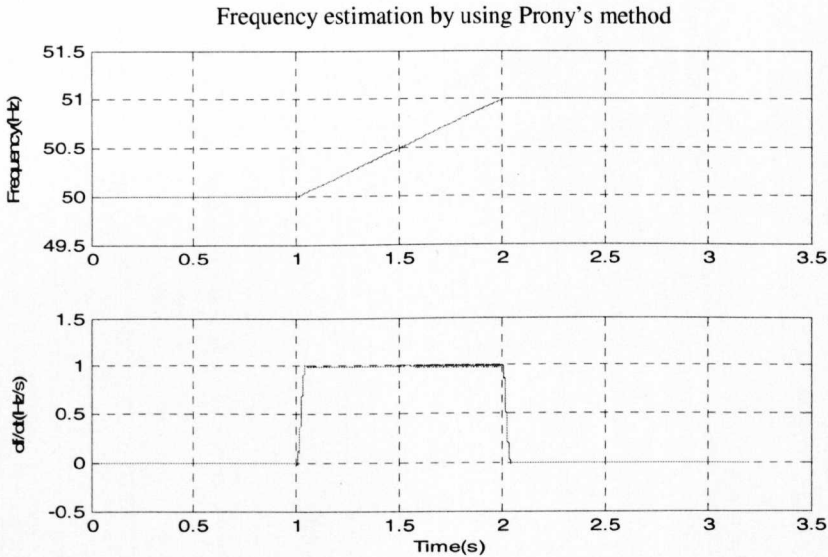


Fig.3.5 The frequency (top) and the rate of change of frequency estimation (bottom) by using Prony's method.

The time delay in the results of ROCOF derived by both methods is mainly due to the measurement window (the data segment taken into processing). For a 10kHz frequency the FFT method uses at least one cycle of data to produce the frequency results, whereas for the Prony's method a shorter data capture window can be used. To obtain accurate results, the delay time must be considered. The notches (odd behaviour part of figure) are because the errors within the frequency calculation results and are greatly amplified by the

procedure of the derivative process. Both algorithms prove that they have the ability to extract the accurate fundamental frequency.

### 3.4 Simulation Results

#### 3.4.1 Islanding

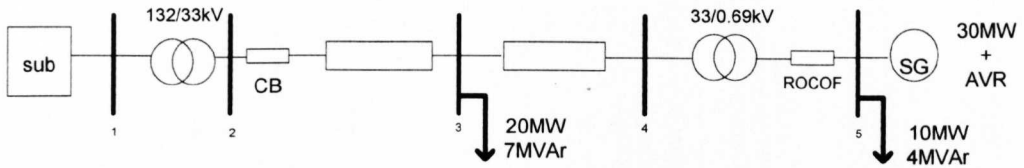


Fig.3.6 Single line diagram of test system

The test system shown in Fig.3.6 was used to evaluate the routines. It comprises a 132kV, 50Hz, sub-transmission system with short-circuit level of 1500MVA, which feeds a 33kV distribution system through a 132/33kV  $\Delta/Y_g$  transformer. In this system there is one 30MW synchronous generator connected at bus 5, which is connected to the network through one 33/0.69kV  $\Delta/Y_g$  transformer. Such a generator is equipped with an excitation system which is used to control the terminal voltage. In all simulated cases, the circuit breaker CB at bus 2 opens at 0.5s, and remains open during the rest of the simulation. Thus, the initial active power imbalance in the islanded system is equal to the active power provided by the substation at the islanding moment. The total simulation time is 1s. Therefore if the ROCOF relay installed at bus 5 does not detect the islanding condition until 0.75s after the circuit breaker opened, it is considered that the device is inoperative for this case [18].

The simulations were carried out to assess the differences seen by a ROCOF relay when employing different frequency determination techniques. In this case, by setting the power imbalance to 0.5 p.u and operating the circuit breaker at 0.5s (see Fig.3.4) the rate of change of frequency as estimated by the Fast Fourier Transform and the Prony's method are depicted in Fig.3.7.

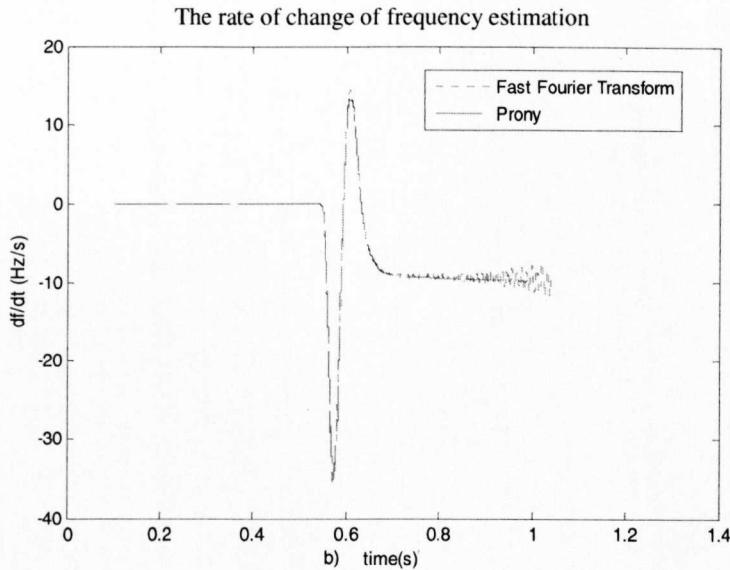
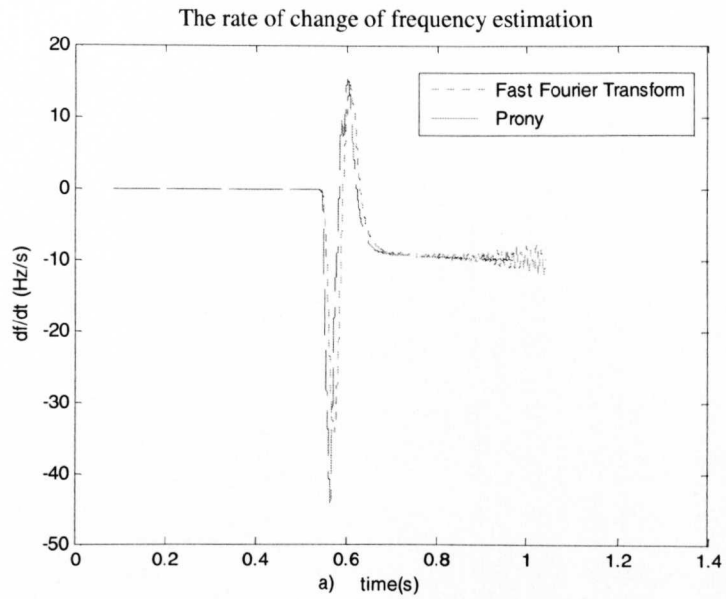


Fig.3.7 a) The rate of change of frequency estimation by Fast Fourier Transform Method and the Prony's method with different length of data processing window. ( $\Delta p = 33\%$ ,  $H = 1.5s$ ,  $\beta = -1$ ) b) The rate of change of frequency estimation by Fast Fourier Transform Method and the Prony's method with same length of data processing window.

Using different lengths of data processing windows it can be observed from Fig.3.7 a) that as the Prony's method uses a 28ms data capture window the relay sees a higher rate of change of frequency than the Fast Fourier Transform which applies 40ms data capture windows algorithm when subjected to the

same disturbance. To choose 28ms data capture window for the Prony's method provides fast islanding detection time and less sensitivity with system noise. The window capture for FFT method could be integral, in order to avoid nuisance tripping caused by the small data capture, 40ms (2cycles) is applied. As mentioned in Section 3.3.2, the Prony's method uses the sampled data to perform a approximation calculation. It does not require a whole cycle of data to estimate the fundamental frequency. Here the 40ms (FFT) and 28ms (the Prony's method) are selected to reduce the influence of system distortion and also offers a fast islanding detection. This explains the detection time calculated by Prony's method is shorter than the Fast Fourier Transform method as shown in Fig.3.7 a). However, if the same integral cycles of data are used, the rate of change of frequency estimated by these two methods is similar as Fig.3.7 b) presents.

Typical performance curves are obtained with the same generator inertia constant  $H$  and relay setting ( $\beta = 1$ ) are presented in Fig.3.8 and Fig.3.9. By changing the active power imbalance level from 0 to 30MW, and keeping the load constant, for each power imbalance value, the detection time is determined.

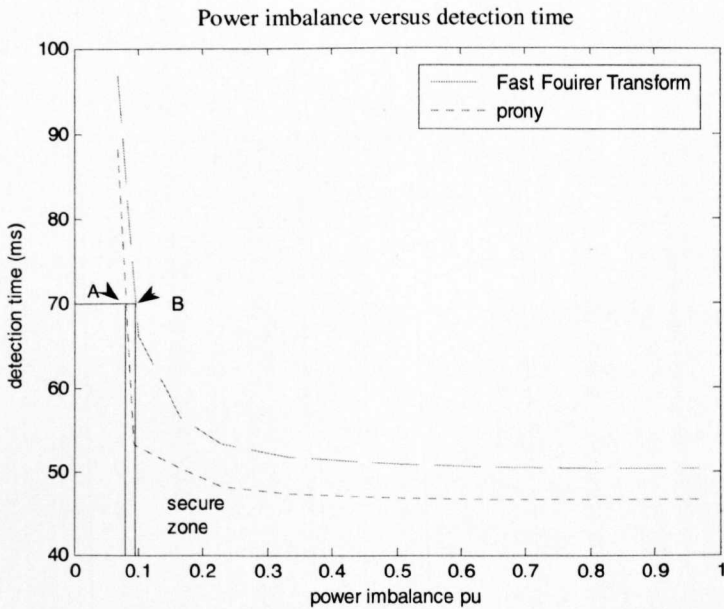


Fig.3.8 Power imbalance versus detection time by using Fast Fourier Transform and the Prony's method with different length of data processing window

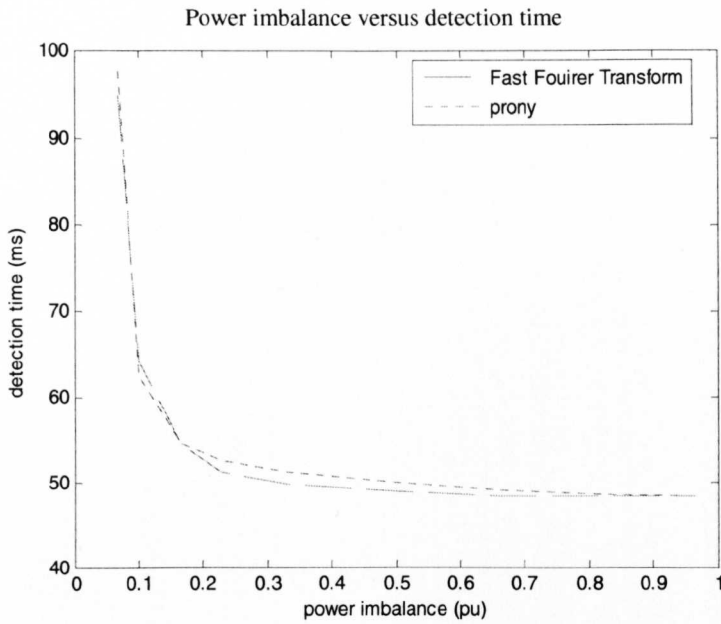


Fig.3.9 Power imbalance versus detection time by using Fast Fourier Transform and the Prony's method with same length of data processing window

Considering the rate of change of frequency calculation, a two cycles time should be added in the detection time. The relay based on the Prony's method provides a faster detection time than the Fast Fourier Transform due to the fact that a small data capturing window is used, as shown in Fig.3.8. It also validates that as the power imbalance increases the detection time decreases according to equation (3.9). It is possible to define critical power imbalance when the relay setting and specified detection are given. For example, if the relay setting is 1Hz/s in Fig.3.8 and assumed the required detection time is 70ms. The point A, B can be determined on the curves which represent the minimum power imbalance 8.2% and 9.4% required for ROCOF relay using Prony or FFT respectively. By crossing between the specified detection time line and the simulation curve to find the vertical line. On the right side of this line is secure zone which means the ROCOF relay operation is less than 70ms, on the left side of the line is insecure zone where the islanding condition can not be detected within the required time. Therefore, the value of power imbalance determined by crossing between the specified detection time line and the simulation curve is defined as the critical power imbalance which means the minimum power imbalance to activate the relay for a required

detection time. The prony's method provides a similar result to the FFT algorithm when integral cycles of data are used, which is presented in Fig.3.9.

Comparing the two estimated frequency result, it can be seen that the trend in frequency is the same. The FFT's method is straightforward but requires integral cycles of the data for frequency estimation. The Prony's method uses an approximation algorithm which does not require integral cycles of data, therefore, it can offer faster frequency estimation. However, for a system with noise or non-linear load, it may cause false operation as the small data capturing window used may amplify the noise and system distortion.

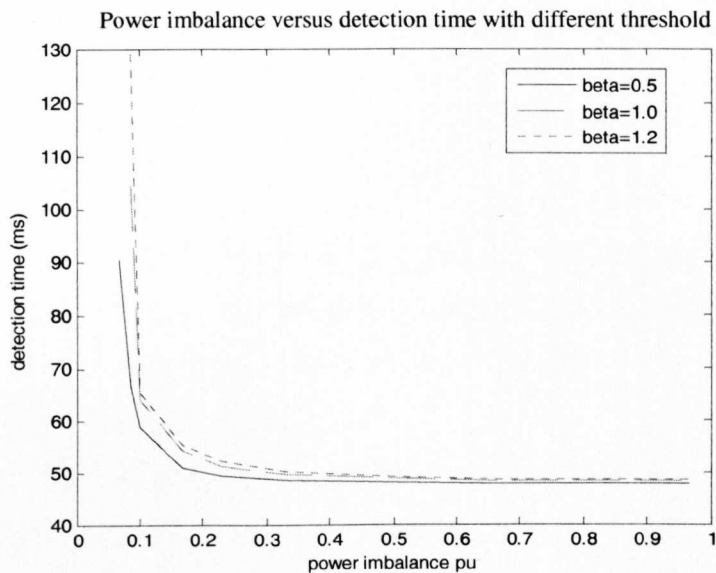


Fig.3.10 The detection time versus power imbalance by using the Fast Fourier Transform method with different relay setting

Fig.3.10 shows the islanding detection time versus power imbalance for different relay settings  $\beta$ . By changing the active power injected by the generator from 0MW to 30MW and keeping the load constant, these curves can be obtained. It is observed that for the same value of power imbalance the detection time increases as the relay setting increases. For the same generator inertia  $H=1.5s$ , the lower the relay setting, the smaller the critical power imbalance.

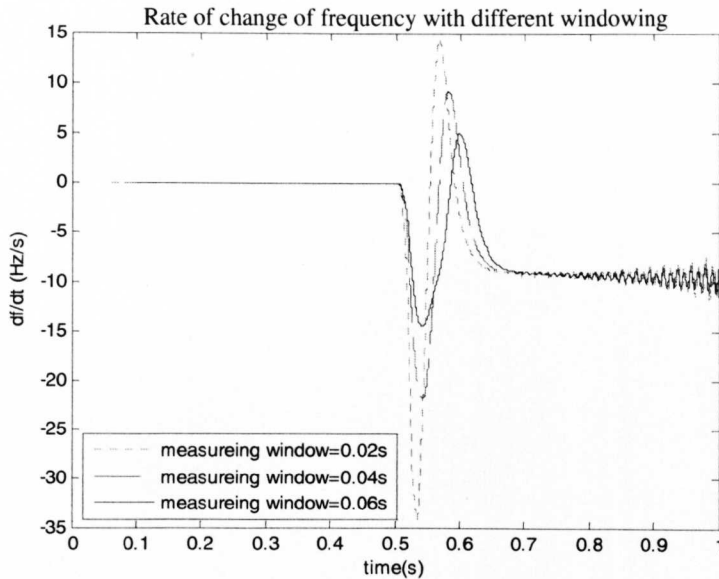


Fig.3.11 Comparison of the rate of change of frequency using different measuring windows

Fig.3.11 shows a comparison of the measured rate of change of frequency by using the Prony's method for different measurement windows, 0.06, 0.04, 0.02 seconds. From Fig.3.11 it can be seen that the duration of the measuring windows used in the calculation of the rate of change of frequency affects the operation of ROCOF relay. The longer the measuring window, the smaller the amplitude of the rate of change of frequency is and the less sensitive relay will be. On the other hand, the shorter measuring windowing, leads to a faster islanding detection. However, the longer measuring window can reduce the false operation during the system disturbance situation.

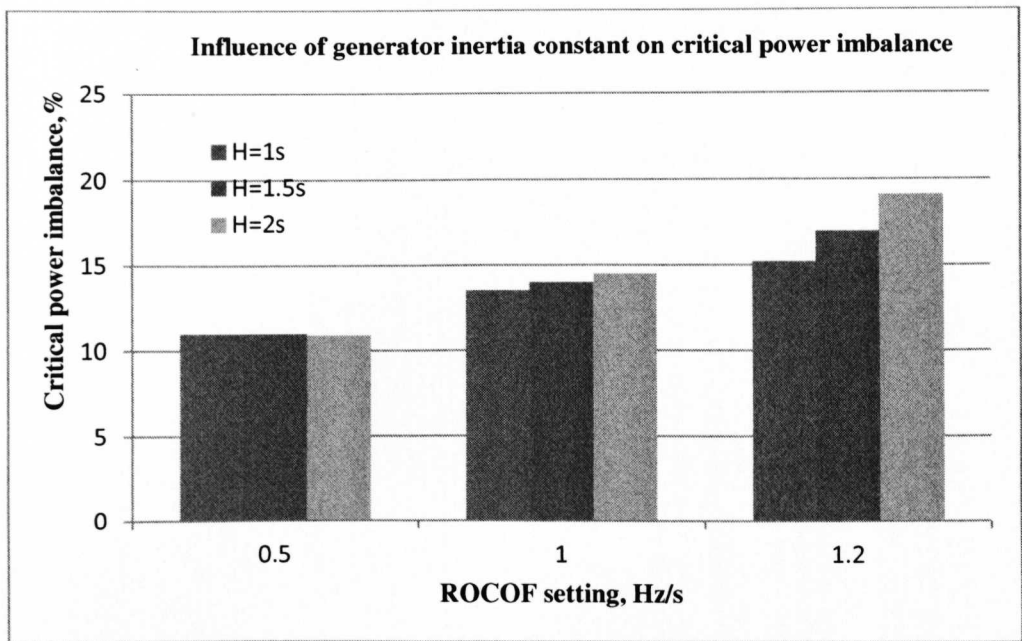


Fig.3.12 The detection time versus power imbalance by using Fast Fourier Transform method with different generator inertia

The inertia constant ( $H$ ) of the original generator is 1.5s, to verify the influence of the generator inertia constant on the ROCOF performance, simulations were done with  $H=1.0s$  and  $2.0s$ . Fig.3.12 shows the values of critical power imbalance to a required detection time of 60ms and different ROCOF relay settings. Such curves were obtained by using the performance curves. If the relay setting is small, the inertia constant does not influence the ROCOF behaviour since the detection time is very fast. However, if the relay setting is large, then the larger the inertia constant, the larger the critical power imbalance will be. This occurs because a generator with a large inertia constant responds more slowly to an islanding situation and consequently, the ROCOF relay takes longer to detect frequency variations.

To analyse the impact of the load power factor on the relay performance the detection time versus power imbalance curves were obtained for the following values of load power factor: 0.8, 0.9, and 0.95 inductive. It can be seen from Fig.3.13 that the load power factor has an impact on the ROCOF curves. For the same relay setting, the lower the power factor is, the higher the detection time is. When the load power factor is lower, the network voltage profile will

present a larger reduction. Consequently, the power imbalance will decrease and it will be more difficult to detect the islanding.

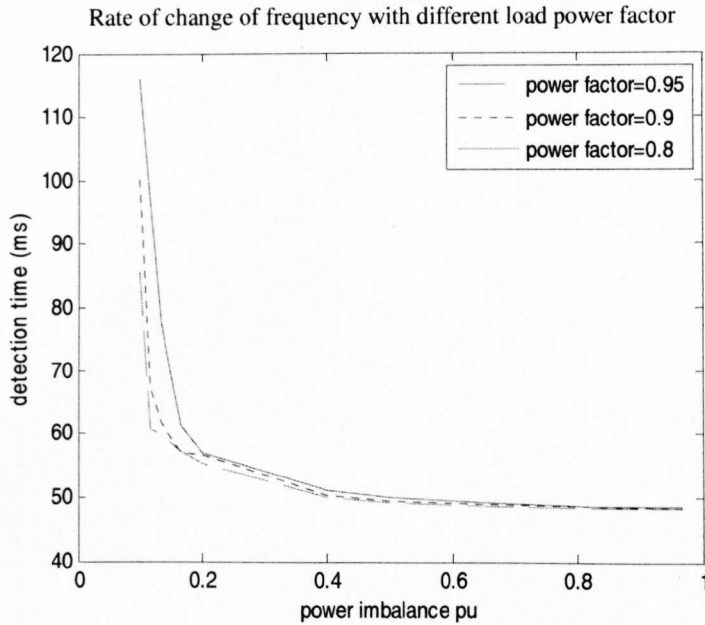


Fig.3.13 The detection time versus power imbalance for different load power factor

The results of system with 5% band-limited white noise and 3MW non-linear load are shown in Fig.3.14 and Fig.3.15 separately. It is observed the ROCOF tripping signal can still operate quickly in the case of system with noise and non-linear load situation. For the system with noise and a non-linear load in non-islanding, this disturbance system would lead to the ROCOF relay nuisance tripping which will result in a larger non-detection zone and will be discussed below.

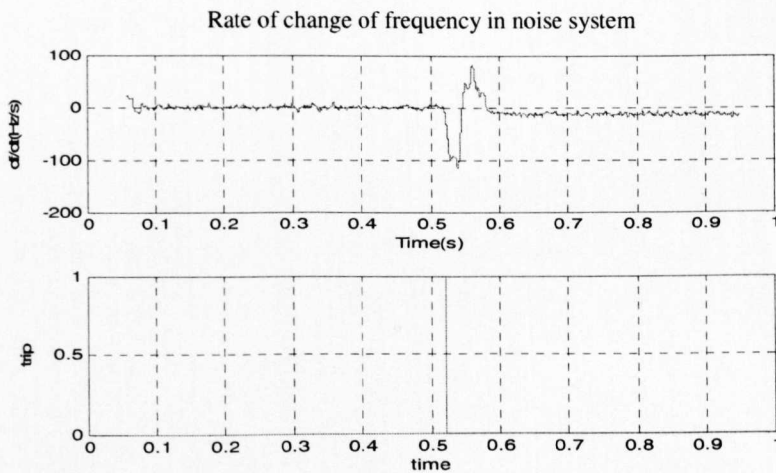


Fig.3.14 ROCOF tripping signal and  $df/dt$  (system with 5% band-limited white noise)

If the ROCOF relay setting is smaller than 0.72, there can be a false tripping even when the system is not islanded in the case of system with 5% band-limited white noise. If the system has 10% band-limited white noise, the ROCOF relay setting should be greater than 1.1, otherwise system disturbances will cause the nuisance tripping.

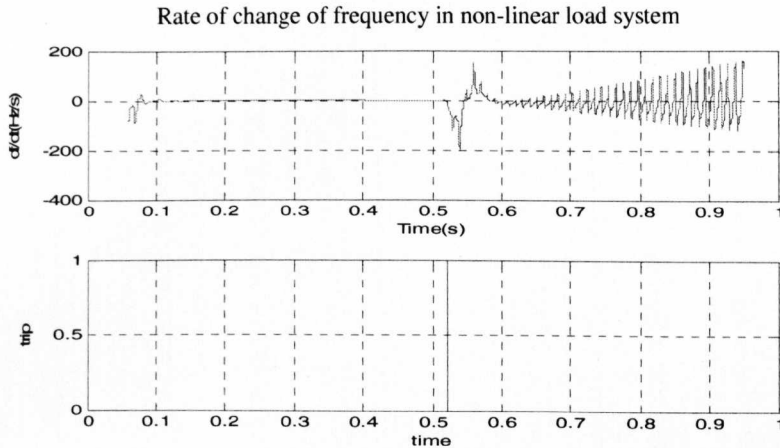


Fig.3.15 ROCOF tripping signal and  $df/dt$  (system with 10MW non-linear load)

Non-linear load mainly causes the distortion in current waveform, and the influence in voltage is small compared with current. Therefore the impact of a small portion of non-linear load in the system for ROCOF relay can be neglected.

### Non-detection Zone

From Fig.3.10 it is clearly observed that the smaller the relay setting the shorter detection time, but a realistic threshold value can not be arbitrarily small due to the sensitivity of ROCOF relays, the disturbance in the system may cause incorrect operation. Table 3.1 shows the ROCOF relays operation in different cases of system with 5%, 10% noise, 33% non-linear load, 5% noise and 33% non-linear load and with different relay settings during the system grid-connected situation.

Table 3.1 ROCOF trip operation during system breaker closed condition in different cases with different relay settings

Trip operation Case	Relay setting		
	1Hz/s	1.5Hz/s	2Hz/s
5% noise	no	no	no
10% noise	yes	no	no
33% non-linear load	no	no	no
5% noise with 33% non-linear load	yes	yes	no

As described in Table 3.1 it can be found that a larger relay setting has the better ability to avoid false tripping, however, it provides a larger non-detection zone. In the case of setting the threshold values of 2Hz/s, by keeping the load constant, and changing the active power output of the synchronous generator from 0MW to 30MW, the power imbalance between the generation and load consumption caused ROCOF relay false tripping can be applied to calculate the non-detection zone, thus the non-detection zone is 6.1%. With the 1Hz/s relay setting, the non-detection zone is only 1.6%, but is sensitive to the system disturbances. Meanwhile, with large load changing, there will be another situation of false tripping which will be discussed in the following sections.

### 3.4.2 Non-islanding

During the non-islanding situation which is shown in Fig. 3.16, false operation of ROCOF relays is of concern. The test system used to investigate false operation is similar to the system in Fig. 3.6. In Fig. 3.16 at 0.5s, a) by closing the circuit breaker the three phase load is added into the system; b) by opening the circuit breaker the three phase load is shed from the system. Under these situations, the ROCOF relays should not operate due to the non-islanding condition and the stable system. However, when the power imbalance occurs in the system during load shedding and load adding, the trip signal operates. In those cases, the interlock function is needed to operate to avoid nuisance tripping.

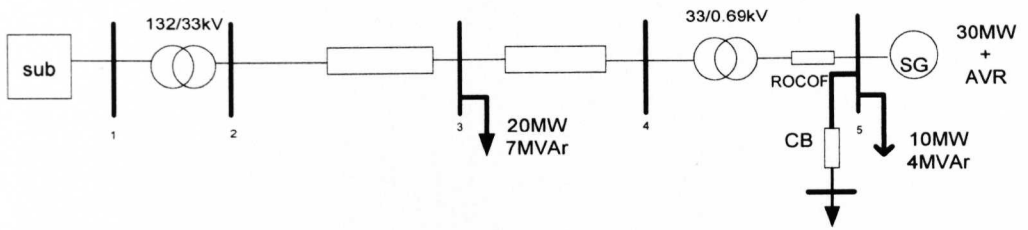


Fig.3.16 Single-line test system (adding or shedding load)

The waveforms of the rate of change of power in system islanding and non-islanding are shown in Fig.3.17, after the transient (130ms) the difference can be found to distinguish these two conditions. Therefore it is proposed that the rate of change of power can be used as an interlock function to avoid false tripping during non-islanding situation.

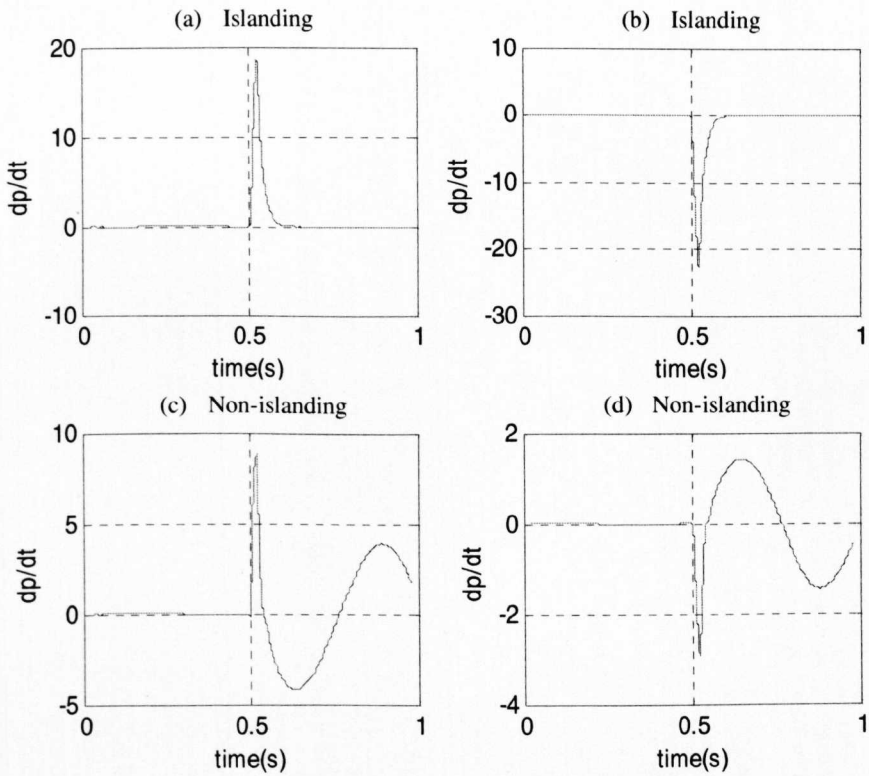


Fig.3.17. a) b) c) d) the rate change of power of islanding (negative power imbalance ( $\Delta p = -0.5$ ), positive power imbalance ( $\Delta p = 0.5$ )) non-islanding (add load ( $\Delta p = -0.5$ ), load shedding ( $\Delta p = 0.5$ ))

### 3.4.2.1 Basic Principle of the Rate of Change of Power

The ROCOF relays can detect an islanding situation very fast, but it may cause nuisance tripping when loads changes occurs. In order to avoid false operation, an estimate of the rate of change of power can be used as a block signal. The power from a generator can be given by:

$$P = \frac{EV \sin \delta}{X} \approx \frac{EV}{X} \delta \quad (3.24)$$

where  $E$  is the generator voltage,  $V$  is the voltage of the system,  $X$  is the impedance between the generator and the grid and  $\delta$  is the relative phase between the generator and the grid. Thus we can put:

$$\frac{dP}{dt} = \frac{EV}{X} \frac{d\delta}{dt} \quad (3.25)$$

where

$$\frac{d\delta}{dt} = \omega - \omega_0 \quad (3.26)$$

When the system is islanding,  $X \rightarrow \infty$  in equation (3.25), which gives  $dP/dt \approx 0$ , and if the system is non-islanding, then  $dP/dt \neq 0$ , a block signal can be provided for the ROCOF that can then be set according to a  $dP/dt$  threshold. This situation can be estimated after a certain delay allowing for the initial transient response.

### 3.4.2.2 System with Induction Motor Load

In the islanding situation, in the presence of system with induction motor loads, the oscillation of the waveform of  $dP/dt$  after the initial transient is difficult to distinguish from the condition of small load variations as shown in Fig.3.18. Therefore, the amplitude of the rate of change of frequency is introduced to cooperate with the  $dP/dt$  interlock. The block structure of this decision process is shown in Fig.3.19.

For example, consider a system with a induction motor load in the case of the system non-islanding situation, the largest amplitude value of the rate of change of frequency is no more than a small certain value. According to Fig.3.19, therefore, if the maximum amplitude value of rate of change of frequency is greater than  $\beta_2$ , and  $df/dt > \beta_1$ , this is definitely an islanding situation and the trip signal is generated. If the maximum  $df/dt < \beta_2$ ,  $df/dt > \beta_1$  and the absolute value of rate of change of power is smaller than  $\beta_3$ , this is also an islanding situation and ROCOF relay trips as well (in this case  $\beta_1 = 1$ ,  $\beta_2 = 10$  and  $\beta_3 = 0.6$ ). The non-islanding conditions are then detected by: if the maximum  $df/dt < \beta_2$ ,  $df/dt < \beta_1$ , and  $abs(dP/dt) < \beta_3$ , this is the situation of non-islanding. Meanwhile if the maximum  $df/dt < \beta_2$ ,  $df/dt > \beta_1$ ,  $abs(dP/dt) > \beta_3$ , this situation is also non-islanding. Because normally the islanding situation should be detected within 300ms, the estimation of  $dp/dt$  should be considered between 130ms to 300ms.

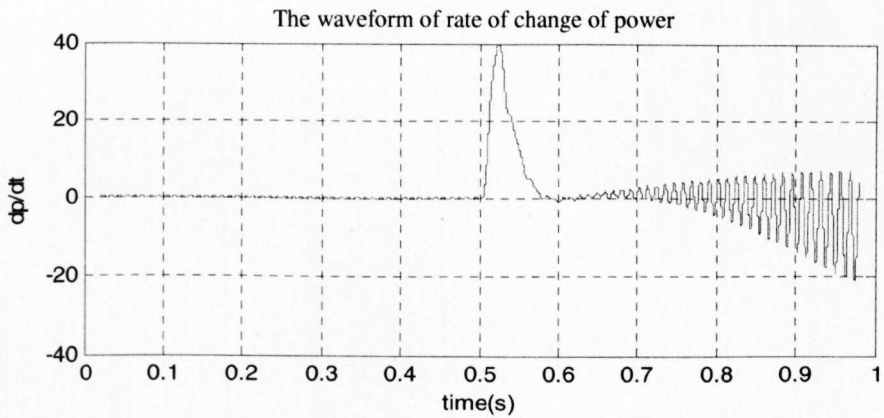


Fig.3.18 The waveform of rate of change of power in the system with induction motor load

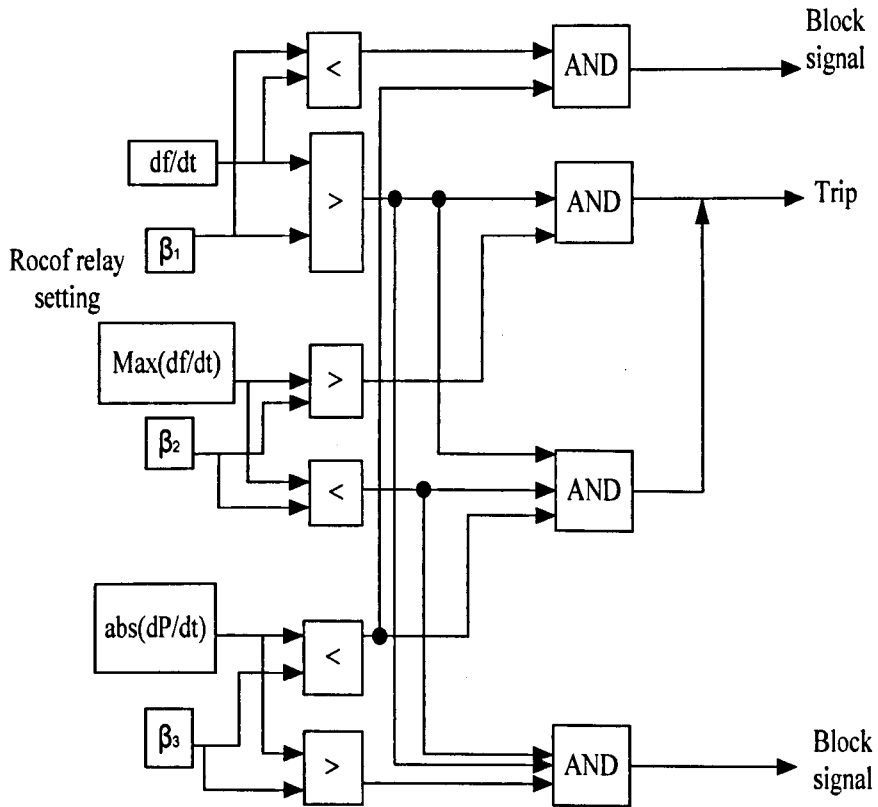


Fig.3.19 The rate of change of power interlock function structure

### 3.4.2.3 Simulation Results of ROCOF Relay with Rate of Change of power Interlock Function

Two sets of test were carried out to demonstrate the combination of ROCOF relay and rate of change of power interlock function. For islanding and non-islanding situations, in the system as described in Fig.3.4 with a 0.33p.u power imbalance and in Fig.3.16 with 10MW load shedding, the ROCOF relay detection results with block signal are shown in Fig.3.20 and Fig.3.21. The circuit breaker opens at 0.5s, and the total simulation time is 1s.

The waveform of  $df/dt$  and  $dP/dt$  during system islanding are depicted in Fig.3.20 (a) and (c) separately, the  $dP/dt$  interlock function should operate after the ROCOF relay tripping, therefore, after 130ms the block tripping signal is then generated. It is found that the ROCOF relay provides a fast islanding detection, as shown in Fig.3.20 (b) and the ROCOF tripping operates

at 0.5495s. The threshold setting for block signal operation is 0.6 in order to avoid system disturbance caused by false tripping, in the case of islanding, there would be no block tripping as depicted in Fig.3.20 (d).

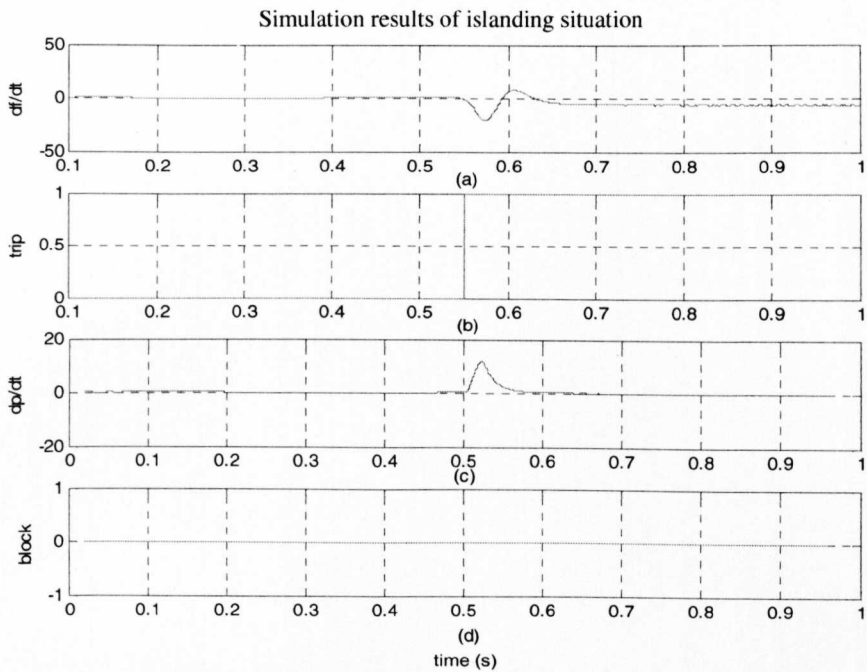


Fig.3.20 Simulation results of islanding situation the ROCOF relays with  $dP/dt$  interlock function

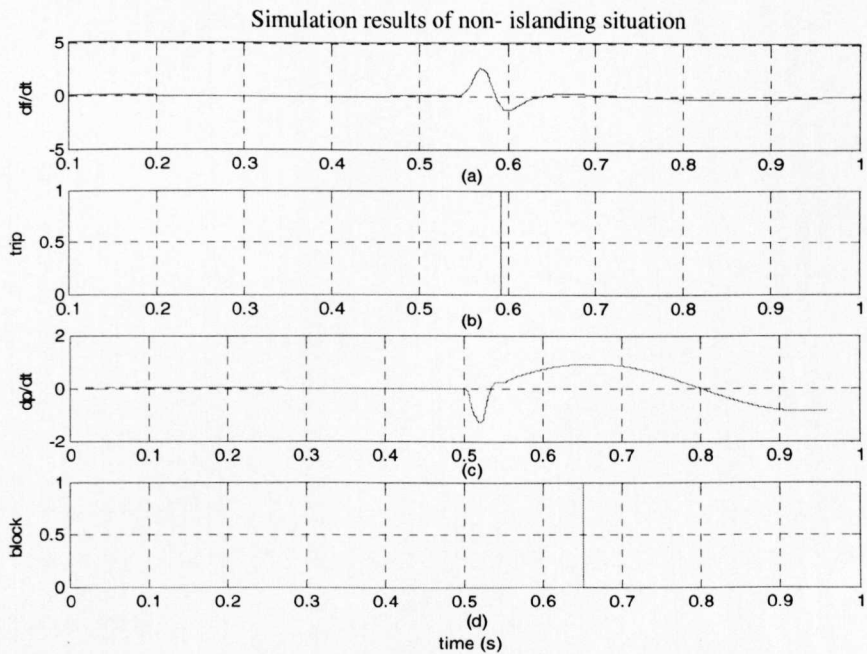


Fig.3.21 Simulation results of non-islanding situation the ROCOF relays with  $dP/dt$  interlock function

In order to verify the rate of change of power interlock function can cooperate with ROCOF relays properly during system load variation condition, Fig.3.21 shows the simulation results of system with 10MW load shedding. It has been observed that the ROCOF relay would operate incorrectly due to the transient caused by the switching off the 10MW load at 0.593s as shown in Fig.3.21 (b). As in Fig.3.21 (d) the rate of change of power interlock function effectively blocks the ROCOF relay tripping at 0.6496s. In the case of a system with small load variations (i.e. smaller than 0.33p.u.), the ROCOF relay would not trip. However, if the system load adding or shedding is greater than 0.33p.u., this may lead to the ROCOF relay operating which then needs to combining  $dP/dt$  interlock to block the false tripping signal quickly. The interlock function  $dP/dt$  may not effective during the small load variation (i.e. smaller than 0.06p.u.), but in this case, the ROCOF relay will not trip. Therefore, there would be no non-detection zone for  $dP/dt$  interlock function.

### 3.5 Summary

Simulation results provide a comprehensive analysis of the ROCOF relay performance, and show how the detection time increases with the power imbalance decreases.

The frequency measuring algorithms, different measuring windows, relay settings, generator inertia and different load power factor which are the characteristics that affect the performance of ROCOF relays were investigated. The shorter the measuring window, the faster the detection time will be, and more sensitive relay is which may cause wrong tripping in noisy environment. Meanwhile, using a smaller relay setting can also reduce the detection time, but it also may easily cause false operation. Therefore a compromise in the relay setting is required to provide a balance between the security and dependability.

During the non-islanding situation the ROCOF relays should not operate for a stable system. A rate of change of power interlock function proposed in this

chapter is introduced to avoid false operation for the load fluctuation. It is shown that the nuisance tripping signal can be blocked quickly and accurately during non-islanding situation.

## **Chapter 4**

# **Advanced ROCOF Protection of DFIG Wind Generator**

### **4.1 Introduction**

Current practice is for renewable resources such as wind, solar, biomass etc to be connected onto the distribution network to contribute to generation, reduce losses, improve voltage quality, and increase the capacity of the network. Due to deregulation and the use of renewable power, the proportion of distributed generation (DG) is rapidly increasing and most of them are connected to distribution networks to supply power to the grid as well as local loads [43]. In recent years, there has been increasing interest in doubly fed induction generator (DFIG)-based wind turbines and many of the large wind turbines that are now commercially available are of this type [81]. There are many power quality issues to be considered with DG and one of the main issues is islanding [13]. As for other generation it is important to estimate and detect an islanding situation quickly and accurately as it can lead to serious plant damage if the grid is suddenly reconnected.

In this chapter, firstly the steady state equivalent circuit and the operation principle of a DFIG based wind turbine as well as the  $dq$ -models both in the arbitrary and rotor fixed reference frame are described. A model of a grid-connected DFIG similar to GE1.5MW wind turbine generators [82] is established in MATLAB. Based on the analysis of the equivalent circuits of the DFIG and its PWM voltage source converter, a vector control scheme is introduced for the grid-side converter, where the reactive power exchange between grid and grid-side converter is zero by controlling  $i_{gq} = 0$ , and the rotor-side converter controller is designed and used to model the GE1.5MW wind turbine generator [82]. The performance of the designed controller is then investigated. For the grid-connected DFIG system the characteristics (i.e. frequency estimation methods, frequency measuring windows, different relay settings) of ROCOF relays which affect their operation responses are analyzed. The ROCOF performances for DFIG wind turbine islanding detection are then investigated. The equivalent impedance value  $v^2/p$  (the reactive power is controlled to be zero, hence  $Z_{est} = v^2/p$ ) is introduced as an interlock function to cooperate with the ROCOF relays to avoid false operation during the non-islanding situation. Due to the reactive power is controlled to be zero, therefore, the

## 4.2 Doubly-fed Induction Generator for Wind Turbines

The grid-connected wind turbine considered here is a DFIG, using back-to-back PWM voltage source converters in the rotor circuit. Fig.4.1 depicts the main components of the grid-connected wind turbine, where  $P, Q$  are the wind turbine output active and reactive power respectively.

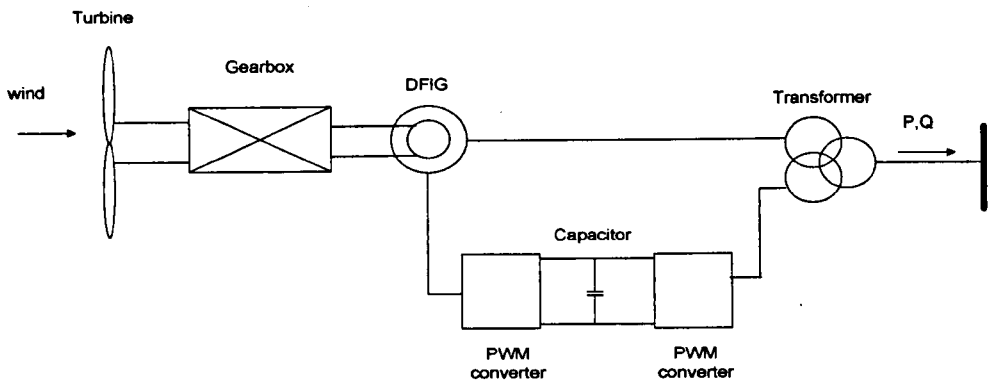


Fig.4.1 Block diagram of a grid-connected wind turbine with a DFIG

The complete grid connected wind turbine model as Fig.4.2 shows includes the wind speed model, the aerodynamic model of wind turbine, the mechanical model of the transmission system, the model of the electrical components (consist of the DFIG, transformer, PWM voltage source converters) and the control system [83].

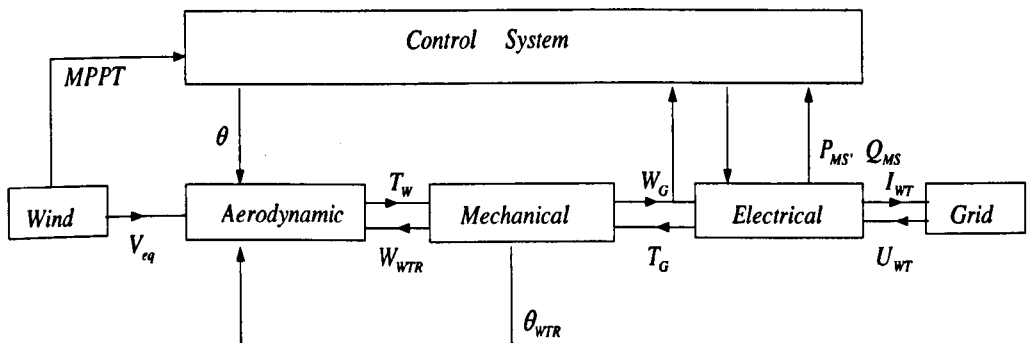


Fig 4.2 Overall structure of the grid-connected wind turbine model

The aerodynamic model and the wind speed model are well researched in [84-87]. The mechanical drive train of a wind power generation system is introduced in [88-90]. This chapter mainly focuses on the design of the DFIG and its PWM voltage source converter controller.

### **4.2.1 The Comparison of Doubly-fed Induction Generator with Other Wind Turbine Systems**

The fixed-speed wind turbine with the induction generator directly connected to the grid is the most common type of wind turbine. The wind turbine will only operate at its maximum aerodynamic efficiency at one particular speed due to the rotational speed of the generator being directly governed by the grid frequency. Therefore, the reactive power and the grid voltage level cannot be controlled. The blade rotation causes power variations due to the variation in wind power which are fed directly into the electrical system since the turbine inertia cannot play a filtering role in a fixed speed system. This causes frequency variation from 1Hz to 2Hz in the grid, which is known as flicker [91]. Compared with fixed-speed system, the variable speed system has some obvious advantages[92]:

- Due to the operation of the wind speed turbine at or close to the maximum aerodynamic efficiency of the wind turbine for a range of wind velocity the energy capture increases.
- Power fluctuations are reduced. Since the speed of the wind turbine generator can change, the inertia of the system acts as a energy buffer for variations in the wind velocities. Kinetic energy can be released into the electrical system when the wind velocity decreases.
- Reduction in the noise at low rotational speed.
- The torque fluctuations are reduced, which means that a cheaper gear box can be used.
- Simplified design of the turbine, since the stall regulation can be used to limit the wind turbine energy capture at above rated wind velocity.
- Improved fault ride-through ability.

The disadvantage of the variable-speed turbine is a more complex electrical system, as a power-electronic converter is required to make variable-speed operation possible. The variable speed system may also inject harmonics into the grid, which may need corrective action or compensation. Usually for a variable speed system, the maximum rotational speed is higher than that of a

fixed-speed energy system and this can lead to mechanical overload. This can increase the cost of the system structure [92].

## 4.3 The Dynamic Operation for Double-fed Induction Generator

### 4.3.1 Steady State Equivalent Circuit of DFIG

The diagram of the steady state equivalent circuit of the DFIG is shown in Fig.4.3 [93], where the quantities on the rotor side are referred to the stator side.

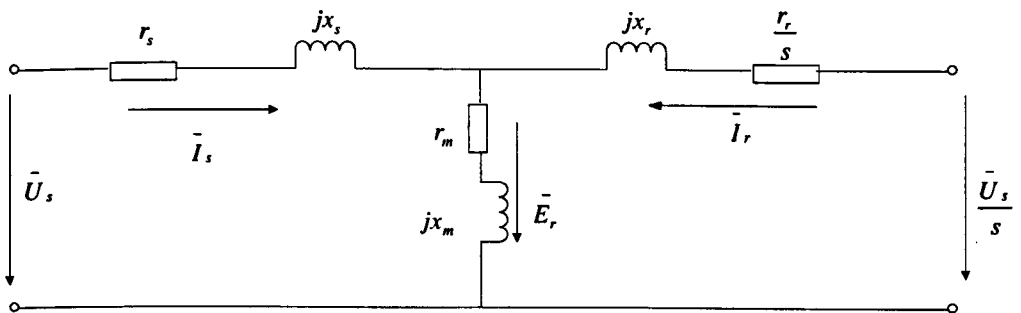


Fig.4.3 Steady state equivalent circuit of the DFIG

In the equivalent circuit,  $\bar{U}_s$  and  $\bar{U}_r$  are the applied stator phase voltage and rotor phase voltage to the induction machine respectively,  $\bar{E}_r$  is the electric motive force,  $\bar{I}_s$  is the stator current,  $\bar{I}_r$  is the rotor current,  $\bar{I}_0$  is the no-load current,  $r_s$  is the stator resistance,  $r_r$  is the rotor resistance,  $x_s$  is the stator leakage reactance,  $x_r$  is the rotor leakage reactance,  $r_m$  represents the magnetizing losses,  $x_m$  is the magnetizing reactance,  $s$  is the generator slip.

Applying Kirchhoff's voltage law to the circuit in Fig.4.3 yields:

$$\begin{aligned}
 \bar{U}_s &= r_s \bar{I}_s + jx_s \bar{I}_s - \bar{E}_r \\
 \frac{\bar{U}_r}{s} &= \frac{r_r}{s} \bar{I}_r + jx_r \bar{I}_r - \bar{E}_r \\
 \bar{E}_r &= -(r_m + jx_m) \bar{I}_0 \\
 \bar{I}_0 &= \bar{I}_s + \bar{I}_r
 \end{aligned} \tag{4.1}$$

This equivalent circuit, based on calculations with rms-values of voltages and currents, can only be applied for steady state analysis of the DFIG. For dynamic analysis of the DFIG, a model in a form of time dependent differential functions has to be employed, which will be introduced in the following section.

### 4.3.2 The Dynamic Equation for Double-fed Induction Generator

The stator of a three-phase DFIG contains a set of windings to which three-phase electrical power is applied. Each winding sets up a field that varies sinusoidally around the circumference of the gap and varies sinusoidally with time. These fields are displaced from one another by  $120^\circ$  in both time and space. The stator windings set up magnetic poles that rotate around the circumference of the stator. The same magnetic distribution can be obtained from an equivalent 2-phase system, called the  $\alpha\beta$  system. This gives the 3-2 transformation, termed the  $abc$  to  $\alpha\beta$  transformation [94].

$$F_{\alpha\beta 0} = \begin{bmatrix} F_\alpha \\ F_\beta \\ F_0 \end{bmatrix} = T_1 F_{abc} \tag{4.2}$$

where  $F_{\alpha\beta 0}$  stands for variables in  $\alpha\beta$  frame,  $F_{abc}$  stands for variables in  $abc$  frame. For a balanced system,  $F_{\alpha\beta 0} = F_{\alpha\beta}$  as  $F_0 = 0$ .

$$T_1 = \frac{2}{3} \begin{bmatrix} 1 & -\frac{1}{2} & -\frac{1}{2} \\ 0 & \frac{\sqrt{3}}{2} & -\frac{\sqrt{3}}{2} \\ \frac{1}{2} & \frac{1}{2} & \frac{1}{2} \end{bmatrix} \quad (4.3)$$

The dynamic equations of DFIG are generally written in terms of the equivalent 2-coil (or 2-phase) variables. Consider the 2-phase stator coils called the  $S_{\alpha\beta}$  coils. These coils are fixed in space on the stator of the machine.

The voltage across each of these coils is written using Kirchhoff's Law:

$$\bar{v}_s = \bar{i}_s R_s + \frac{d}{dt} \bar{\Psi}_s \quad (4.4)$$

Considering the equivalent 2-phase coils on rotor  $R_{\alpha\beta}$ , which rotates at the rotor speed, the voltage across the rotor coils can be written in exactly the same way as (4.4):

$$\bar{v}_r = \bar{i}_r R_r + \frac{d}{dt} \bar{\Psi}_r \quad (4.5)$$

where the direction of flux vector  $\bar{\Psi}_s$  and  $\bar{\Psi}_r$  refer to the direction of peak flux in this space.

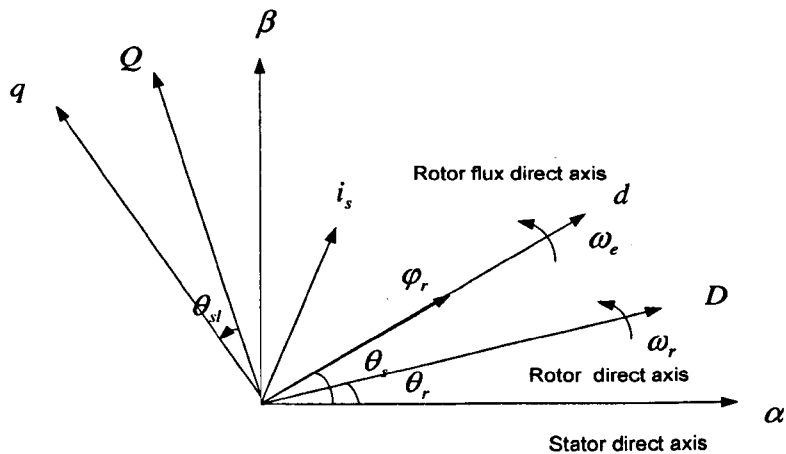


Fig.4.4 Reference frame and space vector representation

Equations (4.4) and (4.5) are the basic equations for the DFIG. They must be transformed to the same frame in practice. Usually these two equations are transformed to the stationary  $\alpha\beta$  stator frame, which as its name suggests is fixed to the stator. They can also be transformed to a rotating  $dq$  frame, which are fixed to the rotating magnetic field produced by the stator. In this case, the  $dq$  frame rotates at speed  $\omega_e$  around the  $\alpha\beta$  frame. The transformation from the stationary  $\alpha\beta$  frame to the rotating  $dq$  frame has the advantage that the fluxes in the two phases or directions do not interact with each other. This means that the time varying parameters of the three-phase system become constant when referred to the rotating  $dq$  frame. This advantage is also independent of the choice of reference frame [95]. In order to develop the  $dq$  frame model, some assumptions are made:

- The stator and rotor windings of the DFIG are assumed symmetric, i.e. resistance, magnetizing and leakage inductances are equal for all three phases. This means the zero-component of the dq-model may be neglected.
- The windings are assumed sinusoidal distributed around the circumference of the DFIG. Thereby, the magnetic motive force produced by the windings will be sinusoidal i.e. no harmonic components will be present.
- The air gap reluctance is assumed constant to ensure constant mutual inductance from stator to stator winding and rotor to rotor winding.
- Saturation of the mutual inductance, or magnetising inductance, is neglected i.e. the magnetizing inductance does not vary as a function of the current.
- Skin effect in the stator and rotor is neglected. As the frequency of the current increases, skin effect will increase the resistance, and decrease the inductance due to increased reluctance in the iron of the DFIG.
- Iron losses are neglected. This means that the real losses in DFIG will be larger than simulated [96].
- Cross saturation effect, the coupling between two perpendicular axes, is neglected [83].

Transformation from the fundamental (4.4) and (4.5) to a rotating frame can be done by substituting the variables in (4.4) by  $x_s = x_{s\alpha\beta} e^{-j\omega_e t}$  and the variable in (4.5) by  $x_r = x_{r\alpha\beta} e^{-j\omega_e t}$ .

where  $x$  stands for  $\bar{I}$ ,  $\bar{v}$  and  $\bar{\psi}$ .  $\omega_e$  is the electrical angular velocity of the rotating frame to be aligned on the stator flux,  $\omega_r$  is the rotor frequency and  $\omega_s$  is the slip frequency, where  $\omega_s = \omega_e - \omega_r$ . The equations in the  $dq$  rotating frame are:

$$\bar{v}_s = \bar{i}_s R_s + \frac{d}{dt} \bar{\psi}_s + j\omega_e \bar{\psi}_s \quad (4.6)$$

$$\bar{v}_r = \bar{i}_r R_r + \frac{d}{dt} \bar{\psi}_r + j\omega_s \bar{\psi}_r \quad (4.7)$$

Separating (4.4) and (4.5) into real and imaginary parts.

$$v_{sd} = i_{sd} R_s + \frac{d}{dt} \psi_{sd} - \omega_e \psi_{sq} \quad (4.8)$$

$$v_{sq} = i_{sq} R_s + \frac{d}{dt} \psi_{sq} - \omega_e \psi_{sd} \quad (4.9)$$

$$v_{rd} = i_{rd} R_r + \frac{d}{dt} \psi_{rd} - \omega_e \psi_{rq} \quad (4.10)$$

$$v_{rq} = i_{rq} R_r + \frac{d}{dt} \psi_{rq} - \omega_e \psi_{rd} \quad (4.11)$$

Combined with flux linkage equations:

$$\bar{\psi}_s = L_s \bar{i}_s + L_m \bar{i}_r \quad (4.12)$$

$$\bar{\psi}_r = L_m \bar{i}_s + L_r \bar{i}_r \quad (4.13)$$

Equations (4.6) and (4.7) can be converted to different combinations of state variables, i.e. there can be many selections of state variables. Selecting  $i_{dr}$ ,  $i_{qr}$ ,  $i_{ds}$ , and  $i_{qs}$  as state variables, the DFIG model can be described as:

$$\begin{aligned}
 \sigma \frac{di_{ds}}{dt} &= -\frac{R_s}{L_s} i_{ds} + \omega_r i_{qs} + \frac{R_r}{L_s} \frac{L_m}{L_r} i_{dr} + \frac{\omega_r L_m}{L_s} i_{qr} + \frac{v_{ds}}{L_s} - \frac{L_m}{L_s L_r} v_{dr} \\
 \sigma \frac{di_{qs}}{dt} &= -\frac{R_s}{L_s} i_{qs} - \omega_r i_{ds} + \frac{R_r}{L_s} \frac{L_m}{L_r} i_{qr} - \frac{\omega_r L_m}{L_s} i_{dr} + \frac{v_{qs}}{L_s} - \frac{L_m}{L_s L_r} v_{qr} \\
 \sigma \frac{di_{dr}}{dt} &= \frac{R_s L_m}{L_s L_r} i_{ds} - \frac{\omega_r L_m}{L_r} i_{qs} - \frac{R_r}{L_r} i_{dr} - \frac{\omega_r L_m^2}{L_s L_r} i_{qr} - \frac{L_m}{L_s} \frac{v_{ds}}{L_r} + \frac{v_{dr}}{L_r} \\
 \sigma \frac{di_{qr}}{dt} &= \frac{R_s L_m}{L_s L_r} i_{qs} + \frac{\omega_r L_m}{L_r} i_{ds} - \frac{R_r}{L_r} i_{qr} + \frac{\omega_r L_m^2}{L_s L_r} i_{dr} - \frac{L_m}{L_s} \frac{v_{qs}}{L_r} + \frac{v_{qr}}{L_r}
 \end{aligned} \tag{4.14}$$

where  $\sigma = \frac{L_s L_r - L_m^2}{L_s L_r}$ . Assuming the scaling convention in which the

magnitude of space vector  $|x| = x_{rms}$  (where  $x$  stands for  $\bar{I}$ ,  $\bar{v}$ , and  $\psi$ ) i.e., the magnitude of the  $\alpha\beta$  vector is equal to the rms phase quantity [92]. The electromagnetic torque  $T_e$  can be calculated as:

$$T_e = \frac{3}{2} p L_m (i_{qs} i_{dr} - i_{ds} i_{qr}) \tag{4.15}$$

where  $p$  is the pole pair number.

## 4.4 Vector Control of PWM Voltage Source Converter

The DFIG is applicable both for connection to the main grids and also to stand-alone or isolated grids. Isolated grids would include controlled loads for power-flow control and energy store to smooth power fluctuations [92]. The wound rotor induction generator for the rotor-side PWM voltage source converter is applied in the GE 1.5MW Wind Turbine Generator as the MATLAB Wind-Farm DFIG Average Model, with a torque controller and terminal voltage regulation (GE1.5MW WindVAR) [24]. The WindVAR emulation function represents a simplified equivalent of the supervisory VAR

controller for the entire wind farm. The function monitors a specified bus voltage, with optional line drop compensation and compares it against the reference voltage [24, 82]. The vector control scheme for grid-side PWM voltage source converter is described as Section 4.4.1.

#### 4.4.1 Vector Control Scheme for Grid-side PWM Voltage Source Converter

The objective of the vector-control scheme for the grid-side PWM converter is to keep the DC-link voltage constant while controlling reactive power flow into the grid. The reference frame used for the grid-side converter control is orientated along the stator (or the grid) voltage vector position. This enables independent control of the DC-link voltage and the reactive power flow between the grid and the grid-side converter. The PWM voltage source converter is current regulated, with the d-axis current used to regulate the DC-link voltage and the q-axis used to regulate the reactive power [92].

The schematic of grid-side PWM voltage source converter is shown in Fig.4.5, where  $V_{gabc}$  are the three phase grid voltages,  $V_{cab}$  are the three phase grid-side converter voltages,  $i_{ga}, i_{gb}, i_{gc}$  are the three phase grid-side converter currents,  $R_f$  and  $L_f$  are the inductor resistance and inductance,  $i_{dcr}$  and  $i_{dcg}$  are the rotor-side and grid-side DC currents,  $C$  is the DC link capacitor.

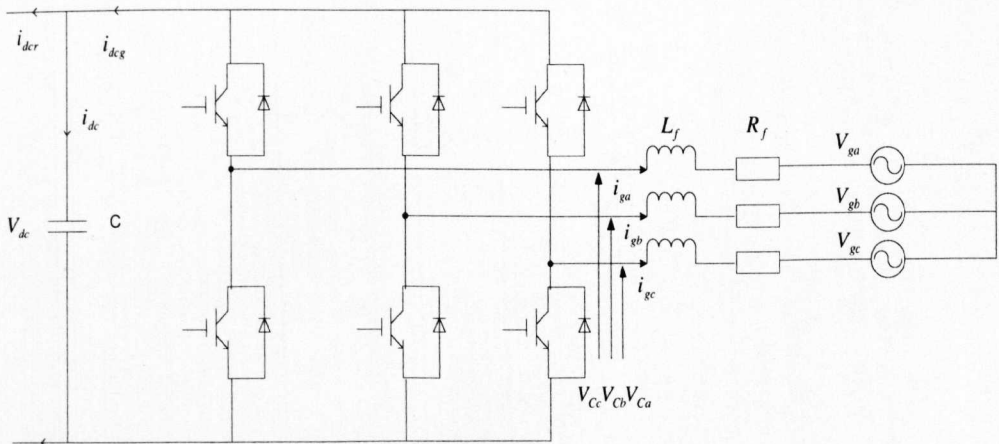


Fig.4.5 Grid-side PWM voltage source converter

The voltage balance across the inductor is:

$$\begin{bmatrix} V_{ga} \\ V_{gb} \\ V_{gc} \end{bmatrix} = R_f \begin{bmatrix} i_{ga} \\ i_{gb} \\ i_{gc} \end{bmatrix} + L_f \frac{d}{dt} \begin{bmatrix} i_{ga} \\ i_{gb} \\ i_{gc} \end{bmatrix} + \begin{bmatrix} V_{Ca} \\ V_{Cb} \\ V_{Cc} \end{bmatrix} \quad (4.16)$$

The three-phase equation relating the converter output voltages and the source voltage is:

$$V_{gabc} - V_{Cabc} = R_f i_{gabc} + L_f \frac{di_{gabc}}{dt} \quad (4.17)$$

Equation (4.17) is a set of equations for the phases, where  $abc$  represents a three-phase variables. These are now transformed into a rotating  $dq$  frame with a frequency of  $\omega_e$ .

$$\begin{aligned} V_{gd} - V_{Cd} &= R_f i_{gd} + L_f \frac{di_{gd}}{dt} - \omega_e L_f i_{gq} \\ V_{gq} - V_{Cq} &= R_f i_{gq} + L_f \frac{di_{gq}}{dt} + \omega_e L_f i_{gd} \end{aligned} \quad (4.18)$$

where  $V_{gd}$ ,  $V_{gq}$  are the grid voltages in d-and q-axis,  $V_{Cd}$ ,  $V_{Cq}$  are the grid-side converter voltages in d-and q-axis,  $i_{gd}$ ,  $i_{gq}$  are the grid-side converter currents in d-and q-axis,  $\omega_e$  is the electrical angular velocity of the grid voltage.

The active  $P_g$  and reactive  $Q_g$  power flow between the grid and the grid-side converter are:

$$\begin{aligned} P_g &= \frac{3}{2} (V_{gd} i_{gd} + V_{gq} i_{gq}) \\ Q_g &= \frac{3}{2} (V_{gq} i_{gd} - V_{gd} i_{gq}) \end{aligned} \quad (4.19)$$

When the  $dq$  rotating frame is orientated on the grid voltage vector, as shown in Fig.4.6  $V_{gd} = V_g$  and  $V_{gq} = 0$ . According to the definition, the calculation of the grid voltage vector angle is derived from:

$$\theta_e = \int \omega_e dt = \tan^{-1} \frac{V_{g\beta}}{V_{g\alpha}} \quad (4.20)$$

where  $V_{g\alpha}$  and  $V_{g\beta}$  are the stationary dq-axis grid voltage components.

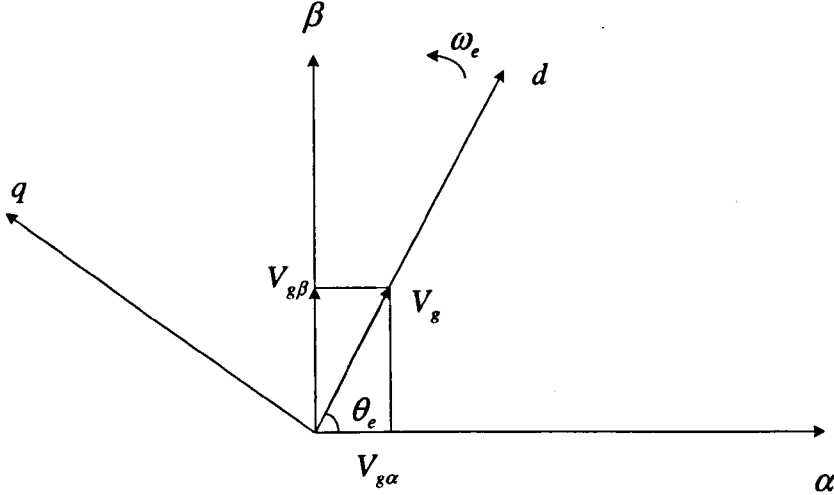


Fig.4.6 Vector diagram of the dq-reference frame alignment for the grid-side converter

The active and reactive power flow between the grid and the grid-side converter are proportional to  $i_{gd}$  and  $i_{gq}$  respectively.

$$\begin{aligned} P_g &= \frac{3}{2} V_{gd} i_{gd} \\ Q_g &= -\frac{3}{2} V_{gd} i_{gq} \end{aligned} \quad (4.21)$$

Neglecting harmonics due to the switching and the losses in the resistance and converter, the following is obtained :

$$\begin{aligned} V_{dc} i_{dcg} &= \frac{3}{2} V_{gd} i_{gd} \\ V_{gd} &= \frac{m}{2} V_{dc} \\ i_{dcg} &= \frac{3}{4} m i_{gd} \\ C \frac{dV_{dc}}{dt} &= i_{dcg} - i_{dcr} \end{aligned} \quad (4.22)$$

where  $m$  is the PWM modulation depth of the grid-side converter.

From (4.22), it is seen that the DC-link voltage can be controlled via  $i_{gd}$ .

The current  $i_{gd}$  and  $i_{gq}$  can be regulated using  $V_{Cd}$  and  $V_{Cq}$  respectively. The control scheme thus utilises current control loops for  $i_{gd}$  and  $i_{gq}$ , with the  $i_{gd}$  demand being derived from the DC-link voltage error. The  $i_{gq}$  demand determines the reactive power flow between the grid and the grid-side converter. Normally the  $i_{gq}$  reference value may be set to zero, which ensures zero reactive power exchange between the grid and the grid-side converter.

The vector control scheme for grid-side PWM voltage source converter [92] is shown in Fig.4.7 where  $V_{Cabc}^*$  are the reference values of the three phase grid-side converter voltages,  $V_{Cd}^*$ ,  $V_{Cq}^*$  are the reference values of the grid-side converter voltages in d-and q- axis,  $i_{gd}^*$ ,  $i_{gq}^*$  are the reference values of the grid-side converter currents in d- and q-axis.

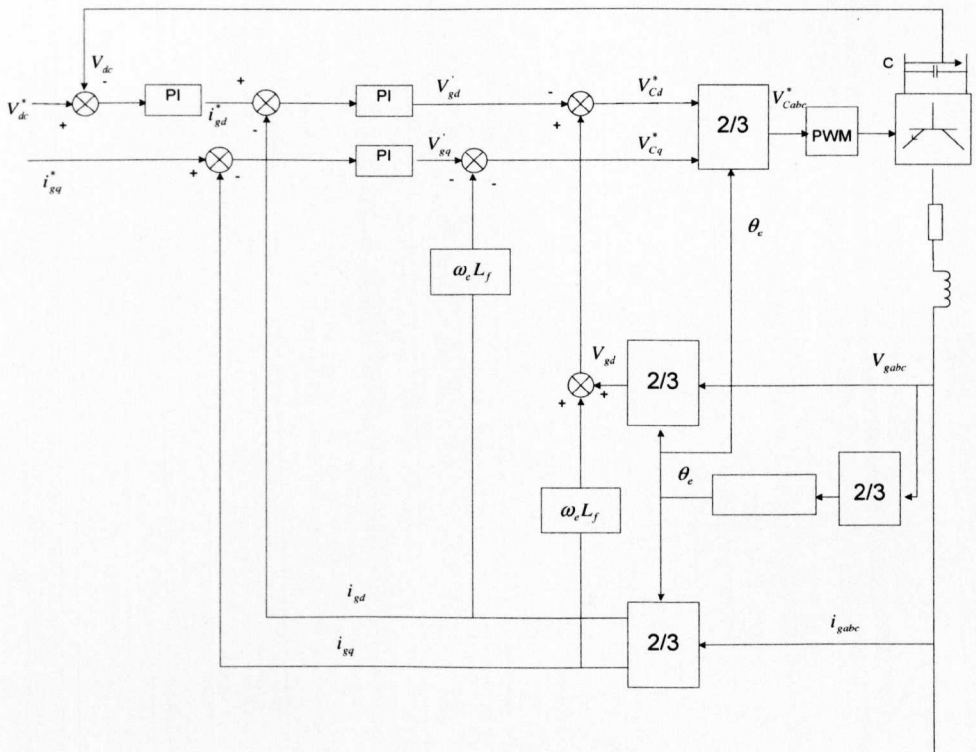


Fig.4.7 Vector control structure for grid-side PWM voltage source converter

Cascade control is used in the vector control scheme. Usually the inner control loop is designed much faster than the outer so that, when designing the outer

control loop, it is possible to neglect the dynamics of the inner control loop. This assumption will make controller design of the outer control loop much easier. In this work PI-controllers are applied in this study for their simplicity and robustness. The PI-controllers may be designed by standard controller design methods.

From (4.18), the plant for the current control loops is given by:

$$\frac{i_{gd}(s)}{V_{gd}'(s)} = \frac{i_{gq}(s)}{V_{gq}'(s)} = \frac{1}{L_f s + R_f} \quad (4.23)$$

where

$$\begin{aligned} V_{Cd}^* &= -V_{gd}' + (\omega_e L_f i_{gq} + V_{gd}) \\ V_{Cq}^* &= -V_{gq}' - (\omega_e L_f i_{gd}) \\ V_{gd}' &= R_f i_{gd} + L_f \frac{di_{gd}}{dt} \\ V_{gq}' &= R_f i_{gq} + L_f \frac{di_{gq}}{dt} \end{aligned} \quad (4.24)$$

In (4.24) the terms in brackets constitute voltage-compensation terms.

The effective transfer function of the DC-link voltage control loop can be derived from (4.22):

$$\frac{V_{dc}(s)}{i_{gd}(s)} = \frac{3m}{4Cs} \quad (4.25)$$

With the plants of the current control loops and the DC-link voltage control loop, the PI-controllers may be designed conveniently.

#### 4.4.1.1 Inner Current Control Loop Design

In the vector-control scheme of the grid-side PWM voltage source converter, the d- and q-axis line currents are decoupled for controlling the DC-link voltage and the reactive power flow between the grid and the grid-side

converter respectively. The plant of the inner current control loop is as (4.23) described, the design method is as follows.

These are several continues-time PI-controller design methods for designing PI-controllers, such as the use of Bode [97-98] and root locus [97, 99], pole-placement [100] and internal model control [101]. Due to its simplicity and straightforwardness, the pole placement method is used for designing PI-controller in the current control loops, the power control loops.

The plant for both d and q current loop can be represented as  $(1/L_f)/(s + R_f/L_f)$ . Assuming the controller can be written as:  $G_c = k_i(s + a_i)/s$ , the schematic diagram of controlled system can be as shown in Fig.4.8.

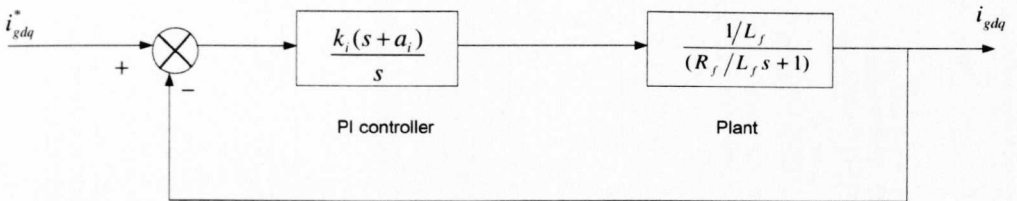


Fig.4.8 The schematic diagram of the current control loop

It is seen from the transfer functions of the current control loops that all the plants for the current control loops are stable with only one single dominant pole. In this condition, a straightforward approach for designing a PI-controller is to place the zero of the PI-controller to cancel the dominant pole of the plant. This method is called pole-placement [100]. The open-loop transfer function of the current control loop is:

$$G(s) = \frac{k_{pc} k(s + a_{ic})}{s(s + p)} \quad (4.26)$$

Let  $a_{ic} = p$ :

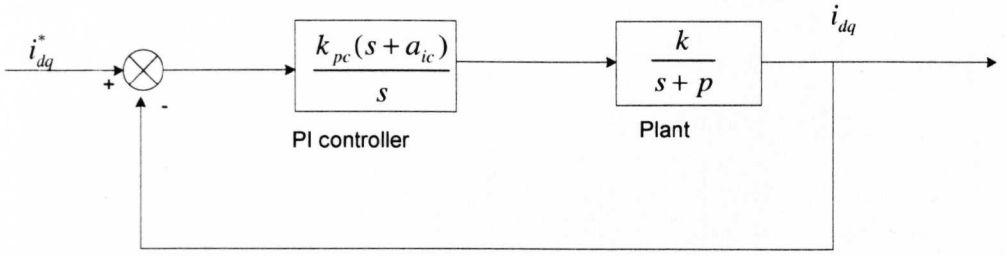


Fig.4.9 Schematic diagram of the current control loop of the generator

$$G(s) = \frac{k_{pc}k}{s} \quad (4.27)$$

The closed-loop transfer function is:

$$\frac{G(s)}{1+G(s)} = \frac{k_{pc}k}{s+k_{pc}k} \quad (4.28)$$

This is a first order system and the bandwidth of the first order system is:

$$\omega_n = k_{pc}k \quad (4.29)$$

The relationship between the bandwidth and the rise time (10-90%) for a first order system is  $\omega_n = \ln 9/t_{r1}$ . Thus the rise time of the system step response is:

$$t_{r1} = \frac{\ln 9}{k_{pc}k} \quad (4.30)$$

Therefore, the  $k_{pc}$  can be determined as:

$$k_{pc} = \frac{\ln 9}{kt_{r1}}(1+m\%) \quad (4.31)$$

where  $m\%$  is the design margin, which guarantees the required rise time will be obtained.

#### 4.4.1.2 Design of the PI-controller in the DC-link Voltage Control Loop

For its straightforwardness and simplicity, the pole-placement method is applied for designing PI-controllers in current control loops and power control

loops. It is seen from the transfer function of the DC-link voltage control loop that the plant has one single zero pole, where the pole-placement method cannot be used directly. Therefore, another method has been employed to design the PI-controller in the DC-link voltage control loop.

Internal model control, which is considered as a robust control method, has been used for AC machine control [102-104]. The benefit of the internal model control is that the controller parameters are expressed directly in the machine parameter and the desired closed-loop rise time. In this investigation, internal model control is utilized to design the DC-link voltage controller.

The idea behind the internal model control is to augment the error between the system  $G(s)$ , and the model of the system,  $\hat{G}(s)$ , by a controller  $C(s)$ , see Fig.4.10. It is just a matter of choosing the right transfer function  $C(s)$ . The closed-loop system will be:

$$G_{cl}(s) = G(s)C(s)/(1 + C(s)(G(s) - \hat{G}(s))) \quad (4.32)$$

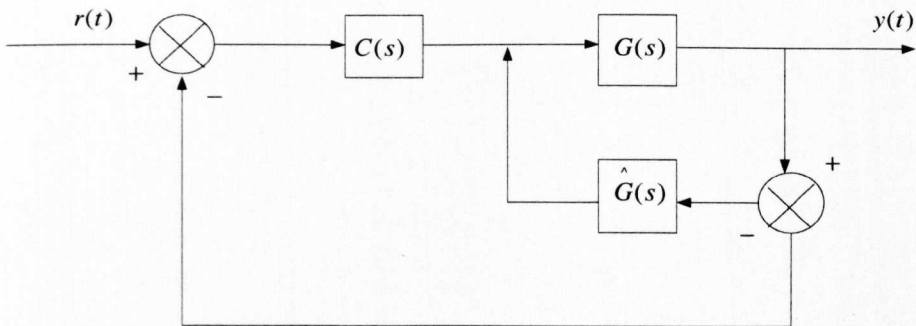


Fig.4.10 Internal model control system structure

If the internal model  $\hat{G}(s)$  is perfect, i.e.  $\hat{G}(s) = G(s)$ , the input-output relation is given as:

$$\frac{Y(s)}{R(s)} = C(s)G(s) \quad (4.33)$$

In this case, letting  $C(s) = G^{-1}(s)$  gives  $Y(s) = R(s)$ , i.e. all plant dynamics will be cancelled and the output signal will attain the input set point

instantaneously. It is clear that this optimal result cannot be accomplished as  $\hat{G}(s)$  is hardly ever perfect.

To solve this problem, one common way of choosing the controller  $C(s)$  when  $\hat{G}(s)$  has more poles than zeros is [83]:

$$C(s) = \left(\frac{\alpha}{s + \alpha}\right)^n \hat{G}^{-1}(s) \quad (4.34)$$

where  $n$  is chosen so that  $C(s)$  become implementable, i.e. the order of the denominator is greater than that of the numerator. For a fast order system,  $n=1$  is sufficient. The parameter  $\alpha$  is a design parameter adjusted to the desired rise time of the closed-loop system.

For a fast order system, substituting formula (4.34) into formula (4.32) with  $n=1$ , the closed-loop system with ideal parameters become:

$$G_{cl}(s) = G(s)C(s) = \frac{\alpha}{s + \alpha} \quad (4.35)$$

The relationship between the bandwidth and the rise time  $t_r$  (10%-90%) for a first order system is  $\alpha = \ln 9/t_r$ .

The internal model control can be considered as a special case of the classic structure shown in Fig.4.11. The controller  $F(s)$  in the system is related to the internal model  $\hat{G}(s)$  and the controller  $C(s)$  in the following way:

$$F(s) = \frac{C(s)}{1 - C(s)\hat{G}(s)} \quad (4.36)$$

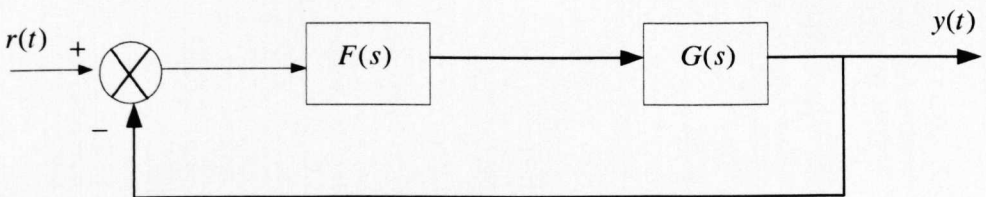


Fig.4.11 Classic control system structure

For a first order system, substituting (4.34) into (4.36) with  $n=1$ , the controller then becomes an ordinary PI-controller:

$$F(s) = \frac{k_p(s+a_i)}{s} = \frac{\alpha}{s} \hat{G}^{-1}(s) \quad (4.37)$$

where  $k_p$  is the proportional gain and  $a_i$  is the integral gain.

Assuming  $\hat{G}(s) = \frac{k}{s-p}$ , then

$$\frac{k_p(s+a_i)}{s} = \frac{\alpha}{s} \hat{G}^{-1}(s) = \frac{\alpha(s-p)}{ks} \quad (4.38)$$

which gives

$$\begin{aligned} k_p &= \frac{\alpha}{k} = \frac{\ln 9}{kt_r} \\ a_i &= -\frac{\alpha p}{kk_p} = -\frac{\ln 9 p}{kk_p t_r} \end{aligned} \quad (4.39)$$

The DC-link voltage is described as:

$$C \frac{dV_{dc}}{dt} = i_{dcg} - i_{dcr} \quad (4.40)$$

where  $i_{dcg}$  and  $i_{dcr}$  are the grid-side and rotor-side currents in the DC-link respectively, assuming the current dynamics is much faster,  $i_{dcg}$  may be expressed as [83]:

$$i_{dcg} = i_{dcg}^{ref} \quad (4.41)$$

where the reference DC current is set to:

$$i_{dcg}^{ref} = i_{dcg}^{ref} - B_a u_{dc} \quad (4.42)$$

where and 'active damping' term  $B_a$  is introduced to damp the disturbance  $i_{dcr}$ .

With the introduction of  $B_a$ , the plant becomes a first order system.

Treating  $i_{dcr}$  as a disturbance, the transfer function becomes:

$$G(s) = \frac{u_{dc}(s)}{i_{deg}^{ref}(s)} = \frac{1}{Cs + B_a} \quad (4.43)$$

Using the internal model control mentioned above, the proportional gain and integral gain of the PI-controller in the DC-link voltage control loop are found as:

$$\begin{aligned} k_{pe} &= C\alpha_e \\ a_{ie} &= \frac{B_a}{C} \end{aligned} \quad (4.44)$$

where  $\alpha_e$  is the desired closed-loop bandwidth of the DC-link voltage control loop. The closed-loop dynamic is then described as:

$$G_{cl}(s) = s \frac{\alpha_e}{s + \alpha_e} \quad (4.45)$$

Fig.4.12 shows a block diagram of the DC-link voltage control system. In this figure  $D(s)$  represents the disturbance, i.e.  $i_{dcr}$  shows a DC-link voltage control system.

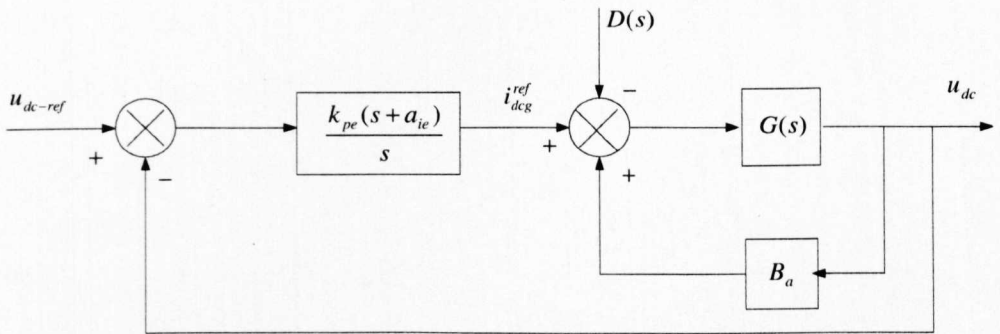


Fig.4.12 Block diagram of the DC-link voltage control system

Choosing  $B_a = C\alpha_e$  [22], and  $\alpha_e = \frac{\ln 9}{t_{re}}$  yields:

$$\begin{aligned}
 k_{pe} &= \frac{\ln 9C}{t_{re}} \\
 a_{ie} &= \frac{\ln 9}{t_{re}}
 \end{aligned}
 \tag{4.46}$$

The parameters of the DFIG applied in the wind turbine are shown in details in Table 4.1 [24].

Table 4.1 Generator parameters

Parameter	Value
Rated Power ( $P_n$ )	1.5 MW
Rated Voltage ( $V_{rated}$ )	575 kV
Rated Frequency ( $f_n$ )	50 Hz
Generator Inertia ( $H$ )	0.185 s
Friction Factor ( $F$ )	0.0001 p.u.
Stator Resistance ( $R_s$ )	0.023 p.u.
Rotor Resistance ( $R_r$ )	0.016 p.u.
Stator leakage inductance ( $L_{ls}$ )	0.18 p.u.
Rotor leakage inductance ( $L_{lr}$ )	0.16 p.u.
Mutual inductance ( $L_m$ )	2.9 p.u.

The parameters of the inductor in series with the grid-side PWM voltage source converter are:  $R_f = 0.00066\Omega$  ,  $L_f = 0.00021H$  . The value of the capacitor in the DC-link is set as:  $C = 0.01F$  .

For the grid-side PWM voltage source converter, the parameters of the PI-controllers in the current control loops may be obtained based on the plant shown in (4.23) and the pole placement method introduced in [100]. The parameters of the PI controller in the DC-link voltage control loop may be calculated with (4.46). Setting the rise time of the current control loops and the DC-link voltage control loop respectively as:  $t_{r1} = 0.002s$  ,  $t_{r2} = 0.02s$  , and applying a 20% design margin, the parameters of the PI-controllers in the vector control scheme for the grid-side converter are listed in Table 4.2.

Table 4.2 PI-controller parameters for grid-side converter

	Proportional gain	Integral gain
Current loops	398.896	3.95896
DC-link voltage loop	1.0986	120.692

## 4.5 Performances of the Control Schemes

### 4.5.1 Performances of Current Control Loops

The control schemes are to be realized using cascade control as described before. For grid-side PWM voltage source converter, the inner current control loops are used for controlling the  $dq$ -axis line currents and the outer voltage control loop is used for keeping the DC-link voltage constant.

The performances of the control loops will be demonstrated from inside to outside step by step. First, to study the performances of the inner current control loops, the outer control loops are removed temporarily, the performances of the inner current control loops will be discussed below. Then, after putting the outer control loop back, the performances of the outer DC-link voltage loop is to be studied next.

The requirements concerning the current control loops are set up as follows [83]:

- The d-and q-axis currents should be decoupled for individual control.
- The current overshoot should not too high since the excessive overshoot may damage the power electronics. It is chosen to accept 5% overshoot.

The control scheme for studying the grid-side current control loops' performances is illustrated in Fig.4.13, in which the outer DC-link voltage control loop is removed. The reference values of the dq-axis line current control loops are shown in Fig.4.14.

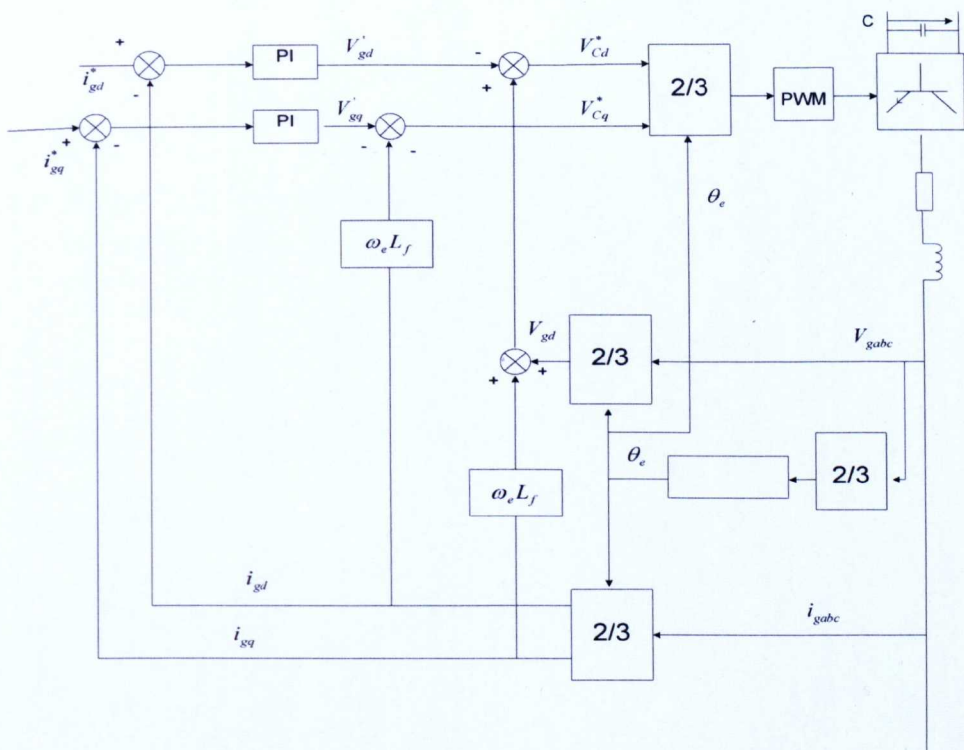


Fig.4.13 Grid-side current control loops implementation

The rise time is approximately 2ms, and there is less than 5% overshoot. It is also seen that a step in either  $i_{gd}$  or  $i_{gq}$  causes the other current to oscillate. The oscillations of the currents are however very small and the obtained decoupling of the currents are therefore found useable.

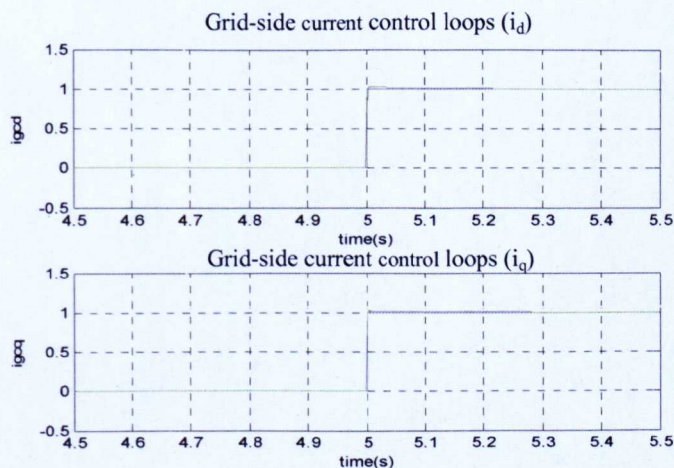


Fig.4.14 Step response of the grid-side current control loops

## 4.5.2 Performance of the DC-link Voltage Control Loop

The aim of the DC-link voltage control is to keep it at a constant value regardless the changes of the wind turbine output power. The control scheme for studying the DC-link voltage control loop's performance is the same as shown in Fig.4.7. The step response of the grid-side DC-link voltage is shown in Fig.4.15. The overshoot is less than 10% and the rise time is approximate 2ms as shown in Fig.4.15.

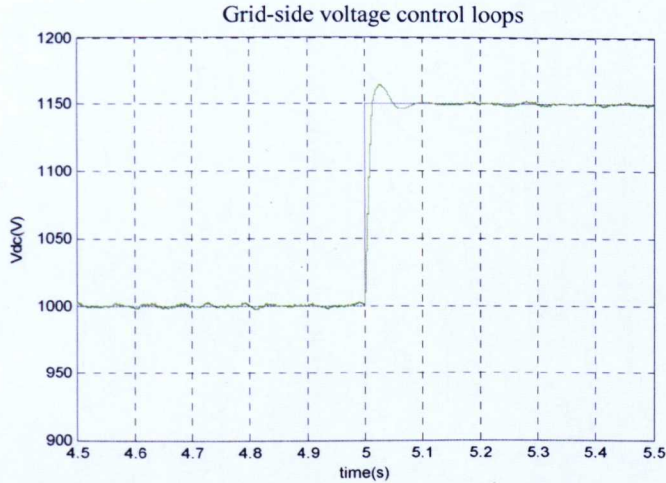


Fig.4.15 Step response of the grid-side DC-link voltage control loops

It can be seen that the DFIG controller has been designed with a performance that meets the normal design specifications. This then enables the DFIG model to be used as a representation example of a typical DFIG performance for the ROCOF study given in the following sections.

## 4.6 Simulation Results

### 4.6.1 Islanding

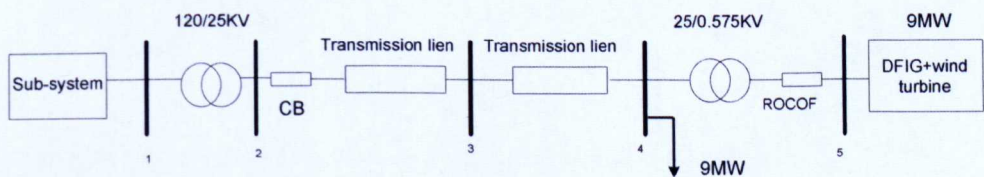


Fig.4.16 Single line diagram of test system

The test system shown in Fig.4.16 was used to evaluate the routines. It comprises a 120kV, 50Hz, which feeds a 25kV distribution system through a 120/25kV  $\Delta/Y_g$  transformer. In this system there are six 1.5MW DFIG wind turbine generators in parallel connected at bus 5, which is connected to the network through one 25/0.575kV  $\Delta/Y_g$  transformer. In all simulated cases, the total simulation time is 10s, the circuit breaker CB at bus 2 opens after 5s which creates an islanding situation, and remains open during the rest of the simulation (data demonstrated from 4.5s to 5.5s in the following sections). Thus, the initial active power imbalance in the islanded system is equal to the active power provided by the substation at the moment of islanding.

Two possible frequency estimation techniques are considered to calculate rate of change of frequency, one is based on Fast Fourier Transforms (FFT) and the other is based on the Prony's method which are described in Chapter 3. The performance of ROCOF relays based on these methods is compared in Fig.4.17.

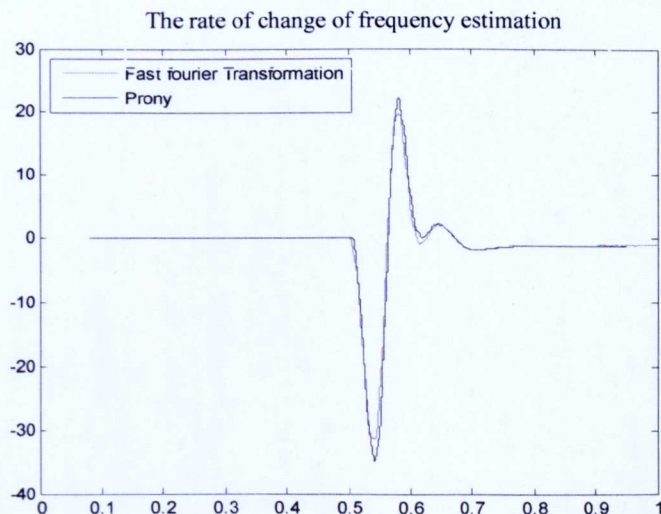


Fig.4.17 The estimation of rate of change of frequency by using FFT and Prony's method

It can be observed in Fig.4.17 that the Prony's method based relay sees a higher rate of change of frequency than that based on the Fast Fourier Transform when subjected to the same disturbance. The Prony method can detect the frequency within data less than one cycle, by using a shorter data

window the detection time calculated by Prony's method is shorter than FFT. Comparing the two frequency estimate algorithm results, it can be seen that the trends with frequency are the same. However, the Prony's method may cause false operation as it is more sensitive during the system disturbance.

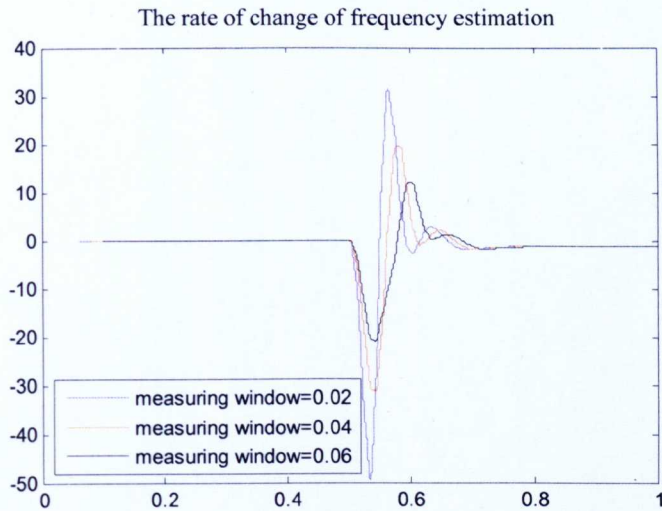


Fig.4.18 Comparison of rate of change of frequency using different measuring window

Fig.4.18 shows a comparison of the measured rate of change of frequency by using the Prony's method for different measurement windows, a 0.06, 0.04, 0.02 seconds. From Fig.4.18 it can be seen that the duration of the measuring windows used in the calculation of rate of change of frequency affects the operation of ROCOF relay. Similar as the simulation results in Chapter3, the longer the measuring window, the smaller the amplitude of the rate of change of frequency becomes and the less sensitive the relay will be. On the other hand, the shorter measuring windowing, the larger rate of change of frequency, hence the more sensitive the relay. However, the main advantage of longer measuring window is the increase in delays improves immunity to network disturbance and a reduction in the number of false trips.

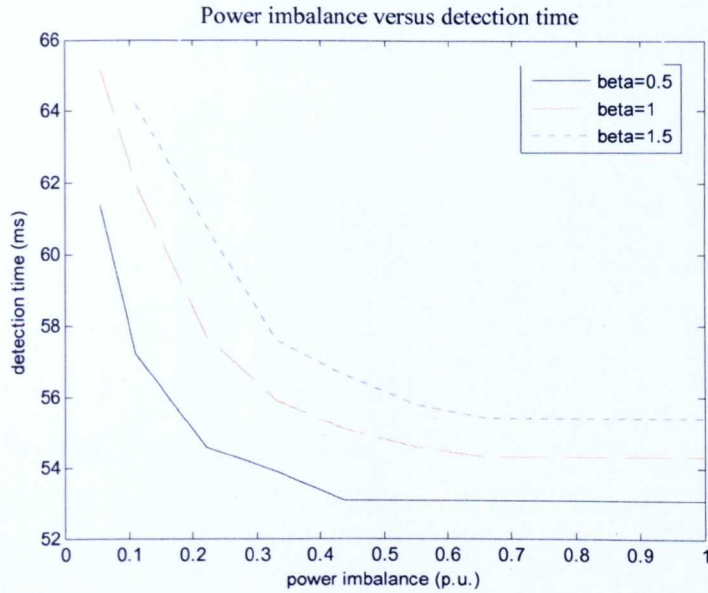


Fig.4.19 The detection time versus power imbalance by using Fast Fourier transform with different relay setting

Fig.4.19 shows the detection time for different relay settings Beta versus power imbalance. The curves are obtained by varying the load from 9MW to 17MW and keeping the DFIG output power constant (9MW). It is observed that for the same value of power imbalance the detection time increases as the relay setting increases.

### Non-detection Zone

Similar analysis considered here as with Chapter 3 for a non-detection in the system with 5% and 10% band-limited white noise. From Fig.4.19 it can be found that the smaller the relay setting, the shorter the detection. However, it would cause false tripping easily in the noisy situation. Table 4.3 shows the ROCOF relays operation in the cases of a system with 5% and 10% band-limited white noise with different relay settings during the system connected situation.

Table 4.3 ROCOF trip operation during system breaker closed condition in different cases with different relay settings

trip relay setting case	0.5Hz/s	1.0Hz/s	1.5Hz/s
5%noise	yes	no	no
10%noise	yes	no	no

Form Table 4.3 it can be found that larger relay setting has a better ability to avoid false tripping during the situation of system disturbances, however, it provides a larger non-detection zone. For example, in the case of setting the threshold value of 1.5Hz/s, the non-detection zone is 5.56%. With the 0.5Hz/s relay setting, the non-detection zone is only 1.12%, but from Table 4.3 it can be found that the ROCOF relay operated in the cases of stable system with 5% or 10% band-limited band noise. Also, with large load changing, it will cause ROCOF relay nuisance tripping as well which will be discussed in the following sections.

#### 4.6.2 False Operation

During the non-islanding situation which is shown in Fig. 4.20, false operation of ROCOF relays is of concern. The test system used to investigate false operation is similar to the system in Fig. 4.16. In Fig. 4.20, by closing the circuit breaker a three phase load is added into the system at 5s (data demonstrated from 4.5s to 5.5s in the following sections). Under this situation, the ROCOF relays must not operate as it is a non-islanding condition and a stable system. However, when the power imbalance occurs in the system during load adding, the trip signal operates. In this case, an interlock function should operate to avoid nuisance tripping.

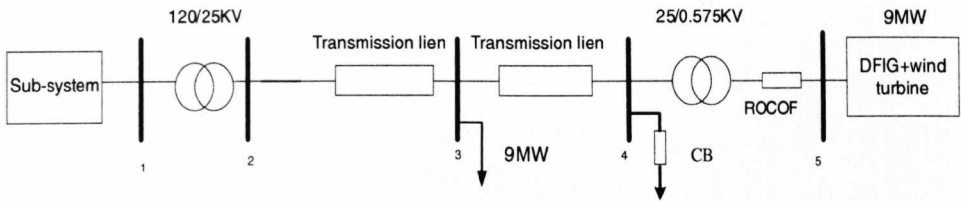


Fig.4.20 Single-line test system (adding load)

An interlock function is needed to stop false trips during a non-islanding condition. In Chapter 3 for synchronous machines it was shown that by combining with ROCOF relays the quantity of  $dP/dt$  is very effective for preventing false trips. However for a DFIG the output power is controlled even during frequency variations. It is difficult to use  $dP/dt$  as a reference for an interlock. Therefore, another interlock scheme has to be found as presented in Fig.4.21.

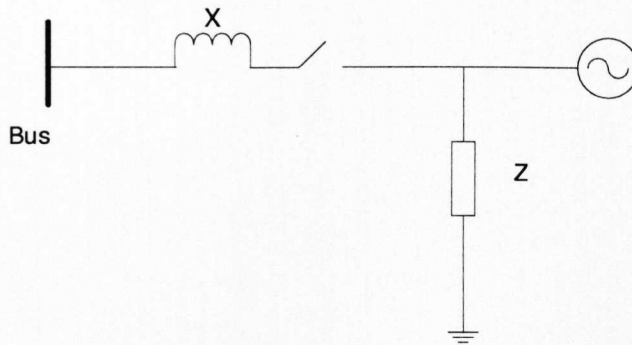


Fig.4.21 System simplified structure

The proposed interlock function is based on the relationship between real power and the impedance of the connected system. For the export of power from a generator with a local load  $z$  across a loss less transmission line of reactance  $x$  we can write:

$$P = \frac{v^2 \sin \delta}{x} + \frac{v^2}{z} \quad (4.47)$$

We can then define a quantity  $Z_{est}$  given by:

$$Z_{est} = \frac{v^2}{p} \quad (4.48)$$

In the islanding condition as the load changes this will cause the machine frequency to vary and will also give rise to a step change in impedance as estimated by (4.48). For a non-islanding case  $Z_{est} \neq v^2/p$  and the estimated impedance will not display a significant step change.

An example, system is as shown Fig.3.6, in order to justify the method, the nominal voltage is set as 690v and the nominal power is 30MW, if the output power of the generator is 30MW with a 20MW load ( $\Delta p = 10\text{MW} > 0$ ), the load estimation value is  $Z_{est} = 690^2 / (20 \times 10^6) = 0.023805$  ( $Z_{est} = 1.5$  p.u.), when the circuit breaker operates at 5s, the total simulation time is 10s (the presented 1s of data is for the period 4.5s-5.5s), from the simulation results which are shown in Fig.4.22, it is found that the value of  $v^2/p$  is 1.5p.u. after islanding.

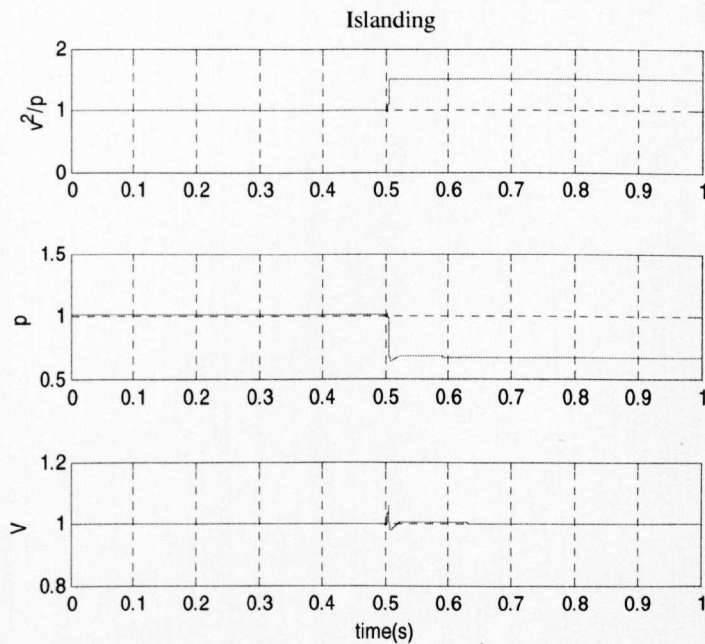


Fig.4.22 The values of estimated load impedance, power and voltage of generator side during islanding situation

From Fig.4.22 it is clearly showed that the load impedance is 1.5pu (which is equal to the real value) after the islanding situation occurs.

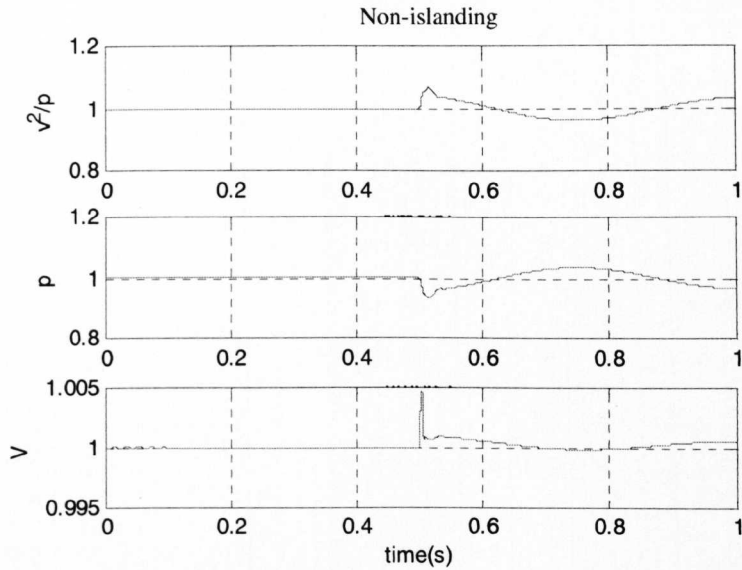


Fig.4.23 The values of estimated load impedance, power and voltage of generator side during non-islanding situation

It is shown from Fig.4.23 that during the non-islanding situation the value of the estimated load impedance varies and it is not equal to the actual value.

In the system which is described in Fig.4.16. During islanding the value of  $Z_{est} = v^2/p$  is defined by the load impedance variation and for the system simulated this was [0.9977 0.4994] p.u. (the values are obtained by keeping the DFIG output power constant and changing the load power). During non-islanding situation, the value of  $Z_{est} = v^2/p$  will return to the original value after a short time. Note that for small load variations (i.e.  $\Delta P \leq 1$  MW) the ROCOF relay does not trip for the non-islanding situation but always trips during islanding. Therefore we only need to block ROCOF trips for large load variations when non-islanding. After a delayed time 130ms, if the value of  $Z_{est} = v^2/p$  is smaller than 0.98, the block signal would not operate.

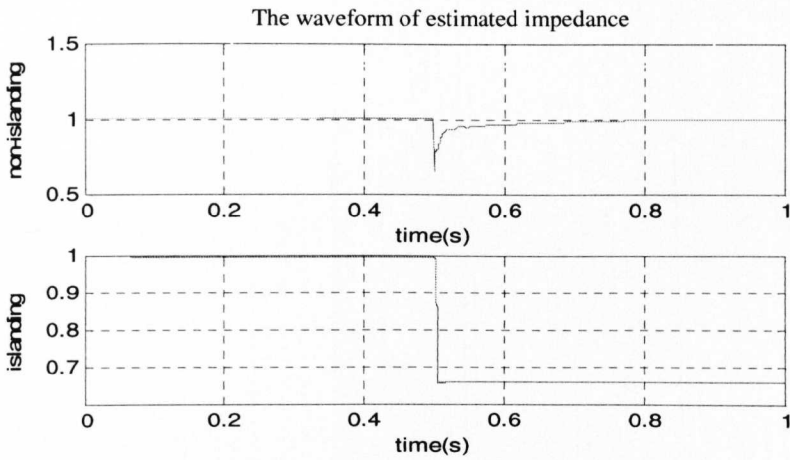


Fig.4.24 The waveform of  $v^2/p$  during non-islanding and islanding situation ( $\Delta p=0.778p.u.$ )

The waveform of the impedance  $Z_{est} = v^2/p$  of islanding and non-islanding is shown in Fig.4.24, after the initial transient a difference can be distinguished between them. Therefore it is proposed that the waveform of the impedance  $Z_{est} = v^2/p$  can be used as an interlock function to avoid false tripping during non-islanding.

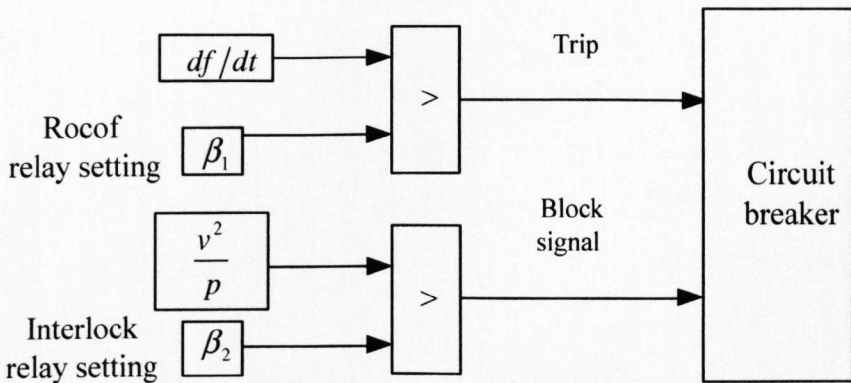


Fig.4.25  $v^2/p$  interlock function structure

The logical interlock function structure is shown in Fig.4.25, if the impedance value  $Z_{est} = v^2/p$  is greater than a block signal trip setting value, the block signal will be sent to the circuit breaker which is applied to stop the ROCOF tripping signal.

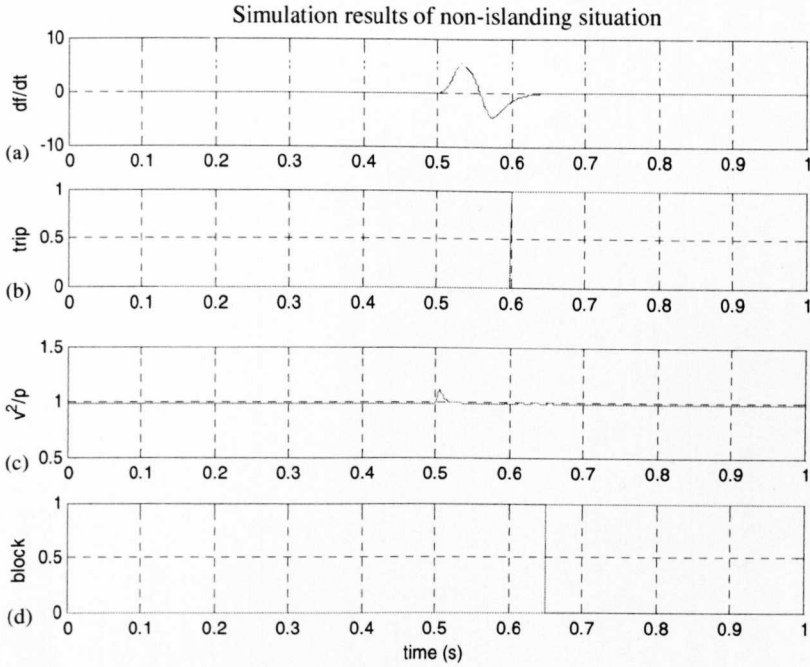


Fig.4.26 Simulation results of non-islanding situation the ROCOF relays with  $v^2/p$  interlock function

In order to verify the impedance  $Z_{est} = v^2/p$  interlock function can cooperate with ROCOF relays properly Fig.4.26 shows the simulation results of system non-islanded as in Fig.4.20. It is found that during non-islanding situation where load shedding occurs at 0.5s, the ROCOF relay operates at 0.592s due to the switching off the 6MW load causes the transient in the rate of change of frequency, the block signal trips at 0.6998s by comparing the  $Z_{est} = v^2/p > 0.98$ , it effectively stops ROCOF relays operation after 159.8ms from the load changing. During the small load variation, the ROCOF relay would not trip, therefore, there is no need to consider the small power imbalance leading to the non-detection zone problem. In this system, if the load shedding or adding is smaller than 14% or 11.1%, there would be no ROCOF tripping signal generated.

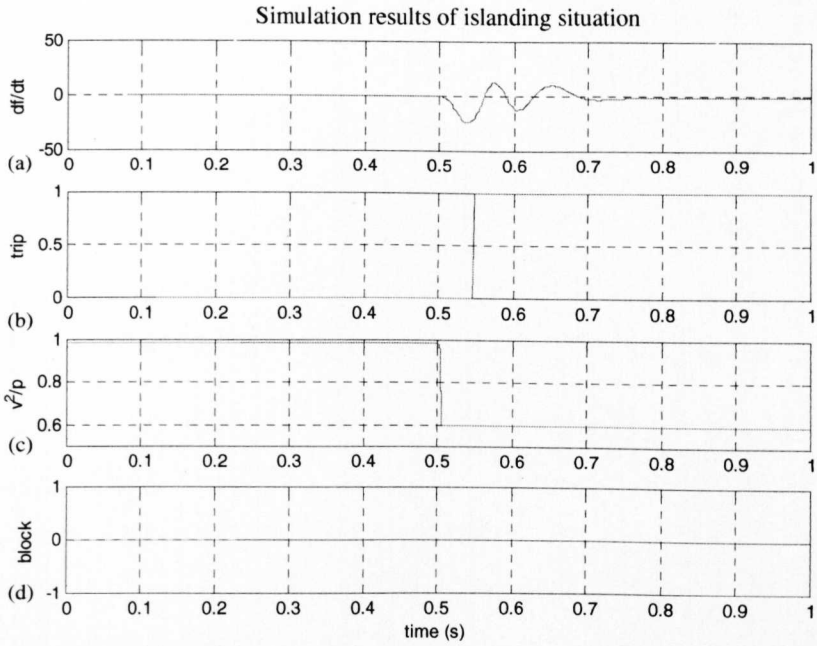


Fig.4.27 Simulation results of islanding situation the ROCOF relays with  $v^2/p$  interlock function

For the islanding situation, in the system as described in Fig.4.16 with a 0.667 p.u. power imbalance, the islanding detected results are shown in Fig.4.27, where the  $df/dt$  and  $Z_{est} = v^2/p$  are depicted in Fig.4.27 (a), (c) respectively. Islanding occurs at 0.5s, ROCOF relay detects this situation quickly at 0.5461s as shown in Fig.4.27 (b), As in Fig.4.27 (d) there is no block signal tripping because after the transient the value of  $Z_{est} = v^2/p$  is smaller than the interlock function threshold setting. Therefore the interlock function of  $Z_{est} = v^2/p$  can distinguish islanding and load variation in the DFIG distributed system effectively.

## 4.7 Summary

In this chapter, the grid-connected DFIG similar to GE1.5MW wind turbine generator [82] is introduced. The vector control scheme is designed and validated for grid-side converter. The objective of the vector-control scheme for the grid-side PWM converter is to keep the DC-link voltage constant while controlling reactive power into the grid. The reference frame used in grid-side

converter control is oriented along the stator (or the grid) voltage vector position, enabling independent control of the DC-link voltage and the reactive power flow between the grid and the grid-side converter. The performance of the control schemes, the inner current control loops, the DC-link voltage control loop are individually investigated. The simulation results show that the designed controller meets the design requirements. The rotor-side converter controller is applied the GE1.5MW wind turbine generator [82].

The fast islanding detection method used for DFIG wind turbine is then investigated. The frequency measuring algorithms, different measuring windows, and the relay settings characteristics that affect the performance of ROCOF relay in DFIG wind turbine system are outlined. The shorter the measuring window, the faster the detection time will be, and more sensitive relay is which may cause an incorrect tripping signal in noisy simulation. Meanwhile, using a smaller relay setting can also reduce the detection time, but it also can easily cause false operation. Therefore a compromise in the relay setting is required to provide a balance between the security and dependability. During the load variation situation the ROCOF relays should not operate for this stable system. The waveform of system impedance estimate  $Z_{est} = v^2/p$  interlock function is proposed to avoid false operation for the load fluctuation. It is shown that the nuisance tripping signal can be blocked quickly and accurately during non-islanding condition.

## Chapter 5

# DFIG Islanding Experiment

### 5.1 Introduction

In this chapter, an experimental test was carried out to verify the proposed islanding detection method. The prototype of DFIG islanding detection test rig consisted of the rotor converter, grid interface active front end, along with the Doubly Fed Induction Generator (DFIG) and the switch box. The control of the DFIG has been implemented in real-time software. Control of the DFIG currents was implemented in the  $dq$  synchronous reference frame following standard DFIG practice in which the q-axis current component provides torque control. An outer speed-control loop sets the reference value for the q-axis current. By operating the DFIG machine in speed-control mode it absorbs whatever mechanical power is required to hold the speed of the prime mover constant. In the tests the prime mover was another electrical machine, operated in torque control mode. In this way, the generated output power of the DFIG machine was dependant on the torque reference used to control the driving (prime-mover) machine.

For the DFIG islanding detection test, two conditions (islanding and non-islanding) with different power imbalance between generation and the load are implemented. Voltage and current values are measured from the common coupling point. ROCOF relays cooperation with the proposed  $v^2/p$  interlock function is verified to have the capability to distinguish the islanding and load changing situations.

## 5.2 Basic Theory

The basis of a DFIG generator equipped with a ROCOF relay operating in parallel with the grid supplying a load is presented in Fig.5.1. The theory is similar to that described in Chapter 3. The system variation (including islanding and load changing) can be detected by applying the rate of change of frequency. During the non-islanding situation (load changing), the  $v^2/p$  block function can be used to stop the ROCOF tripping signal. The principle of  $v^2/p$  block function was introduced in Chapter 4. The DFIG model used in this experiment was built and tested by Dr Andrew Goodman from the PEMC group of the University of Nottingham [105]. This model is different from the simulation model in Chapter 4. The grid-side converter is replaced by a DC active front end from Emerson Industrial Automation, and the outer control loop for the rotor-side converter is speed controlled.

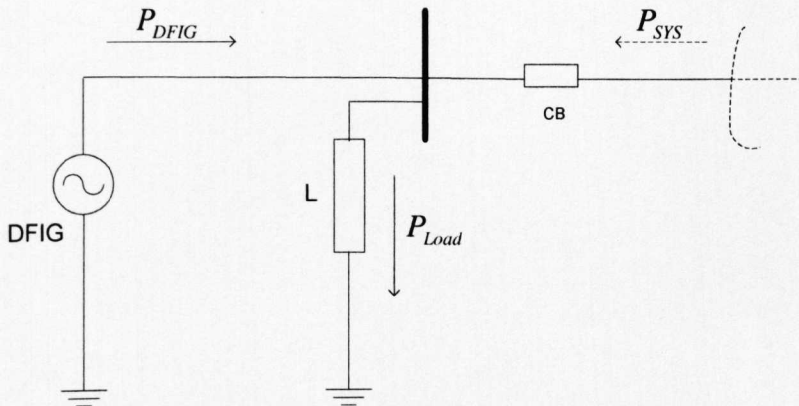


Fig.5.1 Equivalent circuit of a DFIG operating in parallel with the grid

## 5.3 Experiment Setup

### 5.3.1 Experimental Prototype

The hardware implementation of the DFIG islanding detection test rig includes:

- The DSP (Digital Signal Processor)/FPGA (Field Programmable Data Array) control Platform – to perform all measurement and control functions for the basic converter control;
- The Main Power PCB (Printed Circuit Board);
- Active Front End ;
- DFIG – Doubly Fed Induction Generator.

The complete rig is shown in Fig.5.2.

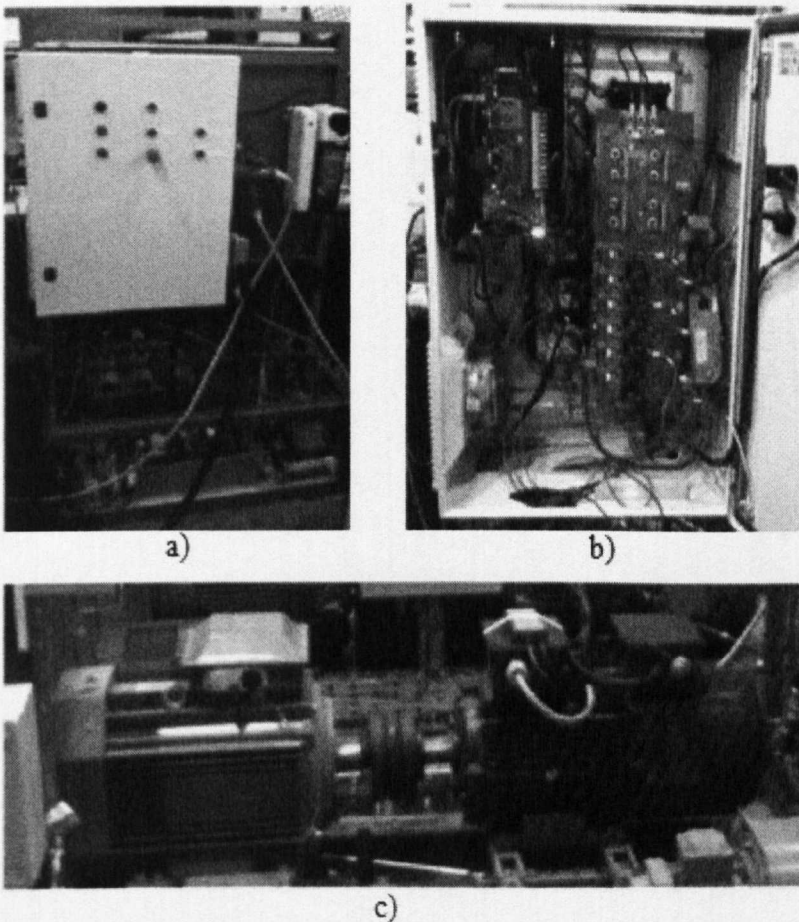


Fig.5.2 a) Complete drive assembly b) drive internals c) DFIG and driving motor

### 5.3.1.1 Main Power PCB

The main power PCB shown in Fig.5.3 includes footprints for direct connection of the input rectifier, DC link capacitors with bleeding resistor (for energy discharging), output IGBT modules, the gate drive circuits for the IGBTs and measurement transducers for DC link voltage and the output currents. The PCB forms the low inductance power planes for interconnection between the DC link capacitors and the IGBT modules.

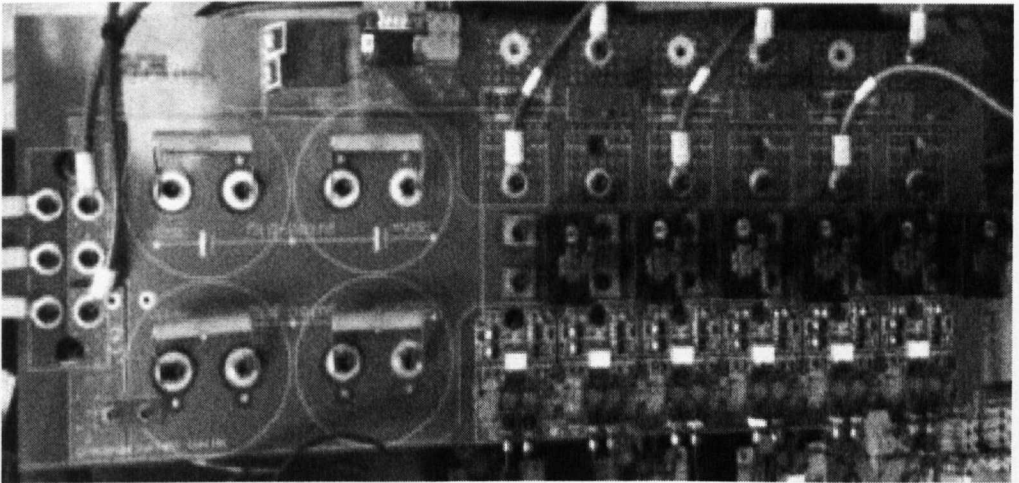


Fig.5.3 Main power PCB

Fig.5.4 shows a schematic representation of the power section of the main power PCB. The three phase supply enters on the left via a diode rectifier. Actually this rectifier was not used and replaced with the Active Front End (AFE) for DC voltage output of the test. The green and brown lines in Fig.5.3 were used to connect the active front end. There are then four electrolytic capacitors (mounted beneath the PCB) forming the main DC link capacitance, connected two in series and then paralleled. Each capacitor also has a bleed resistor connected across the terminals to slowly discharge the DC link when the supply is disconnected. These are the four grey horizontal bars on the left of the PCB photo in Fig.5.3.

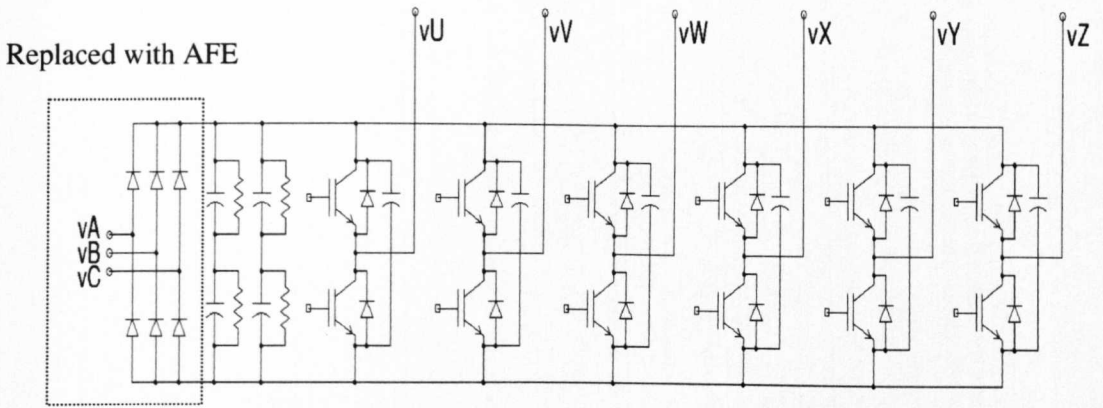


Fig.5.4 Main power PCB basic schematic

The IGBT modules are also mounted below the PCB and are identifiable by the six vertical rows of three bolts on the right of the PCB in Fig.5.3. The original purpose of the six rows of IGBTs was to generate two sets of selectable rotor currents. In this experimental test only three rows of the IGBT modules were used. Attached across the DC link terminals of each IGBT half bridge module is a snubber capacitor ( the black rectangular block). These provide a small amount of capacitance with very low equivalent series inductance (ESL). This compensates for the small inductance of the power planes and electrolytic capacitors, and ensures that the pulsing current flowing through the power planes due to the PWM nature of the output does not causes damagingly high voltage spikes across the IGBT modules.

The gate drive circuits occupy the lower right section of the PCB in Fig.5.3. The IGBT firing signal from the control cards is supplied to receivers along the lower edge of the PCB and converter to a voltage output. Each individual IGBT has its own isolated gate drive circuit. The gate drive signals are passed through an opto-isolator to the floating part of the circuit, while an isolated power supply chip is used to supply the floating part of the gate drive circuit, taking in 5V and producing  $\pm 15V$  output, with reference to the IGBT emitter voltage. The output of the opto-isolator is used to drive a push/pull amplifier stage, which applies  $\pm 15V$  to the IGBT gate terminal, via current limiting gate resistors. Zener diodes are also used to ensure no over-voltage spikes are applied to the gate terminal, as these would damage the IGBT.



Proportional Integral (PI) controllers. Any unbalance present in the form of negative sequence are transformed to double harmonics and can not be suppressed completely by the PI controllers, resulting in a non-zero steady-state error. A solution to this problem is the use of decoupled dual reference frame control for both negative and positive sequence components [101].

### 5.3.1.2 Active Front End

As an addition to the input stage of the DFIG inverter, the diode rectifier was replaced with a control techniques 3-phase PWM rectifier active front end shown in Fig.5.6. This allowed for regenerative control of the DC link voltage. Without this, the DFIG could only be used to generate below synchronous speed (1500rpm). If it were allowed to accelerate above synchronous speed, it would generate through both the stator and rotor, charging the DC link to dangerous levels.

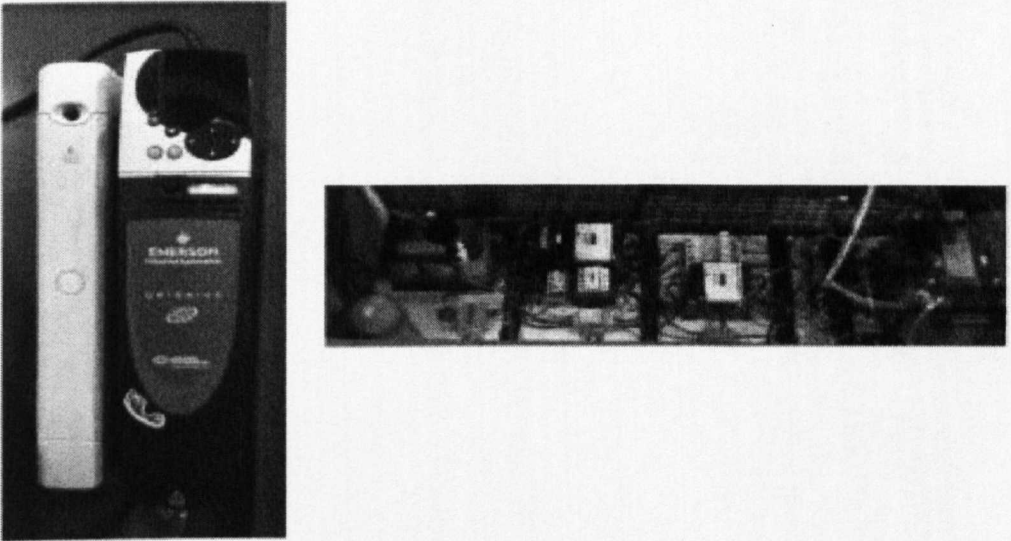


Fig.5.6 Active Front End and its relay circuit

With the active front end in place, it was possible to both motor and generate at both sub and super synchronous speeds. The AFE (Active Front End) [106] however was only capable of controlling the DC link voltage above the rectified grid voltage, and so had a DC link reference value of 700V.

The control system of the grid side converter is used to regulate the DC-link voltage and reactive output power, which is controlled as an active rectifier using stator voltage oriented unity power factor control in the synchronous reference frame.

### 5.3.1.3 The Switch Box

The switch box used for the experiment is shown in Fig.5.7. The green and red button in the bottom side are used for switching on and off the system load which can provide the load adding and shedding situation. The key in upper the middle of the green and red buttons is applied as a lock function to ensure the operation security. Once the islanding occurs (press the red button), it requires the key to turn on the green button to connect the DFIG to the grid. This ensure that during islanding situation, the machine is not able to be reconnected to the main power supply by miss-operation.

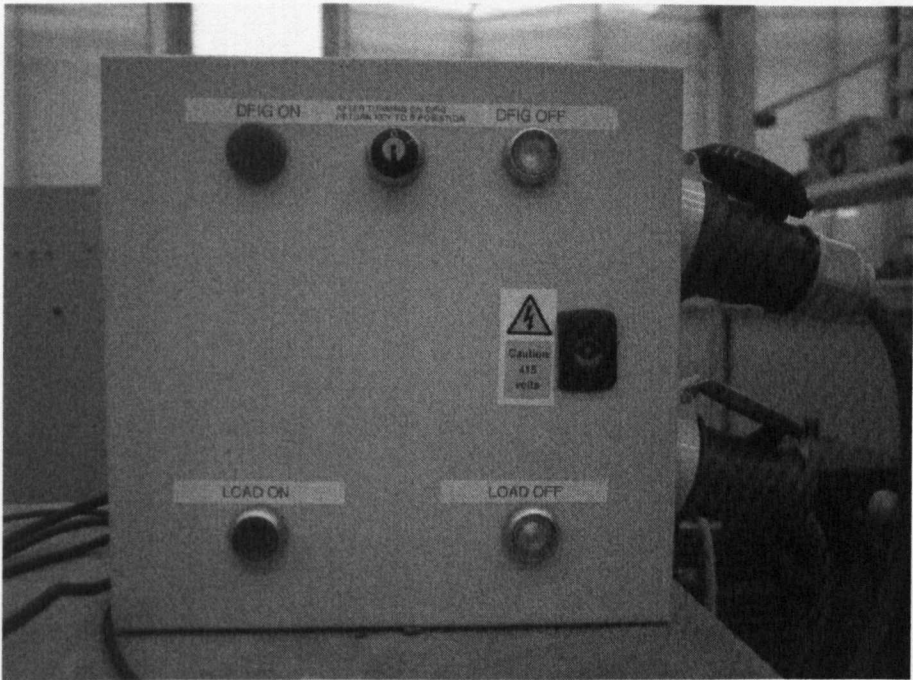


Fig.5.7 The switch box for creating islanding and load changing situation

The simplified structure of the switch box designed for this experiment is shown in Fig5.8. The main function of the box is to control connection of the DFIG and the load with the grid. The DFIG can be connected to the grid by

closing circuit breaker S1, circuit breaker S2 is applied for providing non-islanding situation.

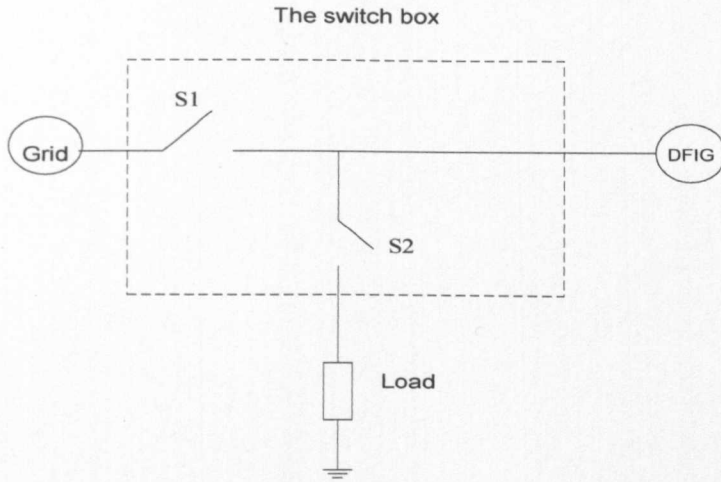


Fig.5.8 Simplified structure of the switch box

#### 5.3.1.4 DFIG

The DFIG used for this experiment was a standard 7.5kW machines as shown in Fig.5.9. It used three sliprings to transfer the current to the rotor windings, which were housed beneath the inspection cover on the right of the motor. Attached to the right hand end of the motor is a 2500 pulse per revolution optical position encoder [107]. The parameters of this DFIG is shown in Table5.1.

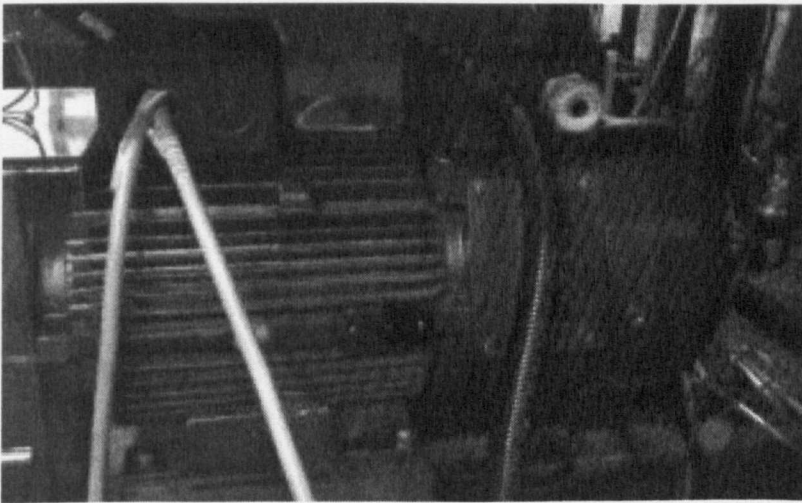


Fig.5.9DFIG

Table 5.1 DFIG parameters

Parameter	Value
Rated Power ( $P_n$ )	7.5kW
Rated Voltage ( $V_{rated}$ )	440kV
Rated Frequency ( $f_n$ )	50 Hz
Generator Inertia ( $H$ )	0.09 s
Pole pairs ( $P$ )	2
Stator Resistance ( $R_s$ )	0.45 p.u.
Rotor Resistance ( $R_r$ )	0.2 p.u.
Stator leakage inductance ( $L_{ls}$ )	0.01 p.u.
Rotor leakage inductance ( $L_{lr}$ )	0.007 p.u.
Mutual inductance ( $L_m$ )	0.088 p.u.

### 5.3.1.5 Prime Mover

The prime mover used for this experiment is shown in Fig.5.10. During normal operation, the prime mover and the generator will operate in torque and speed control respectively. The generator is operated such that its electrical torque matches the mechanical torque of the prime mover. If the shaft speed exceeds the upper limit, an over-speed trip will be issued.

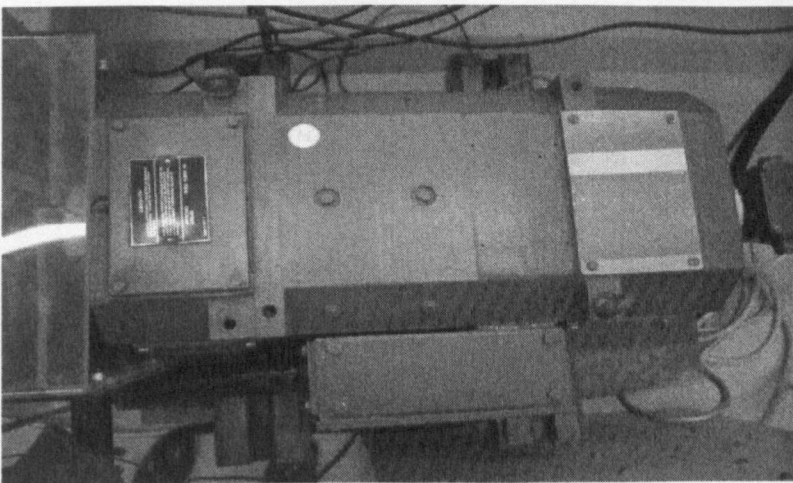


Fig.5.10 Prime Mover

### 5.3.1.6 DC Voltage Supply and Speed Measurement Equipment

The DC voltage supply and speed measurement equipment are shown in Fig.5.11. The speed measurement equipment in the upper side of Fig.5.11 is Philip 6671 PM high resolution timer/counter which is used for monitoring the real time speed of the prime mover [108], to make sure the speed of the prime mover can reach the speed value of DSP control, and to ensure that the speed does not go too high to cause an accident a failure, the machine need to be shut down immediately.

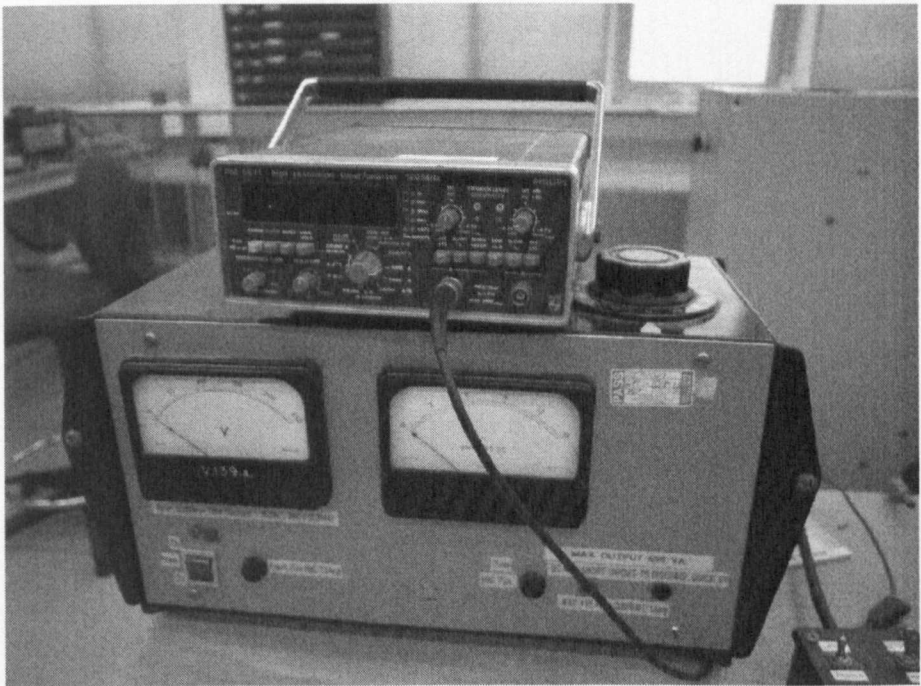


Fig.5.11 DC voltage supply and speed measurement equipment

The DC voltage supply in the bottom side of Fig.5.11 is for supplying the DC field voltage of the prime mover, the maximum output power of the equipment is 600VA, the maximum output voltage and current are 200V and 15A. The DC voltage used in this experimental test is 50V.

### 5.3.1.7 Software Development

Fig.5.12 shows a DFIG standard speed control structure, the control of the DFIG currents is implemented in the  $dq$  synchronous reference frame. An

inner control loop using angles derived from both the DFIG stator terminal voltage measurements ( $\theta_s$ ) and the DFIG rotor angular position ( $\theta_r$ ) to control the currents to reference values.  $\theta_r$  is recorded by the rotor shaft optical position encoder,  $\theta_s$  is derived by measuring the grid side voltage and using a PLL to control the quadrature component to zero. Both of these angles allow for rotor currents synchronised to stator voltage to be generated at any rotor speed. Proportional plus integral (PI) controllers were used to control the d and q axis currents to their reference values.

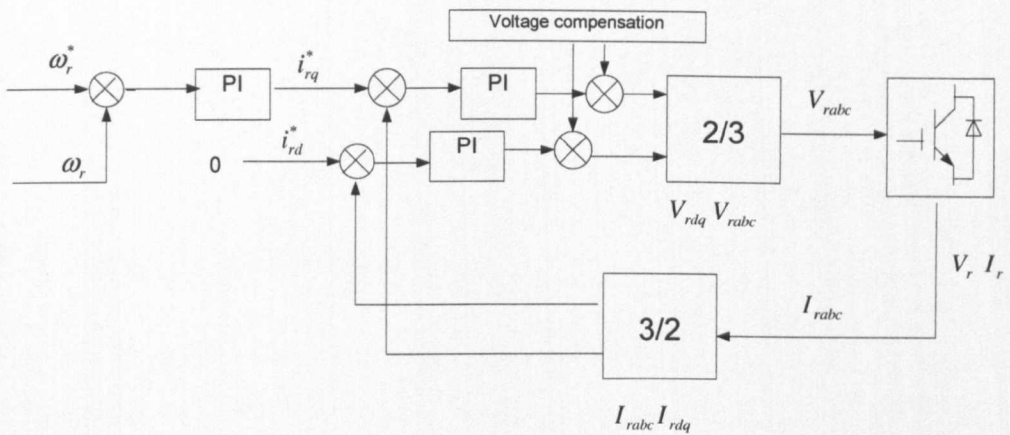


Fig.5.12 DFIG dq current frame controller structure

The inner control loop provides torque control of the DFIG. This allowed for the driving machine to operate in speed control mode, and the  $q$  axis current reference of the DFIG to be used to set a torque demand, which in turn governed the generated output current of the DFIG.

An outer speed control loop was also implemented, again using a PI controller, to set the  $q$  axis reference current. This allowed for the driving machine to operate in torque control mode, and the DFIG to operate in speed control mode. In this case, the generated output of the DFIG was dependant on the torque reference used to control the driving machine.

The  $d$  axis rotor reference current was fixed at zero. The outputs of the  $d$  and  $q$  axis current controllers were then converted back to three phase reference voltages, and IGBT switching pulses calculated via the naturally sampled

PWM method. These pulses were supplied to the PWM generation units in the FPGA, to produce the IGBT firing signals. Voltage feed forward compensation was also implemented, which took into account the slip frequency of the DFIG improving the current control response for larger values of slip.

DFIG rotor-side PWM voltage source converter was applied in Chapter 4 the GE1.5MW Wind Turbine Generator (WTG) mode, with a torque controller and terminal voltage regulation (GE1.5MW WindVAR) [24]. The experiment test rig does not have the grid-side voltage control function. Therefore, once system islanded in this experiment, the Phase Lock Loop (PLL) which controls the stator side voltage will lose the reference of the grid side voltage, leading to a significant frequency change.

## 5.4 Implementing the Test

The islanding detection experiment circuit set up is shown in Fig.5.13. The simplified experimental structure is depicted in Fig.5.14. The switch S1 is used to create an islanding situation and S2 is applied to change the load during non-islanding condition. The reactance  $L$  (1.3mH) is in series combined with the grid to reduce the grid side harmonic and produce a voltage drop during a non-islanding situation. Once S1 opens, the DFIG will provide power into the load on its own, which means the reference of the PLL will be lost. There is no reference for frequency control, the frequency would vary, therefore, the islanding condition can be tested. The machine will accelerate until it reaches the speed limit and trip. When S2 is opened, which creates a load variation condition (non-islanding), there is also a voltage change at the measurement point, the ROCOF relay will then falsely operate. Therefore, the block function of  $v^2/p$  will be applied to avoid ROCOF relay nuisance tripping.

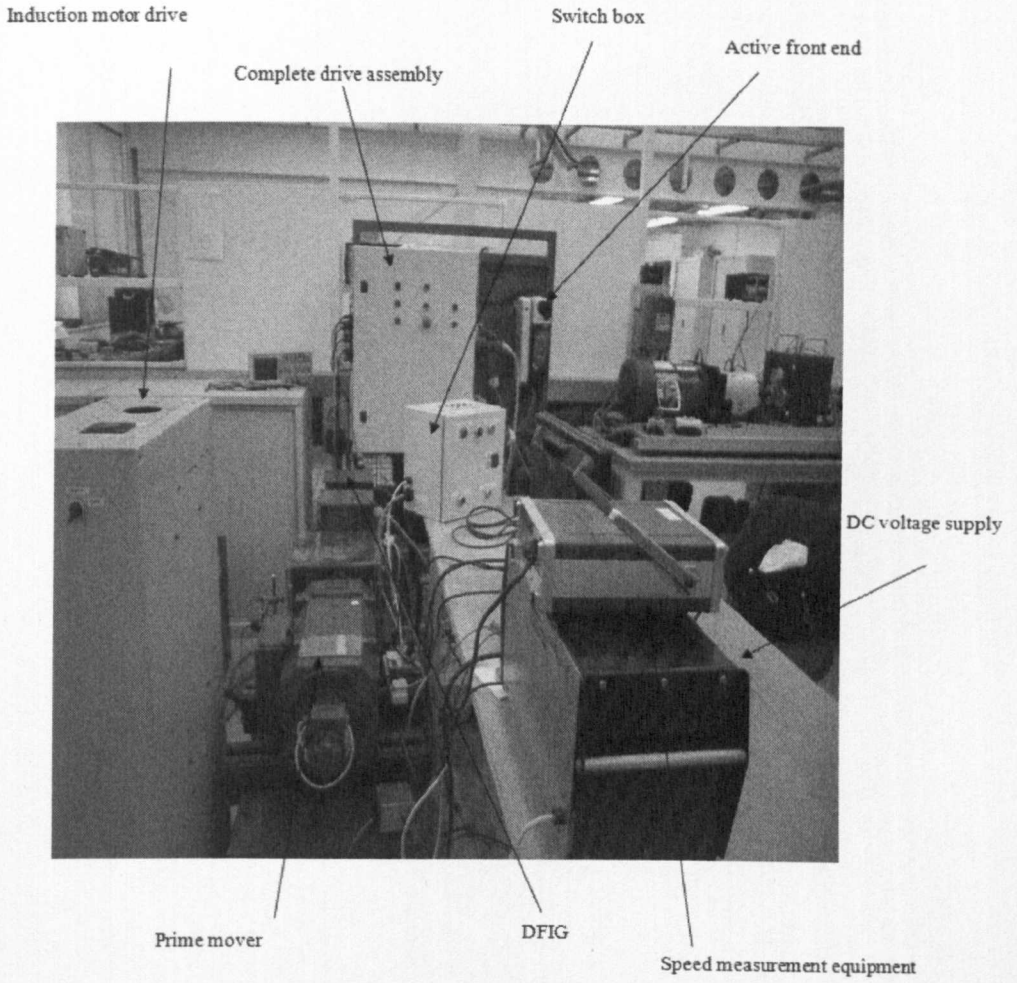


Fig.5.13 Picture of test set up

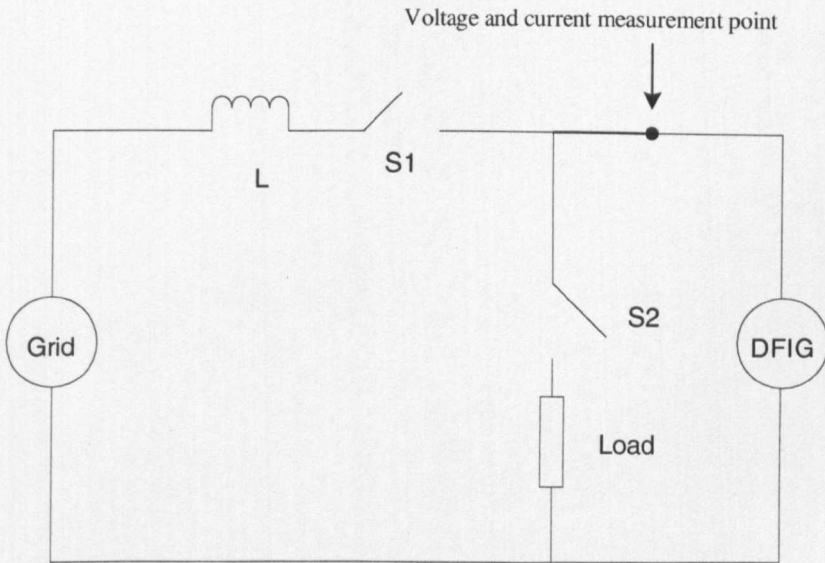


Fig.5.14 Circuit diagram of test set up

## Set up checks

The following checks were made prior to commencing the tests:

1. Set to the torque mode and fix speed limit, i.e. 1400rpm.
2. Ensure the machine can reduce the speed to a set value, i.e. 1200rpm.
3. Ensure variation of drive motor torque changes output power at the DFIG stator.

## 5.5 Test Results

### 5.5.1 Islanding Test Results

#### 5.5.1.1 Results of 3kW Load Islanding Test

The DFIG was connected to the 440V (phase to phase rms) 50Hz main supply and a 3kW (or 2kW for the test of the influence of difference power imbalance on the islanding detection) during the test. For safety reason, the output power of the DFIG is limited to be within 3kW. The generator operation speed is 1200rpm (round per minute).

The first islanding test was carried out with a 2kW DFIG output power. The measured three phase voltages and currents from the Point of Measurement (POM) at the stator side are shown in Fig.5.15.

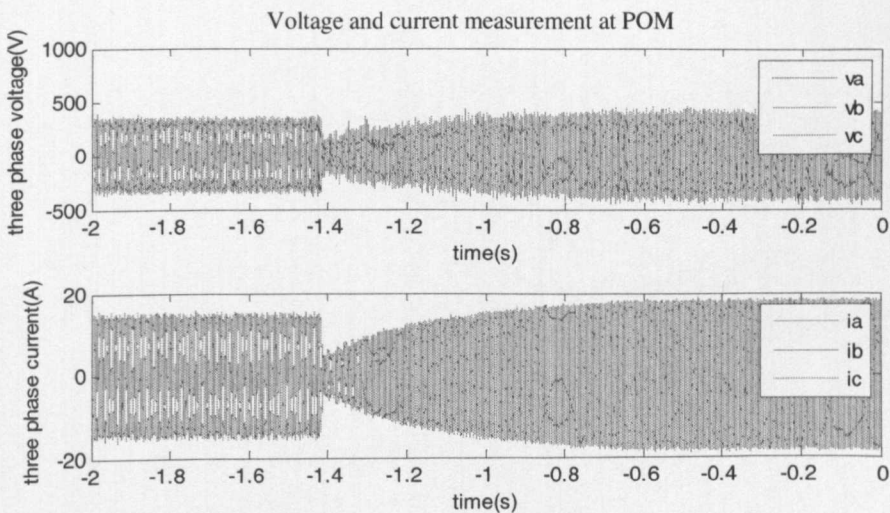


Fig.5.15 The measured three phase voltage and current

The three phase current and voltage data were measured using two oscilloscopes [109], three voltage probes [110] and three current probes [111]. The measured voltage is used for output frequency calculation and the current measurement is involved for estimating the output power and the power information as used during the interlock function which prevents relay miss-operation during large load variations. As shown in Fig.5.15, the islanding takes place at about -1.42s in the time domain (the time data is directly used from the oscilloscope, reference to the triggering signal, there is negative value). Even without analysing, it is easy to find that the output frequency increases after the islanding occurs directly from the waveform of the measured data.

The two oscilloscopes were synchronised with internal triggering signal to make sure the measured voltage and current data are synchronizing with each other. The tested data recording time difference between the two oscilloscopes is about 300ns. This error can be ignored during this test. The Analog to Digital converter (ADC) channel inside the scopes offers 8 bit accuracy the sampling frequency is selected at 40kHz which is enough for the islanding detection. The measured data is then processed with an analogue low pass filter with a cut-off frequency of 400Hz to remove the noise generated by the IGBT converter, the noise is from the main supply and the measurement. The filtered voltage and current data and the calculated amplitude results are shown in Fig.5.16.

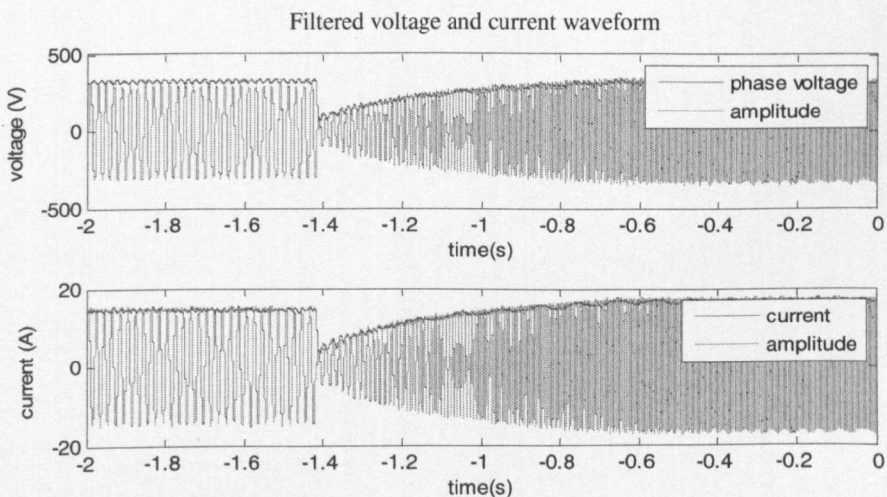


Fig.5.16 Filtered current and voltage calculated amplitude value

Compared with Fig.5.15, the filtered current and voltage data has less noise and the calculated amplitude results match with the measured values. The filtered voltage data is used for the DFIG output frequency estimation using the proposed algorithm given in Chapter 3. The results are shown in Fig.5.17.

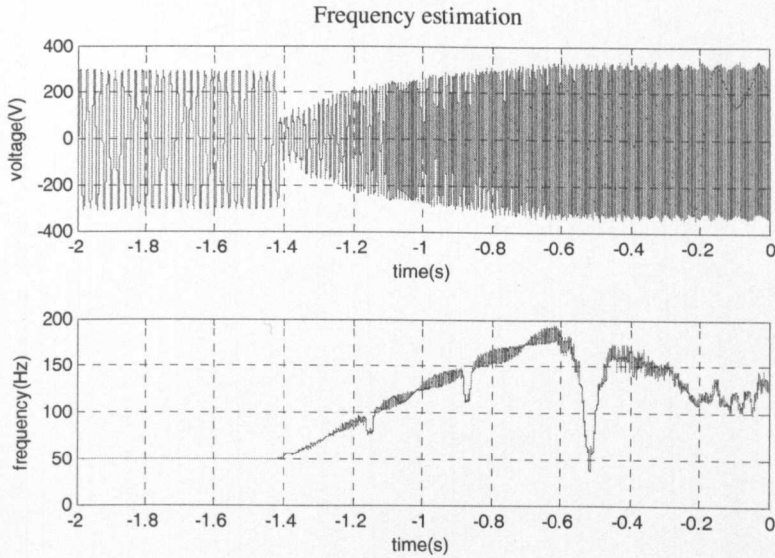


Fig.5.17 The estimated frequency and the voltage waveform

As shown in Fig.5.17, the frequency of the DFIG output voltage increases due to the islanding situation. The DFIG used for experiment test is designed with speed control. During islanding its Phase Lock Loop (PLL) which controls the stator side voltage referred to the d axis loses the reference of the grid side voltage. The output errors from the PLL cause the rotor speed and current to increase which leads to more error in the stator side measured voltage frequency. In this way, the PLL will create a loop and increase the frequency error. Without the speed regulation, the rotor speed will keep on increasing and the motor will stop working when its speed reaches the speed trip limitation (set in the DSP code for motor protection). Fig.5.18 shows the measured rotor speed from the encoder output signal and the rotor side  $i_q$  current results. These results, read from the DSP are over the length of 10 seconds.

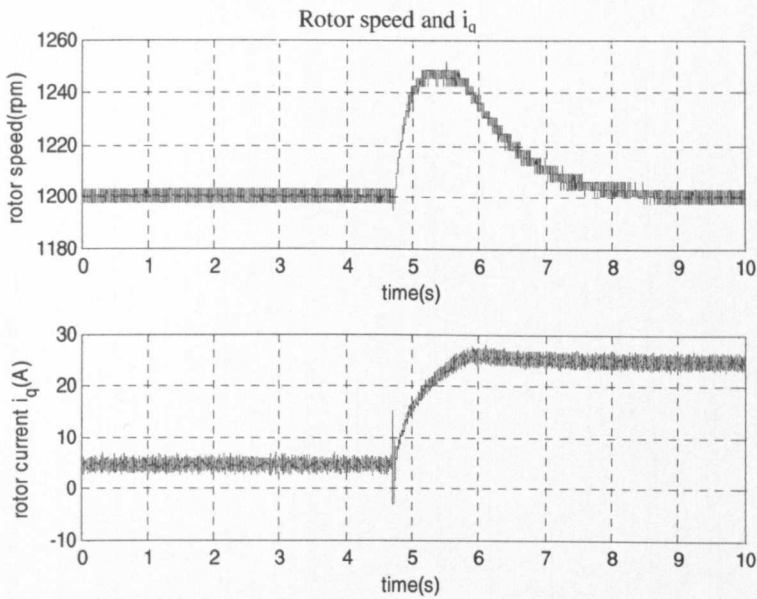


Fig.5.18 Speed and the rotor side  $i_q$  read from the DSP board

As shown in Fig.5.18, the speed control loop in order to control the speed back to the reference value (1200rpm) increases the rotor side current  $i_q$  significantly. The rotor side current  $i_q$  variation will lead to the output power changes. For a ROCOF relay, the islanding situation can be detected very fast.

As shown in Fig.5.19, the value of  $df/dt$  is large enough for the islanding detection. The relay threshold value is set to be 7 so that it can avoid the influence of noise from system and the data acquisition units and also offer very fast islanding detection. As in this test, if the value of  $df/dt$  is continuous larger than 7 for 40 samples (for a sampling frequency of 40kHz, it wait 0.001s) the trip signal will be generated. For this test, the islanding is detected at -1.38s after the DFIG is disconnected from the mains at -1.42s.

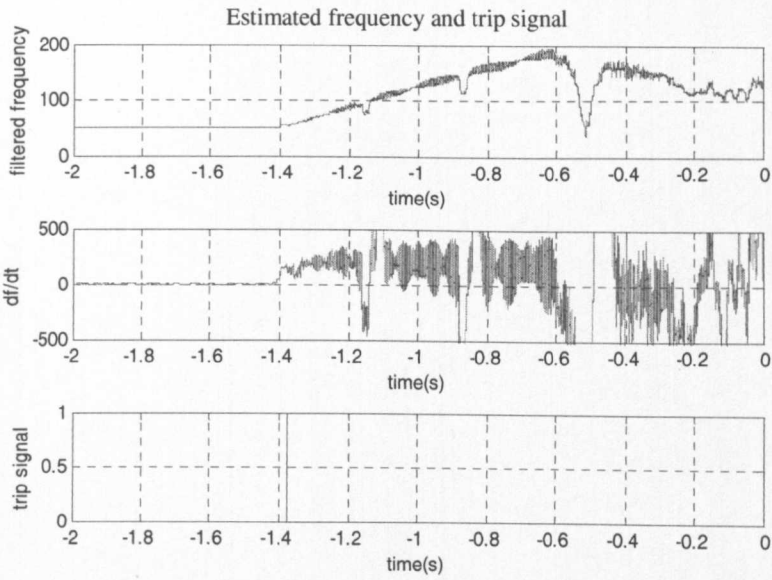


Fig.5.19 The estimated frequency information for islanding with a 3kW load

As mentioned in Chapter 4, the generator output power and voltage is used (value of  $v^2/p$ ) to verified the islanding situation. The measured line voltage (rms value), output power and system impedance are shown in Fig.5.20.

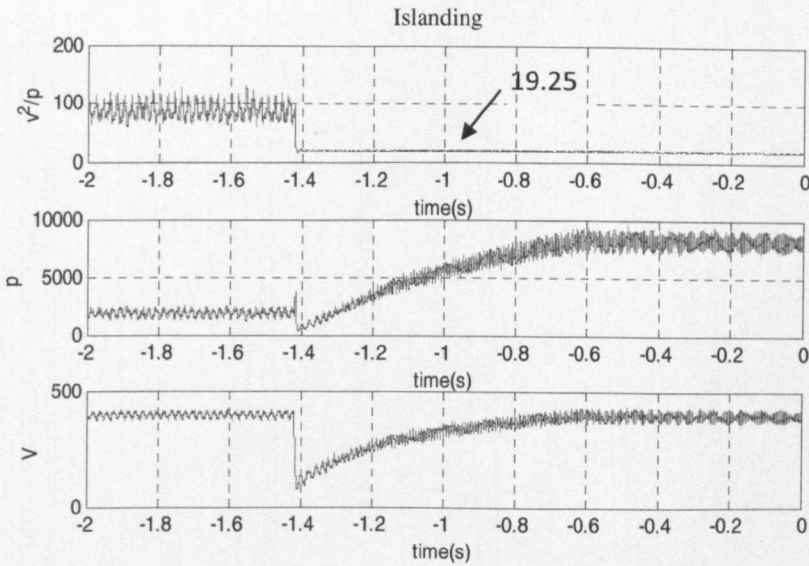


Fig.5.20 System impedance estimation

Fig.5.20 gives a view of how the apparent system impedance varies (looking from the point of measurement) when the generator is disconnected from the mains. As described previously, when islanding happens, the speed control loop forces the  $i_q$  current increases to control the speed back to the reference

value. This increased  $i_q$  is reflected in the calculated stator side output power, as shown in the Fig.5.20, the power increases significantly after islanding. The voltage amplitude reduces initially and then increases back to about rated value. Obviously, it is difficult to verify the islanding just by monitoring the voltage amplitude (conventional interlock function) as a reference to verify. The system impedance (the value of  $v^2/p$ ), once the system variation is finished, will not change any more. Meanwhile the impedance variation before and after islanding is large enough to be distinguished as shown in the Fig.5.20.

The impedance estimation accuracy can be proved using the value after the islanding occurs. The 3kW load is a resistive load bank which consists of three 1kW load which have a value of  $57\Omega$  (as labelled) and star connected. The total load resistance is about  $19\Omega$ . As shown Fig.5.20 the value of  $v^2/p$  after islanding is about  $19.25\Omega$ . This error is mostly caused by the cable impedance, measurement offset and the load resistor itself (the resistance of each load is not exactly  $57\Omega$  as labelled).

### 5.5.1.2 Results of 2kW Load Islanding Test

With the same power output setting of 1kW, another islanding test was carried out with a 2kW load. The measured frequency, the rate of change of frequency and the tripping signal information is shown as in Fig.5.21.

Fig.5.21 and Fig.5.19 (results of 3kW load test) are plotted with the same scale range. The differences between the two figures are obvious. Both the frequency and the ROCOF results of the 3kW load test changes faster than the results of the 2kW load test due to a larger power imbalance. Although the stator side frequency loses its reference and becomes out of control, the frequency error is still proportional to the system power imbalance. Using the same ROCOF setting as in the first test, the islanding detection time is 22ms slower.

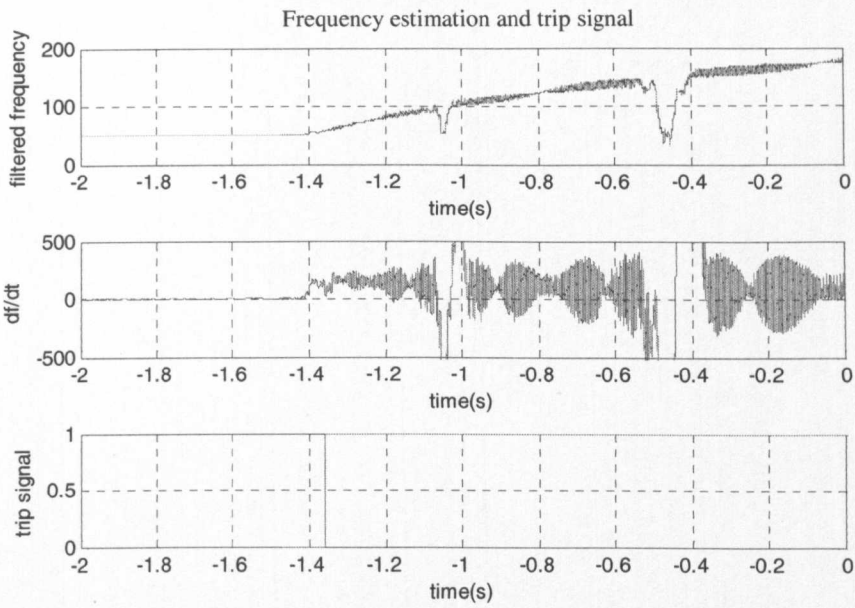


Fig.5.21 The estimated frequency information for system islanded with a 2kW load

The measured power and system impedance values changes for islanding situation as shown in Fig.5.22.

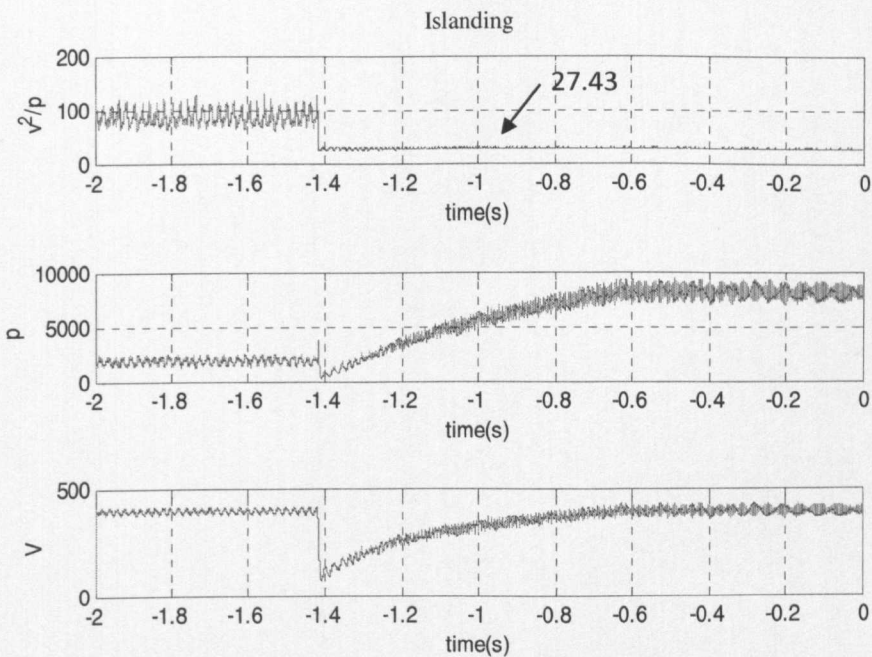


Fig.5.22 Impedance estimation results of system islanded with 2kW load test

The system impedance value, after islanding occurs, increase to  $27.43\Omega$  compared with the results shown in Fig.5.20 ( $19.25\Omega$ ) due to different load impedances. For systems with different load regulation, the estimated system

impedance given after islanding varies. This variation is small compared with the larger impedance difference before and after islanding. By selecting an impedance threshold value which is higher than the largest possible load impedance, the islanding detection provided by the rate of change of frequency results can be verified. In the same way, a load changing which may also be detected by the ROCOF can be blocked from sending tripping signal to the relay.

## 5.5.2 Load Variation Test Results

### 5.5.2.1 Results of 3kW Load Variation Test

For a load variation test, the DFIG is always connected to the grid and different loads are added to or removed from the grid. The DFIG output power is 2kW (same as in the islanding test). In the first load variation test, a 3kW load is connected to the system with the system initially running at a no local load situation (DFIG is directly connected to the grid). The measured voltage and its frequency data are shown in Fig.5.23.

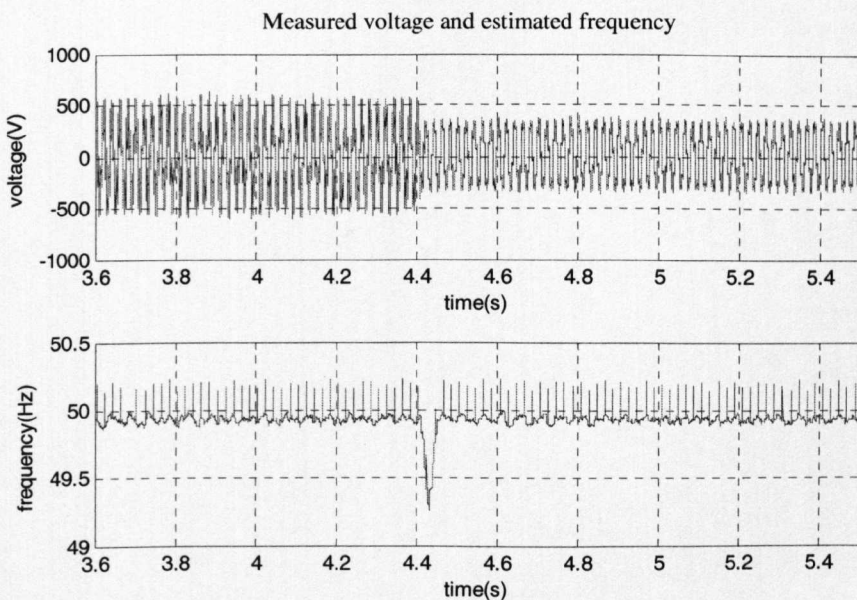


Fig.5.23 Measured voltage and frequency after a 3kW load added to system

As shown in Fig.5.23, after the load is connected to the system at about 4.4s, the voltage harmonic noise is attenuated (the actual voltage amplitude is not

changed very much) and there is a frequency dip within the measured frequency results. The frequency changes can be detected by the ROCOF algorithm and the relay can be tripped if the tripping signal is not blocked as shown in Fig5.24.

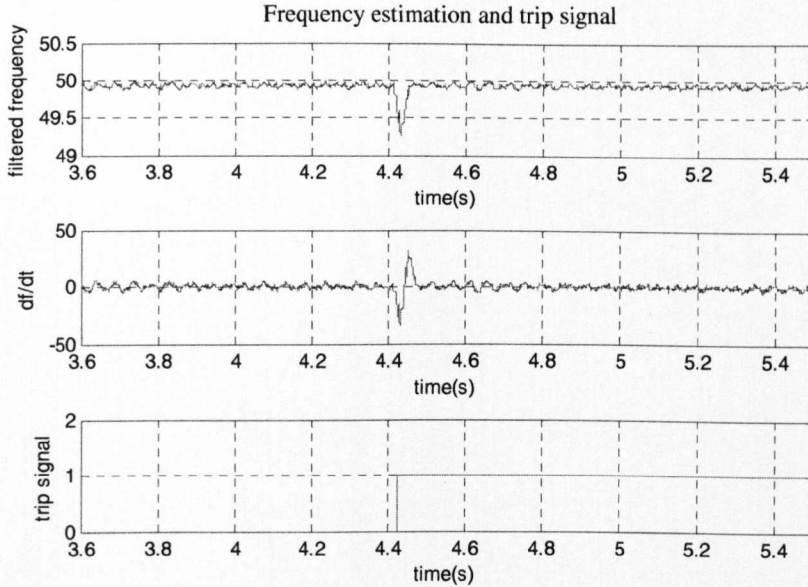


Fig.5.24 The ROCOF results of a 3kW load added to the system

As mentioned in Section 5.5.1.1, the ROCOF relay setting is chosen to be 7 and if the measured value is larger than it for a continuous 40 samples, the relay tripping signal will be sent as shown in Fig.5.24. However, using the result of  $v^2/p$  and set a threshold value to be 62 which is larger than the than the largest possible load impedance in this system ( $57\Omega$  for a 1kW load), the tripping signal can be blocked.

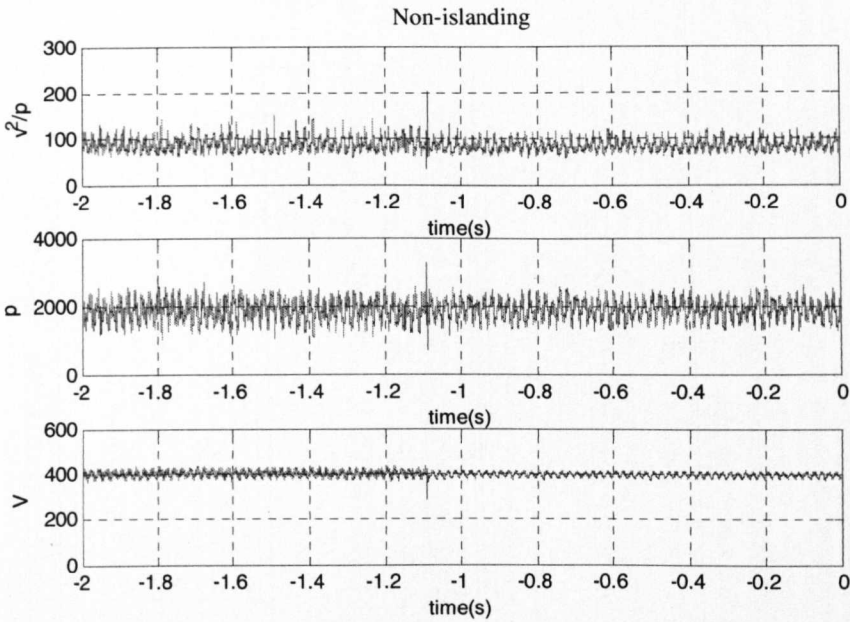


Fig.5.25 The output power and voltage of a 3kW load added to the system

As shown in Fig.5.25, the output power and voltage is not influenced by the 3kW load variation. There is a small ‘spike’ in the waveforms during the load adding. Due to the fact that the ‘spike’ has a very short duration in time domain and has lowest value of 64 in the waveform of  $v^2/p$ . If the value of  $v^2/p$  is lower than the set threshold value 62 for a continuous 40 sample, the block signal will not be sent. In a load changing situation, this will not happen for either adding or reducing load.

### 5.5.2.2 Results of 1kW Load variation test

The load shedding test was carried out with a 1kW load disconnected from the system. After the load is disconnected, the DFIG is directly connected to the mains. And the measured voltage, frequency, the result of ROCOF and relay tripping signal are presented in Fig.5.26 and Fig5.27.

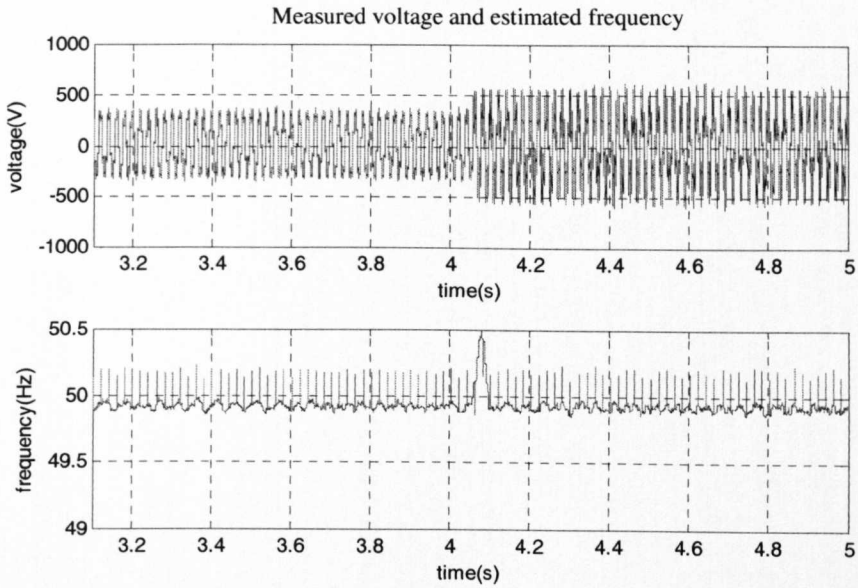


Fig.5.26 The voltage and frequency results for a 1kW load shedding

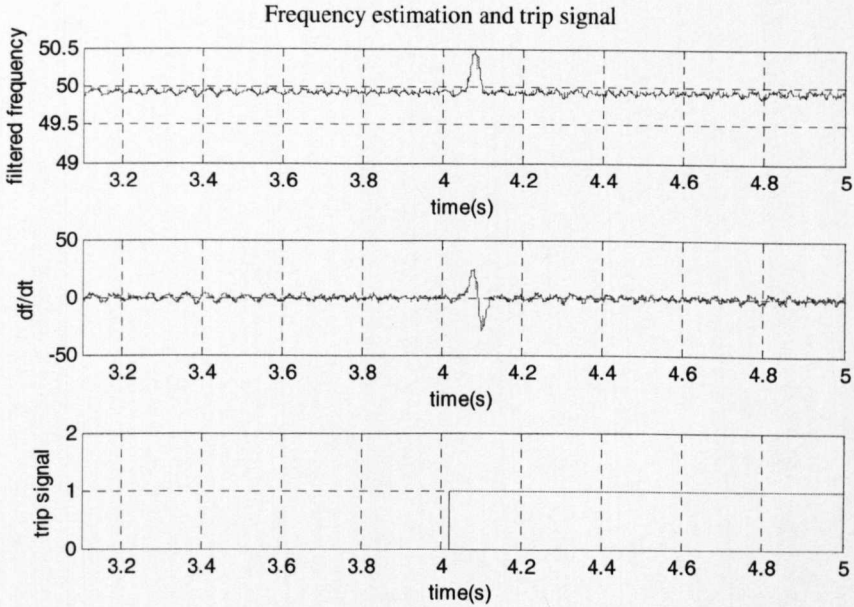


Fig.5.27 The ROCOF and trip signal results for a 1kW load shedding

Although with a smaller load variation, the ROCOF can still detect the frequency difference within the measured voltage and send tripping signal to relay. Comparing Fig.5.24 and Fig.5.27 with the load adding results, the frequency variation is smaller for the 1kW load changing. As in Fig.5.24 the largest  $df/dt$  error is about 27 and in Fig.5.27 the error is about 36. This shows that the error of the  $df/dt$  increases with the value of load variation. It is not able to avoid miss-tripping, by simply increase the setting threshold of ROCOF

relay to certain value due to the effect of the load variations within a power system is not predictable.

Similar to the  $v^2/p$  results derived from the 3kW load adding test, the load shedding test offers a constant results in the estimated system power, voltage and impedance waveform as shown in Fig5.28.

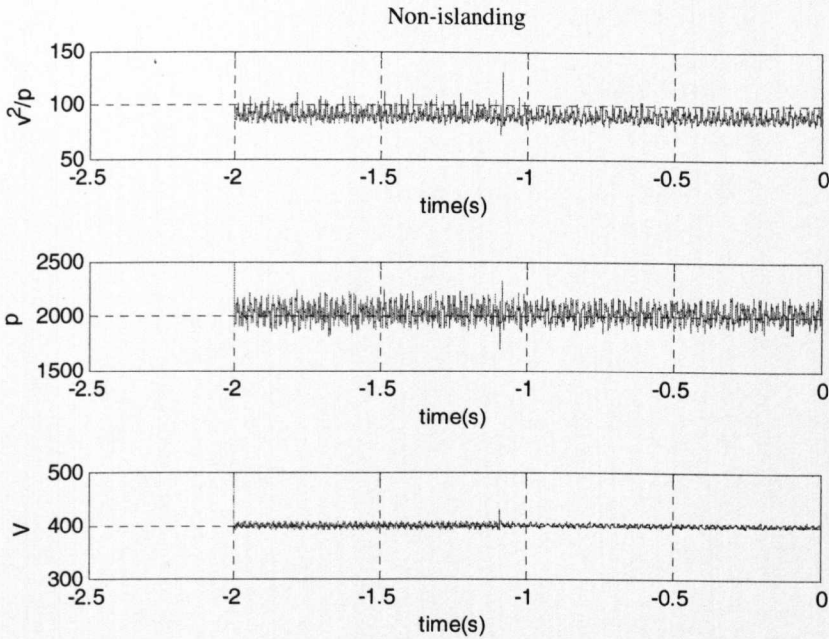


Fig.5.28 The output power and voltage of a 1kW load adding situation

## 5.6 Summary

The DFIG islanding detection experiment is demonstrated in this chapter. The experimental prototype consists of the rotor converter, with grid interface active front end, along with the Doubly Fed Induction Generator (DFIG) and the switch box. The islanding and non-islanding situations are created by controlling the switch box which is able to connect and disconnect the main power and load from the DFIG. System islanding and non-islanding conditions with different power imbalance between generation and the load (1kw,2kw,3kw) are implemented. The experiment results showed that the rate of frequency variation is smaller with smaller load for the islanding situation. This leads to a longer detection time compared with islanding with a larger power imbalance.

The load impedance calculated by  $v^2/p$  interlock function is close to the actual local load when islanding with small error caused by the cable impedance, measurement offset and the load resistor itself. Both islanding and load changing test shows that by involving the measured power, the value of  $v^2/p$  can be used as an inter lock reference to prevent the miss-tripping of ROCOF relays caused by load variation.

## **Chapter 6**

# **Islanding Detection Method for Microgrid**

### **6.1 Introduction**

Microgrids are part of the modern trend towards decentralised management of energy production through distributed generation. A microgrid (MG) is a low voltage coordinated assemblage of modular generator systems, loads and energy storage devices [112-115]. There is normally one master unit responsible for maintaining the voltage and frequency which could be a generator unit or it can be the point of connection to the wider network. There could also be a range of supporting power units under the control of the master unit. The rest of the system is composed of loads and uncontrollable generators (e.g. wind energy). MG generators have a power rating in the range of a few kW to a hundred kW. Typical MG generators are fuel cells, wind turbines, photo-voltaic systems, combined heat and power systems, photo-voltaic systems, and diesel gensets as Fig.6.1 shown.

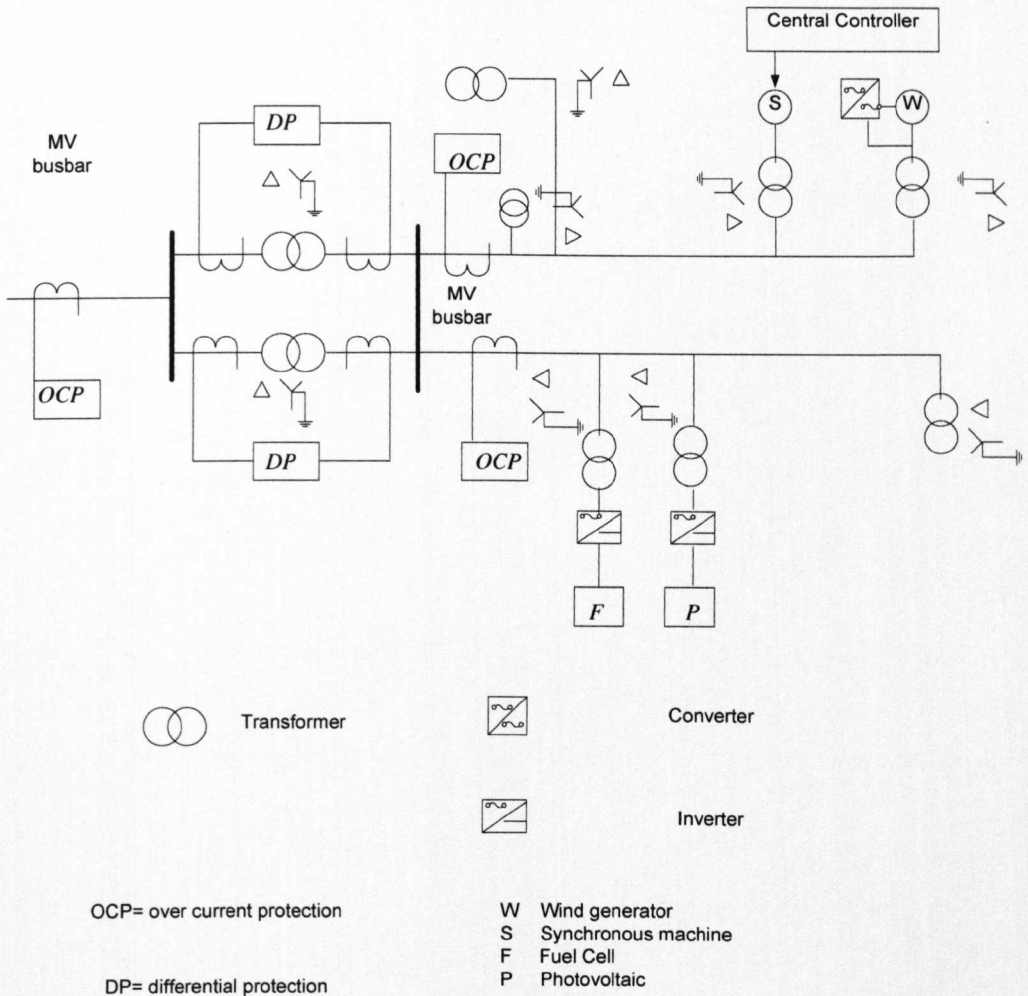


Fig.6.1 The structure of microgrid [116]

The MG can be interconnected as a controllable element of the power network, or it can be an emergency back up system when a power outage occurs or a completely autonomous or islanded unit. But if the MG is not interconnected with appropriate control, in the case of loss of grid, present technical recommendations specify that the microsources allocated in the microgrid must be disconnected as soon as possible [112-113]. Islanding of MG can take place by unplanned events like faults in the main grid or by planned actions like maintenance requirements [113, 117]. The fact that in islanded mode the microsources would not be controlled by the utility grid, could lead to operation beyond the grid requirements, which could prove hazardous, not only for the utility equipment, but also for personnel.

This chapter introduces the grid-forming inverter modelling for a simple photovoltaic system. The islanding detection for the microgrid which consists of synchronous generator, photovoltaic system, and DFIG wind turbine is demonstrated. The ROCOF relays with  $v^2/p$  interlock function applied for the grid-connected microgrid to avoid false tripping during system load variation are also investigated in two cases of different proportion of synchronous generator, photovoltaic system, and DFIG wind turbine generation during the islanding and non-islanding situations. The effectiveness of the ROCOF relays cooperating with  $v^2/p$  interlock function is also discussed.

## 6.2 Islanding Detection for Grid-connected PV System

### 6.2.1 Effects of Islanding for Grid-connected PV system

Photovoltaic (PV) technique is gaining more and more visibility due to many national incentives [118]. With a continuous reduction in system costs (solar panels, dc/ac converters, cables), the PV technology has the prospect to play an important role towards a sustainable energy system. Power electronics is used to efficiently interface renewable energy systems with the grid. The purpose is to convert the clean energy into electrical energy with the highest possible efficiency and the lowest cost. The use of photovoltaic distributed power generation systems requires the compliance with standards whose important issues are harmonic level in the grid current and islanding detection.

Islanding is a potential dangerous mode of operation of a grid-connected PV inverter [118]. Islanding is here defined as a continued operation of a grid connected inverter when the utility grid has been switched off or the distribution lines have been damaged so that no electric energy is delivered by the utility to the load [119]. Islanding is a very dangerous condition because two conditions can no longer guaranteed [119]:

1. Safety of persons : if the utility grid is switched off , line workers can suppose that lines are no longer energized and do not use common safety measures with consequence of electrical shock (direct effect) or

falling of the worker from the working platform after touching an energized line (indirect effect).

2. Safety of equipments: voltage amplitude and frequency provided to customers connected to the utility grid are usually controlled to be in a specific range; when islanding occurs voltage amplitude and frequency are no longer controlled by the grid and their fluctuation might damage or destroy customer's equipments.

Because of the grave consequences that could follow if islanding is not detected, islanding detection is an indispensable feature for photovoltaic distributed generation system. Many islanding detection methods have been developed for grid-connected PV systems; these methods can be divided into four categories [55, 118]:

1. Passive inverter-resident methods, which are based on the monitoring of the voltage at the point of common coupling (PCC) and the detection of its disturbances;
2. Active inverter-resident methods, which deliberately cause a disturbance on the PCC voltage;
3. Active methods not resident in the inverter, which work similar to the previous methods but the perturbation is produced from the utility side of the PCC.
4. Communication-based methods which involve the transmission of data between the inverter and the grid.

In this chapter passive method based on the monitoring of the voltage at the PCC of calculating the  $df/dt$  and combining with the  $v^2/p$  is applied to detect loss of main condition.

### **6.2.1 Grid-Connected Inverter Modelling**

The grid-connected inverter model used in this chapter is grid-forming inverter which can be used for both grid-connected system and stand-alone operation. As their name indicates, they form the grid by enforcing a certain voltage and

frequency. Fig. 6.2 shows the basic control scheme of a three-phase grid-forming inverter. The scheme consists of a primary output current control loop and a secondary output voltage control loop. By applying the Park transformation with a transformation angle  $\theta$  synchronous with the system frequency, both current and voltage are transformed to dc values in the dq domain, enabling straightforward control by using proportional integral controllers. In the scheme of Fig.6.2, the quadrature component of the voltage  $u_q$  equals the amplitude of the voltage. Also, if  $u_q$  is equal to zero, the direct and quadrature components of the current  $i_d$  and  $i_q$  become equal to the active and reactive current components, respectively.

Whereas the control scheme of Fig.6.2 is focused on a three-phase inverter, a similar scheme is applicable to single-phase grid-forming inverters. Most often, these inverters are controlled in the stationary reference frame, rather than the rotating reference.

The PI controller for inner current control loop is found through the pole-placement method which is described in Chapter4. The plant of the inner current control loop is  $1/(L_g s + R_g)$ .  $R_g$  and  $L_g$  are the line resistance and reactance respectively as shown in Fig.6.2.

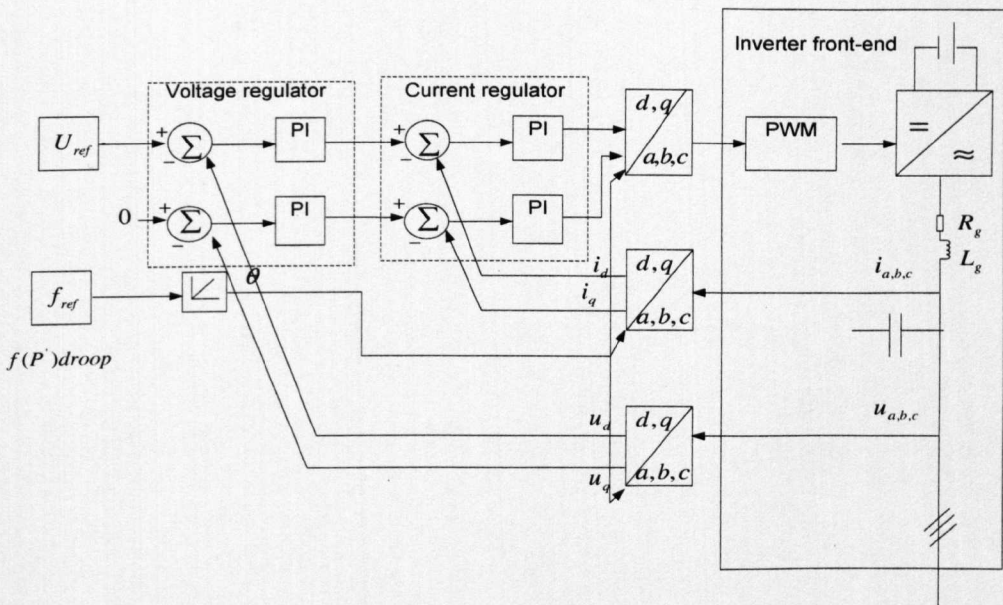


Fig.6.2 Basic control scheme of a grid-forming inverter

## 6.3 Simulation results

### 6.3.1 Case One

The grid-connected microgrid test system considered is shown in Fig.6.3. It comprises a 120kV, 50Hz, which feeds a 25kV distribution system through a 120/25kV  $\Delta/Y_g$  transformer. In this system there is one 4.5MW DFIG wind turbine generator connected at bus 5, which is connected to the network through one 25/0.575kV  $\Delta/Y_g$  transformer. A 1.5MW PV system and 1MW synchronous generator are also connected at bus 5, which constitutes the microgrid system, in all simulated cases, the circuit breaker CB1 at bus 2 opens at 5s which creates an islanding situation, and remains open during the rest of the simulation as is shown in Fig.6.3. Therefore, the initial active power imbalance in the islanded system is equal to the active power provided by the substation at the islanding moment. The non-islanding situation as depicted in Fig.6.3 is created by keeping the circuit breaker CB1 closing at bus 2, and using the circuit breaker CB2 at bus 3 for switching off the 6MW load. The ROCOF relays with an interlock function are applied for three of the systems separately, and the  $v^2/p$  interlock functions is utilized to cooperate with the ROCOF relays, the performances of each interlock function will be discussed below. The total simulation time is 10s for all of the scenarios. The frequency estimation method for ROCOF relay setting is based on the Fast Fourier Transforms (FFT) method as described in Chapter 3.

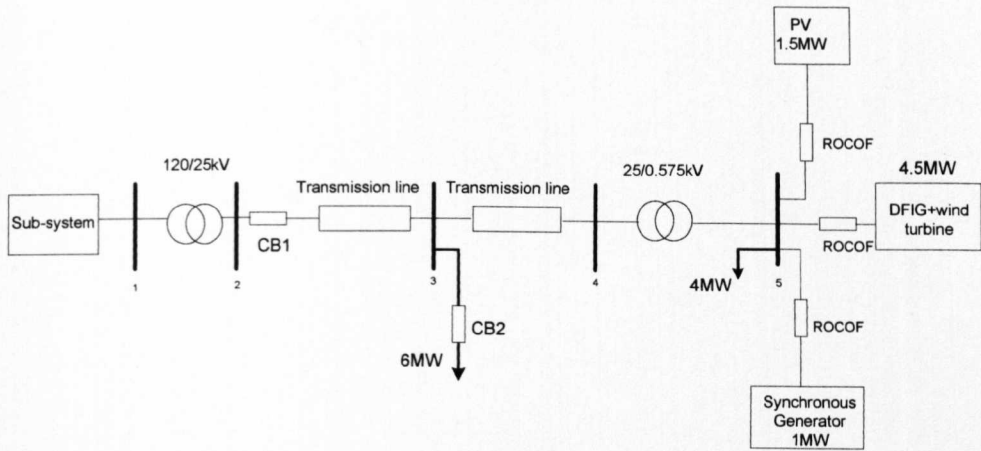


Fig.6.3 The grid-connected microgrid islanding test system

The simulation results of islanding for the DFIG wind generator, photovoltaic system and synchronous generator of the microgrid are shown in Fig.6.4, Fig.6.5 and Fig.6.6 separately.

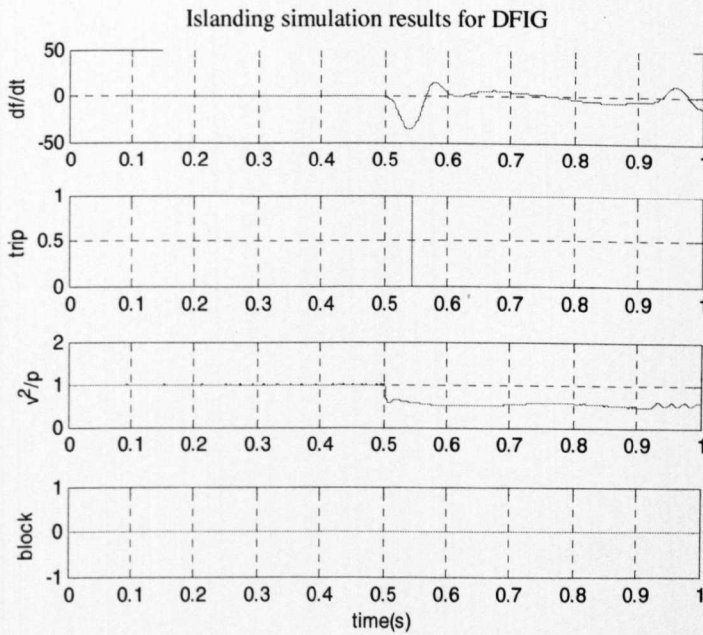


Fig.6.4 The islanding situation performance for DFIG ROCOF relay

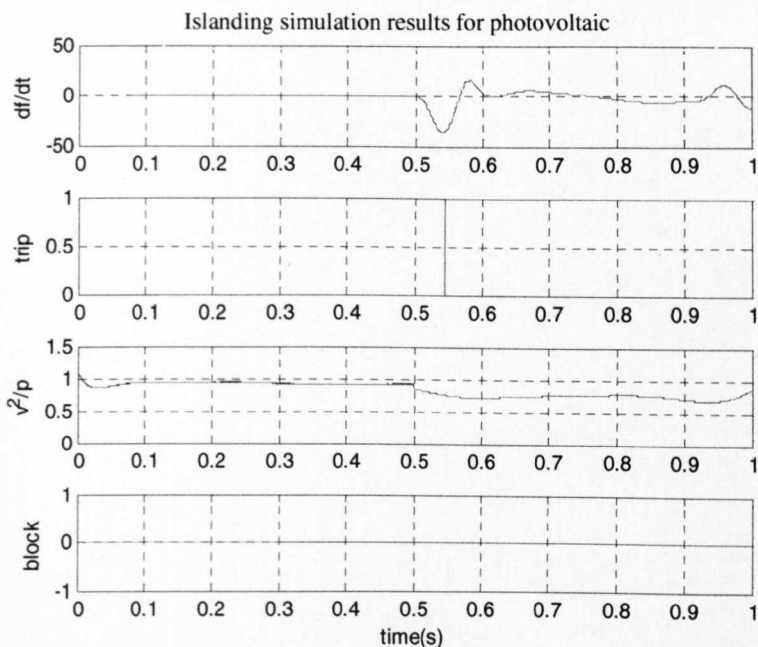


Fig.6.5 The islanding situation performance for photovoltaic system ROCOF relay

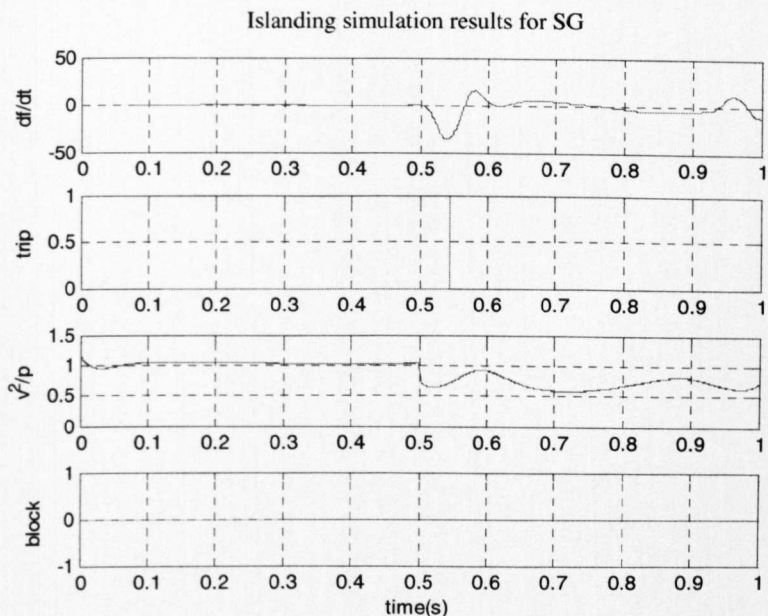


Fig.6.6 The islanding situation performance for synchronous generator ROCOF relay

The estimated rate of change of frequency of these three generators is calculated from the same common coupling point, therefore, the tripping time of these three ROCOF relays are the same (58ms after islanding occurs). The interlock function, involving the value of  $v^2/p$  does not send the block signals

during islanding as shown in the figures. The simulation results of non-islanding for DFIG wind generator, photovoltaic system and synchronous generator of the micro-grid are shown in Fig.6.7, Fig.6.8 and Fig.6.9 separately.

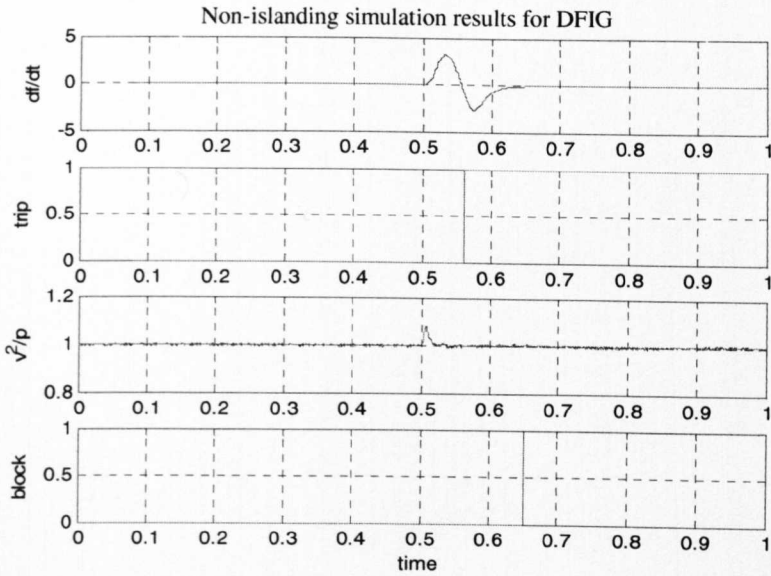


Fig.6.7 The non-islanding situation performance for DFIG ROCOF relay

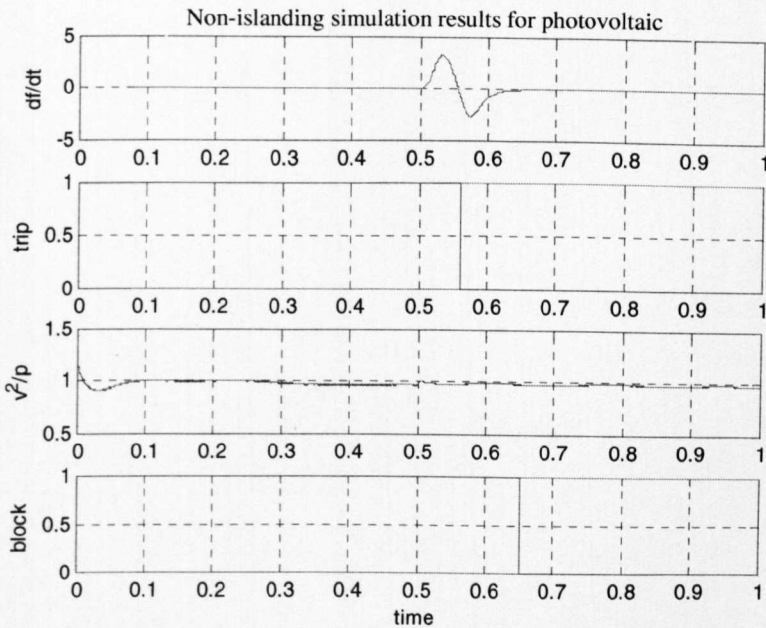


Fig.6.8 The non-islanding situation performance for photovoltaic system ROCOF relay

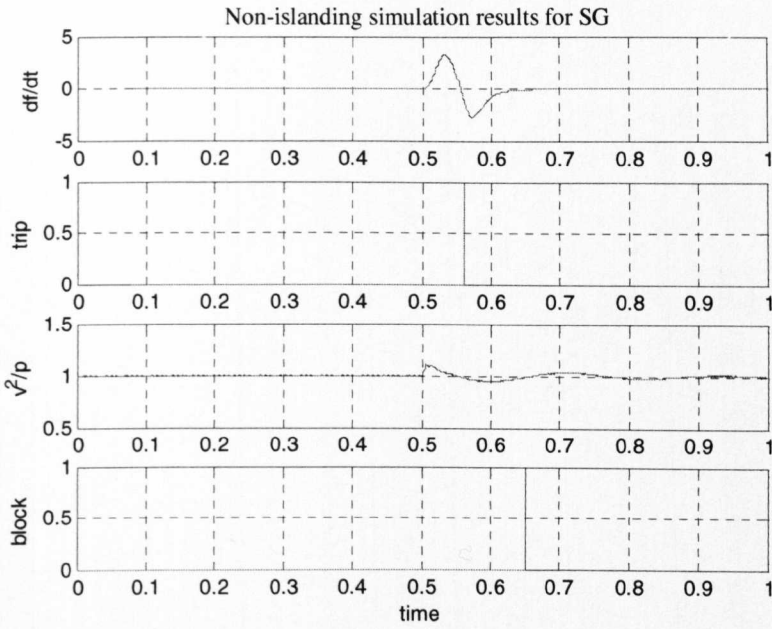


Fig.6.9 The non-islanding situation performance for synchronous generator ROCOF relay

Based on this study, during the system non-islanding situation, if there is a 6MW load shedding from the system at 5s, the rate of change of frequency will have a transient condition which would create a tripping signal to these three generators' circuit breakers, the  $v^2/p$  interlock function is used to generate the block signal to avoid the relay miss-operation. The non-islanding situation can be blocked at 149.8ms after load variation.

In order to evaluate the non-detection zone (NDZ), such as the locus of operating points where the islanding is not detected, the proposed method has been tested for different load levels between the total microgrid generation power and the load demand. The results are presented in Table 6.1.

Table 6.1 Evaluation of the non-detection zone

Active power mismatch(Islanding)	$\Delta p = 5\%$	$\Delta p = 10\%$	$\Delta p = 15\%$
DFIG( $df/dt + v^2/p$ )	No trip	Trip	Trip
PV( $df/dt + v^2/p$ )	No trip	Trip	Trip
SG( $df/dt + v^2/p$ )	No trip	No trip	Trip

During the small system power imbalance, in order to avoid system disturbances affecting the ROCOF and causing nuisance tripping, the ROCOF relay setting can not be too small which will provide a non-detection zone, meanwhile, in the situation of system small power imbalance the value of  $v^2/p$  will decrease but with an oscillation, this will also cause the block signal tripping. If the power imbalance is greater than 15%, ROCOF relay with  $v^2/p$  interlock function applied in the three generation systems will effectively trip during islanding situation.

In the non-islanding situation (system load variation), when the power imbalance is smaller than 40% , the ROCOF relay will not operate. Systems with a large load change ( $\Delta p > 40\%$ ), the  $v^2/p$  interlock function will block the ROCOF tripping signal accurately and fast.

### 6.3.2 Case Two

Similar work has been done for the case of 4.5MW photovoltaic system, 1.5MW DFIG wind generator, and 1MW synchronous generator, the simulation results are in appendix C. The simulation results for case two are similar as case one, the ROCOF relays with  $v^2/p$  interlock function are well performance in non-islanding situation and islanding situation with the power imbalance greater than 10%, however, due to the photovoltaic system which is frequency and voltage controlled provides the main power in the microgrid in case two, the ROCOF relay tripping time is longer than the other two cases with the same power imbalance between the generation and load demand.

## 6.4 Summary

The potential hazardous of loss of grid for the microgrid and photovoltaic system are introduced, once the system has islanded, the present technical recommendations specify that the microsources allocated in the microgrid

must be disconnected as soon as possible. In this chapter, the grid-forming photovoltaic system modelling is investigated. Islanding and non-islanding situations for grid-connected microgrid are demonstrated. Simulation results of islanding detection for microgrid which includes photovoltaic system, synchronous generator and DFIG wind turbine are investigated. In the two cases of different generation portion of synchronous generator, photovoltaic system, and DFIG wind turbine, for both islanding and non-islanding situations, the effectiveness of ROCOF relays with  $v^2/p$  is discussed. The grid-connected inverter model is voltage and frequency controlled, with a larger portion generation in the microgrid, once the system has islanded, the detection time would be increased.

## **Chapter 7**

# **Impedance Estimation and Total Harmonic Distortion Methods for Islanding Detection**

### **7.1 Introduction**

The main philosophy for detecting an islanding situation is to monitor the distributed generator output parameters or system parameters and decide whether or not an islanding situation has occurred from a change in these parameters. As mentioned in Chapter 2 islanding detection techniques can be divided into passive methods, active methods and remote methods. In this chapter, the principle of active impedance estimation method is introduced as an active method. It is implemented to detect an islanding situation and distinguish it from a non-islanding situation (system load variation). Then the Total Harmonic Distortion method which is a passive method for islanding detection is also investigated. Most of the passive islanding detection methods can not distinguish the islanding and system load variation situations by

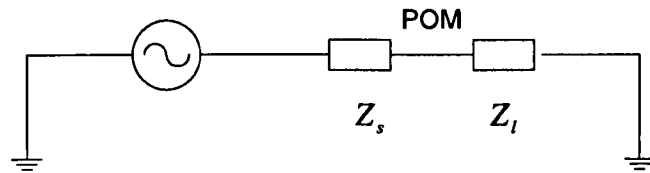
themselves. Therefore, the performance of this method in cooperation with ROCOF relays is investigated. Finally, a comparison of the impedance estimation method and the Total Harmonic Distortion method is discussed.

## **7.2 Impedance Estimation Method for Islanding Detection**

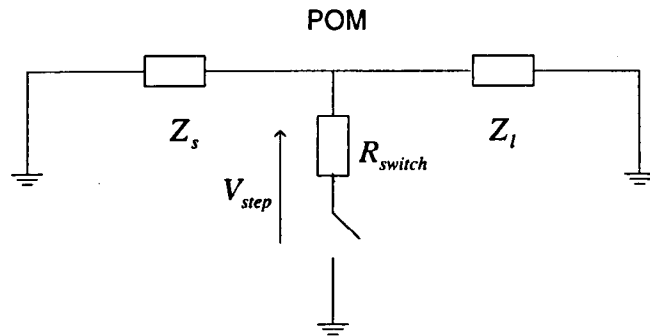
Active methods for detecting the island act by introducing deliberate changes or disturbances to the connected circuit and then monitoring the response to determine if the utility grid, considered as an infinite bus, with its stable frequency, voltage and impedance is still connected. The small perturbation must affect the parameters of the load within prescribed requirements when applying active methods, in the case when system islanded situation can be detected. Some of the active techniques are, methods based on frequency and phase shift techniques [120-123], methods based on reactive power injection [124-125], methods based on positive feedback and methods based on current injection [126-128]. These methods are widely applied because the DG is normally connected to the grid via an inverter which makes it easier to inject any kind of disturbance and are highly effective even if there is a close mismatch between the generated power and the size of the load. These can detect the islanding but the disadvantages of these methods are that they decrease the power quality of the system and are not as fast as the passive counterparts.

### **7.2.1 Transient Injection Principle**

According to the Thevenin's theory, any single phase linear system can be simplified to an equivalent circuit as given in Fig.7.1. The voltage source AC is an ideal sinusoidal source of frequency  $f_0$ .  $Z_s$  is a Thevenin equivalent source impedance of the network seen from the Point of Measurement(POM).  $Z_l$  is a Thevenin equivalent load impedance of several loads connected at POM.



a) At Supply Frequency



b) At Other Frequency

Fig.7.1 Thevenin Equivalent Circuit

The active estimation technique introduced here estimates the system harmonic impedance by causing a voltage transient at the POM, as shown in Fig.7.1 b). Since a Thevenin voltage source can be treated as a short circuit at the frequencies other than its supply frequency, the system shown in Fig.7.1 a) is as in Fig.7.1 b) at harmonic frequencies.

If the corresponding voltage potential at the POM and the current flowing through it are measured, then the system impedance can be determined by Ohm's law. Since the impedance values  $Z_f$  also have frequency-dependent characteristics, the calculation can be implemented in the frequency domain using a frequency domain analysis tool and using the measured voltage " $V_f$ " and current " $I_f$ " to give:

$$Z_f = \frac{V_f}{I_f} \quad (7.1)$$

The subscript  $f$  in (7.1) refers to the value at a specific frequency. In this way, the system's harmonic impedances can be estimated.

When a system is at steady state and there are no non-linear components, the voltages and currents will not contain any components at frequencies other than the supply frequency if all conditions are ideal. The key point for the harmonic impedance measurement is that the voltage transient injected at POM should contain components with enough energy to produce measurable changes over a wide frequency range of interests. Also for the requirement of “online measurement”, the amplitude and the time of the voltage and current transients should be short enough so that it does not affect the normal operation of the system.

The required voltage transient can be generated by a very short voltage transient via a switch resistance, as shown in Fig.7.2 the trigger signal can be fully adjusted to give the transient voltage source a voltage output of any shape and duration demanded.

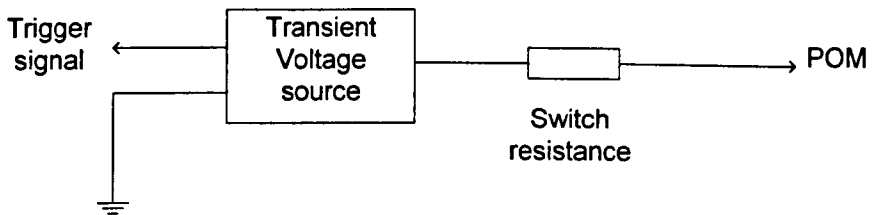


Fig.7.2 Transient injection scheme

Because the system is in normal operation in the online scheme, in order to obtain measurements of just the pure transient response, measurements of voltage and current have to be processed with a Blackman window to smooth out the edges of the recorded data and avoid effects in the frequency domain [129].

$$Z_f = \frac{\Delta V_f}{\Delta I_f} = \frac{V_{measured} \times W_n}{I_{measured} \times W_n} \quad (7.2)$$

where  $V_{measured}$  and  $I_{measured}$  are the voltages captured directly from the POM.  $\Delta V_f$  and  $\Delta I_f$  are the voltage and current after being processed with a Blackman window in the time domain with response  $W_n$ .

The algorithm of the ‘Blackman’ for a N sample data window is:

$$W_n = 0.42 - 0.5 \cos \frac{2\pi n}{N-1} + 0.08 \cos \frac{4\pi n}{N-1} \quad (7.3)$$

Based on the equivalent circuit in Fig.7.1 b), when the DG is islanded the measured system impedance at a DG terminal is much larger than that when the DG is connected in parallel to the grid. The reason is that the utility impedance is typically much smaller than the impedance of the DG. Therefore, an increase in system impedance measured at the DG terminals, to a value much higher than that under DG normal operation, is used as a criterion to determine DG status. If an island forms, a signal will be sent to trip the DG [130-131].

### 7.2.2 Single Phase System Studied

Fig.7.3 is a single phase RL circuit built in the Matlab/Simulink simulation environment to demonstrate the transient injection method discussed above and the islanding behaviour.

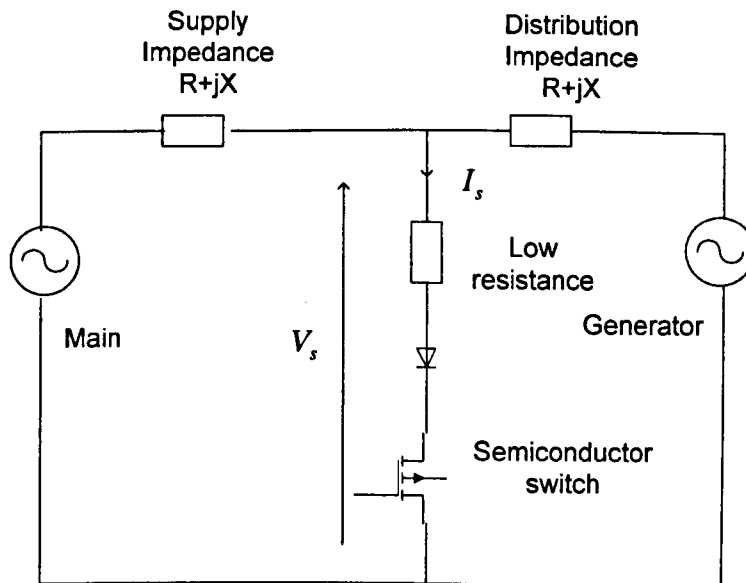


Fig.7.3 Source impedance measurement circuit

As shown in Fig.7.3, the generator and mains are simplified by voltage sources. The supply impedance for a strong mains and a weak mains is the same. The

distribution network impedance consists of generator impedance and the transformer impedance.

The parameters of the example system depicted in Fig.7.3 , where the circuit breaker opens to create an islanding situation, is provided in Table7.1 [130].

Table 7.1 Source impedance of supplies

Supply type	Resistance $R(\Omega)$	Reactance $jX(\Omega)$
1MVA transformer busbar	0.0022	0.0086
Strong mains	0.05	0.03
Weak mains	0.05	0.03
Small generator only(1.1MW)	5.5	6.3

In Table7.1, the grid supply impedance, compared to the local generator impedance is significant.

For utilization in a AC system, to work as a switch which could operates at both positive and negative cycle of the voltage waveform, the IGBT has to be reverse blocked as in Fig.7.4.

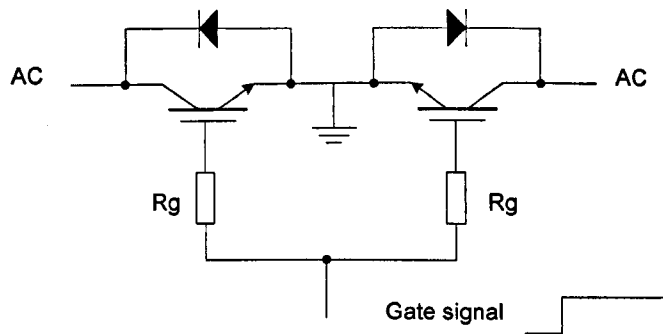


Fig.7.4 The IGBT as a switch in AC system

As shown in Fig.7.4, once the switch on the IGBT gate signal is sent to the reverse blocked IGBT, current will only flow through one IGBT and one diode during each half cycle of the AC voltage across the IGBTs. In other words, the turned on IGBT works as a diode and conduction is as shown in Fig. 7.5.

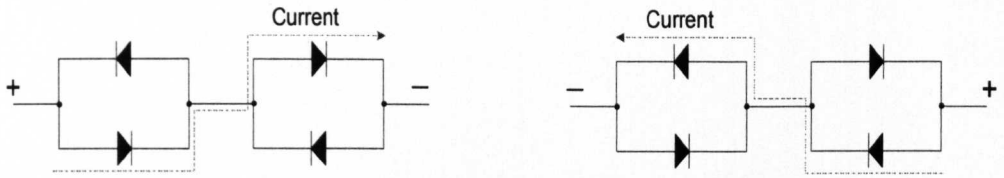


Fig.7.5 Current flow during switch on situation

Fig.7.5 shows the switch current flow through the switch components during each half cycle of the voltage. The switch current should be high enough to provide a good signal to noise ratio (SNR) for an accurate impedance calculation .

Fig.7.6 shows the voltage and current measurement at the injection point. In order to detect the islanding situation, the system impedance has to be continuously monitored.

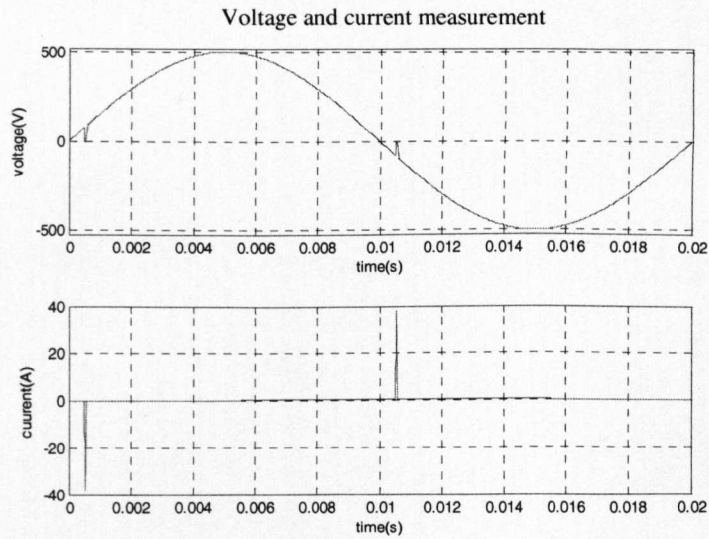


Fig.7.6 The voltage and current measurement at the injection point

To minimum the distortion influence to the system caused by the injections, the switch actions take place close to the voltage zero crossing point. For every cycle two injections are applied in the positive and negative part of the measured voltage. The length of the injected pulses is 1ms.

As shown in Fig.7.7 are the frequency ranges of the current and the corresponding voltage transient that are introduced as given by using a Fast

Fourier Transform of the transient. It is observed that a good frequency ratio can be provided over a wide frequency range.

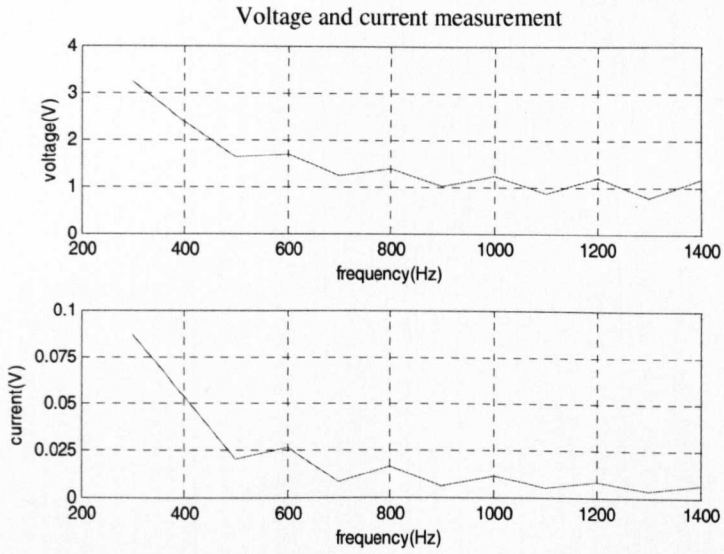


Fig.7.7 Frequency ranges of the current and the corresponding voltage transient

The estimated impedance value is depicted in Fig.7.8 and Fig.7.9 for the situation when islanding occurs at 0.1 seconds. The resistance and the reactance are measured at 1kHz for good estimation accuracy.

Fig.7.9 shows that, for this demonstration system, the reactance variation before and after island is more dramatic compared with the resistance results.

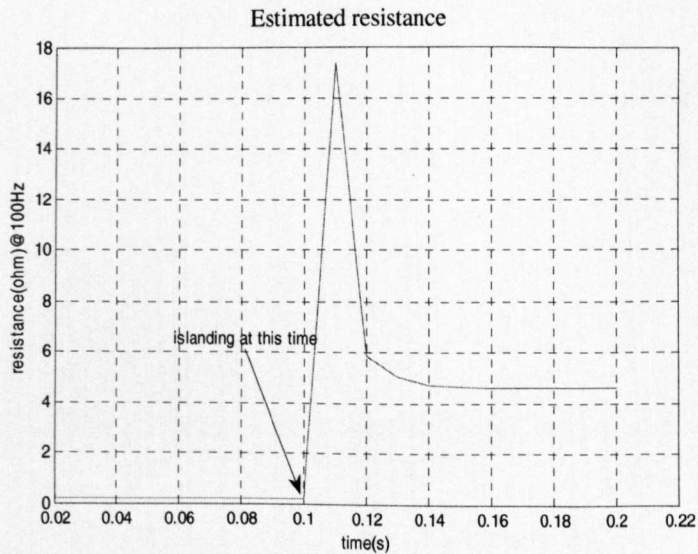


Fig.7.8 The waveform of estimated resistance value on time at 1kHz

After islanding at 0.1s the impedance increased significantly, after 0.12ms it reaches a steady state value which is much larger than the value derived before islanding. Therefore Islanding can be easily detected by using an active impedance estimation method and by comparing the impedance difference a trip signal could be sent to the generator within a cycle.

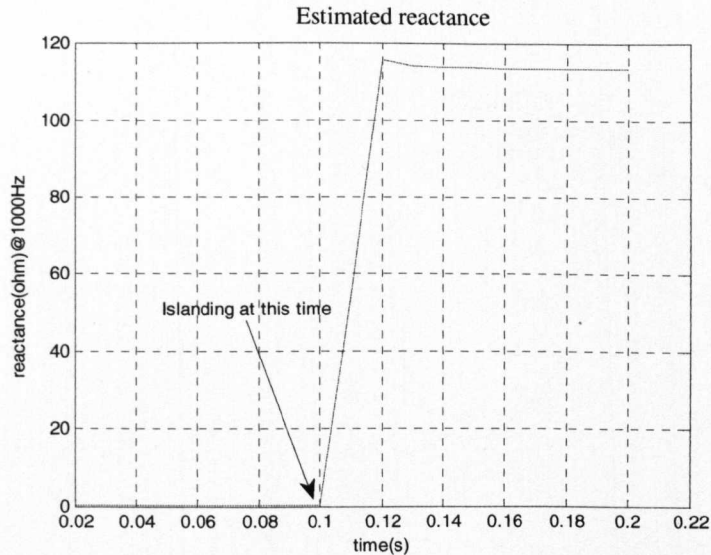


Fig.7.9 The waveform of estimated reactance value on time at 1kHz

### 7.2.3 Impedance Estimation Method Used in DFIG Wind Generation Grid-connected Distributed System

The impedance estimation method utilized in the DFIG wind generation grid-connected distributed system as described in Chapter 4 is investigated. The impedance based injection method works for different power imbalances between generation and load demand during system islanded, even in the circumstance when DG output power and load demand closely match. But, for systems with a small generator and supply impedance, this method may have limitations when it is used to distinguish the islanding and load changing situation. By using the system described in Chapter 4, the active impedance estimation method in this chapter is used to distinguish islanding and non-islanding situations (system load variation) for different power imbalances and validating the effectiveness of the islanding detection during the coordination when DG and load demand closely match.

The islanding situation with zero power imbalance between DFIG output power and load demand (the initial power of DFIG output and load demand are 9MW), and system load variation by adding and removing load of between 1MW to 4MW, are depicted in Fig.7.10.

The measured real and imaginary parts of the system impedance against frequency are shown in Fig.7.10. The dashed lines are the impedance value of non-islanding situation with a load range from 5MW to 13MW. The solid line is the estimated system impedance after islanding with a zero power imbalance. It is clear that by using the real part of the system impedance (below 500Hz) it is possible to distinguish the islanding and the load variation. Even during the case that the generation and the load demand closely match, the loss of mains condition can still be detected.

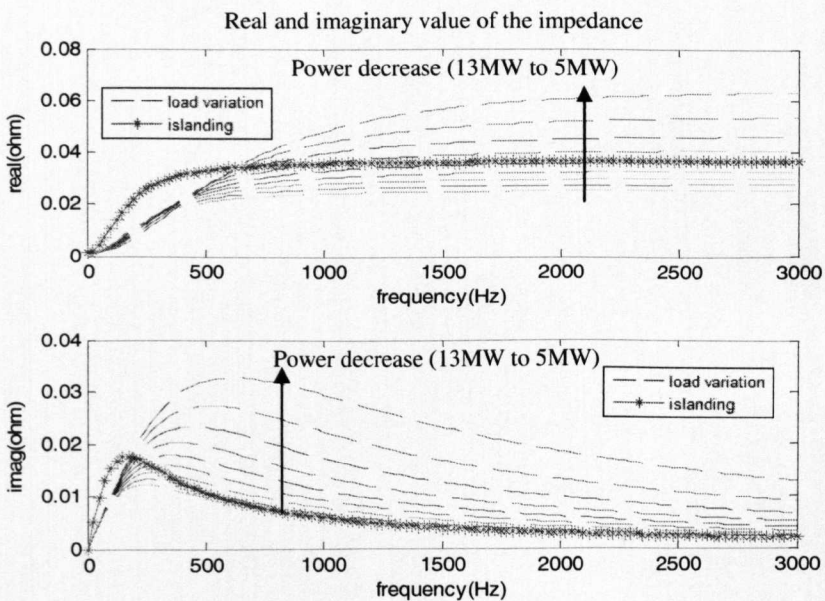


Fig.7.10 The real and imaginary value of system impedance with zero power imbalance during islanding and non-islanding load variation (5MW to 13MW)

The real and imaginary values of impedance measurement when the system is islanded with 3MW power imbalance and system load variations from 2MW to 10MW are shown in Fig.7.11. The real part of the impedance still can be used to classify the load changing and islanding conditions effectively (below 1000Hz).

As Fig.7.12 shows for a negative power imbalance (-3MW) results in the impedance estimation method also works (below 500Hz and by using the real part of the impedance). The impedance estimation method applied here is to provide a comparison of the effectiveness with other passive method with interlock functions during the non-islanding condition. Compared with other researchers' work on impedance estimation methods [130], this work is more focused on distinguishing islanding and load variation.

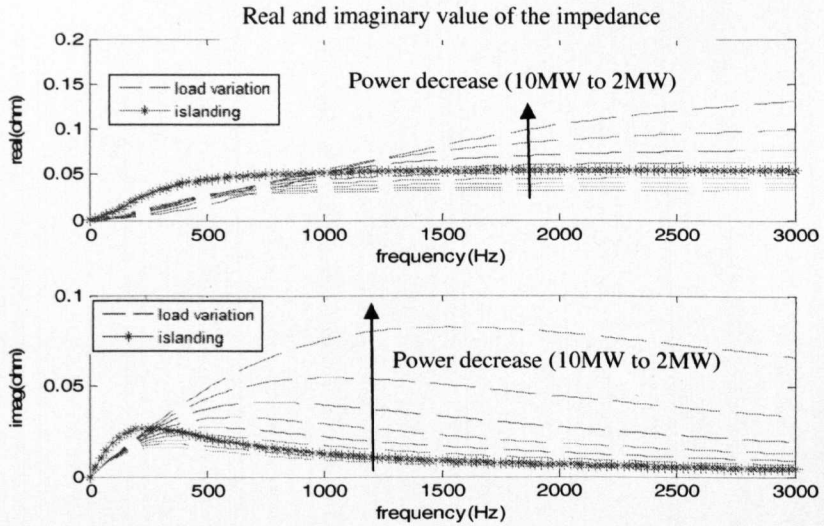


Fig.7.11 The real and imaginary value with 3MW power imbalance during islanding and non-islanding load variation (2MW to 10MW)

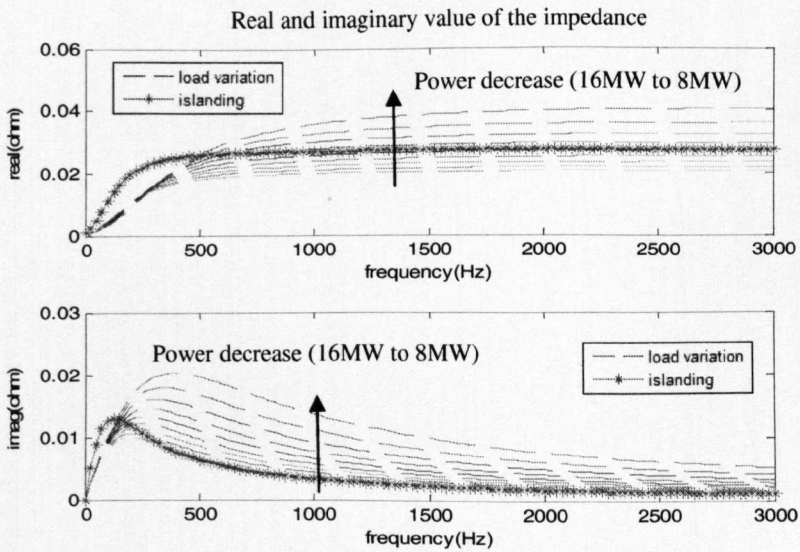


Fig.7.12 The real and imaginary value with -3MW power imbalance during islanding and non-islanding load variation (8MW to 16MW)

### 7.3 The Proposed Method of THD

Under the islanded condition DG has to take charge of local load and other network conditions. So the loading of DG can suddenly be changed. This sudden change causes voltage fluctuation and also fluctuations in the harmonic currents. Therefore, examining the total harmonic distortion of distributed generation system phase currents can be used to detect islanding [52-53]. The THD method applied here is used to avoid false tripping by cooperating with ROCOF relays during load variations, in addition, the comparison with active method and ROCOF relays with other interlock functions will be discussed.

The changes in loading for DG due to loss of mains power source obviously result in variations on the harmonics of the current. It is therefore proposed to use the THD of the DG current at the monitoring parameters. The total harmonic distortion of the current at the monitoring time  $t$  is defined as [52]:

$$THD_t = \frac{\sqrt{\sum_{h=2}^H I_h^2}}{I_1} \times 100 \quad (7.4)$$

where:

$I_1$ : rms value of the first component of the signal

$I_h$ : rms value of the  $h^{th}$  component of the signal

H: number of harmonics

During each cycle with N samples per cycle, the average of THD will be obtained by:

$$THD_{avg} = \frac{1}{N} \sum_{i=0}^{N-1} THD_{t-i} \quad (7.5)$$

where:

N: number of samples in each cycle

$THD_{avg}$ : one cycle average of THD

During normal operation, the difference between  $THD_t$  and  $THD_{avg}$  is small and varies around small values, but when wind turbines are disconnected from the distribution network it is expected that the difference will be high enough to distinguish the islanding of the network. Therefore, a normalized parameter based on the difference of  $THD_t$  and  $THD_{avg}$  will be defined as [52]:

$$Delta = \left| \frac{THD_{avg} - THD_t}{THD_{avg}} \right| \quad (7.6)$$

If the value  $Delta$  is more than a given threshold then the islanding detection conditions will be detected. Therefore, the islanding detection of wind turbines will be based on the value of expression (7.6) and its threshold. The proposed algorithm is shown in Fig 7.13.

The algorithm starts by the sampling of three-phase currents and calculates their THD. When the distribution power system is working in a balance condition then only one phase sampling is adequate otherwise sampling of three-phase currents is necessary. For each cycle, the  $THD_t$ ,  $THD_{avg}$  and  $Delta$  are calculated. If the value of  $Delta$  is greater than 1.3 at least for 2 cycles then the islanding detection algorithm issues a trip command. The threshold value of  $Delta$  is decided to avoid system disturbance caused false tripping and reduced the non-detection zone at the same time.

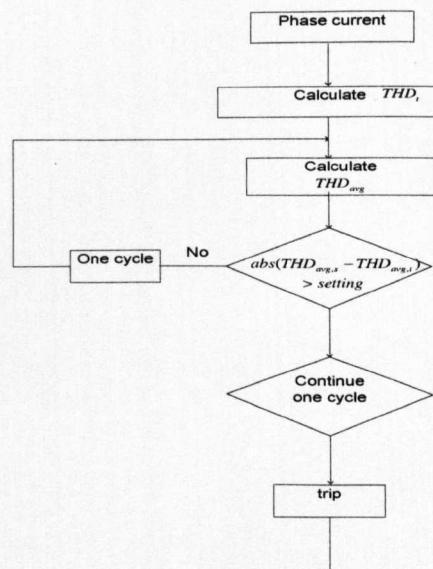


Fig.7.13 Proposed algorithm for islanding detection

The system under consideration is as given before in Fig.4.16. The circuit breaker opens at 5s which created an islanding situation. The Total Harmonic Distortion Value after islanding happens is depicted in Fig.7.14.

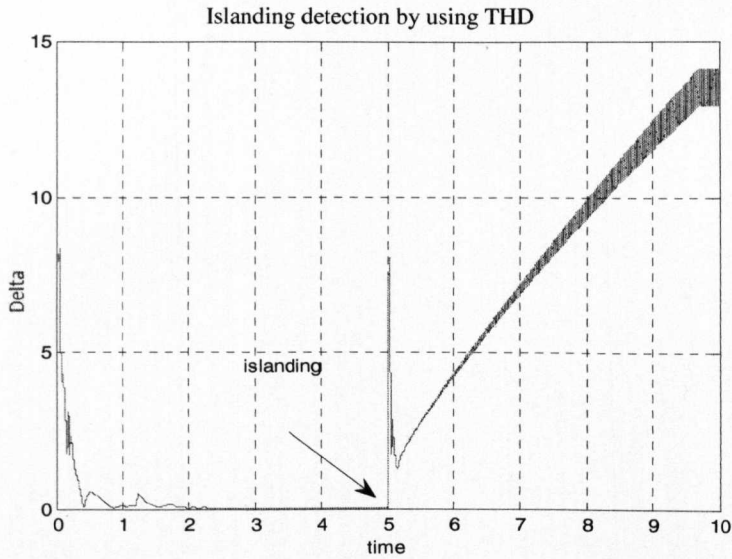


Fig.7.14 THD value as used for islanding condition

As Fig.7.14 shows, the THD value increases after islanding occurs, therefore the islanding situation can be detected quickly by using this method. But it is sensitive to grid perturbations, which makes the threshold establishment more difficult for islanding detection. For instance, with non-linear loads, the current distortion at PCC can be so high that a fault may be erroneously detected even if the grid is present [132]. But if a larger relay setting is chosen, there will be a large non-detection zone. Additionally, with linear loads the THD variation may be too low to be detected. Also in the non-islanding situation, especially for large load changing, the THD trip signal may trip incorrectly. In particular, RLC loads with high Q factor give problems to the islanding detection using this method [12]. Quality factor for RLC circuit is defined as [132]:

$$Q = R\sqrt{\frac{C}{L}} \quad (7.5)$$

This parameter describes the relationship between stored and dissipated energy in the RLC circuit. Loads with a high Q have large capacitance and small inductances and/or big parallel resistances according to (7.5). The large

capacitor could be acting as a power factor correction unit that can reduce system harmonics. In addition, as (7.6), the higher Q factor the lower the bandwidth accepted by the resonant filter characterized by this factor, in other words, more harmonics are suppressed for bigger values of Q factor [133]. In this case, the THD method could fail to detect islanding situation because the harmonics will be filtered out. The relationship of Q and bandwidth is given as:

$$Q = \frac{1}{F_b} = \frac{f_0}{\Delta f} \quad (7.6)$$

Therefore, in order to avoid an unnecessarily trips with serious consequences during the load changing situation, the THD value can be used to cooperate with ROCOF relay as a block signal, the system used for simulating the non-islanding situation is as described in Chapter 4 (as shown in Fig.4.23) In Chapter 3 and Chapter 4 the interlock functions  $dp/dt$  and  $v^2/p$  were investigated. Comparing with interlock function  $v^2/p$  for DFIG wind turbine distributed system, the Total Harmonic Distortion Method is faster, but this method has some limitations, such as it is more suitable for the system with inverter based DGs [13], and for a high quality of power factor this method fails and the threshold is difficult to set (i.e. for the system implemented in Chapter 3, the Total Harmonic Distortion Method is not efficient due to the linear load applied in this system) [12]. The interlock function of  $v^2/p$  works for both synchronous generator DG system [134] and DFIG wind turbine DGs which is validated in Chapter 4. Although the detection time is longer compared with using the THD interlock function, the total detection time with the block signal delay time is still within 300ms. The interlock function  $dp/dt$  can not be used for rotor-side outer power controlled DFIG wind turbine due to the well controlled power output from the DG side, it is difficult to distinguish islanding and non-islanding with the similar values of  $dp/dt$  between these two conditions.

Fig.7.15 and Fig.7.16 provide the simulation results of the islanding and non-islanding situation with cooperation with ROCOF relays and the total-THD% interlock function.

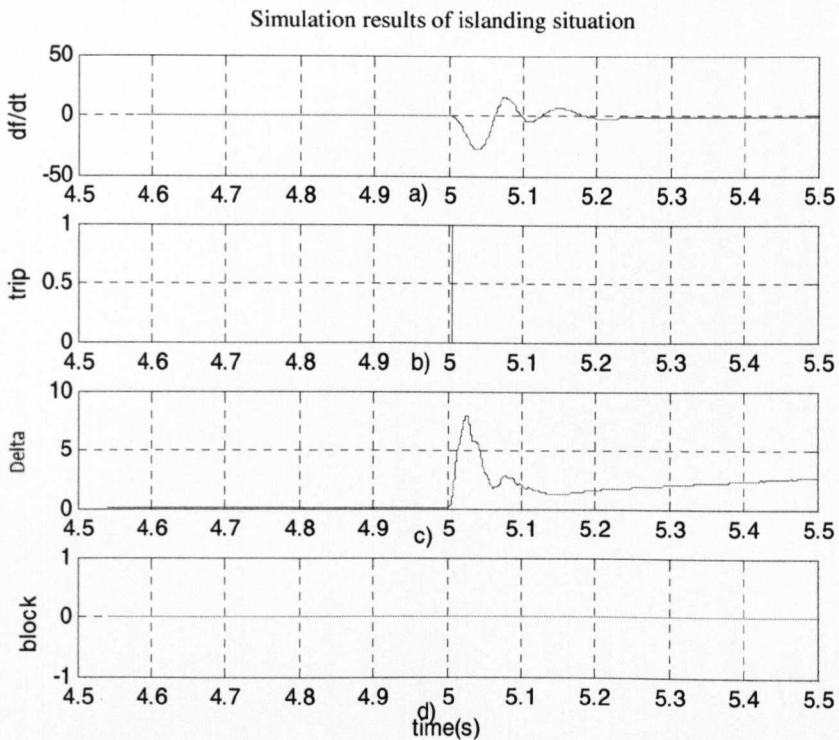


Fig.7.15 Simulation results of the islanding situation with the ROCOF relays with the THD interlock function

For the islanding situation, in the DFIG distributed system introduced in Chapter 4 and described in Fig.4.16 with a 0.667 p.u. power imbalance, the detected result with block signal is as shown in Fig.7.15 (b) and (d) separately. The circuit breaker opens at 5s where  $df/dt$  and  $\Delta$  are depicted in Fig.7.15 (a) and (c) separately. After islanding occurs ROCOF tripping signal is generated as depicted in Fig.7.15 (b). The block signal tripping setting is delayed 100ms after ROCOF relay operates. As the result of the  $\Delta$  value is greater than threshold Value, the block signal is not initiated as shown in Fig.7.15 (d).

Fig.7.16 shows the simulation results of system when it is non-islanded as described in Fig.4.20. At 5s 5MW load is added into the system, which creates a transient in rate of change of frequency, in this case the trip signal of ROCOF relay would falsely operate at 5.0609s. By combining the THD interlock function, it effectively blocks the ROCOF relays operation at 5.0998s.

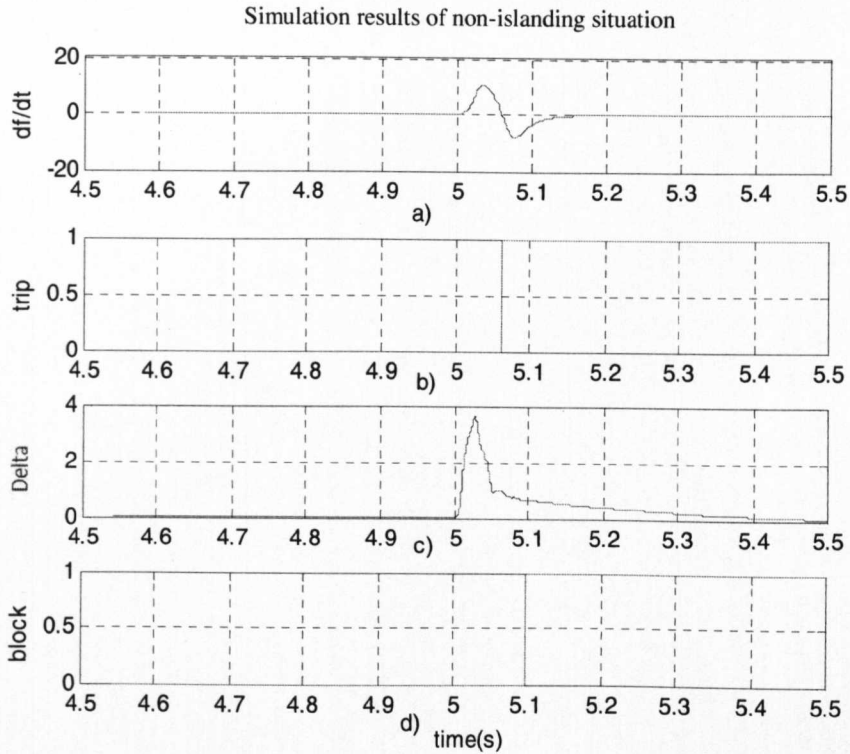


Fig. 7.16 Simulation results of non-islanding situation the ROCOF relays with the THD interlock function

## 7.4 Comparison of the Impedance Estimation and the Total Harmonic Distortion Method

The Total Harmonic Distortion techniques focus on monitoring the variation of the total harmonic distortion of a distributed generation system phase currents to detect the islanding situation. Once the system islanded, this sudden change causes voltage fluctuation and also gives rise to a change in harmonic currents. Detection of the difference between islanding and grid connected depends on the threshold setting for the parameters. In order to avoid the system disturbance causing false tripping, special consideration should be taken into the threshold value setting. Therefore, for the Total harmonic Distortion method, it is difficult to set a proper threshold value. The smaller threshold value, the shorter islanding detection time, but this would be more sensitive to system noise. The larger threshold setting could reduce the nuisance tripping, but with a larger non-detection zone. Compared with the impedance estimation

method, from the islanding simulation results of the same DFIG wind generation system, ROCOF relays and the THD interlock method (described in this chapter) provides a fast islanding detection time. Also, due to it not introducing a disturbance into the system this method would not affect system power quality. However, in order to avoid the sensitivity with system disturbances, increasing the relay setting would provide a non-detection zone. The Total Harmonic Distortion method fails for high values of system quality factor [12].

Impedance estimation techniques are based on measurement of the system source impedance at the local site. During system islanding condition, the system impedance is significantly greater than that of any grid-connected supply. The advantage of impedance estimation method is that islanding condition can be detected even under the condition of a perfect match between generation and load demand, which is not possible for passive detection schemes. Without cooperating with other islanding detection methods, it can avoid false tripping during a non-islanding condition (system load variation). But the detection time of this method is not as fast as passive methods. Also an impedance estimation method directly interacts with the power system operation by introducing perturbations. Therefore, the system power quality will be affected by the introduced harmonics. Meanwhile, it is reliable for a suitable system, otherwise, it would cause false tripping during the case of system load changing (non-islanding). For example, for a system with a small generator and large supply impedance, it would be difficult for impedance measurement method to distinguish islanding and non-islanding.

Table 7.2 summarises the disadvantages and drawbacks of the active and passive islanding detection methods. To choose an islanding detection technique will largely depend on the type of the DG and system characteristics. There is no single detection method which will satisfy for all systems requirements under all circumstances.

Table 7.2 Summarises the disadvantages and advantages of the islanding detection techniques.

Islanding Detection Techniques	Advantages	Disadvantages
Passive Methods	<ol style="list-style-type: none"> <li>1. Short detection time</li> <li>2. Do not affect power quality</li> <li>3. If there is a large enough power imbalance between the generator and the load when islanded, it is very accurate</li> </ol>	<ol style="list-style-type: none"> <li>1. A large non-detection zone, if there is a large mismatch in generation and demand in the islanded system</li> <li>2. Special consideration should be taken into the threshold value setting</li> <li>3. The system disturbance will cause the false tripping, if the setting is too aggressive</li> </ol>
Active Methods	<ol style="list-style-type: none"> <li>1. Small non-detection zone</li> <li>2. Even in the case of small mismatch in generation and demand in the islanded system</li> </ol>	<ol style="list-style-type: none"> <li>1. long detection time due to the result of extra time needed to see the system response for perturbation</li> <li>2. Introduce perturbation in the system</li> <li>3. Perturbation often degrades the power quality and if significant enough, it may degrade the system stability even when connected to the grid</li> </ol>

## 7.5 Summary

In this chapter the impedance estimation method of the active methods and the Total Harmonic Distortion of the passive methods for islanding detection applied in grid-connected DFIG wind generator as utilized in Chapter 4 are investigated. The performances of these two methods are discussed with two scenarios (islanding and non-islanding conditions). The advantage of impedance estimation method is that it can detect an islanding situation even when the generation and load demands are closely matched. This was demonstrated in the DFIG wind generator grid-connected distributed system described in Chapter 4. It can avoid false tripping during system load variation without adding any interlock function. But if the system has a small generator and large supply impedance, it would be difficult for an impedance measurement method to distinguish islanding and non-islanding. Therefore, the impedance measurement method is more suitable for particular systems with small supply impedance and large generator impedance. For the Total Harmonic Distortion method, in order to avoid incorrect tripping especially in

the circumstance of a system with a non-linear load, the relay setting can not be too small, but this will lead to a larger non-detection zone and when the system power imbalance is small, the islanding situation can not be detected. Therefore the threshold is difficult to set. The Total Harmonic Distortion method cooperating with ROCOF relays to avoid nuisance tripping during system non-islanding was investigated. From the simulation results it can be observed that it can block ROCOF relays tripping signal accurately during load variation. Compared with the impedance estimation method, this method can detect islanding faster. However, this method fails for high values of system quality factor.

# Chapter 8

## Conclusions and Future Work

### 8.1 Research objectives

The research project mainly focused on developing fast and reliable islanding detection method based on combining ROCOF relays and the rate of change of power or  $v^2/p$  interlock functions which can be utilized in synchronous generator, DFIG wind generator, grid-connected inverter and microgrid grid-connected distributed systems. The main objectives of the thesis which are introduced in Chapter 1 are summarised as:

1. Review and discuss all major islanding detection techniques published or developed.
2. Develop a new islanding detection method based on combining ROCOF relays and  $dp/dt$  interlock function applied to synchronous generators in distributed systems to provide a more fast and accurate anti-islanding protection scheme.
3. For DFIG grid-connected distributed system the ROCOF relays with  $v^2/p$  for islanding detection is investigated. It can avoid false tripping

due to a system load variation situation effectively which reduced the non-detection zone of ROCOF relays. This scheme is also validated by a laboratory experiment for DFIG islanding detection.

4. The proposed ROCOF relays with the  $v^2/p$  interlock algorithm utilized in grid-connected inverter and microgrid systems was evaluated.
5. Investigated impedance measurement (active method) and the Total Harmonic Distortion method (passive method) in grid-connected DFIG wind generation system. Discussion has been made according to the advantages and drawbacks of the active and passive methods.

## 8.2 Conclusions

Passive islanding detection methods are based on monitoring system parameters at the DG site. The significant problem of a passive islanding detection method is the large non-detection zone. Especially in the circumstance of the system load changing, the trip signal should not operate due to the system being stable and the non-islanding situation. By combining ROCOF relays and  $dp/dt$  or  $v^2/p$  interlock function, the false tripping can be effectively avoided. Compared with the traditional under voltage interlock function, the detection time is much faster and more accurate.

### 8.2.1 Objective 1

The new islanding detection method which is based on ROCOF relays and the rate of change of power which was applied to a synchronous generator in a distributed system was developed in Chapter 3. The characteristics of different frequency estimation algorithms, different measuring windows, relay settings, generator inertia and different power factor which would affect the performance of the ROCOF relays were described. The shorter the measuring window, the faster the detection time will be, and more sensitive relay is which may cause nuisance tripping signal in a noisy situation. However, the larger measuring window relay setting may increase the non-detection zone. Therefore a compromise in the relay setting is required to provide a balance

between the security and dependability. Meanwhile, the smaller the inertia constant, the smaller the critical power imbalance will be as a generator with a large inertia constant will respond more slowly to an islanding situation. Therefore, the ROCOF relay takes longer to detect frequency variations. Also, the load power factor has an impact on the ROCOF curves. For the same relay setting, the lower the power factor is, the longer the detection time is.

During the non-islanding situation the ROCOF relays should not operate for this stable system. A rate of change of power interlock function proposed in Chapter 3 is introduced to avoid false operation for the load fluctuation. It is shown that the nuisance tripping signal can be blocked quickly and accurately during non-islanding situation. In the case of small load variation, the ROCOF relay would not trip, therefore, by cooperation with rate of change of power interlock function, there would be no non-detection zone in the whole range of load variation.

### **8.2.2 Objective 2**

A model of a grid-connected DFIG similar to a GE1.5MW wind turbine generators [24] is established in MATLAB which is introduced in Chapter 4. Based on the analysis of the equivalent circuits of a DFIG and its PWM voltage source converter, a vector control scheme is introduced for grid-side converter design, and the rotor-side converter controller design is used in the model of GE1.5MW wind turbine generator. The performance of the designed controller of grid-side converter is demonstrated. The new islanding detection method of ROCOF relays with  $v^2/p$  interlock function is applied in the grid-connected DFIG wind generator system. Once the system is islanded, the performance of ROCOF relays with different characteristics which includes frequency measuring algorithms, different measuring windows, and the relay settings are investigated. Simulation results show that the shorter the measuring window, the faster the detection time will be, but the more sensitive the relay is. Also, using a larger relay setting can avoid false tripping with the system disturbance situation, but it will increase the non-detection zone and increase the islanding detection time. Load changing could also make ROCOF

relays operate, by using the estimated system impedance  $Z_{est} = v^2/p$  interlock function proposed in Chapter 4 it is shown that the nuisance tripping signal can be blocked effectively during non-islanding condition.

The islanding detection for DFIG (standard 7.5kw machine) laboratory experiment is implemented. The prototype DFIG islanding detection test rig consisted of the rotor converter, with grid interface active front end, along with the Doubly Fed Induction Generator (DFIG) and the switch box, which is introduced in Chapter 5. The idea of the ROCOF relays combined with  $v^2/p$  interlock function for two conditions (islanding and non-islanding) with different power imbalance conditions between generation and the load is provided by the experiment results. It is shown that that it has the capability to distinguish the islanding and load changing situations with a short detection time. The traditional under voltage interlock function would fail due to the voltage at PCC being unpredictable within short time, therefore, compared with the proposed estimated impedance  $v^2/p$  interlock function, it is less reliable.

### 8.2.3 Objective 3

As microgrids are part of the modern trend towards decentralised management of energy production through distributed generation, Islanding is a potential dangerous mode of operation of a microgrid. The grid-connected microgrid islanding detection was introduced in Chapter 6. Simulation results of islanding detection for a microgrid which includes a photovoltaic system, synchronous generator and DFIG wind turbine are investigated. In three cases of different generation proportions of synchronous generator, photovoltaic system, and DFIG wind turbine, for both islanding and non-islanding situations, the effectiveness of ROCOF relays with  $v^2/p$  is discussed. Due to the grid-connected inverter model being voltage and frequency controlled, with a larger portion of the generation in the microgrid, once the system is islanded, the detection time would be increased.

### **8.2.4 Objective 4**

In Chapter 7, two islanding detection methods of impedance measurement (active method) and the Total Harmonic Distortion Method (passive method) utilized in grid-connected DFIG wind generator are investigated. Both islanding and non-islanding situations are simulated, even during the situation when the generation and load demands are closely matched, the islanding situation can still be detected by using an impedance measurement method, which is the limitation of the passive method. However, with a small generator impedance and supply impedance, during system load variations, it would be difficult for an impedance measurement method to distinguish islanding and non-islanding. Therefore, the impedance measurement method is more suitable for a particular system with small supply impedance and large generator impedance. Meanwhile, due to it introducing a perturbation into the system, an active method would affect the system power quality. The Total Harmonic Distortion Method which cooperates with ROCOF relays is also analyzed in Chapter 7. It can block the ROCOF relays tripping signal during a load changing situation accurately. But this method fails for high values of system quality factor. The threshold is also difficult to set. Small relay settings would provide a fast detection time but would be sensitive to disturbances in the system.

All the objectives outlined represent a substantial contribution to the research in islanding detection.

### **8.3 Future Work**

Current utility practices do not permit autonomous microgrid operation and except in special cases, require that all down stream DG units to be disconnected after both planned and unplanned switching events [117]. But in the future the appropriate control for the power electronically interfaced DG unit can ensure stability and maintain voltage quality at designated buses, even during islanding transient. Therefore, it is suggested to carry out further research on more detailed and complicated microgrid system modelling which

can operate in grid-connected mode or in islanded mode. In grid-connected mode, the microgrid either draws or supplies power from or to the main grid, depending on the generation and load with suitable market policies. The microgrid can separate itself from the main grid whenever a power quality event in the main grid occurs [135].

Microgrid can be connected to the main power grid or be operated autonomously. In this way, during disturbances, the generation and corresponding loads can be separated from the distribution system to isolate the microgrid's load from the disturbance without harming the transmission grid's integrity. Intentional islanding of generation and loads have the potential to provide a higher local reliability than that provided by the power system as a whole.

Flexible and fast control techniques for a micro-grid system to allow it to work properly during transient and steady-state autonomous (islanding) operation are necessary. The objective of the control scheme used for microgrid is faced with the following issues:

### **1. Voltage and frequency management**

Good voltage and frequency management is required. The voltage and frequency are established by the grid when the microgrid is connected. When the microgrid islands, one or more primary or intermediate energy sources should be controlled by adjusting its voltage and frequency, otherwise, the microgrid will collapse [135]. Both voltage and frequency should be regulated within acceptable limits. If the frequency has dropped to excessively low level, loads may be temporarily shed to hasten its recovery towards the nominal value [113, 136].

### **2. Balance between supply and demand**

Methods to maintain a balance between supply and demand should be investigated. If the microgrid is exchanging power to the grid before disconnection, then secondary control actions should be implemented to balance generation and consumption in island mode. If the connected load exceeds the available generation, demand side management should be

implemented. Also, there should be enough energy storage capacity to ensure initial balance after an abrupt change in load or generation [135-136].

### **3. Power quality**

The microgrid should maintain an acceptable power quality while in island operation. There should be an adequate supply of reactive energy to mitigate voltage sags. The energy storage device should be capable of reacting quickly to frequency and voltage deviations and injecting or absorbing large amounts of real and reactive power. Finally, the microgrid should be able to supply the harmonics required by non-linear load.

### **4. Microsource issues**

A major difference between the primary energy sources in the grid and microsourses connected to the microgrid is that the latter has no inertia [136-137]. The microgrid does not have the spinning reserves that are inherently present in the conventional grid. Most microsourses (e.g. turbines and fuel cells) have slow response or ramp-time when implementing secondary voltage and frequency control. The intermediate storage units and microsourses with built-in battery banks are therefore expected to offer advantages like spinning reserves [135-136]. The power electronics devices react promptly to fast demand signals and adjust the power flow levels.

In addition, for the wind turbines, due to the small wind speed the output power of the wind turbine would be out of control. This can lead to the ROCOF relay false tripping as well. Therefore, the nuisance tripping problem at low wind speed situation should also be considered in the future work.

### **5. Communication among microgrid components**

The availability of communication infrastructure between the microgrid components is another aspect to be considered when choosing the control approach on an islanded microgrid. The microsourses and storage devices should co-operate with each other to maintain the integrity of the islanded microgrid.

## **6.Planned microgrid islanding**

Including the above factors, the microgrid should be prepared for planned islanding which is an important aspect in the microgrid concept used to maintain the continuity of supply during planned outages, like for a substation maintenance period [135, 137].

Based on the islanded operation of microgrid, several control techniques should be considered to be implemented in the future work which can overcome the issues caused by islanding.

Several methods for coordination of microsources have been suggested:

- A. **Primary Energy Source Control:** When the microgrid islands, the storage device behaves like a synchronous generator to restore the voltage and frequency to pre-island values [135].
- B. **Pure Droop Control:** The storage device and all microsources will be able to regulate their power outputs to droop control when the microgrid islands [136]. One promising approach is the implementation of conventional frequency/voltage droops into respective inverters thus down scaling the conventional grid control concept in low voltage microgrid [138].
- C. **Power Quality Control in Hybrid Microgrid System:** Application of different kinds of power source would impact the quality of power supply within the microgrid and causes many control problems. In this type of hybrid system, computer based monitoring system may be provided for power quality control to resist frequency fluctuation due to random load fluctuation [135, 139].
- D. **Synchronous Islanded Operation Control:** This will keep the islanded system in synchronous with the main system while not being electrically connected. It can be achieved by transmitting a reference signal from a secure part of the network and using global positioning satellite (GPS) synchronized time stamping to make sure that the island and mains voltage waveforms can be aligned with minimum phase difference error [140-141]. Therefore, out-of-phase synchronization can be avoided by applying this control scheme.

These are all worthy of future investigation.

# Reference

1. Chiradeja, P. *Benefit of Distributed Generation: A Line Loss Reduction Analysis*. in *Transmission and Distribution Conference and Exhibition: Asia and Pacific, 2005 IEEE/PES*. 2005.
2. Shahidehpour, M. and F. Schwarts, *Don't let the sun go down on PV [photovoltaic systems]*. *Power and Energy Magazine, IEEE*, 2004. 2(3): p. 40-48.
3. *World Wind Energy Report 2010*, G.E.C.D.i. Powerhouses, Editor. Nov,2011, 10th world wind energy conference and renewable energy exhibition.
4. *Wind Power Increase in 2008 Exceeds 10-year Average Growth Rate*. Nov,2011; Available from: <http://www.worldwatch.org/node/6102?emc=el&m=239273&l=5&v=c a5d0bd2df>.
5. *BTM Forecasts 340-GW of Wind Energy by 2013*. Dec,2011; Available from: <http://www.renewableenergyworld.com/rea/news/article/2009/03/btm-forecasts-340-gw-of-wind-by-2013?src=rss>.
6. *Global Status report*. Dec,2011; Available from: [http://www.ren21.net/Portals/97/documents/GSR/GSR2011\\_Master18.pdf](http://www.ren21.net/Portals/97/documents/GSR/GSR2011_Master18.pdf).
7. *Global Wind Report 2010*. Dec,2011; Available from: <http://www.gwec.net/index.php?id=180>.
8. *Solar Energy News*. Dec,2011; Available from: <http://www.brighterenergy.org/9715/news/solar/sunpower-offers-solar-modules-boasting-19-efficiency/>.
9. *Leading the solar energy revolution with Concentrator Photovoltaic (CPV) technology*. Dec,2011; Available from: <http://www.soitec.com/en/solar-energy/>.
10. Strath, N., *Islanding Detection in Power System*. 2005, Lund University: SWEDEN.
11. Wilsun Xu, K.M., Sylvain Martel, *An Assessment of Distributed Generation Islanding Detection Methods and Issues for Canada*, C.E.T.C. (CETC), Editor. July 2004, Natrul Resource Canada.
12. Kunte, R.S. and W.Z. Gao, *Comparison and Review of Islanding Detection Techniques for Distributed Energy Resources*. 2008 40th North American Power Symposium (Naps 2008), 2008: p. 209-216.
13. Mahat, P., C. Zhe, and B. Bak-Jensen. *Review of islanding detection methods for distributed generation*. in *Electric Utility Deregulation and Restructuring and Power Technologies, 2008. DRPT 2008. Third International Conference on*. 2008.
14. *IEEE Standard for Interconnecting Distributed Resources With Electric Power Systems*. IEEE Std 1547-2003, 2003: p. 0\_1-16.
15. Rifaat, R.M. *Critical considerations for utility/cogeneration inter tie protection scheme configuration*. in *Industrial and Commercial Power*

- Systems Technical Conference, 1994. Conference Record, Papers Presented at the 1994 Annual Meeting, 1994 IEEE. 1994.*
16. *IEEE Application Guide for IEEE Std 1547, IEEE Standard for Interconnecting Distributed Resources with Electric Power Systems. IEEE Std 1547.2-2008, 2009: p. 1-207.*
  17. Hedquist, T., *IEEE 1547 UNINTENTIONAL ISLANDING PROTECTION FOR LANDFILL GAS POWER GENERATION FACILITIES.* July 2011, Director of Standards and Development Electric Power Division.
  18. Vieira, J.C.M., et al., *Formulas for predicting the dynamic performance of ROCOF relays for embedded generation applications.* Generation, Transmission and Distribution, IEE Proceedings-, 2006. **153**(4): p. 399-406.
  19. Affonso, C.M., et al., *Performance of ROCOF relays for embedded generation applications.* Generation, Transmission and Distribution, IEE Proceedings-, 2005. **152**(1): p. 109-114.
  20. W.Bower , M.R., *Evaluation Of Islanding Detection Methods For Photovoltaic Utility.* 2002, International Energy Agency.
  21. Hagh, M.T., et al. *New islanding detection algorithm for wind turbine.* in *Environment and Electrical Engineering (EEEIC), 2011 10th International Conference on.* 2011.
  22. Aljankawey, A.S., et al. *Passive method-based islanding detection of Renewable-based Distributed Generation: The issues.* in *Electric Power and Energy Conference (EPEC), 2010 IEEE.* 2010.
  23. N. Cullen, J.T., A. Collinson, *Risk Analysis of Islanding of Photovoltaic Power Systems Within Low Voltage Distribution Networks.* March,2002, International Energy Agency.
  24. Nicholas W. Miller, W.W.P., Juan J. Sanchez-Gasca, *Dynamic Modeling of GE 1.5 and 3.6 Wind Turbine-Generators.* 2003, GE-Power Systems Energy Consulting.
  25. Grau, I., et al. *Microgrid intentional islanding for network emergencies.* in *Universities Power Engineering Conference (UPEC), 2009 Proceedings of the 44th International.* 2009.
  26. Funabashi, T., K. Koyanagi, and R. Yokoyama. *A review of islanding detection methods for distributed resources.* in *Power Tech Conference Proceedings, 2003 IEEE Bologna.* 2003.
  27. Redfern, M.A., O. Usta, and G. Fielding, *Protection against loss of utility grid supply for a dispersed storage and generation unit.* Power Delivery, IEEE Transactions on, 1993. **8**(3): p. 948-954.
  28. Wilsun, X., et al. *A Power Line Signaling Based Technique for Anti-islanding Protection of Distributed Generators: Part I: Scheme and Analysis.* in *Power Engineering Society General Meeting, 2007. IEEE.* 2007.
  29. Ropp, M.E., et al. *Using power line carrier communications to prevent islanding [of PV power systems].* in *Photovoltaic Specialists Conference, 2000. Conference Record of the Twenty-Eighth IEEE.* 2000.
  30. Wencong, W., et al., *A Power Line Signaling Based Scheme for Anti-Islanding Protection of Distributed Generators&mdash;Part II: Field*

- Test Results*. Power Delivery, IEEE Transactions on, 2007. **22**(3): p. 1767-1772.
31. Redfern, M.A., J. Barrett, and O. Usta, *A new microprocessor based islanding protection algorithm for dispersed storage and generation units*. Power Delivery, IEEE Transactions on, 1995. **10**(3): p. 1249-1254.
  32. Yanwei, Z. and S. Xinchun. *Analysis of the influence of load to islanding passive detection method*. in *Information Management and Engineering (ICIME), 2010 The 2nd IEEE International Conference on*. 2010.
  33. Vieira, J.C.M., et al., *Efficient coordination of ROCOF and frequency relays for distributed generation protection by using the application region*. Power Delivery, IEEE Transactions on, 2006. **21**(4): p. 1878-1884.
  34. Vieira, J.C.M., et al., *Performance of frequency relays for distributed generation protection*. Power Delivery, IEEE Transactions on, 2006. **21**(3): p. 1120-1127.
  35. John, V., Y. Zhihong, and A. Kolwalkar, *Investigation of anti-islanding protection of power converter based distributed generators using frequency domain analysis*. Power Electronics, IEEE Transactions on, 2004. **19**(5): p. 1177-1183.
  36. Vieira, J.C.M., et al. *Evaluation of the distributed generators frequency protection due to changes in the anti-islanding requirements*. in *Power Engineering Society General Meeting, 2006. IEEE*. 2006.
  37. Yongzheng, Z. and L.A.C. Lopes. *Design and Compliance of Frequency Drifting Islanding Detection Methods with the IEEE Standard 1547.1*. in *Electrical and Computer Engineering, 2007. CCECE 2007. Canadian Conference on*. 2007.
  38. Ward, B.M.R., *Evaluation of islanding detection methods for utility-interactive inverters in photovoltaic systems*, S.N. Laboratories, Editor. 2002.
  39. Fei, W. and X. Zigang. *Evaluation of inverter resident passive islanding detection method for grid connected PV system under constant power mode*. in *Control and Decision Conference, 2009. CCDC '09. Chinese*. 2009.
  40. Freitas, W., et al., *Comparative analysis between ROCOF and vector surge relays for distributed generation applications*. Power Delivery, IEEE Transactions on, 2005. **20**(2): p. 1315-1324.
  41. Freitas, W., H. Zhenyu, and X. Wilsun, *A practical method for assessing the effectiveness of vector surge relays for distributed generation applications*. Power Delivery, IEEE Transactions on, 2005. **20**(1): p. 57-63.
  42. Fu-Sheng, P. and H. Shyh-Jier, *A detection algorithm for islanding-prevention of dispersed consumer-owned storage and generating units*. Energy Conversion, IEEE Transactions on, 2001. **16**(4): p. 346-351.
  43. Sung-Il, J. and K. Kwang-Ho, *An islanding detection method for distributed generations using voltage unbalance and total harmonic distortion of current*. Power Delivery, IEEE Transactions on, 2004. **19**(2): p. 745-752.

44. Jang, S.I. and K.H. Kim. *A new islanding detection algorithm for distributed generations interconnected with utility networks*. in *Developments in Power System Protection, 2004. Eighth IEE International Conference on*. 2004.
45. De Mango, F., et al. *Overview of Anti-Islanding Algorithms for PV Systems. Part I: Passive Methods*. in *Power Electronics and Motion Control Conference, 2006. EPE-PEMC 2006. 12th International*. 2006.
46. Kaura, V. and V. Blasko, *Operation of a phase locked loop system under distorted utility conditions*. *Ieee Transactions on Industry Applications*, 1997. **33**(1): p. 58-63.
47. Katiraei, F., et al. *Dynamic analysis and field verification of an innovative anti-islanding protection scheme based on directional reactive power detection*. in *Electrical Power Conference, 2007. EPC 2007. IEEE Canada*. 2007.
48. Bright, C.G. *COROCOF: comparison of rate of change of frequency protection. A solution to the detection of loss of mains*. in *Developments in Power System Protection, 2001, Seventh International Conference on (IEE)*. 2001.
49. Rajabi-Ghahnavie, A., M. Parniani, and M. Fotuhi-Firuzabad. *Investigating the effects of reactive power on islanding detection*. in *Power System Technology, 2004. PowerCon 2004. 2004 International Conference on*. 2004.
50. Wen-Yeau, C. *An Islanding Detection Method for Grid-Connected Inverter of Distributed Renewable Generation System*. in *Power and Energy Engineering Conference (APPEEC), 2011 Asia-Pacific*. 2011.
51. Salman, S.K., D.J. King, and G. Weller. *New loss of mains detection algorithm for embedded generation using rate of change of voltage and changes in power factors*. in *Developments in Power System Protection, 2001, Seventh International Conference on (IEE)*. 2001.
52. Karegar, H.K. and A. Shataee. *Islanding detection of wind farms by THD*. in *Electric Utility Deregulation and Restructuring and Power Technologies, 2008. DRPT 2008. Third International Conference on*. 2008.
53. Sung-Il, J. and K. Kwang-Ho. *Development of a logical rule-based islanding detection method for distributed resources*. in *Power Engineering Society Winter Meeting, 2002. IEEE*. 2002.
54. Eltawil, M.A. and Z. Zhao, *Grid-connected photovoltaic power systems: Technical and potential problems—A review*. *Renewable and Sustainable Energy Reviews*, 2010. **14**(1): p. 112-129.
55. De Mango, F., M. Liserre, and A.D. Aquila. *Overview of Anti-Islanding Algorithms for PV Systems. Part II: Active Methods*. in *Power Electronics and Motion Control Conference, 2006. EPE-PEMC 2006. 12th International*. 2006.
56. Du, P., J.K. Nelson, and Z. Ye, *Active anti-islanding schemes for synchronous-machine-based distributed generators*. *Generation, Transmission and Distribution, IEE Proceedings-*, 2005. **152**(5): p. 597-606.
57. Smith, G.A., P.A. Onions, and D.G. Infield, *Predicting islanding operation of grid connected PV inverters*. *Electric Power Applications, IEE Proceedings -*, 2000. **147**(1): p. 1-6.

58. Jones, R.A., T.R. Sims, and A. Imece, *Investigation of potential islanding of dispersed photovoltaic systems*, in *Other Information: Portions of this document are illegible in microfiche products*. 1988. p. Medium: X; Size: Pages: 317.
59. Yuyama, S., et al., *A high speed frequency shift method as a protection for islanding phenomena of utility interactive PV systems*. *Solar Energy Materials and Solar Cells*, 1994. **35**(0): p. 477-486.
60. Jeraputra, C., P.N. Enjeti, and H. In Ho. *Development of a robust antiislanding algorithm for utility interconnection of distributed fuel cell powered generation*. in *Applied Power Electronics Conference and Exposition, 2004. APEC '04. Nineteenth Annual IEEE*. 2004.
61. G. A. Kern, J.G., and S. Gonzalez, *Results of Sandia National Laboratories Grid-Tied Inverter Testing*, in *2nd World Conference and Exhibition on Photovoltaic Solar Energy Conversion*, -. July, Editor. July 1998, Sandia National Laboratories: Vienna, Austria.
62. Geng, H., et al. *Design and comparison of active frequency drifting islanding detection methods for DG system with different interface controls*. in *Power Electronics for Distributed Generation Systems (PEDG), 2010 2nd IEEE International Symposium on*. 2010.
63. Yafaoui, A., W. Bin, and S. Kouro, *Improved Active Frequency Drift Anti-islanding Detection Method for Grid Connected Photovoltaic Systems*. *Power Electronics, IEEE Transactions on*, 2012. **27**(5): p. 2367-2375.
64. Guo-Kiang, H., C. Chih-Chang, and C. Chern-Lin, *Automatic phase-shift method for islanding detection of grid-connected photovoltaic inverters*. *Energy Conversion, IEEE Transactions on*, 2003. **18**(1): p. 169-173.
65. Menon, V. and M.H. Nehrir, *A Hybrid Islanding Detection Technique Using Voltage Unbalance and Frequency Set Point*. *Power Systems, IEEE Transactions on*, 2007. **22**(1): p. 442-448.
66. Wen-Yeau, C. *A hybrid islanding detection method for distributed synchronous generators*. in *Power Electronics Conference (IPEC), 2010 International*. 2010.
67. Jun, Y., C. Liuchen, and C. Diduch. *A New Hybrid Anti-Islanding Algorithm in Grid Connected Three-Phase Inverter System*. in *Power Electronics Specialists Conference, 2006. PESC '06. 37th IEEE*. 2006.
68. Mahat, P., C. Zhe, and B. Bak-Jensen, *A Hybrid Islanding Detection Technique Using Average Rate of Voltage Change and Real Power Shift*. *Power Delivery, IEEE Transactions on*, 2009. **24**(2): p. 764-771.
69. Ten, C.F. and P.A. Crossley. *Evaluation of Rocof Relay Performances on Networks with Distributed Generation*. in *Developments in Power System Protection, 2008. DPSP 2008. IET 9th International Conference on*. 2008.
70. I.N. Jenkins , R.A., P. Crossley , D. Kirschen and G. Strbac *Embedded Generation*. 2000, Bristol,U.K.
71. Thomas, D.W.P. and M.S. Woolfson. *Voltage and current phasor estimation during abnormal conditions for transmission line protection schemes*. in *Developments in Power System Protection, Sixth International Conference on (Conf. Publ. No. 434)*. 1997.

72. Hirodantis, S., H. Li, and P.A. Crossley. *Load shedding in a distribution network*. in *Sustainable Power Generation and Supply, 2009. SUPERGEN '09. International Conference on*. 2009.
73. Hirodantis, S. and H. Li. *An adaptive load shedding method for intentional islanding*. in *Clean Electrical Power, 2009 International Conference on*. 2009.
74. Lobos, T. and J. Rezmer, *Real-time determination of power system frequency*. *Instrumentation and Measurement, IEEE Transactions on*, 1997. **46(4)**: p. 877-881.
75. Balmer, L., *Signals and systems an introduction*. second edition ed. 1998: Prentice Hall press.
76. Kumar, M.D., *Digital signal processing: a computer based approach*. May, 2011, New York: McGraw-Hill.
77. Zhou, Q., *Fault Identification for Aircraft Distribution System Using Harmonic Impedance Measurement*. May, 2009, the University of Nottingham.
78. Lobos, T., *Nonrecursive methods for real-time determination of basic waveforms of voltages and currents*. *Generation, Transmission and Distribution, IEE Proceedings C*, 1989. **136(6)**: p. 347-352.
79. Eichhorn, K.F. and T. Lobos, *Recursive real-time calculation of basic waveforms of signals*. *Generation, Transmission and Distribution, IEE Proceedings C*, 1991. **138(6)**: p. 469-470.
80. Eichhorn, K.F., T. Lobos, and P. Ruczewski, *Constrained frequency domain algorithms for determination of parameters of fundamental sinewave of signals*. *Generation, Transmission and Distribution, IEE Proceedings C*, 1993. **140(6)**: p. 477-480.
81. Ekanayake, J. and N. Jenkins, *Comparison of the response of doubly fed and fixed-speed induction generator wind turbines to changes in network frequency*. *Energy Conversion, IEEE Transactions on*, 2004. **19(4)**: p. 800-802.
82. Miller, N.W., et al. *Dynamic modeling of GE 1.5 and 3.6 MW wind turbine-generators for stability simulations*. in *Power Engineering Society General Meeting, 2003, IEEE*. 2003.
83. Sun, T., *Power Quality of Grid-connected Wind Turbines with DFIG and Their Interaction with The Grid*, in *Institute of Energy Technology*. 2004, Alborg University: Denmark.
84. Burges, K., *Dynamic Modelling of Wind Farms in Transmission Networks*. p. 8.
85. Burton, T., Sharp, D., Jenkins, N., Bossanyi, E., *Wind Energy handbook*, ed. J.W.S. Ltd. 2001, Chichester.
86. Heier, S., *Grid integration of wind energy conversion systems*, ed. W.S. Ltd. 1998, Chichester.
87. Slootweg, J.G., Polinder, H., Kling, W. L., *Dynamic modeling of a wind turbine with direct drive synchronous generator and back to back voltage source converter and its control*. *Proc. of the European Wind Energy Conference*, July 2001: p. 1014-1017.
88. Akhmatov, V., Knudsen, H., *Modelling of windmill induction generators in dynamic simulation programs*. *Proc. of International Conference on Electric Power Engineering*, Aug./Sept. 1999: p. 108.

89. Salman, S.K. and A.L.J. Teo. *Improvement of fault clearing time of wind farm using reactive power compensation*. in *Power Tech Proceedings, 2001 IEEE Porto*. 2001.
90. Salman, S.K. and A.L.J. Teo, *Windmill modeling consideration and factors influencing the stability of a grid-connected wind power-based embedded generator*. *Power Systems, IEEE Transactions on*, 2003. 18(2): p. 793-802.
91. Muller, S., Deicke, M., De Doncker, R. W., *Doubly fed induction generator systems for wind turbine*. *IEEE Industry Applications Magazine*, June 2002. 8(3): p. 26-33.
92. Risheng, L., *Control of offshore wind farm grid with line commutated HVDC link connection* in *Electrical Electronic Engineering*. 2007, The University of Nottingham: Nottingham.
93. I.Boldea, S.A.N., *The induction machine handbook*. 2002, Boca Raton: CRC Press.
94. Pena, R., J.C. Clare, and G.M. Asher, *Doubly fed induction generator using back-to-back PWM converters and its application to variable-speed wind-energy generation*. *Electric Power Applications, IEE Proceedings -*, 1996. 143(3): p. 231-241.
95. Yen-Shin, L., C. Jian-Ho, and L. Chang-Huan. *A universal vector controller for induction motor drives fed by voltage-controlled voltage source inverter*. in *Power Engineering Society Summer Meeting, 2000. IEEE*. 2000.
96. Sung-Don, W., S. Myoung-Ho, and H. Dong-Seok, *Stator-flux-oriented control of induction motor considering iron loss*. *Industrial Electronics, IEEE Transactions on*, 2001. 48(3): p. 602-608.
97. R.S.Burns, *Advanced control engineering*, ed. Butterworth-Heinemann. 2001, Oxford.
98. R.N.Bateson, *Introduction to control system technology*. 1996, New Jersey: Prentice Hall.
99. S.E.Lyshevski, *Control system theory with engineering applications*. 2001, Boston.
100. P.H.Lewis, C.Y., *Basic control system engineering*. 1997, New Jersey: Prentice Hall.
101. W.S.Levine, *Control system fundamentals*. 2000, Boca Raton: CRC Press.
102. Harnefors, L. and H.P. Nee, *Model-based current control of AC machines using the internal model control method*. *Industry Applications, IEEE Transactions on*, 1998. 34(1): p. 133-141.
103. Harnefors, L. and H.P. Nee. *Robust current control of AC machines using the internal model control method*. in *Industry Applications Conference, 1995. Thirtieth IAS Annual Meeting, IAS '95., Conference Record of the 1995 IEEE*. 1995.
104. Hentabli, K., M.E.H. Benbouzid, and D. Pinchon. *CGPC with internal model structure: application to induction motor control*. in *Control Applications, 1997., Proceedings of the 1997 IEEE International Conference on*. 1997.
105. Walton, C., *The Zero Fault Level Generator for Active Urban Networks*. Jan, 2011.
106. *Emerson Industrial Automation, Unidrive, SP2403*. Jan, 2012.

107. *Encoder model 725*. 2012; Available from: [http://www.encoder.co.uk/products/product.asp?id=20070604151900\\_ENCODER\\_7055](http://www.encoder.co.uk/products/product.asp?id=20070604151900_ENCODER_7055).
108. *High Resolution Timer Counter, PM6671* 1982; Available from: [http://www.radiomuseum.org/r/philips\\_frequenzaehler\\_pm6671.html](http://www.radiomuseum.org/r/philips_frequenzaehler_pm6671.html).
109. *Waverunner 6000 series*. Available from: [http://www.livingston-products.com/products/pdf/126466\\_1\\_en.pdf](http://www.livingston-products.com/products/pdf/126466_1_en.pdf).
110. *ADP300 ADP305*. Available from: [http://cdn.lecroy.com/files/manuals/cp150\\_im.pdf](http://cdn.lecroy.com/files/manuals/cp150_im.pdf).
111. *Instruction Manual LeCroy CP150 Current Probe*. Available from: [http://cdn.lecroy.com/files/manuals/cp150\\_im.pdf](http://cdn.lecroy.com/files/manuals/cp150_im.pdf).
112. Lopes, J.A., C.L. Moreira, and A.G. Madureira. *Defining control strategies for analysing microgrids islanded operation*. in *Power Tech, 2005 IEEE Russia*. 2005.
113. Lopes, J.A.P., C.L. Moreira, and A.G. Madureira, *Defining control strategies for MicroGrids islanded operation*. Power Systems, IEEE Transactions on, 2006. **21**(2): p. 916-924.
114. Eto, J., et al. *Overview of the CERTS Microgrid laboratory Test Bed*. in *Integration of Wide-Scale Renewable Resources Into the Power Delivery System, 2009 CIGRE/IEEE PES Joint Symposium*. 2009.
115. Basak, P., et al. *Microgrid: Control techniques and modeling*. in *Universities Power Engineering Conference (UPEC), 2009 Proceedings of the 44th International*. 2009.
116. Thomas, D., *Power system lecture handouts*. 2007, The University of Nottingham.
117. Katiraei, F., M.R. Iravani, and P.W. Lehn, *Micro-grid autonomous operation during and subsequent to islanding process*. Power Delivery, IEEE Transactions on, 2005. **20**(1): p. 248-257.
118. Valentini, M., et al. *A new passive islanding detection method for grid-connected PV inverters*. in *Power Electronics, Electrical Drives, Automation and Motion, 2008. SPEEDAM 2008. International Symposium on*. 2008.
119. IEA, I.E.A., *Utility aspects of gridconnected photovoltaic power system*. December 1998.
120. Singam, B. and L.Y. Hui. *Assessing SMS and PJD Schemes of Anti-Islanding with Varying Quality Factor*. in *Power and Energy Conference, 2006. PECon '06. IEEE International*. 2006.
121. Xuancai, Z., S. Guoqiao, and X. Dehong. *Evaluation of AFD islanding detection methods based on NDZs described in power mismatch space*. in *Energy Conversion Congress and Exposition, 2009. ECCE 2009. IEEE*. 2009.
122. Liu, F., et al., *Improved SMS islanding detection method for grid-connected converters*. Renewable Power Generation, IET, 2010. **4**(1): p. 36-42.
123. Jaeho, C., J. Youngseok, and Y. Gwongjong. *Novel AFD method with pulsation of chopping fraction for islanding prevention of grid-connected photovoltaic inverter*. in *Power Electronics and Applications, 2005 European Conference on*. 2005.
124. Benato, R., R. Caldon, and S. Corsi. *Protection requirements in distribution systems with high penetration of DG and possibility of*

- intentional islanding*. in *Electricity Distribution, 2005. CIRED 2005. 18th International Conference and Exhibition on*. 2005.
125. Abdolrasol, M.G.M. and S. Mekhilef. *Robust hybrid anti-islanding method for inverter-based distributed generation*. in *TENCON 2010 - 2010 IEEE Region 10 Conference*. 2010.
  126. Zhongnan, G., et al. *Comparative evaluation of current injection based islanding detection methods for distributed generation systems*. in *Electrical Machines and Systems (ICEMS), 2011 International Conference on*. 2011.
  127. Karimi, H., A. Yazdani, and R. Iravani, *Negative-Sequence Current Injection for Fast Islanding Detection of a Distributed Resource Unit*. Power Electronics, IEEE Transactions on, 2008. **23**(1): p. 298-307.
  128. Hernandez-Gonzalez, G. and R. Iravani, *Current injection for active islanding detection of electronically-interfaced distributed resources*. Power Delivery, IEEE Transactions on, 2006. **21**(3): p. 1698-1705.
  129. Oppenheim, A.V., and R.W. Schaffer., *Discrete-Time Signal Processing*. 1989, Upper Saddle River, NJ: Prentice-Hall.
  130. Hopewell, P.D., N. Jenkins, and A.D. Cross, *Loss-of-mains detection for small generators*. Electric Power Applications, IEE Proceedings -, 1996. **143**(3): p. 225-230.
  131. Kliber, J.W., Wang Wilsun, Xu. *Local anti-islanding protection for distributed generators based on impedance measurements*. in *Electric Power Conference, 2008. EPEC 2008. IEEE Canada*. 2008.
  132. César Trujillo, D.V., Emilio Figueres and Gabriel Garcerá, *Local and Remote Techniques for Islanding Detection in Distributed Generators*, Universidad Politécnica de Valencia, Universidad Distrital Francisco José de Caldas
  133. Lucas F. Aguiar, E.G., João Paulo C. L. da Costa and Rafael A. Shayani. *Tradeoff Between Total Harmonic Distortion and Efficiency in Coupling of a Classical Bridge Inverter and A Photovoltaic System*. Available from: [http://www.pgea.unb.br/~lasp/papers/Tradeoff\\_Lucas.pdf](http://www.pgea.unb.br/~lasp/papers/Tradeoff_Lucas.pdf).
  134. Bohan, L. and D. Thomas. *ROCOF protection in distributed system with noise and non-linear load*. in *Environment and Electrical Engineering (EEEIC), 2011 10th International Conference on*. 2011.
  135. Basak, P.S., A. K. Chowdhury, S. Chowdhury, S. P. *Microgrid: Control techniques and modeling*. in *Universities Power Engineering Conference (UPEC), 2009 Proceedings of the 44th International*. 2009.
  136. Michael Angelo Pedrasa, T.S., *A Survey of Techniques Used to Control Microgrid Generation and Storage during Island Operation*.
  137. Lasseter, R.H. *MicroGrids*. in *Power Engineering Society Winter Meeting, 2002. IEEE*. 2002.
  138. Engler, D.-I.A., *Applicability of Droops in Low Voltage Grids*. DER Journal January 2005. **No.1**.
  139. Xiangjun Li, Y.-J.S.a.S.-B.H., *Study on Power Quality Control in Multiple Renewable Energy Hybrid Microgrid System*. Power Tech, 2007.
  140. Best, R.J., D.J. Morrow, and P.A. Crossley. *Out-of-Phase Synchronization of a Small Alternator*. in *Power Engineering Society General Meeting, 2007. IEEE*. 2007.

141. Best, R., et al. *Universal application of synchronous islanded operation. in SmartGrids for Distribution, 2008. IET-CIRED. CIRED Seminar. 2008.*

## Appendix A

# Synchronous Generator Model

A synchronous generator model can be found in the machine library of SimPowerSystems BlockSet. In principle, this synchronous generator model is operated associating to the two input quantities—field excitation voltage ( $V_f$ ) and mechanical input power ( $P_m$ ). The generator model also gives the useful measured output signals ‘ $m$ ’ such as rotor speed deviation, electrical power generated, rotor speed, rotor angle deviation, load angle etc., which is necessary for the closed-loop control of the operation of the generator.

The magnitude of the terminal output voltage is proportional to the field excitation voltage, and the ability to supply the electrical power to loads is dependant on the mechanical input power. Therefore in order to keep the operation of the mechanical input power. Therefore in order to keep the operation of the generator in a stable condition, its output quantities are needed to be monitored and fed back to the control unit using the measured signals ‘ $m$ ’, as shown in Fig.A.1, to modulate the input values of both  $V_f$  and  $P_m$  corresponding to the electrical power output.

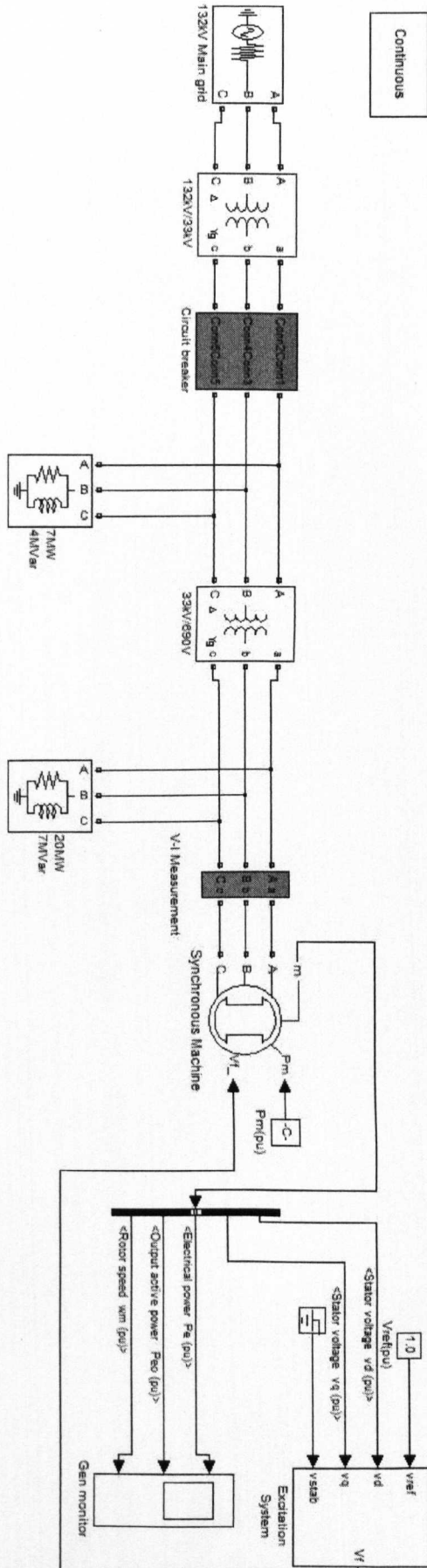


Fig. A.1 Simulation model of grid-connected synchronous generator

## Appendix B

# Controller Parameters for Grid-connected Inverter

The PI controller for inner current control loop is found through the pole-placement method which is described in Chapter 4. The plant of the inner current control loop is  $1/(L_g s + R_g)$  (where  $L_g = 0.2\Omega$ ,  $R_g = 0.002\Omega$ ). The outer DC-link voltage loop control is applied internal model control method as described in Chapter 4 as well. The parameters of the controller are shown in Table B.1.

Table B.1. PI-controller parameters for grid-connected inverter

	Proportional gain	Integral gain
Current loops	8.397	0.37
DC-link voltage loop	0.1	1318

## Appendix C

# Islanding Detection for Microgrid

### Case Two

The microgrid applied for islanding detection which consists 4.5MW photovoltaic system, 1MW synchronous generator, and 1.5MW DFIG wind turbine. The simulation results of ROCOF relays cooperation with  $v^2/p$  interlock function are shown below.

The system islanding simulation results for the microgrid are shown in Fig.C.1, Fig.C.2 and Fig.C.3 separately.

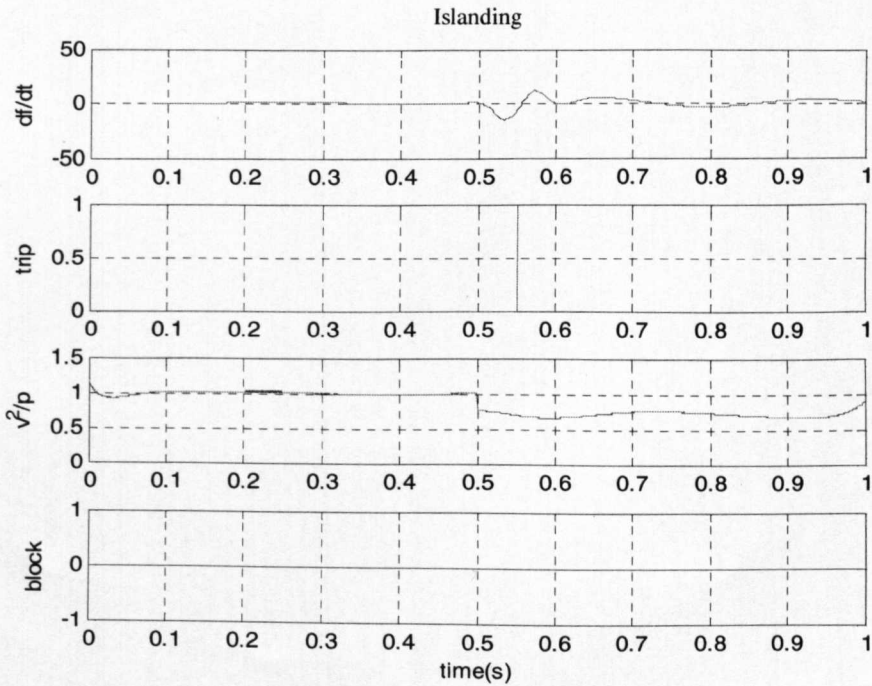


Fig.C.1 The islanding situation performance for DFIG ROCOF relay

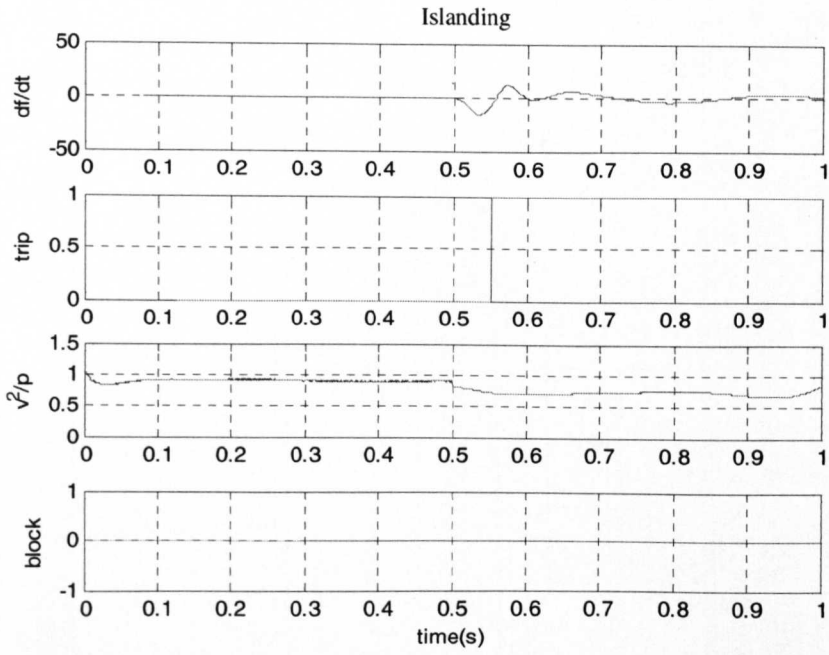


Fig.C.2 The islanding situation performance for photovoltaic system ROCOF relay

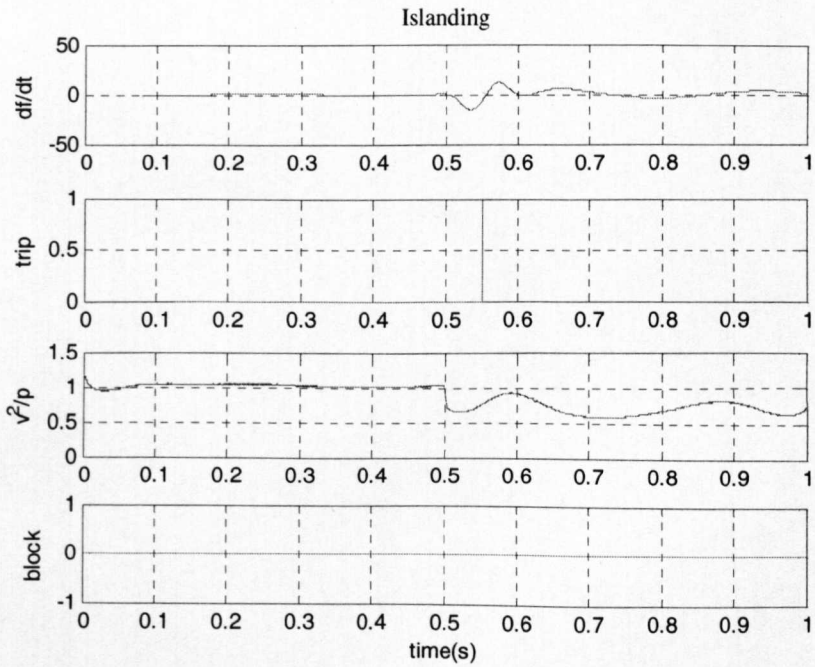


Fig.C.3 The islanding situation performance for synchronous generator ROCOF relay

The simulation results of system non-islanding for DFIG wind generator, photovoltaic system and synchronous generator of the micro-grid are shown in Fig.C.4, Fig.C.5 and Fig.C.6.

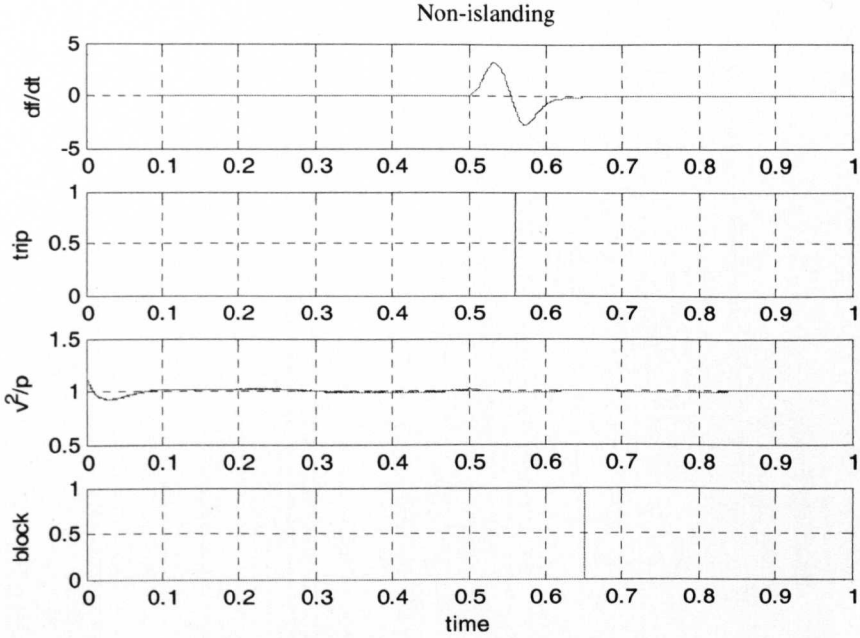


Fig.C.4 The non-islanding situation performance for DFIG ROCOF relay

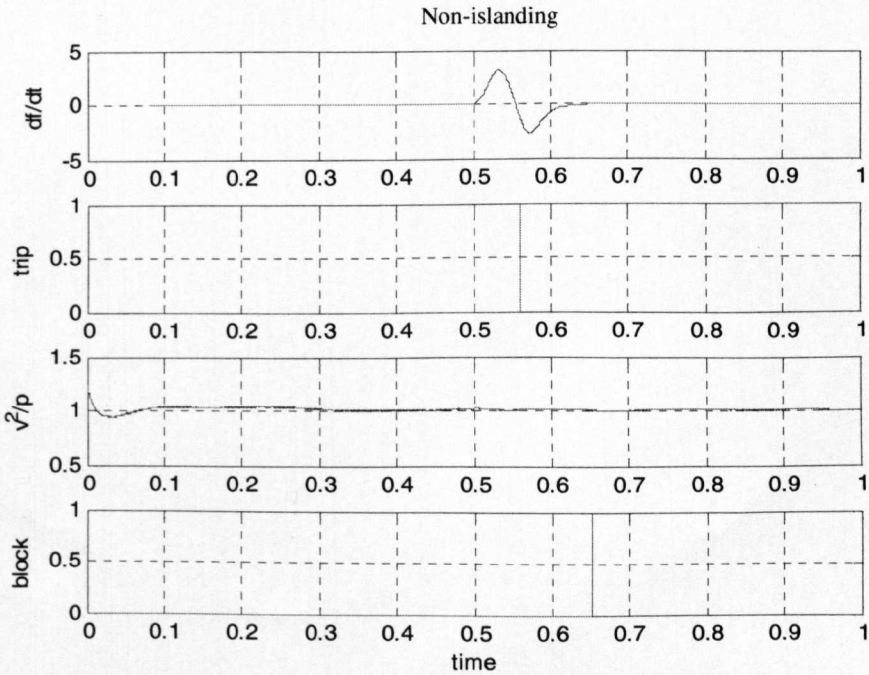


Fig.C.5 The non-islanding situation performance for photovoltaic system ROCOF relay

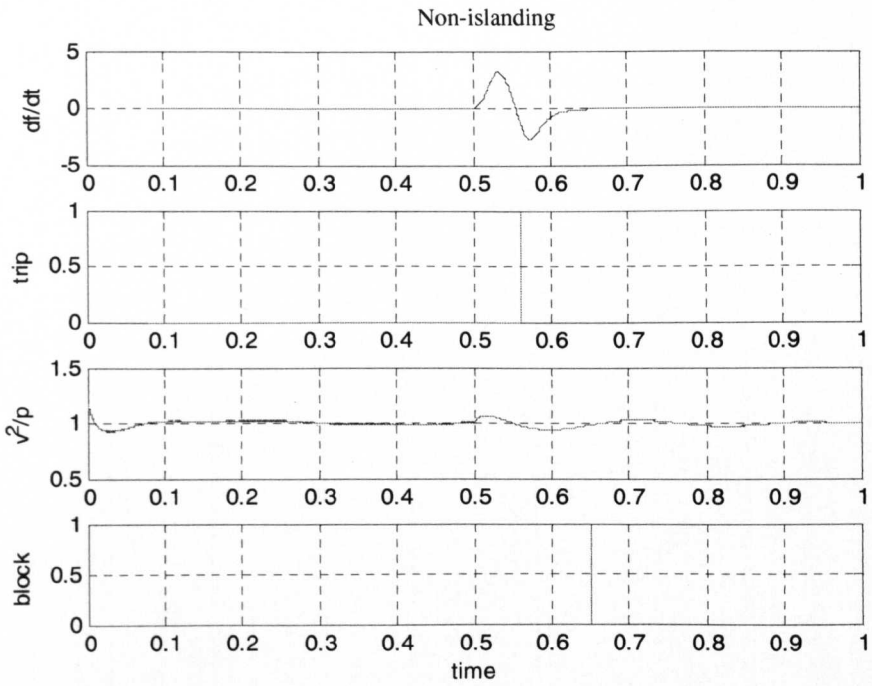


Fig.C.6 The non-islanding situation performance for synchronous generator ROCOF relay

For different load levels between the total microgrid generation power and the load demand, the evaluation of non-detection zone of ROCOF relay with  $v^2/p$  interlock function is shown in TableC.1.

Table C.1 Evaluation of the non-detection zone

Active power mismatch(Islanding)	$\Delta p = 5\%$	$\Delta p = 10\%$	$\Delta p = 15\%$
DFIG( $df/dt + v^2/p$ )	No trip	Trip	Trip
PV( $df/dt + v^2/p$ )	No trip	Trip	Trip
SG( $df/dt + v^2/p$ )	No trip	No trip	Trip